THE UNIVERSITY OF TEXAS AT AUSTIN
CENTER FOR TRANSPORTATION RESEARCH

TECHNICAL REPORT 0-6919-1
TxDOT PROJECT NUMBER 0-6919

Evaluation of Structural Cracking in Concrete: Final Report

Jarrod Zaborac
Apostolos Athanasiou
Salvatore Salamone
Oguzhan Bayrak
Trevor Hrynyk

August 2018; Published: April 2019

http://library.ctr.utexas.edu/ctr-publications/0-6919-1.pdf

Technical Report Documentation Page

1. Report No. FHWA/TX-19/0-6919-1	2. Government Accession No.	3. Recipient's Catalog No.
4. Title and Subtitle Evaluation of Structural Cracking in Concrete: Final Report		5. Report Date August 2018; Published: April 2019
		6. Performing Organization Code
7. Author(s) Jarrod Zaborac, Apostolos Athanasiou, Salvatore Salamone, Ph.D., Oguzhan Bayrak, Ph.D., and Trevor Hrynyk, Ph.D.		8. Performing Organization Report No. 0-6919-1
9. Performing Organization Name and Address Center for Transportation Research The University of Texas at Austin 3925 W. Braker Lane, 4th Floor Austin, TX 78759		10. Work Unit No. (TRAIS) 11. Contract or Grant No. 0-6919
12. Sponsoring Agency Name and Address Texas Department of Transportation Research and Technology Implementation Division P.O. Box 5080 Austin, TX 78763-5080		13. Type of Report and Period Covered Technical Report January 2016 – August 2018
		14. Sponsoring Agency Code

15. Supplementary Notes
Project performed in cooperation with the Texas Department of Transportation.

16. Abstract

Current methods used to assess structural cracking in concrete bridge infrastructure consist of various rating criteria in the form of pre-established concrete crack width and crack density limits. While cracking data obtained from routine inspections can aid in identifying bridge degradation, typical inspection techniques provide limited insight regarding the severity of structural distress. Further, inspection evaluation criteria are almost always independent of member-specific design details. The primary objective of this project was to develop crack-based strength assessment procedures that employ visual concrete crack data as input (e.g., measured crack widths, crack inclinations, crack patterns, etc.) and provide quantitative output related to bridge member health. Focus was given to developing procedures that require easy-to-obtain bridge member cracking data and the execution of low-cost analyses that can be performed using basic, and readily-available, software (e.g., MS-Excel or similar). Two different crack-based assessment procedures for in-service concrete bridge members were developed: i) a cracked continuum shear strength assessment procedure that is rooted in concepts of reinforced concrete mechanics and is used to examine shear-related distress in concrete bridge members, and ii) crack pattern quantification procedures that employ fractal analysis techniques to perform image-based assessments of crack patterns for the purpose of gaining insight into bridge member health. Research findings confirmed that diagonal crack widths, on their own, do not serve as reliable indicators of concrete member shear distress; however, mechanical modeling techniques that incorporate crack related input parameters can be used to conduct meaningful structural assessments for shear cracked bridge members. Further, the experimentally-validated cracked continuum assessment procedure can be used to develop member-specific crack inspection field aids to be employed on-site for the assessment of diagonal cracking in reinforced concrete bent caps.

17. Key Words Bent Caps, Crack Widths, Diagonal Cracking, Evaluation and Assessment, Shear Strength, Concrete Mechanics, Fractal Analysis, Visual Assessment		18. Distribution Statement No restrictions. This document is available to the public through the National Technical Information Service, Springfield, Virginia 22161; www.ntis.gov.	
19. Security Classif. (of report) Unclassified	20. Security Classif. (of this page) Unclassified	21. No. of pages 172	22. Price

Form DOT F 1700.7 (8-72) Reproduction of completed page authorized

THE UNIVERSITY OF TEXAS AT AUSTIN
CENTER FOR TRANSPORTATION RESEARCH

Evaluation of Structural Cracking in Concrete: Final Report

Jarrod Zaborac
Apostolos Athanasiou
Salvatore Salamone
Oguzhan Bayrak
Trevor Hrynyk

CTR Technical Report:	0-6919-1
Report Date:	Submitted: August 2018; Published: April 2019
Project:	0-6919
Project Title:	Evaluation of Structural Cracking in Concrete
Sponsoring Agency:	Texas Department of Transportation
Performing Agency:	Center for Transportation Research at The University of Texas at Austin

Project performed in cooperation with the Texas Department of Transportation and the Federal Highway Administration.

Disclaimers

Engineering Disclaimer

Research Supervisor: Trevor Hrynyk

Acknowledgments

The authors are sincerely grateful to the Texas Department of Transportation (TxDOT) for providing the funds to conduct this research study. The contributions of the project director, Chris Glancy, and the TxDOT project advisors including Andrew Smyth, Christopher Miller, Daniel Richardson, Jason Tucker, Kathleen Newton, Kevin Moyer, Kevin Pruski, and Todd Speck are greatly appreciated.

Table of Contents

List of Figures

List of Tables

Chapter 1. Introduction

This chapter serves as the introduction to the project report for Texas Department of Transportation (TxDOT) Project 0-6919. It discusses the project overview, the key objectives, and overall scope of the work performed. Additionally, the organization of this report is detailed at the end of this chapter.

1.1. Overview

Diagonal cracking of reinforced concrete (RC) bent caps has been reported across the state of Texas; however, standard procedures for the assessment of visually observed cracking lacks the necessary insight into structural performance associated with structural cracking in concrete. To address this need, TxDOT funded Project 0-6919 with the objective of developing procedures which can assist in quantitatively interpreting the structural implications of cracking in RC infrastructure.

1.2. Project Objectives

As RC bridge infrastructure ages, it has become increasingly important to have damage assessment techniques which are not only practical and reliable, but also provide quantitative insight into the implications of observed cracking. While traditional methods of damage assessment can aid in identifying signs of distress, they typically have not been used to link visual crack data to meaningful assessments regarding structural capacity. Different methods have been proposed in the past several decades to address this problem and have met with varying levels of success.

This project aims to develop and verify crack-based shear strength assessment procedures which can be used as supplemental tools for decision making, to assist in prioritizing maintenance and repair efforts, and to identify critical strength-related deficiencies. In that light, two assessment procedures were developed, and subsequently evaluated and refined, to address these needs.

1.3. Project Scope

In working toward accomplishing the objectives established for TxDOT Project 0-6919, the following tasks were developed and carried-out:

1. Conduct a review of technical literature and review of relevant field data to determine:

    - State of the art in damage-based structural assessment
    - Available experimental structural crack measurement data
    - State of structural cracking in existing TxDOT Bridges
2. Assemble a Visual Crack Measurement Evaluation Database using data collected during the literature review
3. Develop two crack-based shear strength assessment procedures:
    - Cracked continuum shear strength assessment on the basis of cracked concrete mechanics
    - Crack pattern quantification using fractal analysis
4. Evaluate and refine preliminary crack-based strength assessment procedures
5. Create "visual crack inspection field aids" based on the refined procedure

The literature review and database assembly directly informed the development, as well as the evaluation and refinement, of the procedures developed. It was determined that while some variants of mechanics-based and fractal analysis techniques existed in the database of literature, they were yet to be extensively validated and generally had limited ranges of applicability making them unsuitable for real-world usage. Moreover, the available experimental structural crack measurement data was also typically limited, which led to significant data processing and classification work to determine the best way to develop, evaluate, and refine the damage-based structural assessment procedures proposed herein. The two procedures (cracked continuum shear strength assessment and crack pattern quantification) were carefully developed and refined to provide recommendations about their implementation for the assessment of in-service structures. Further, a visual crack inspection field aid construction method was proposed for application to TxDOT bridge members.

1.4. Organization

This report is divided into six chapters. Chapter 2 presents an overview of the state-of-the-art in damage-based structural assessment of RC members. Moreover, it discusses those tools which are employed in practice and those which exist in the literature and have yet to be widely adopted.

Chapter 3 details the development of the Visual Crack Measurement Evaluation Database. It begins with a summary of structural cracking in existing TxDOT bridges and follows with a discussion of the type of data comprising the database. Lastly, it presents the usage of the database.

The first of the two procedures, the cracked continuum shear strength assessment, is presented in Chapter 4. First a preliminary procedure method is presented. Then, findings obtained from evaluating and subsequently refining that procedure are presented. Lastly, the application of the proposed/refined procedure for the purpose of constructing of a visual crack inspection field aid is discussed.

Chapter 5 presents background information related to the fractal and multifractal analysis approaches for the quantification of crack patterns. The approaches are then applied to two different structural members: a pretensioned Tx-girder and a series of RC panel elements under shear. For both datasets the results obtained by the analysis of the crack patterns are compared with the structural response of the specimens. Each section of Chapter 5 is accompanied with a short discussion summarizing the influence of the measured structural performance (i.e., development of new cracks, increased damage levels, etc.) on the fractal and multifractal properties of the crack patterns.

The final chapter, Chapter 6, summarizes the key findings and conclusions obtained from the work comprising TxDOT Project 0-6919.

Chapter 2. State-of-the-Art in Damage-Based Structural Assessment

Currently, the state of damage in cracked reinforced and prestressed concrete structures is commonly categorized by comparing crack data obtained from visual inspections with some form of pre-established crack-width, or crack density, limits. Unfortunately, this practice typically provides limited information pertaining to the structural capacity implications of concrete cracking observed in the field. While many procedures have been proposed in the literature to address this limitation, the existing procedures vary in terms of accuracy, ease of use, level of validation, and applicability. This chapter provides an overview of previously-established damage-based structural assessment techniques, ranging from methods regularly employed in practice to those which have been proposed in the literature.

The organization of this chapter is as follows: Tools Employed in Practice, Existing Strength Assessment Techniques, and, lastly, a Summary.

2.1. Tools Employed in Practice

Current methods used for the evaluation of reinforced concrete (RC) structures rely on several different standards. Department of Transportation (DOT) requirements vary slightly from state to state, but the standards can ultimately be tied back to guidelines from two organizations: the Federal Highway Administration (FHWA) and the American Association of State Highway and Transportation Officials (AASHTO). Additionally, the International Atomic Energy Agency (IAEA) provides general information on RC tools for the assessment of damaged structures, and details pertaining to inspection methods ranging from visual inspection methods to other, more rigorous and advanced, techniques.

The FHWA maintains a database of the nation's bridges called the National Bridge Index (NBI). The *Recording and Coding Guide of the Structure Inventory and Appraisal of the Nation's Bridges* (FHWA, 1995) provides a standard for recording relevant data to meet federal requirements. Most of the information stored on the "Structure Inventory and Appraisal Sheet" is related to identifying and locating the bridge as well as classifying geometric and navigation data. Of interest for the damage assessment of in-service bridges is the "Condition" subsection, which contains lines for coding the condition of the deck, superstructure, and substructure. Channel and channel protection, as well as culverts, also have condition ratings. The condition ratings are done using the ten-point scale shown in Table 2.1. Additionally, the "Load Rating and Posting" subsection of the guidelines classify the operating rating and the maximum load considered safe for the structure. The following methods are permissible for calculating this value: load factor (LF), allowable stress (AS), load and resistance factor (LRFR), and load testing. These methods use the condition ratings, in addition to other design details, to apply a reduction to the capacity of a member/structure. The condition factor from the LRFR method is divided into three categories: good or satisfactory (1.00), fair (0.95), or poor (0.85). These factors are analogous to typical safety factors from the traditional design process, that is, the factors are associated with anticipated variability in capacity based on member deterioration (AASHTO, 2005). The LF method is used for recording in the NBI, although the other methods may be used for posting.

Table 2.1 FHWA codes and descriptions (reproduced from FHWA, 1995)

Code	Description
N	NOT APPLICABLE
9	EXCELLENT CONDITION
8	VERY GOOD CONDITION – no problems noted.
7	GOOD CONDITION – some minor problems.
6	SATISFACTORY CONDITION – structural elements show some minor deterioration.
5	FAIR CONDITION – all primary structural elements are sound but may have minor section loss, cracking, spalling or scour.
4	POOR CONDITION – advanced section loss, deterioration, spalling or scour
3	SERIOUS CONDITION – loss of section, deterioration, spalling or scour have seriously affected primary structural components.
2	CRITICAL CONDITION – advanced deterioration of primary structural elements. Fatigue cracks in steel or shear cracks in concrete may be present or scour may have removed substructure support. Unless closely monitored it may be necessary to close the bridge until corrective action is taken.
1	“IMMINENT” FAILURE CONDITION – major deterioration or section loss present in critical structural components or obvious vertical or horizontal movement affecting structure stability. Bridge is closed to traffic, but corrective action may put back in light service.
0	FAILED CONDITION – out of service – beyond corrective action.

Appendix B of the *Recording and Coding Guide of the Structure Inventory and Appraisal of the Nation’s Bridges* contains a potentially useful tool called the Sufficiency Rating Formula. The formula is used to estimate a bridge’s serviceability. Using information from the Structure Inventory and Appraisal Sheet, the Sufficiency Rating Formula provides a value ranging between 0 and 100 %, wherein 0 % is considered “entirely insufficient” and a 100 % is “entirely sufficient” (FHWA, 1995). The sufficiency rating uses four primary categories: structural adequacy and safety, serviceability and functional obsolescence, essentiality for public use, and special reductions. Note that although structural adequacy and safety (which includes results from inspection of bridge damage) is included in the Sufficiency Rating, it is not necessarily indicative of structural capacity; however, a bridge inspector may use this rating to assist in making decisions about whether a bridge should remain in service or not.

AASHTO produces the *AASHTO Bridge Element Inspection Manual* (2010) which, when used as input in the bridge management system provided by the FHWA, is considered a satisfactory substitute for these provisions. While the *Recording and Coding Guide of the Structure Inventory and Appraisal of the Nation's Bridges* uses a broad rating system for deck, superstructure, and substructure, the *Bridge Element Inspection Manual* (AASHTO, 2010) contains more explicit guidance for the classification of various bridge elements. Additionally, the rating system uses four condition states, rather than the ten-point code system. Table 2.2 shows condition states and descriptions of typical defects associated with a RC closed web/box girder element. Table 2.3 provides some quantitative guidance on the qualitative traits (e.g., hairline, narrow, and medium) given in Table 2.2, to assist condition state classification.

Table 2.2 Condition state definitions for RC closed web/box girder elements (reproduced from AASHTO, 2010)

Defect	Condition State 1	Condition State 2	Condition State 3	Condition State 4
Cracking	None to hairline	Narrow size and/or density	Medium size and/or density	The condition is beyond the limits in condition state (3) and/or warrants a structural review to determine the strength or serviceability of the element or bridge.
Spalls/ Delaminations/ Patched Areas	None	Moderate spall or patch areas that are sound	Severe spall or patched area showing distress	
Efflorescence	None	Moderate without rust	Severe with rust staining	
Load Capacity	No reduction	No reduction	No reduction	

Table 2.3 Defect guidelines (reproduced from AASHTO, 2010)

Defect	Hairline-Minor	Narrow- Moderate	Medium-Severe
Cracking	< 0.0625 inches (1.6 mm)	0.0625 – 0.125 inches (1.6 – 3.2 mm)	> 0.125 inches (3.2 mm)
Spalls/ Delaminations	N/A	Spall less than 1 inch (25 mm) deep or less than 6 inches in diameter	Spall greater than 1 inch (25 mm) deep or greater than 6 inches in diameter or exposed rebar
Cracking Density	Spacing Greater than 3.0 feet (0.33 m)	Spacing of 1.0 – 3.0 feet (0.33 – 1.0 m)	Spacing of less than 1 foot (0.33 m)
Efflorescence	N/A	Surface white without build-up or leaching	Heavy build-up with rust staining

Many states have published their own reference manuals or tools that provide more state specific guidance for bridge inspection (Michigan Department of Transportation, 2011; Montana Department of Transportation, 2015; Ohio Department of Transportation, 2014; Oregon Department of Transportation, 2009;

Pennsylvania Department of Transportation, 2009; Texas Department of Transportation, 2013). The contents of these publications vary from state to state and range from summaries and modifications of federal standards to "pocket coding guides" to create a standardized, uniform inspection processes across the state. Some states, such as Texas, refer to FHWA standards while others refer more directly to AASHTO. The ODOT (2009) *Bridge Inspection Pocket Coding Guide* uses the provisions from the *AASHTO Bridge Element Inspection Manual*, but includes visual standards, such as the examples shown in Figure 2.1, to assist in the classification of the condition state of a structural element.

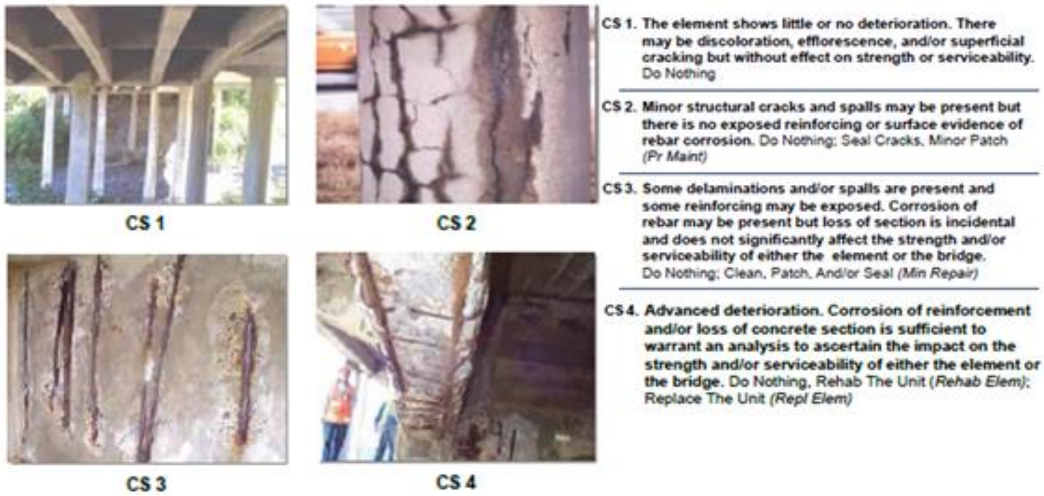

CS 1. The element shows little or no deterioration. There may be discoloration, efflorescence, and/or superficial cracking but without effect on strength or serviceability. Do Nothing

CS 2. Minor structural cracks and spalls may be present but there is no exposed reinforcing or surface evidence of rebar corrosion. Do Nothing; Seal Cracks, Minor Patch *(Pr Maint)*

CS 3. Some delaminations and/or spalls are present and some reinforcing may be exposed. Corrosion of rebar may be present but loss of section is incidental and does not significantly affect the strength and/or serviceability of either the element or the bridge. Do Nothing; Clean, Patch, And/or Seal *(Min Repair)*

CS 4. Advanced deterioration. Corrosion of reinforcement and/or loss of concrete section is sufficient to warrant an analysis to ascertain the impact on the strength and/or serviceability of either the element or the bridge. Do Nothing, Rehab The Unit (*Rehab Elem*); Replace The Unit *(Repl Elem)*

Figure 2.1 Visual reference for evaluating condition states (ODOT, 2009)

The *Guidebook on Nondestructive Testing of Concrete Structures* (IAEA, 2002) has similar criteria to the *Bridge Element Inspection Manual*, shown in Tables 2.4 and 2.5. It utilizes a three-stage grading scale and provides explicit crack width ranges for severity classification. Additionally, it provides further details for crack damage classification based on crack location. The IAEA *Guidebook* also contains details regarding the tools required for a variety of common inspection procedures, such as the visual inspection. Furthermore, if it were required based on the results of a visual inspection, the guidebook provides additional details pertaining to more in-depth inspection procedures involving as ultrasound or infrared thermography inspection techniques.

Table 2.4 Criteria for assessment of degree of deterioration (reproduced from IAEA, 2002)

Kind of deterioration	Unit for classification	Grade I	Grade II	Grade III
Cracks along main bars	No. of 1 m crack lengths per 100 m^2	0	1-2	3 and over
Cracks along supplementary bars	No. of 1 m crack lengths per 100 m^2	0-2	3-4	5 and over
Cracks around openings	Number of cracks for 10 openings	0-2	3-4	5 and over
Mesh cracks	Area of meshed cracks as a %	less than 5%	5-10%	10% and over
Other cracks	No. of 1 m crack lengths per 100 m^2	0-4	5-9	10 and over

Table 2.5 Guide to assess grade of crack (reproduced from IAEA, 2002)

Crack severity	Crack width in mm Outdoor crack	Crack width in mm Indoor crack
I	< 0.05	< 0.2
II	0.05~0.5	0.2~1.0
III	> 0.5	> 1.0

The methods currently employed in practice to evaluate RC structures are practical in terms of their ability to recommend action based on visually inspected damage without the use of overly complicated or costly tools. Additionally, these methods are typically simple to implement as they usually require little input and the output is straightforward with clear guidelines for remedial action. Furthermore, these methods are well established and have been used for several decades; as such, there is a level of comfort and trust in their use. However, the quality of the observations and results from current methods are highly dependent on the individual inspector's experience. Additionally, these methods typically provide little information on the calculation of residual structural capacity. These two factors may lead to rehabilitation money being prioritized for bridges that, from a load-resisting standpoint, are structurally adequate while others that have suffered damage more likely to reduce a bridge's capacity may be deemed lower priority or may potentially be insufficiently rehabilitated.

2.2. Existing Strength Assessment Techniques

There are several methods available for estimating the residual capacity of cracked concrete sections. These methods range from visual inspections and empirically derived tools, to theoretical models based on fracture mechanics, fractal analysis, multi-fractal analysis, and concrete mechanics. A number of these methods are reviewed in the following subsections of this chapter.

2.2.1. Finite Element Analysis

Several researchers have attempted to use Finite Element Analysis (FEA) procedures to estimate the structural capacity of cracked concrete sections. There are two main approaches in modeling cracking in concrete members. One of the original approaches used in such analyses is the discrete crack model, where cracks are explicitly modeled in the finite element analysis by creating new nodes for crack surfaces when cracks start to form (de Borst et al., 2012). An alternative, which has garnered more attention in recent decades, is the smeared crack approach, where cracks are assumed to be smeared over a continuum and the deterioration is captured through use of a constitutive model (de Borst et al., 2004). The behavior of cracked concrete can be modeled in FEA using several different methods, including: fracture mechanics models, concrete plasticity models, concrete nonlinear elasticity models, or some combination thereof.

2.2.1.1. Computational Fracture Mechanics

Hillerborg et al. (1976) reported the use of a crack tip plasticity model based on fracture mechanics principles together with FEA that seemed to result in *"realistic results regarding crack formation and propagation"* in concrete. Since that time, computational fracture mechanics of concrete has undergone significant progress, and has been used in the seismic safety evaluation of dams, nuclear power plants, and other structures (Wang et al., 2013). An example of computational fracture mechanics used as a structural assessment tool is the fracture mechanics model proposed by Sain and Kishen (2007) that aims to predict the residual flexural capacity of cracked plain or RC beams on the basis of damage. For RC beams, the normalized moment capacity ($\frac{M_f}{K_c D^{3/2} t}$), as a function of relative crack depth ($\frac{a}{D}$), can be calculated from Equation 2.1, where a is the crack length, D is the beam depth, and d_s is the concrete cover. N_p can be calculated from Equation 2.2, where reinforcement is assumed to have yielded. Y_M and Y_F are geometric factors that are proportional to the relative crack depth. The values of the material fracture toughness (K_c) of specimens tested by Bažant and Xu (1991) and Slowik et al. (1996) are listed in Table 2.6.

$$\frac{M_f}{K_c D^{3/2} t} = \frac{1}{Y_M(a/D)} + N_p \left[\frac{Y_F(a/D)}{Y_M(a/D)} + \frac{1}{2} - \frac{d_s}{D} \right] \qquad 2.1$$

$$N_p = \frac{f_y D^{2/3} A_s}{K_c A} \qquad 2.2$$

Table 2.6 Geometry and material properties of specimens

Specimen	Depth, mm	Width, mm	Span, mm	Initial notch, mm	E, MPa	K_c, MN/m$^{3/2}$
Compact tension	900	400	—	230	17,000	1.48
Compact tension	300	100	—	50	16,000	0.95
Beam	152.4	38.1	381	25.4	27,120	1.41
Beam	76.2	38.1	191	12.7	27,120	1.51
Beam	38.1	38.1	95	6.35	27,120	1.66

Note: 25.4 mm = 1 in.; 1 MPa = 145 psi; 1 MN/m$^{3/2}$ = 907 lbs/in.$^{3/2}$.

The results obtained from applying Equation 2.1 to perform a parametric investigation on a 14-inch deep by 4-inch wide RC beam with an initial notch length of 1.5 inches subjected to three-point bending are presented in Figure 2.2. As the amount of steel reinforcement increases, N_p correspondingly increases, and the normalized moment capacity is increased, as expected. For the same N_p value, the normalized moment capacity decreases as the relative crack depth increases from an initial small value. In this example case, the authors obtained normalized moment at failure of 0.3 using their proposed method, which corresponds to a failure load of 6.4 kips. This is very close to the experimental failure load of 6.5 kips reported by Carpinteri (1984).

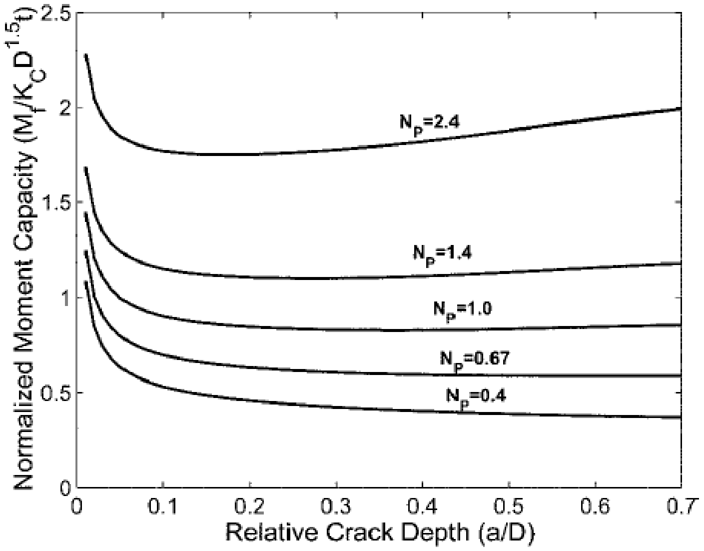

Figure 2.2 Normalized moment capacity corresponding to different N_p values (Sain & Kishen, 2007)

2.2.1.2. Combination of Fracture Mechanics and Concrete Mechanics Models

Other researchers have suggested the use of different types of finite element analyses. For example, Wang et al. (2013) proposed using a mixed modeling approach for crack analysis. In this approach, a discrete crack procedure was used to model the existing cracks on a beam and the smeared crack approach was used to simulate new cracks forming under incremental monotonic loading using a live load factor ρ. They performed a structural analysis of an existing 80-year old bridge using the commercial software DIANA to estimate its load carrying capacity by considering the effects of the existing cracks. Figure 2.3 shows the finite element (FE) model of the bridge and the applied loads on the bridge.

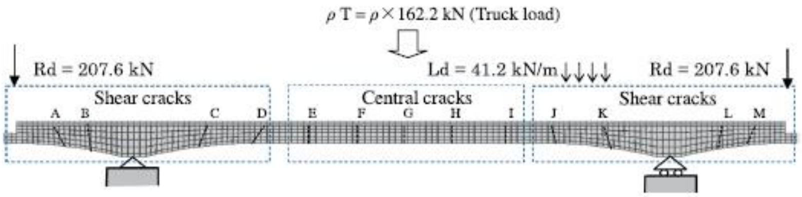

Note: 1 m = 39.37 in. ; 1 kN = 224.8 lbs

Figure 2.3 FE model of the bridge and applied loading conditions (Wang et al., 2013)

The existing cracks were modeled using interface elements that allowed the initial cracks to open once the surface of these interface elements was subject to tension. The angle of inclination for each initial crack was intended to match the cracks observed from field inspection as closely as possible. However, since it is difficult to estimate the extent of the crack depth from visual inspection, the researchers carried out a parametric study by varying the size of all the initial crack depths from H/5 to 4H/5, where H is the girder depth. This was done for three scenarios: incorporating existing damage attributed to (i) only the shear cracks, (ii) only the flexural cracks, and (iii) both the shear cracks and the flexural cracks. The effect of the depth of the initial cracks on the computed structural behavior of the girder can be observed in the load-displacement curves for the three analysis scenarios, as shown in Figure 2.4.

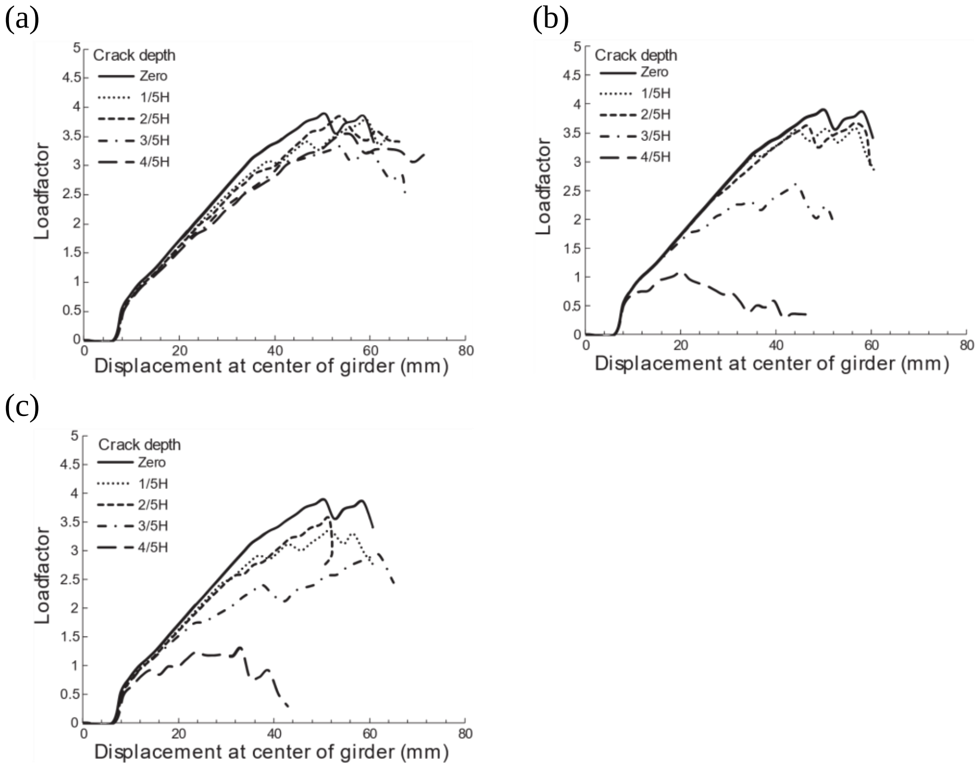

Figure 2.4 Load-displacement curves for: (L to R) increasing initial flexural crack depths, increasing initial shear crack depths, and increasing initial flexural and initial shear crack depths (Wang et al., 2013)

Based on the results of their study, they concluded that changing the depth of the initial flexural cracks did not change the failure mode of the structure, which remained governed by flexure. Further, only limited reduction in the load carrying capacity resulted from increasing the initial crack depth. However, increasing the crack depths of the initial shear cracks changed the failure mode from flexure to shear-controlled. For the third scenario where both the initial flexural and shear crack depths were increased, the mode of failure remained flexure, until the crack depth was increased to 4H/5 and a shear failure was estimated to control.

Another parametric study was recently carried out to estimate the residual capacity of concrete bridge columns. Talley et al. (2014) tested four column specimens and then used the computer software ATENA (Červenka & Červenka, 2015) to simulate initial column damage, as well as to predict residual capacities for a range of damage levels measured by varying the initial crack widths. The critical crack width was then be estimated by finding the initial crack width that would reduce the column capacity to its nominal design load. ATENA was chosen because it could model various levels of pre-existing cracks in the columns, as well as the subsequent crack propagation and column capacities. Concrete constitutive modeling was done according to a three-dimensional fracture-plastic model that combines tension fracturing with compressive plastic behavior. The material modeling parameters were calibrated by varying the user-specified fracture energy of the concrete material until the computed peak capacities and crack patterns matched experimental results.

The existing through-section vertical cracks in the columns were created by applying through-section line loads in the concrete voids. For initial crack widths 0.5 inches and smaller, the predicted capacity was close to the experimental capacity for two of the column specimens. For the two remaining columns that had initial crack widths of 1.22 inches and larger, the FEA predicted capacity was found to be about 80 % of the measured experimental capacity. The load-displacement behavior for a column with an initial crack width of 1.22 inches is shown in Figure 2.5. The researchers believed that this discrepancy was due to local crushing at the column base that governed the analytical response; however, this was not observed experimentally. Additionally, a parametric study was carried-out using larger initial crack widths to estimate the critical crack width at which the column capacity would be the same as the nominal design load of the column, as shown in Figure 2.6.

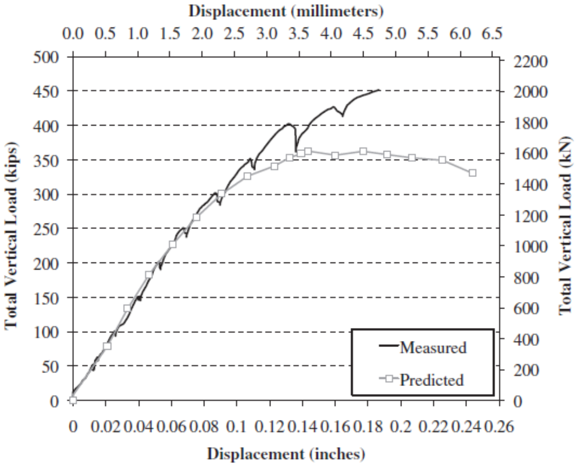

Figure 2.5 Load-displacement behavior for a column with an initial crack width of 1.22 inches (Talley et al., 2014)

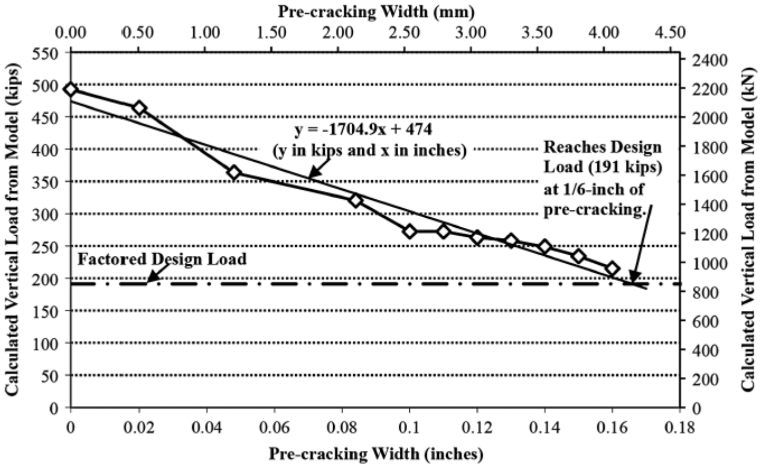

Figure 2.6 Estimating the critical crack width based on results from ATENA analyses (Talley et al., 2014)

2.2.1.3. Damage Index Based on FEA

Some researchers have used finite element analyses to numerically develop RC structure relevant damage indices. For instance, Alembagheri & Ghaemian (2013) created a finite element model of an arch dam and carried out nonlinear incremental dynamic analyses (Vamvatsikos & Cornell, 2002) to estimate damage from different intensity earthquakes. They subjected the dam to a series of 12 seismic ground motions with 12 increasing intensity levels for each earthquake. Based on the numerical results obtained from their study, they developed a damage index (DI) based on maximum dam crest displacement. For example, if the DI was found to equal a value of 1.0, the current maximum crest displacement would be equal to the maximum crest displacement at "ultimate" and thus, the residual capacity of the dam would be zero.

Others have also proposed using damage indices arising from finite element analyses. Park et al. (2001) developed a finite element model to predict potential crack locations for a box-girder bridge. Results were shown to closely correlate with observed crack locations from two separate visual inspections. Similarly, some researchers have used FEA to predict damage or residual capacity for RC columns subjected to earthquake loads (Kono et al., 2006) or even blast (Li et al., 2012).

2.2.1.4. Discussion

From the examples reviewed in this subsection, FEA can be a useful tool in predicting the structural capacity of cracked concrete members. However, it is important to note that using FEA can be very time consuming, and it requires experienced users to build high resolution finite element models that adequately reflect the structure details and damage. Furthermore, it should also be noted that accurate modeling of RC infrastructure still presents an existing challenge as a result of complex behavior, and no single approach or material model has been shown capable of providing good results over the large spectrum of structural details and loading conditions encountered in practice (Vecchio, 2001).

2.2.2. Structural Assessment Based on Observed Damage

Attempts have been made to mitigate the shortcomings of visual inspections by trying to correlate residual capacities of cracked concrete members to the visual damage observed from field inspections. For example, Abi Shdid et al. (2006) proposed a visual rating system with categories ranging from 1 to 4, as well as an estimate in the loss of capacity corresponding to different levels of visible damage on prestressed concrete bridge piles. Visual inspections were carried out on 12 piles before they were removed from the field. These piles were then loaded to failure in flexure under four-point bending. The actual loss of capacity from the test was then compared to the predicted loss of capacity from the visual rating system. The researchers found that for 6 of the 12 piles, the loss of capacity predicted from visual inspection was within 10 % of the actual loss in capacity. However, the procedure overestimated the actual capacity for 2 of the piles, and 4 of the piles were found to have an actual flexural capacity that was greater than that predicted. Ultimately, they concluded that the assessments arising from visual inspection may not necessarily correlate well with the actual flexural capacity of piles.

Similarly, there have been studies attempting to correlate damage states to observed damage after earthquakes (Gulkan & Yakut, 1996; Melchor-Lucero & Ferregut, 1996; Paal et al., 2015). In a report prepared for the California Department of Transportation, Veletzos et al. (2008) proposed a methodology to estimate the residual seismic capacity of damaged RC bridge columns after an earthquake, based on visual damage measurements. The first step of the methodology was to assign a performance member curve that was either ductile, strength degrading, or brittle, as shown in Figure 2.7. The second step of the methodology was to assess the damage level by checking for diagonal cracks, horizontal cracks, incipient concrete crushing or spalling, longitudinal bar buckling, and rupture of transverse reinforcement during field inspections. The engineer was pointed to the information provided in Tables 2.7 and 2.8, as well as a Visual Catalog of Bridge Damage (Veletzos et al., 2008) for guidance on appropriate damage assessment. The third step of the methodology was to plot the residual capacity on the performance curve based on the level of damage estimated in the previous step.

It is pertinent to note that this procedure would likely be of limited applicability for typical Texas bridge members, particularly in the cases of deep beams or bent cap members as their load-displacements would be expected to be much stiffer, and potentially even brittle, and would certainly vary based on reinforcement ratio and shear span to depth ratio. Thus, it is worth noting that the performance of such

Texas bridge members would be expected to be markedly different from the ductile columns comprising this specific performance evaluation research program.

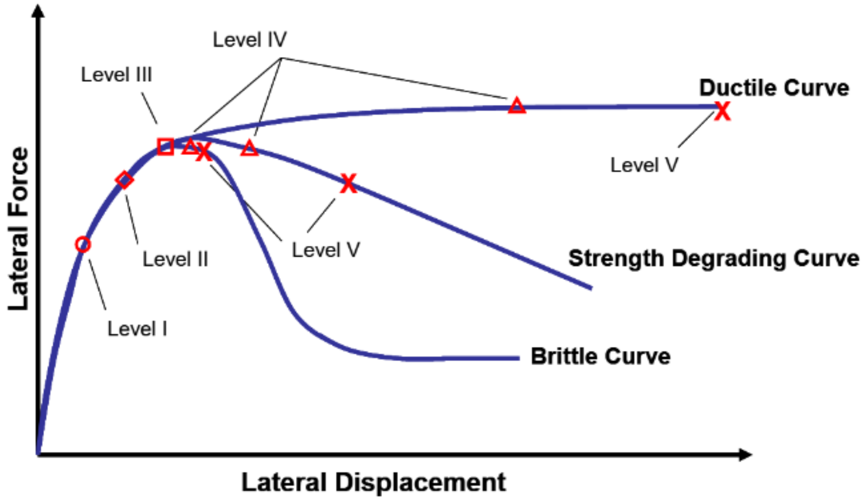

Figure 2.7 Performance curves (Veletzos et al., 2008)

Table 2.7 Performance assessment of damaged bridge columns *(Veletzos et al., 2008)*

Damage Level	Performance Level	Qualitative Performance Description	Quantitative Performance Description
I	Cracking	Onset of hairline cracks	Barely visible residual cracks
II	Yielding	Theoretical first yield of longitudinal reinforcement	Residual crack width ~ 0.008in
III	Initiation of Local Mechanism	Initiation of inelastic deformation. Onset of concrete spalling. Development of diagonal cracks.	Residual crack width 0.04in – 0.08in Length of spalled region > 1/10 cross-section depth.
IV	Full Development of Local Mechanism	Wide crack widths/spalling over full local mechanism region.	Residual crack width > 0.08in. Diagonal cracks extend over 2/3 cross-section depth. Length of spalled region > ½ cross-section depth.
V	Strength Degradation	Buckling of main reinforcement. Rupture of transverse reinforcement. Crushing of core concrete.	Lateral capacity below 85% of maximum. Measurable dilation > 5% of original member dimension.

Table 2.8 Decision making matrix for damaged bridge columns *(Veletzos et al., 2008)*

Field Observations				Conclusions	
Pronounced Horizontal Cracks	**Pronounced Diagonal Cracks**	**Incipient Concrete Crushing/ Spalling**	**Long. Bar Buckling**	**Damage Level**	**Possible Failure Type**
No	Yes	No	No	III	Shear
Yes or No	Yes	Yes	Yes or No	IV or V	Shear
Yes	No	No	No	II or III	Flexure
Yes	No	Yes	No	IV	Flexure
Yes	No	Yes	Yes	V	Flexure

2.2.3. Empirical Methods

The University of Texas at Austin carried out a series of experiments on 37 RC deep beams under Texas Department of Transportation (TxDOT) Project 5253 (Birrcher et al., 2009). To correlate residual capacity to diagonal crack widths, the results of 21 RC deep beams with a shear-span-to-depth (a/d) ratio of 1.85 were plotted and used to examine the relationship between diagonal crack width and the applied load level, as shown in Figure 2.8. A chart, shown in Figure 2.9, was also provided to assist field engineers in obtaining a quick estimate of the residual capacity of deep beams based on diagonal crack widths measured on site. It was noted that for the beams with an a/d ratio of 1.2 the chart worked well up to a load level on the order of 60 to 70 % of the ultimate capacity, as shown in Figure 2.10. It was recommended that the use of the chart be limited to deep beams with a/d ratios ranging from 1.0 to 2.0.

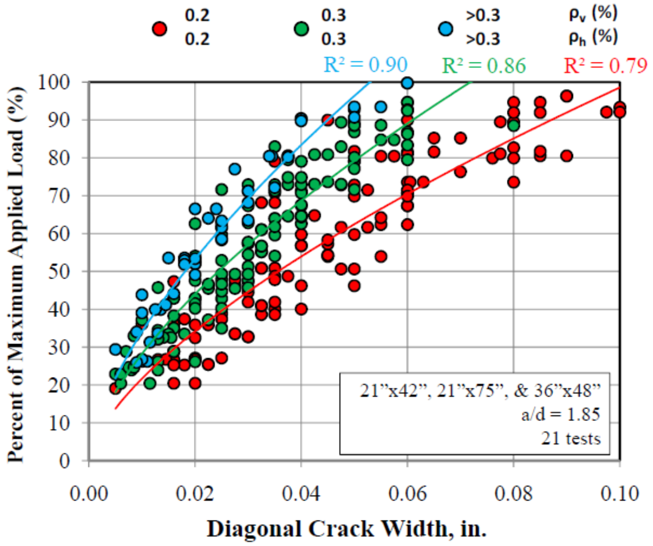

Figure 2.8 Applied load to diagonal crack width relationship (Birrcher et al., 2009)

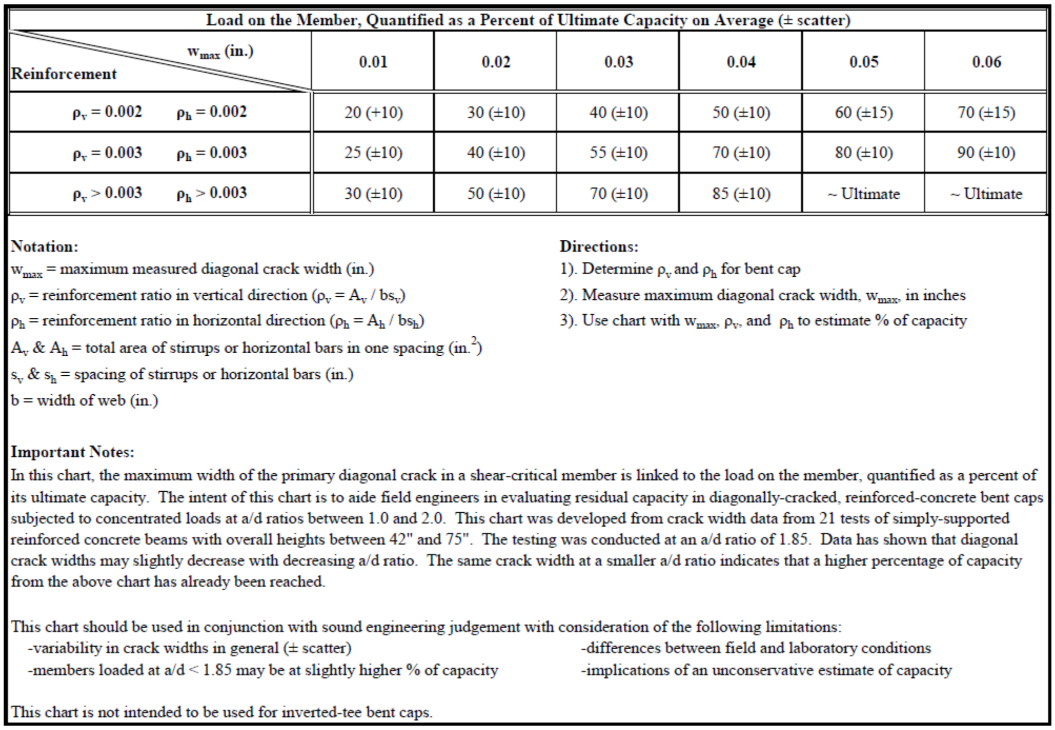

Reinforcement \ w_{max} (in.)	0.01	0.02	0.03	0.04	0.05	0.06
	Load on the Member, Quantified as a Percent of Ultimate Capacity on Average (± scatter)					
$\rho_v = 0.002$ $\rho_h = 0.002$	20 (+10)	30 (±10)	40 (±10)	50 (±10)	60 (±15)	70 (±15)
$\rho_v = 0.003$ $\rho_h = 0.003$	25 (±10)	40 (±10)	55 (±10)	70 (±10)	80 (±10)	90 (±10)
$\rho_v > 0.003$ $\rho_h > 0.003$	30 (±10)	50 (±10)	70 (±10)	85 (±10)	~ Ultimate	~ Ultimate

Notation:

w_{max} = maximum measured diagonal crack width (in.)
ρ_v = reinforcement ratio in vertical direction ($\rho_v = A_v / bs_v$)
ρ_h = reinforcement ratio in horizontal direction ($\rho_h = A_h / bs_h$)
A_v & A_h = total area of stirrups or horizontal bars in one spacing (in.^{2})
s_v & s_h = spacing of stirrups or horizontal bars (in.)
b = width of web (in.)

Directions:

1). Determine ρ_v and ρ_h for bent cap
2). Measure maximum diagonal crack width, w_{max}, in inches
3). Use chart with w_{max}, ρ_v, and ρ_h to estimate % of capacity

Important Notes:

In this chart, the maximum width of the primary diagonal crack in a shear-critical member is linked to the load on the member, quantified as a percent of its ultimate capacity. The intent of this chart is to aide field engineers in evaluating residual capacity in diagonally-cracked, reinforced-concrete bent caps subjected to concentrated loads at a/d ratios between 1.0 and 2.0. This chart was developed from crack width data from 21 tests of simply-supported reinforced concrete beams with overall heights between 42" and 75". The testing was conducted at an a/d ratio of 1.85. Data has shown that diagonal crack widths may slightly decrease with decreasing a/d ratio. The same crack width at a smaller a/d ratio indicates that a higher percentage of capacity from the above chart has already been reached.

This chart should be used in conjunction with sound engineering judgement with consideration of the following limitations:

- variability in crack widths in general (± scatter)
- members loaded at a/d < 1.85 may be at slightly higher % of capacity
- differences between field and laboratory conditions
- implications of an unconservative estimate of capacity

This chart is not intended to be used for inverted-tee bent caps.

Figure 2.9 Chart linking diagonal crack width to percent of ultimate capacity (Birrcher et al., 2009)

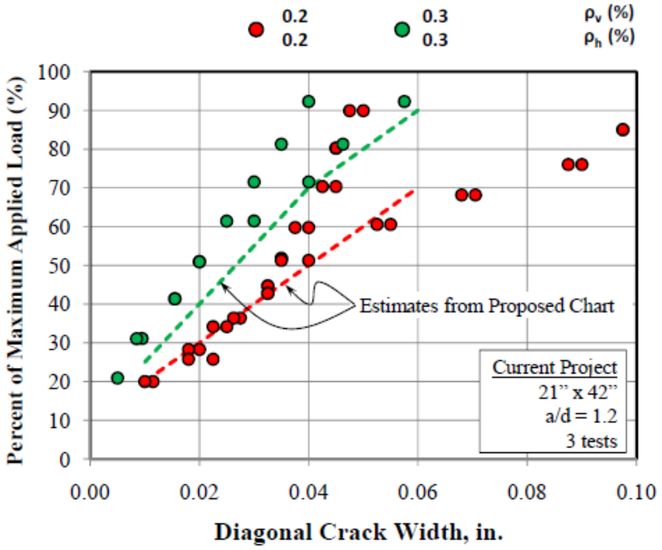

Figure 2.10 Comparison between estimates and experimental for beams with a/d = 1.2 (Birrcher et al., 2009)

Following the experiments performed on deep beam specimens, the University of Texas at Austin later studied how the behaviors of 33 RC inverted-T beams (Larson et al., 2013) were affected by different parameters, such as ledge depth and ledge length, quantity of web reinforcement, number of point loads, member depth, and a/d ratio. The relationship between measured diagonal crack widths and the applied load level was plotted for a/d ratios of 1.85 and 2.50, as shown in Figure 2.11.

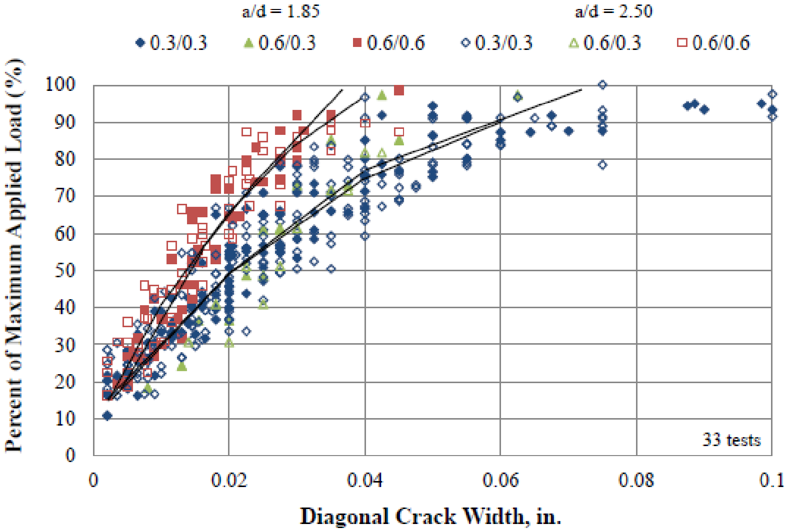

Figure 2.11 Percent of maximum applied load to diagonal crack width (Larson et al., 2013)

Further, a chart like that developed for the RC deep beams was provided for the RC inverted-T beams as well and is shown in Figure 2.12. As the test specimens used to generate the chart had a/d ratios of 1.85 and 2.5, it was suggested that the chart only be used for diagonally cracked RC bent caps with a/d ratios ranging from 1.0 to 2.5.

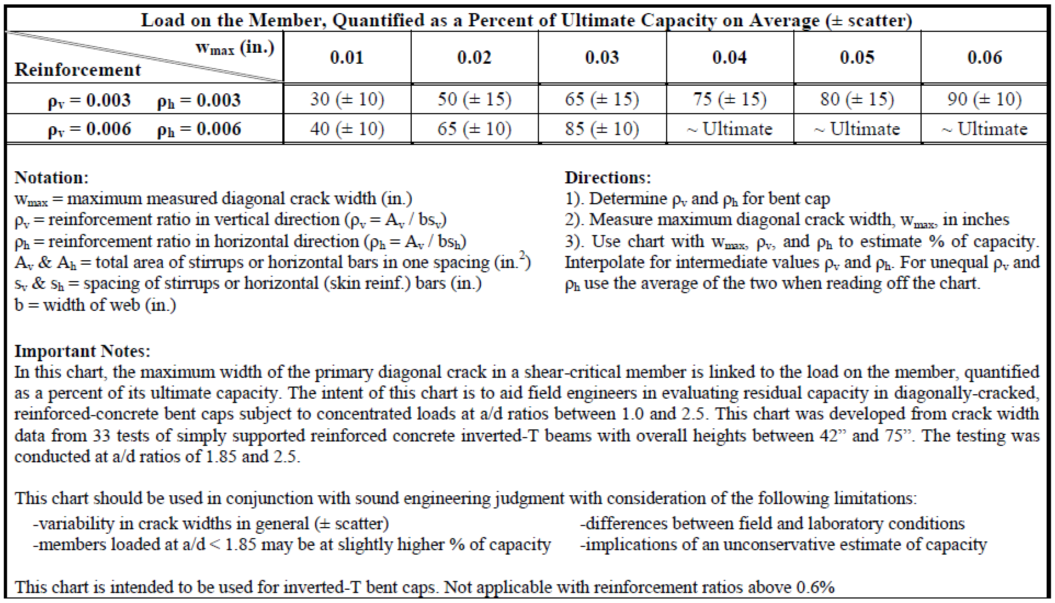

Load on the Member, Quantified as a Percent of Ultimate Capacity on Average (± scatter)						
Reinforcement / **w_{max} (in.)**	**0.01**	**0.02**	**0.03**	**0.04**	**0.05**	**0.06**
$\rho_v = 0.003$ $\rho_h = 0.003$	30 (± 10)	50 (± 15)	65 (± 15)	75 (± 15)	80 (± 15)	90 (± 10)
$\rho_v = 0.006$ $\rho_h = 0.006$	40 (± 10)	65 (± 10)	85 (± 10)	~ Ultimate	~ Ultimate	~ Ultimate

Notation:
w_{max} = maximum measured diagonal crack width (in.)
ρ_v = reinforcement ratio in vertical direction ($\rho_v = A_v / bs_v$)
ρ_h = reinforcement ratio in horizontal direction ($\rho_h = A_v / bs_h$)
A_v & A_h = total area of stirrups or horizontal bars in one spacing (in.^{2})
s_v & s_h = spacing of stirrups or horizontal (skin reinf.) bars (in.)
b = width of web (in.)

Directions:
1). Determine ρ_v and ρ_h for bent cap
2). Measure maximum diagonal crack width, w_{max}, in inches
3). Use chart with w_{max}, ρ_v, and ρ_h to estimate % of capacity. Interpolate for intermediate values ρ_v and ρ_h. For unequal ρ_v and ρ_h use the average of the two when reading off the chart.

Important Notes:
In this chart, the maximum width of the primary diagonal crack in a shear-critical member is linked to the load on the member, quantified as a percent of its ultimate capacity. The intent of this chart is to aid field engineers in evaluating residual capacity in diagonally-cracked, reinforced-concrete bent caps subject to concentrated loads at a/d ratios between 1.0 and 2.5. This chart was developed from crack width data from 33 tests of simply supported reinforced concrete inverted-T beams with overall heights between 42" and 75". The testing was conducted at a/d ratios of 1.85 and 2.5.

This chart should be used in conjunction with sound engineering judgment with consideration of the following limitations:
-variability in crack widths in general (± scatter)
-members loaded at a/d < 1.85 may be at slightly higher % of capacity
-differences between field and laboratory conditions
-implications of an unconservative estimate of capacity

This chart is intended to be used for inverted-T bent caps. Not applicable with reinforcement ratios above 0.6%

Figure 2.12 Chart linking diagonal crack width to percent of ultimate capacity (Larson et al., 2013)

In general, empirical methods, such as charts or equations, are easy to use and usually do not require a lot of computational power. However, because they are derived from limited, often highly focused, and often not field-representative experimental data, such empirical tools are typically restricted in their scope and will not apply to the broad range of cases encountered in regular practice.

2.2.4. Concrete Mechanics

In linking observed damage to residual capacity, some researchers have relied on concrete mechanics. An example of this is a study done by Zhu et al. (2003) that proposes using a compatibility-aided strut-and-tie model (CASTM) to predict diagonal crack widths at re-entrant corners of structures such as the dapped ends of bridge girders and the ledges of inverted-T bent caps. The procedure proposed by Zhu et al. (2003) requires both equilibrium of forces and compatibility of deformations to be satisfied. Parameter L_{HF}, which is the CASTM gage length for hanger and flexural steel strains, was obtained by calibration of data obtained from six inverted-T bent cap specimens that were tested. The diagonal crack width (w) was calculated using Equation 2.3.

$$w = L_{HF}\varepsilon_{HF} \tag{2.3}$$

where,

$L_{HF}(in.) = 9500\varepsilon_{HF} - 3.0(in.)$

$\varepsilon_{HF} = \sqrt{\varepsilon_H{}^2 + \varepsilon_F{}^2}$ (diagonal crack strain)

ε_H = CASTM hangar strain,

ε_F = CASTM flexural strain

A comparison between the computed crack width using Equation 2.3 and the experimental results from the six specimens is shown in Figure 2.13. The CASTM predictions match the test results reasonably well in the service load range, and for specimens reinforced with various combinations of hangar bars, flexural bars, diagonal bars, and shear-friction bars.

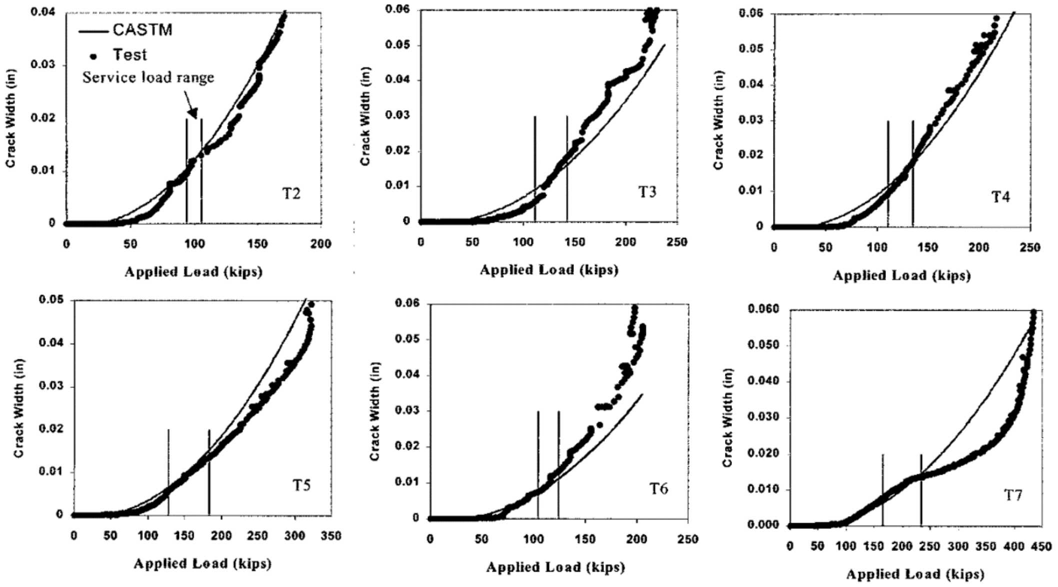

Figure 2.13 Comparison of experimental results with CASTM crack width predictions (Zhu et al., 2003)

However, it is pertinent to note that the CASTM gage length (L_{HF}) was calibrated using the same six inverted-T bent cap specimens later used to compare results with the computed crack widths from the CASTM model. Thus, there is no evidence to support whether the proposed procedure would be suitable for structural elements not included in the initial model calibration.

Another concrete mechanics model proposed by Birrcher et al. (2009) attempted to analytically correlate deep beam shear forces to measured crack widths. This was done by assuming a simple strut-and-tie model to estimate the perpendicular tensile force, *T*, comprising the assumed bottle shaped strut, as shown in Figure 2.14.

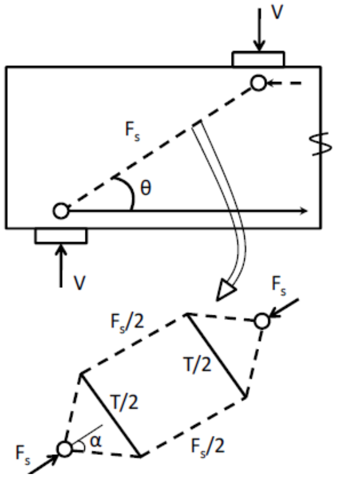

Figure 2.14 Analytical model for estimating diagonal crack widths (adapted from Birrcher et al., 2009)

The angle of spreading, α, was assumed and used to calculate *T*, as shown in Equation 2.4. The area of reinforcement in the perpendicular direction was broken into vertical and horizontal components, as shown in Equation 2.5. Combining Equations 2.4 to 2.8, one can obtain Equation 2.9, which correlates the crack width, *w*, to the applied load, *V*.

$$T = \frac{V \tan \alpha}{\sin \theta} \tag{2.4}$$

$$A_{\perp} = A_v \cos \theta + A_h \sin \theta \tag{2.5}$$

$$s_{\perp} = s_l \sin \theta \tag{2.6}$$

$$\varepsilon_{\perp} = \frac{T}{E_s A_{\perp}} \tag{2.7}$$

$$w = \varepsilon_{\perp} s_{\perp} \tag{2.8}$$

$$w = \frac{V s_l \tan \alpha}{E_s \left(A_v \cos \theta + A_h \sin \theta \right)} \tag{2.9}$$

However, Birrcher et al. (2009) also noted some issues with this approach. Firstly, it was difficult to justify an assumed angle of spreading. Secondly, a full strut-and-tie model must be analyzed to estimate the capacity of the member. This required detailed calculations which could be inaccurate due to the fact that the field and laboratory conditions, such as boundary conditions, axial restraint, long term effects, and the presence of repeated loads, were different than the simple model that was used in establishing equilibrium relations shown above.

Another potential solution for crack-based strength assessment that has been investigated is the use of crack kinematics (Campana et al., 2013; Cavagnis et al., 2018). While the focus of these programs was to analyze the different shear-transfer actions in one-way RC members, as shown in Figure 2.15, and not to assess the implication of observed cracking on member health, the results are relevant to mechanics-based damage assessment procedures. Note that forces designated with an "*N*" are axial components and those with "*V*" are vertical (shear) components. The following forces were considered:

- Chord forces in uncracked concrete (V_{ch}, N_{ch})
- Residual tensile stresses in concrete (V_{res}, N_{res})

- Forces developed in shear reinforcement (V_{sw})
- Aggregate interlock (V_{agg}, N_{agg})
- Dowel action (V_{dow})
- Tensile force in the flexural reinforcement (N_s)

By using crack kinematics (i.e., crack widths, crack slips, and crack inclinations, etc.) measured at load levels near failure (0.88~1.00V_u) and constitutive models to calculate the forces shown in Figure 2.15, the researchers were able to estimate the experimentally measured shear strength within 30 % for 21 beams. Example results for three specimens are shown in Figure 2.16. These results clearly show the potential ability of mechanics-based procedures using measured crack input; however, it is important to note that this type of analysis generally requires high-resolution data be measured over the entire crack length. As such, this type of procedure may not be particular suitable as an "everyday" tool. Furthermore, results presented to date have only been for load levels at or near failure which is arguably of limited relevance to typical in-service bridge infrastructure.

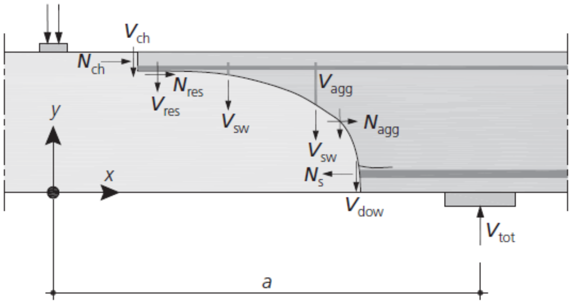

Figure 2.15 Shear-transfer mechanisms in RC (Campana et al., 2013)

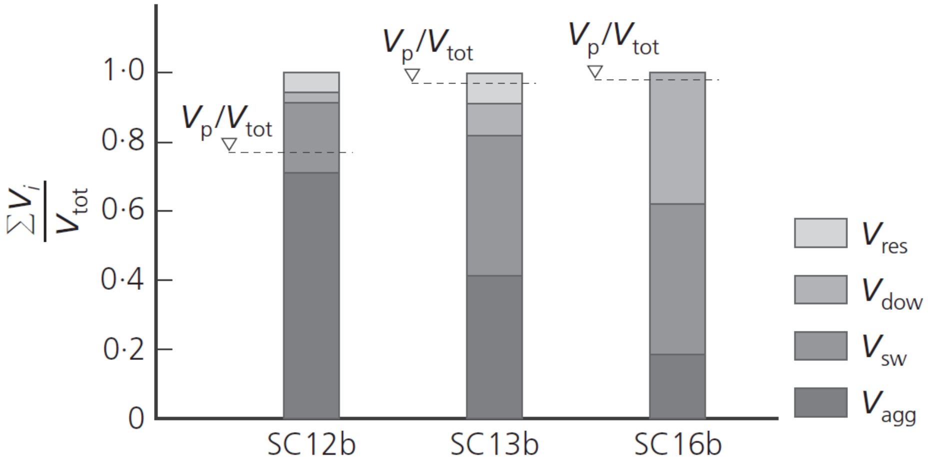

Figure 2.16 Shear transfer estimates for three specimens (Campana et al., 2013)

Another recent example of research using concrete mechanics to estimate the shear capacity of cracked RC members was carried out by Lantsoght et al. (2016). They proposed assessing the residual shear capacity of a fully cracked concrete bridge section using an aggregate interlock model. In this model, the shear resistance (V_{agg}) of a RC section with a through-thickness crack is assumed to be solely due to aggregate interlock, and it is calculated from Equation 2.10.

$$V_{agg} = \tau_u db \tag{2.10}$$

where,
$\tau_u = C_1\left(\rho f_y\right)^{C_2}$
$C_1 = (f'_c)^{0.36}$
$C_2 = 0.09(f'_c)^{0.46}$
ρ = reinforcement ratio,
f_y = yield stress of the reinforcement,
f'_c = cube crushing strength of concrete,
d = effective depth of the considered cross section,
b = width of the cross section

For an unreinforced concrete section with a constant crack width over the depth, the shear capacity (V_{u_unr}) can be calculated from Equation 2.11 using Walraven's model for aggregate interlock (Walraven, 1980, 1981a, 1981b).

$$V_{u\_unr} = \tau bh \tag{2.11}$$

where,
$\tau = -\frac{f'_c}{30} + [1.8w^{-0.8} + (0.234w^{-0.707} + 0.20)f'_c]\Delta$
w = crack width,
Δ = shear displacement,
h = height of the cross section

For normal strength concrete with a maximum aggregate size of 32 mm, it is assumed from the relationship between crack width and crack slip (Walraven, 1981a) that the shear displacement can be calculated from Equation 2.12.

$$\Delta = 1.25w \tag{2.12}$$

These equations were used to provide a relationship between crack widths and shear capacity for an unreinforced concrete section with a constant crack width through the member depth, as shown in Figure 2.17. These shear capacity estimates are compared alongside the capacity estimates provided by the Dutch design provisions (NEN Committee 351001, 1995). It is pertinent to note that validation of this model against experimental data has not been identified in the literature.

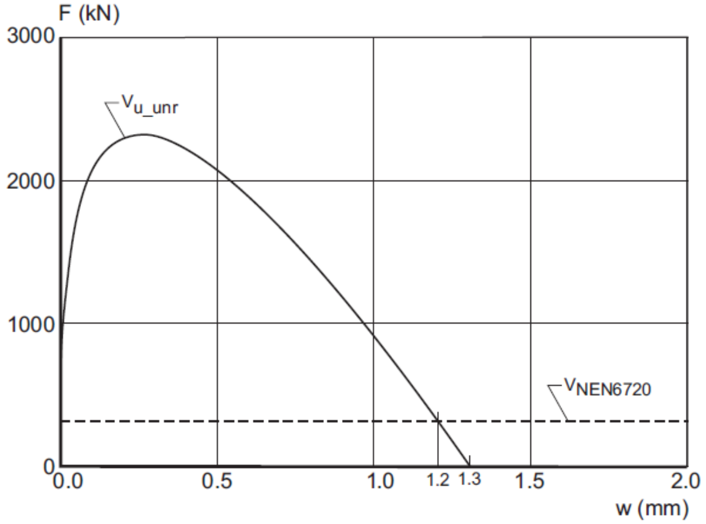

Figure 2.17 Shear capacity from NEN 6720 ($V_{NEN6720}$) and from aggregate interlock of an unreinforced section (V_{u_unr}) as a function of crack width, w (Lantsoght et al., 2016)

Recent work completed at the University of Toronto (Calvi et al., 2018) has investigated the use of crack measurements to assess the health of membrane elements subjected to shear and axial loads. Many types of structures can be approximated using membrane elements, for example, a beam web or a shear wall.

Using a combination of equilibrium and compatibility requirements on the crack surface and globally (i.e., on average in the element), shown in Figure 2.18, Calvi et al. were able to provide reasonable load estimates for RC membrane elements. The procedure relates crack widths and slips to element strains which are subsequently used to calculate stresses on the crack surface and on average in the element. Reserve capacities for the reinforcement and concrete components can then be made on individual bases using yield strengths, concrete crushing strength, and estimates regarding aggregate interlock capacity. An overall strength check can be made by calculating shear strength using a typical forward RC membrane element modeling procedure, for example the Modified Compression Field Theory (MCFT) (Vecchio & Collins, 1986), and comparing it to the stress estimated on the basis of the crack input.

Figure 2.19 shows a panel element at failure and the shear stress versus crack width plot. Note that reasonable estimates of shear stress were made for each measured crack width; however, this procedure has primarily been validated for panel elements and requires more rigorous validation for bridge members encountered in practice, such as bent caps. This procedure employs a similar methodology to the procedure proposed in Chapter 4 of this report, and the successes of Calvi et al.

suggests that this type of membrane element analysis procedure is a rational approach for the damage assessment of RC members.

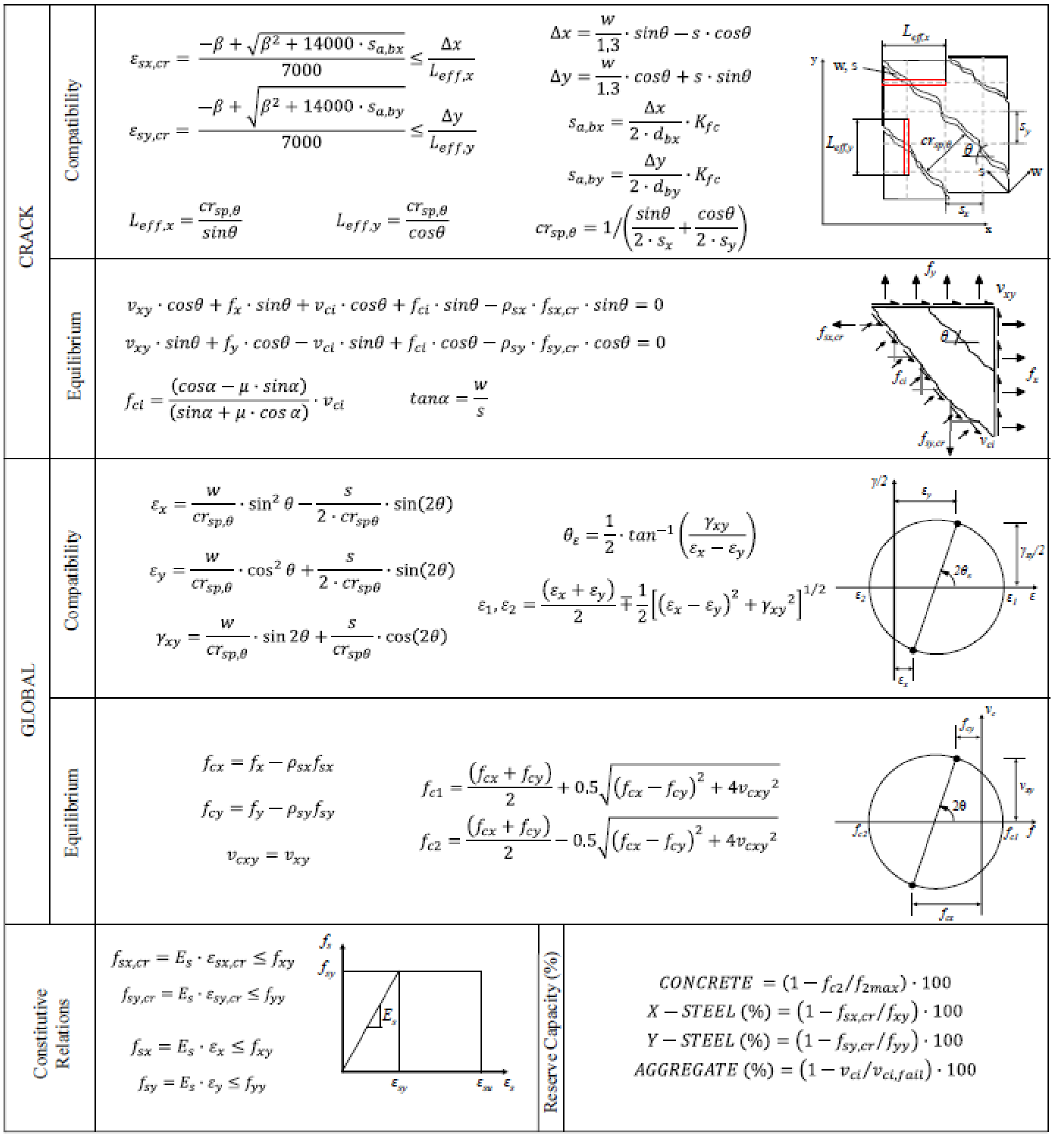

CRACK

Compatibility

$$\varepsilon_{sx,cr} = \frac{-\beta + \sqrt{\beta^2 + 14000 \cdot s_{a,bx}}}{7000} \le \frac{\Delta x}{L_{eff,x}}$$

$$\varepsilon_{sy,cr} = \frac{-\beta + \sqrt{\beta^2 + 14000 \cdot s_{a,by}}}{7000} \le \frac{\Delta y}{L_{eff,y}}$$

$$L_{eff,x} = \frac{cr_{sp,\theta}}{sin\theta} \qquad L_{eff,y} = \frac{cr_{sp,\theta}}{cos\theta}$$

$$\Delta x = \frac{w}{1,3} \cdot sin\theta - s \cdot cos\theta$$

$$\Delta y = \frac{w}{1.3} \cdot cos\theta + s \cdot sin\theta$$

$$s_{a,bx} = \frac{\Delta x}{2 \cdot d_{bx}} \cdot K_{fc}$$

$$s_{a,by} = \frac{\Delta y}{2 \cdot d_{by}} \cdot K_{fc}$$

$$cr_{sp,\theta} = 1/\left(\frac{sin\theta}{2 \cdot s_x} + \frac{cos\theta}{2 \cdot s_y}\right)$$

Equilibrium

$$v_{xy} \cdot cos\theta + f_x \cdot sin\theta + v_{ci} \cdot cos\theta + f_{ci} \cdot sin\theta - \rho_{sx} \cdot f_{sx,cr} \cdot sin\theta = 0$$

$$v_{xy} \cdot sin\theta + f_y \cdot cos\theta - v_{ci} \cdot sin\theta + f_{ci} \cdot cos\theta - \rho_{sy} \cdot f_{sy,cr} \cdot cos\theta = 0$$

$$f_{ci} = \frac{(cos\alpha - \mu \cdot sin\alpha)}{(sin\alpha + \mu \cdot cos\,\alpha)} \cdot v_{ci} \qquad tan\alpha = \frac{w}{s}$$

GLOBAL

Compatibility

$$\varepsilon_x = \frac{w}{cr_{sp,\theta}} \cdot \sin^2\theta - \frac{s}{2 \cdot cr_{sp\theta}} \cdot \sin(2\theta)$$

$$\varepsilon_y = \frac{w}{cr_{sp,\theta}} \cdot \cos^2\theta + \frac{s}{2 \cdot cr_{sp\theta}} \cdot \sin(2\theta)$$

$$\gamma_{xy} = \frac{w}{cr_{sp,\theta}} \cdot \sin 2\theta + \frac{s}{cr_{sp\theta}} \cdot \cos(2\theta)$$

$$\theta_\varepsilon = \frac{1}{2} \cdot tan^{-1}\left(\frac{\gamma_{xy}}{\varepsilon_x - \varepsilon_y}\right)$$

$$\varepsilon_1, \varepsilon_2 = \frac{(\varepsilon_x + \varepsilon_y)}{2} \mp \frac{1}{2}\left[(\varepsilon_x - \varepsilon_y)^2 + {\gamma_{xy}}^2\right]^{1/2}$$

Equilibrium

$$f_{cx} = f_x - \rho_{sx} f_{sx}$$

$$f_{cy} = f_y - \rho_{sy} f_{sy}$$

$$v_{cxy} = v_{xy}$$

$$f_{c1} = \frac{(f_{cx} + f_{cy})}{2} + 0{,}5\sqrt{(f_{cx} - f_{cy})^2 + 4{v_{cxy}}^2}$$

$$f_{c2} = \frac{(f_{cx} + f_{cy})}{2} - 0{,}5\sqrt{(f_{cx} - f_{cy})^2 + 4{v_{cxy}}^2}$$

Constitutive Relations

$$f_{sx,cr} = E_s \cdot \varepsilon_{sx,cr} \le f_{xy}$$

$$f_{sy,cr} = E_s \cdot \varepsilon_{sy,cr} \le f_{yy}$$

$$f_{sx} = E_s \cdot \varepsilon_x \le f_{xy}$$

$$f_{sy} = E_s \cdot \varepsilon_y \le f_{yy}$$

Reserve Capacity (%)

$$CONCRETE = (1 - f_{c2}/f_{2max}) \cdot 100$$

$$X - STEEL\,(\%) = (1 - f_{sx,cr}/f_{xy}) \cdot 100$$

$$Y - STEEL\,(\%) = (1 - f_{sy,cr}/f_{yy}) \cdot 100$$

$$AGGREGATE\,(\%) = (1 - v_{ci}/v_{ci,fail}) \cdot 100$$

Figure 2.18 Equations for assessing element health using measured crack input (Calvi et al., 2018)

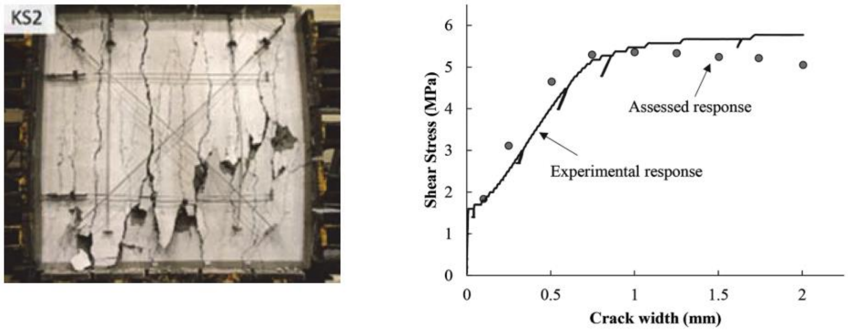

Figure 2.19 Specimen KS2 at failure and comparison of assessed response to experimental response (Calvi et al., 2018)

2.2.5. Crack Pattern Quantification

Fractal analysis has been used widely in image analysis problems (Lopes & Betrouni, 2009). In relation to performance of cracked concrete bridge elements, Farhidzadeh et al. (2013) proposed a procedure for estimating the structural integrity of concrete elements by way of quantified crack patterns that were examined through fractal analysis. Two large scale shear wall specimens were loaded cyclically, and photographs were taken of the cracks at the end of each load step. These cracks were then mapped onto square grids that ranged from a very coarse mesh (of size R_S) to a much finer mesh (of size R_T), as illustrated in Figure 2.20. The number of squares that had cracks (N(r)), where r is the size of each square in general, was then used to obtain the fractal dimension D by plotting the results of log(N(r)) versus log(1/r) for the different mesh sizes ranging from R_T to R_S. The fractal dimension D is a ratio that describes how a detail in a pattern changes relative to the scale that it is measured (Falconer, 2014).

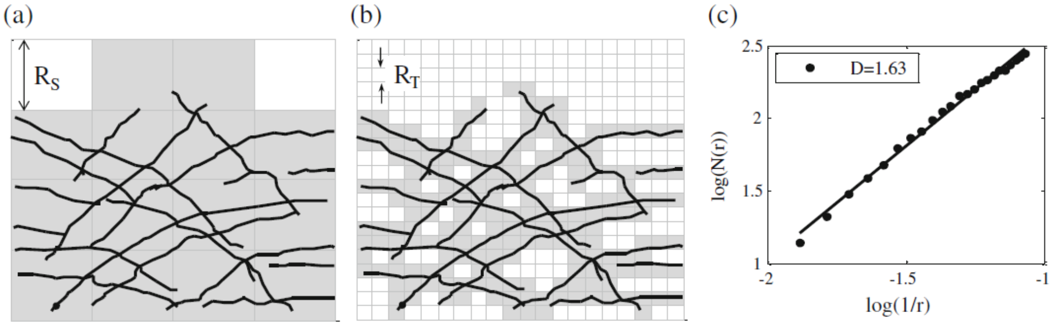

Figure 2.20 a) Coarse mesh, b) fine mesh, c) estimate of fractal dimension D from meshes (Farhidzadeh et al., 2013)

After calculating D, the researchers proposed a damage index (DI) on the basis of Equation 2.13, where D_i is the fractal dimension at the current load step, D_1 is the fractal dimension at the first load step when cracks first become visible, and 2 is the limiting value for the fractal dimension as cracks start to cover the entire surface area of the shear wall.

$$DI = \frac{D_i - D_1}{2 - D_1} \tag{2.13}$$

The relative stiffness loss (RSL) was calculated from Equation 2.14, where K_i is the lateral secant stiffness at load step i, and K_1 is the initial lateral stiffness of the wall.

$$RSL = 1 - \frac{K_i}{K_1} \tag{2.14}$$

From Figure 2.21, it can be seen that the DI curves computed for the shear walls matched the RSL curves fairly well, suggesting that the proposed methodology may be a suitable method of estimating member damage attributed to concrete cracking.

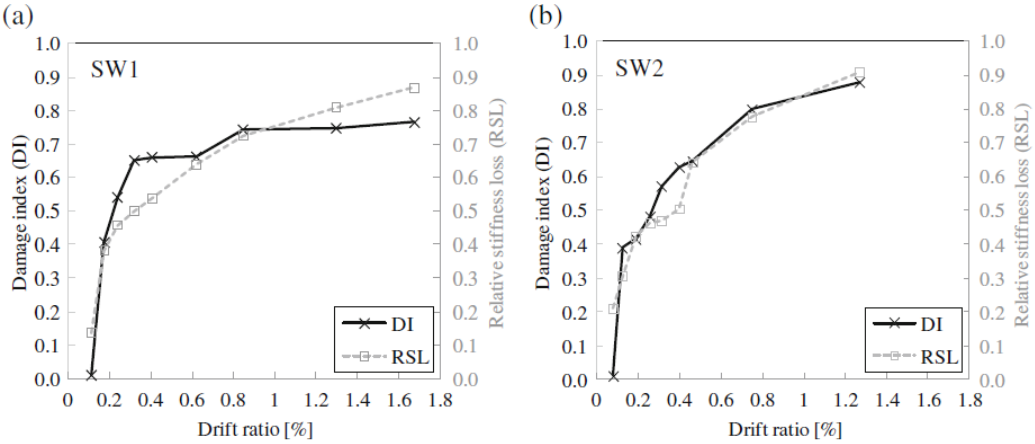

Figure 2.21 Comparison of DI to RSL for a) SW1, and b) SW2 (Farhidzadeh et al., 2013)

More recently, Ebrahimkhanlou et al. (2016) extended the study of the same two shear wall specimens (SW1 and SW2) to a multifractal analysis. The motivation for doing so was because the authors felt that using a single exponent, the fractal dimension, may not adequately describe overall crack patterns and noted that a multifractal analysis may serve as a more generalized approach to the problem. The authors compared the results of the multifractal analysis to the experimental results from the tests of the two shear wall specimens and concluded that the multifractal parameters could be correlated to wall structural behavior.

Another method of estimating residual capacity using crack pattern quantification was suggested by Kabir et al. (2009). They proposed using a statistical-based approach to estimate the damage in concrete structures using data collected from acoustic borehole imagery. These results were then verified against the damage observed on the extracted cores. The different types of damages were categorized into horizontal cracks, void damage, rust stain damage, or foundation damage. The extent of damage was then estimated by quantifying the number of damaged pixels as a percentage of the total number of pixels. An example of this procedure is presented in Table 2.9.

Table 2.9 Example of damage percentages according to damage types (Kabir et al., 2009)

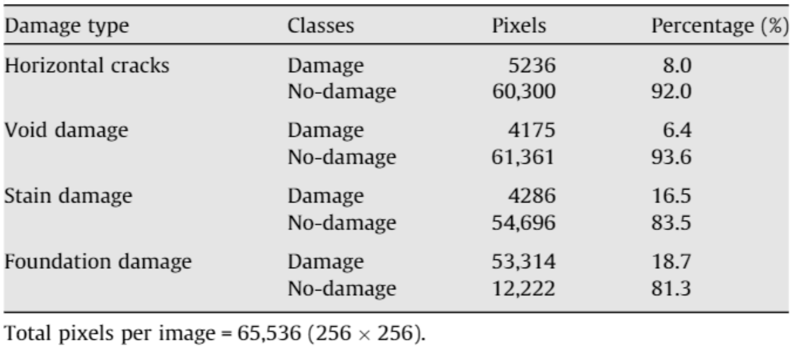

Damage type	Classes	Pixels	Percentage (%)
Horizontal cracks	Damage	5236	8.0
	No-damage	60,300	92.0
Void damage	Damage	4175	6.4
	No-damage	61,361	93.6
Stain damage	Damage	4286	16.5
	No-damage	54,696	83.5
Foundation damage	Damage	53,314	18.7
	No-damage	12,222	81.3

Total pixels per image = 65,536 (256 × 256).

The binary image was also used to estimate the extent of the crack width openings, as shown in Figure 2.22.

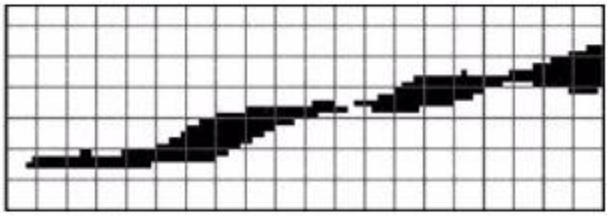

Figure 2.22 Segment of horizontal crack (Kabir et al., 2009)

2.2.6. Summary and Discussion

Various methods of estimating the residual capacity of damaged concrete structures have been discussed in the previous sections. They were grouped broadly into several categories: 1) finite element analysis, 2) structural assessment based on observed damage, 3) empirical methods, 4) concrete mechanics, and 5) crack pattern quantification.

Each of these methods has their own advantages and disadvantages. For example, finite element analysis techniques can be accurate in predicting the critical crack width (Talley et al., 2014), but building a model is often a time consuming process, and experience is required in both developing the model and interpreting the results correctly. On the other hand, empirical methods are much easier to use, but are limited in their ranges of applicability (Birrcher et al., 2009; Larson et al., 2013).

Existing structural assessment methods based on measured crack details do not necessarily correlate well with the actual residual capacity of cracked concrete members (Abi Shdid et al. 2006) and the methods proposed for some specific concrete infrastructure or member types (e.g., Veletzos et al. 2008) are likely of little value in the context of RC members comprising typical bridge infrastructure. On that basis, methods that utilize concrete mechanics-based procedures may have the potential to be the most general in terms of their applicability to real world scenarios yet retain the balance between required computational time and ease of use. A review of existing literature thus far indicates that while several potential mechanics-based solutions have been proposed (Calvi et al., 2018; Campana et al., 2013; Cavagnis et al., 2018; Lantsoght et al., 2016), virtually none have been extensively validated with members typical of TxDOT bridge infrastructure. However, note that the procedures that have been preliminarily validated (Calvi et al., 2018; Campana et al., 2013; Cavagnis et al., 2018), show promise and lend credence to the logic behind the cracked continuum approach proposed in Chapter 4 of this report.

2.3. Summary

There are several methods for the damage assessment of RC structures, both in practice and research. Many of these models rely on similar underlying assumptions about the behavior of RC, but vary in their levels of accuracy, ease-of-use, and level of validation. The following presents the key findings obtained from the literature:

- Methods currently employed in practice to evaluate RC structures are practical in regards to their ability to recommend action based on visually inspected damage without the use of advanced or expensive tools. Additionally, these methods are easy to implement as they usually require limited user-input and the output is straightforward with clear guidelines for remedial action. Furthermore, these methods are well established and have been used for several decades; as such, there is a level of comfort and trust in their use. However, the quality of the observations and results from current methods are highly dependent on the individual inspector’s experience. Additionally, these methods typically provide little information regarding the actual structural implications of diagonal concrete cracking.

- FEA can be a useful tool for estimating the structural capacity of cracked concrete members. However, it is important to note that using FEA can be very time consuming, and it requires experienced users to build high resolution finite element models that adequately reflect the structure details and damage. Furthermore, it should also be noted that accurate modeling of RC infrastructure still presents an existing challenge as a result of complex behavior, and no single approach or material model has been shown capable of providing good results over the large spectrum of structural details and loading conditions encountered in practice (Vecchio, 2001).

- Empirical methods, such as charts or equations, are easy to use and usually do not require computational power. However, due to the fact that they are derived from limited, and often highly focused, experimental data, these empirical tools are likely restricted in that they are limited to the specific member types, scales, reinforcement conditions, and loading conditions that were employed in their development.

- Methods that utilize concrete mechanics-based procedures have the potential to be the most general in terms of their applicability to real world scenarios yet retain the balance between required computational time and ease of use. A review of existing literature thus far indicates that there are no concrete mechanics-based models which have been extensively validated with members typical of TxDOT bridge infrastructure. Further, it should also be noted that the few mechanics-based procedures that have been identified from the literature, were formulated using assumptions that would severely limit their applicability for the assessment of much of the TxDOT bridge infrastructure that has historically shown to require crack assessment (e.g., RC bent caps).

Chapter 3. Visual Crack Measurement Evaluation Database

This Chapter highlights existing structural crack records and measurements. The first section discusses known locations of cracking of in-service bridges in Texas. The second section provides an overview of experimental structural cracking data from the literature which was compiled to form the Visual Crack Measurement Evaluation Database (VCMED). Next, the organization, functions, and applications of the VCMED are discussed. Finally, the notation of the VCMED is listed.

3.1. Structural Cracking in Existing TxDOT Bridges

In an effort to identify Texas relevant member types experiencing in-service cracking that may pose challenges related to assessing structure safety, available field data from in-service Texas Department of Transportation (TxDOT) bridges were collected and reviewed. A previous project completed at The University of Texas at Austin, TxDOT Project 0-6416, had compiled relevant structural cracking measurements, member details, and associated photographs from across the state of Texas. Additionally, the project team consulted with TxDOT personnel to identify additional sites and the common problems associated with aging infrastructure in Texas.

Chapter 6 of TxDOT Project Report 0-6416-1 contains a summary of eight in-service inverted-T bridge bents with noteworthy diagonal cracking. Locations include the following cities: Austin, El Paso, San Antonio, and Waco. An example of the data logged is shown in Table 3.1, reproduced from the original report. A sample photograph and crack pattern are also shown in Figure 3.1. Additional information, including plans, details, and photographs, was also compiled into an Excel database by TxDOT personnel.

Table 3.1 Important characteristics of Waco straddle bents (reproduced from Larson et al., 2013)

Bent	Location	ρ_v	ρ_h	a/d	Ledge Length	Ledge Height/ Cap Height	No. of U-Beams
17	(31.496031, -97.148663)	0.46%	0.30%	2.5	Short	36%	2
19	(31.496476, -97.148489)	0.46%	0.30%	2.5	Short	36%	3

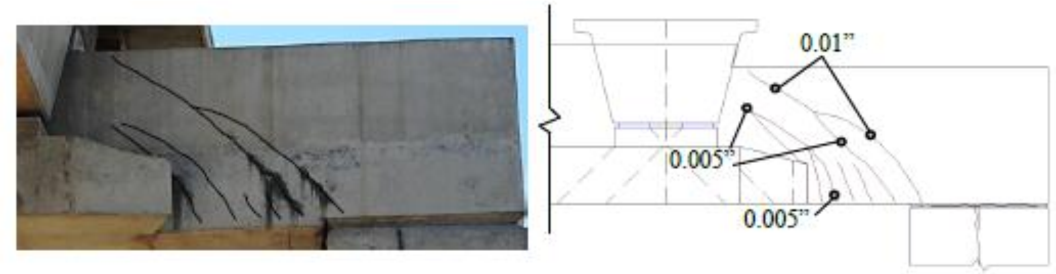

Figure 3.1 Crack size and location on the northwest corner of Waco bent 17 (Larson et al., 2013)

Correspondence with TxDOT personnel also yielded the following bridges with cracking-related concerns: Interstate Highway 20 Eastbound and Westbound at State Highway 351, Interstate 10 off-ramp at El Paso, and FM 652 at Salt Creek. Issues at these sites included cracked straddle caps and pan girders. Furthermore, diagonal cracking in cantilever bent caps has been identified as an area of concern across the state. Figure 3.2 shows locations where bent cap cracking has been recorded as potential areas of concern for the bridge's maintenance cycle. Although specific field data has not been collected for some of these locations, the noted concrete cracking experienced by these bridges informed the type of field guides that were ultimately proposed in Chapter 4.

Figure 3.2 Locations where bent cap cracking has been recorded throughout Texas

3.2. Experimental Structural Crack Measurement Data

Upon completion of the initial literature review, data collected for the purpose of populating the VCMED have been sorted, classified, and processed. An extensive review regarding current methods of bridge inspection was completed, as discussed in Chapter 1, and sources identified as containing potentially useful visual crack measurement data were set aside for further examination. The data sources were subsequently sorted into the three categories based on the types of specimens and the level of detail that was provided regarding the recorded data. The sorting and classification of the data has been done using three data categories: Category 1, Category 2, and Category 3, summaries of which are given in Sections 3.2.1, 3.2.2, and 3.2.3, respectively, of this report. For instance, data sources providing recorded crack widths, crack inclinations, and reported crack patterns were placed in higher data categories than sources that only provided crack width data. Upon completion of the initial sorting process, the data were examined further and subsequently filtered. Some examples of data that were filtered out from inclusion in the database included reinforced concrete (RC) members that failed in modes other than shear, crack data that were tracked in locations outside of web or “web-equivalent” locations, and crack data that were reported using relatively broad ranges of measurements. The use of these filters ensured that complete, quality datasets were used in the development and refinement of the crack-based assessment procedures developed through this research project.

In examining the inventory of Texas infrastructure that has exhibited structural cracking issues under typical service loading conditions, non-prestressed bent caps were deemed to be of primary interest. As such, the data comprising the VCMED exclusively pertains to non-prestressed RC members with an emphasis on deep beams. Details regarding the data filtering process employed is outlined in Sections 3.2.1, 3.2.2, and 3.2.3. Data processing included tasks such as measuring crack inclinations from crack patterns and digitizing load level versus crack width plots. All data were entered and independently verified by different members of the research team to ensure that data were correctly entered into the database. An overview of the final format of the database is provided in Section 3.2.3.1 and the data comprising the database are attached as Appendices A and B of this report. The following sections provide an overview of the data categories, summaries of the sources used in the database, and a brief discussion on sources that were omitted.

3.2.1. Category 1 Data

Category 1 test data pertains to test specimens that are directly relevant to TxDOT bridge infrastructure, that is, specimens that were constructed with typical TxDOT design details and reported crack data that were documented over several load levels. In total, there were three project reports that were deemed as Category 1 data, and these sources are listed in Table 3.2. There is a total of 77 specimens in this data category.

Table 3.2 Category 1 data comprising the VCMED

Source Name	Number of tests	Included in database
0-1851-1	16	16
0-5253-1	37	35
0-6416-1	33	26

3.2.1.1. TxDOT Project 0-1851-1

Research Project 0-1851 was conducted in an effort to determine the causes of unexpected cracking in RC bent caps and includes tests from sixteen full-scale bent cap specimens that were constructed with nominally identical geometries but employed different reinforcement details. The specimens were subjected to monotonic loading up to their ultimate resistances and the researchers provided detailed information about the maximum crack width at a series of load steps.

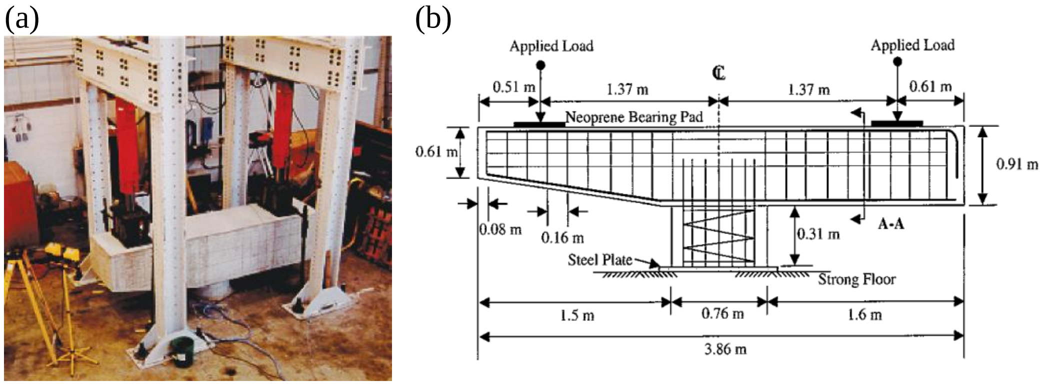

Figure 3.3 (a) Experimental test set-up, (b) general specimen layout and reinforcement details, TxDOT Project 0-1851 (Bracci et al., 2001)

3.2.1.2. TxDOT Project 0-5253

TxDOT Project 0-5253 was also used to populate the Category 1 data comprising the VCMED. In this experimental program, 37 deep beam specimens were tested, with various geometries, web reinforcement details, and shear span-to-depth ratios. The specimens include some of the largest of this type in the history of shear research. During the experimental procedure two of the specimens experienced flexural failures, so the total number of tests included in the VCMED is 35.

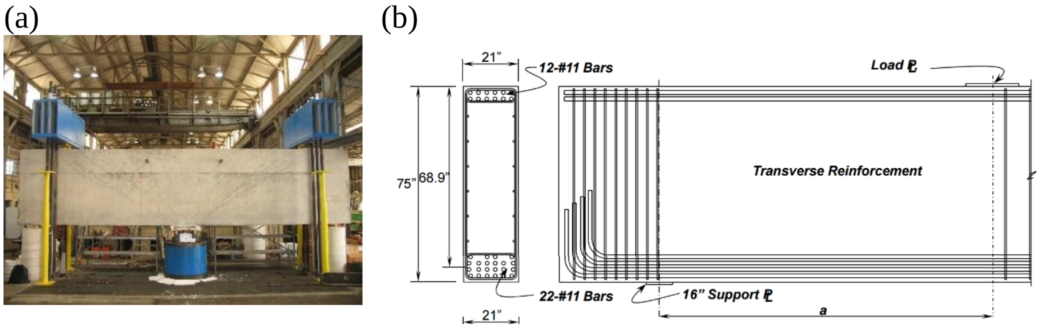

Figure 3.4 (a) Experimental test set-up, (b) general specimen section and layout, TxDOT Project 0-5253 (Birrcher et al., 2009)

3.2.1.3. TxDOT Project 0-6416

The last set of Category 1 data included in the VCMED pertains to inverted-T beams tested as part of TxDOT Project 0-6416. In this program, 33 full scale RC inverted-T beams with variable ledge and web properties were tested. Note that one of the objectives of this specific experimental program was to examine the web shear cracking of the beams' end portion (longitudinal direction), and not the cracking in the interior portion of the inverted-T bent caps (i.e., at re-entrant corners, stemming from the ledge-to-web interface). The vast majority of the research conducted prior to this project in the area of inverted-T beams has focused on ledge cracking and, as a result, experimental results from project 0-6416 are somewhat unique in the literature. Specimens that experienced flexural failure, shear friction failures of the web-to-ledge interface, or punching shear failures were excluded from the database. As a result, experimental data from 26 of the specimens were extracted from the results of 0-6416.

A summary of the Category 1 data, including the number of test specimens from each project that were included in the database, is presented in Table 3.2.

Figure 3.5 Experimental test set-up for TxDOT Project 0-6416 (Larson et al., 2013)

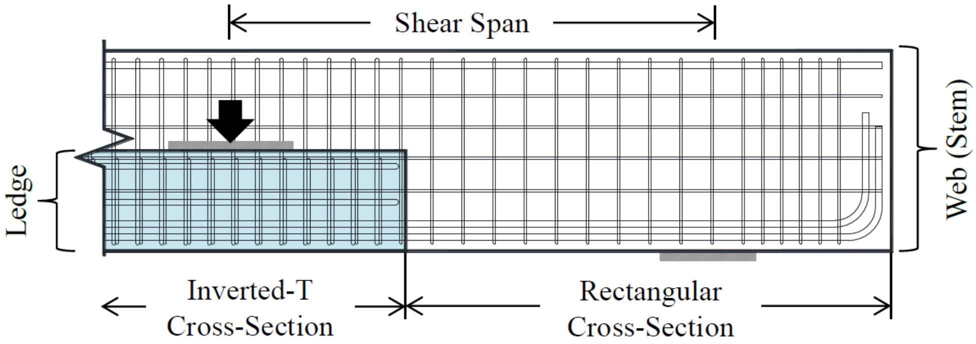

Figure 3.6 Elevation of inverted-T bent cap with discontinuous ledges (Larson et al., 2013)

3.2.1.4. Non-utilized data

The initial literature review included a larger number of test data comprising Category 1 data; however, much of that data were excluded in the final version of the database as they pertain to prestressed RC members. Although TxDOT has conducted several well documented research projects involving prestressed concrete members (with some examples including TxDOT Research Projects 0-1364, 0-5197-3, 0-5831-3, 0-6652-1, and others), the prestressed bent caps are considered out of the scope of the current research. As such, 40 test results were excluded from the VCMED.

Furthermore, 16 test results were excluded because they were focused on investigating cracking at the interface of the web and ledge regions of RC inverted-T bent caps. An example of this cracking is presented in Figure 3.7.

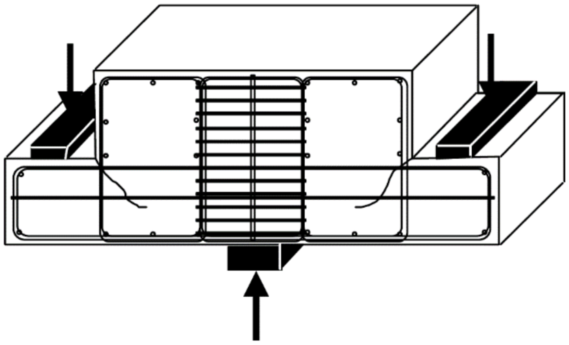

Figure 3.7 Cracking at the web-ledge interface (Bracci et al., 2001)

3.2.2. Category 2 Data

Test data for specimens that were similar in scale or detailing to bridge members employed in Texas and were well documented comprised Category 2 data. For example, many experimental research programs have been performed considering RC elements employing reinforcement or design details that differ from those typically employed in Texas; yet, still provide test data that are deemed relevant to the structural cracking performance of real-world RC bridge members. As summarized in Table 3.3, five sources were included as Category 2 data, and were made up of a total of 58 test specimens.

Table 3.3 Category 2 data comprising the VCMED

Source Name	Number of tests	Included in database
Aguilar (2011)	20	8
De Silva et al. (2008)	7	3
Pang (1991)	12	10
Sherwood (2008)	35	35
Susetyo (2009)	10	2

3.2.2.1. Aguilar (2011)

This project involved the testing of I-girders to examine the effect of the high strength concrete on the shear capacity of bridge girders. A cross-section and test schematic are shown in Figure 3.8. Because the specimen properties (concrete strength and section geometry) were not the same as those which can be found at TxDOT bent caps, the data extracted are included in Category 2. This research included the following subseries of specimens:

- RC beam members without shear reinforcement (eight specimens)
- RC beam members with shear reinforcement (eight specimens)
- Prestressed concrete beam members (four specimens)

The subseries pertaining to RC beam members containing shear reinforcement were included in the VCMED. All other tests performed in this project were deemed to be of little relevance with respected to the performance of RC bent caps.

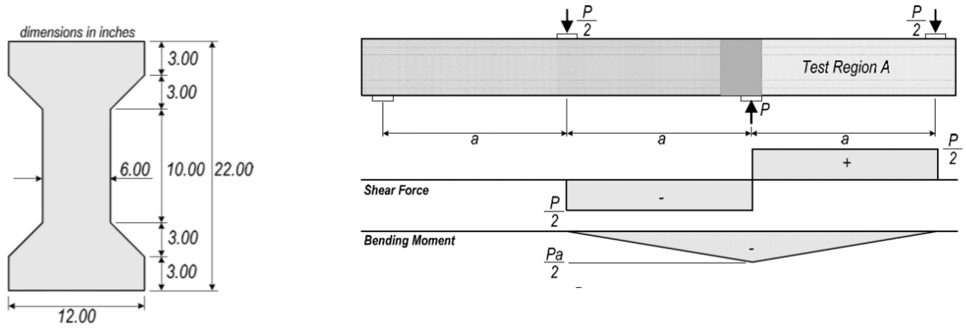

Figure 3.8 Cross section used in all 8 specimens (Left), test set-up and corresponding shear & bending moment diagrams for test specimens (Right) (Aguilar, 2011)

3.2.2.2. De Silva et al. (2008)

This research program was focused on investigating the behavior of prestressed RC beams, but it also included the testing of three specimens that were constructed without any prestressing forces. The tests were performed used a conventional three-point bending test setup and examined the side clear cover detailing of the I-girders as a primary test variable. The cross sections of the beams that have been included in the VCMED are shown in Figure 3.9.

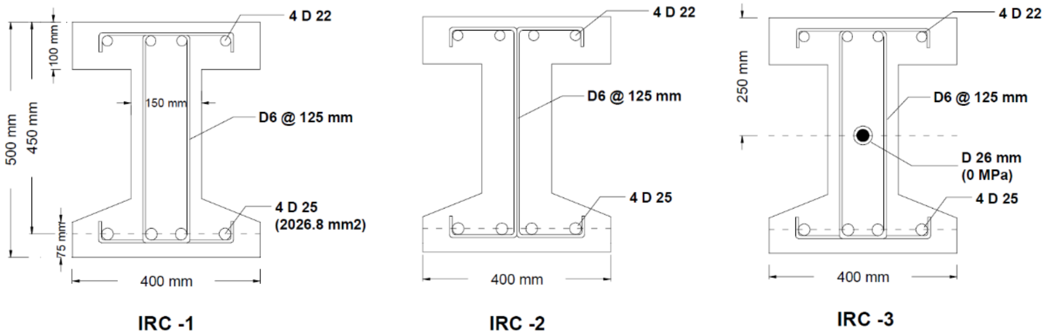

IRC -1 IRC -2 IRC -3

Figure 3.9 Cross section details of RC beams (De Silva et al., 2008)

3.2.2.3. Pang (1991)

In the process of creating a general behavioral model for estimating the shear response of RC elements, 13 RC panels were tested in the universal panel tester at University of Houston. The panels were used to represent idealized RC elements comprising part of a larger structure, like the web of an I-girder, a portion of a RC shear wall, or a section of a shell structure like a nuclear containment or an offshore platform. Ten out of the thirteen panel specimens have been included in the VCMED. Figure 2.8 shows a photograph of the University of Houston universal panel tester used to perform the panel tests.

Figure 3.10 Universal panel tester (Pang, 1991)

3.2.2.4. Sherwood (2008)

Inspired by oversized transfer girders that are more commonly used to increase the spacing between the columns of building structures, three series of large beam specimens (AT, L and S series) were tested in an attempt to investigate the effect of several parameters on RC size effect in shear. These parameters included: beam width, aggregate size, material strengths, and steel reinforcement ratios (longitudinal and shear). Although all 35 experimental results are well documented and presented, the geometries and reinforcement details of most of the specimens are atypical of common RC bridge members and are thus included as a part of Category 2 in the VCMED.

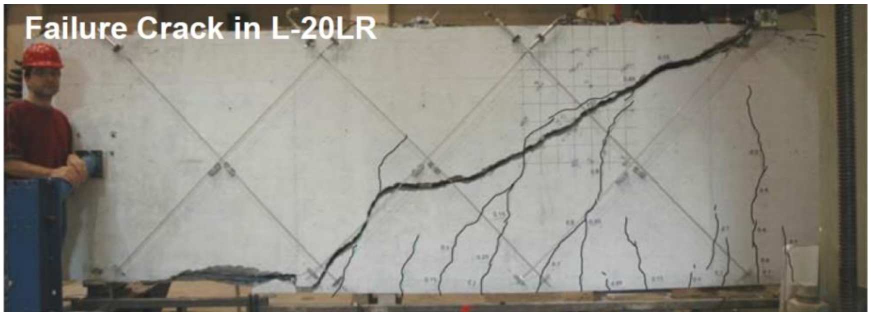

Figure 3.11 Shear failure, crack pattern on specimen L-20LR (adapted from Sherwood, 2008)

3.2.2.5. Susetyo (2009)

This research program was focused on investigating the shear behavior of fiber-reinforced concrete elements; however, the testing program included two control panels that were constructed with conventional concretes and were very well documented. These control panels contained typical reinforcement ratios and were tested using a detailed crack measurement documentation program. The panel elements were tested in the panel element tester at University of Toronto.

Figure 3.12 Failure crack pattern of RC panel C1C-R, (Susetyo, 2009)

3.2.3. Category 3 Data

The Category 3 dataset is comprised of data that were not extensively tracked and/or documented over the course of several load stages. That is, test data comprising Category 3 are typically only provided at failure load levels or at very few load stages. There are two sources that were classified as Category 3 data with a total of 21 specimens, as shown below in Table 2.3.

Table 3.4 Category 3 data comprising the VCMED

Source Name	Number of tests	Included in database
Lee et al. (2015)	18	12
Yoon et al. (1996)	12	9

3.2.3.1. Lee et al. (2015)

This project investigated the influence of high-strength shear reinforcement on RC beam shear behavior, with an emphasis on diagonal cracking. 18 tests were completed on rectangular specimen with shear reinforcement strengths ranging from 48 to 97 ksi and a shear-span-to-depth ratio of 2.56. Note that 6 of the tests were excluded for the following reasons: no shear reinforcement (three tests), non-shear related failure (one test), and no yielding of the shear reinforcement (two tests). Although crack widths were well documented, there was very little information regarding crack inclinations; as such, this data was included in Category 3.

3.2.3.2. Yoon et al. (1996)

To evaluate the influence of minimum shear reinforcement on RC beams with normal, medium, and high-strength concrete, 12 tests were completed on six rectangular beams. The following concrete strengths were investigated: 5200 psi, 9700 psi, and 12,600 psi. As before, specimen without shear reinforcement were omitted. This data was classified as Category 3 because crack patterns were only presented at failure.

3.3. The Visual Crack Measurement Evaluation Database (VCMED)

This section of the report presents a brief overview of the organization of the database, the functions currently available within the database, and envisioned uses for the database.

3.3.1. Organization

The database is organized first by data category and subsequently by alphabetical source name. Member organization typically followed the order in which they were presented in the original source material. Each member is tagged with a member number and each entry within the member was given an entry number to homogenize how members were named across sources. There were six general subdivisions on entries in the database: member information, geometric properties, reinforcement details, material properties, crack data, and miscellaneous. Details on each of these subdivisions are given below.

Note that the entries comprising the VCMED are provided in Appendices A and B of this report. Appendix A provides member relevant data and Appendix B presents load stage specific member cracking information.

Entries comprising VCMED:

- Member information includes source name and member name within the source.
- Geometric properties included dimensional classification of the member.
    - Web width (in.): width of specimen web or "web equivalent." For example, in a panel test, the panel thickness was taken as the width.
    - Total height (in.): total height of specimen.
    - Effective depth (in.): depth from compressive surface to the centroid of the tensile reinforcement.
    - Shear span-to-depth ratio: ratio between shear span and effective depth. Shear span is given as the distance between the applied point load and the support point.
    - Clear cover (in.): distance between nearest face and reinforcement in that region of specimen.
- Reinforcement details contains reinforcement bar information.
    - Reinforcement ratio (%): ratio between area of steel and area of concrete. Calculation varies based on location of steel (top, bottom, side, etc.).
    - Number of bars: number of bars for each given reinforcement type (e.g., tension, compression, shear, and skin reinforcement).
    - Bar diameter (in.): bar diameters corresponding to the respective bar types noted above (refer to 'Number of bars').
    - Bar spacing (in.): maximum spacing for similar bars.
- The values for concrete and steel strength are recorded in the material properties section.
    - Concrete compression strength (psi): traditional concrete cylinder compression strength.
    - Maximum aggregate size (in.): maximum nominal coarse aggregate size specified in mix design.
    - Steel yield strength (ksi): traditional steel yield strength.

- The visual crack measurements and related information are recorded in the crack data section.
  - Shear loads – cracking and failure (kips): shear cracking loads recorded where applicable, otherwise only failure shear load was recorded.
  - Maximum (characteristic) crack width (in.): the maximum diagonal crack width recorded on the specimen for a given load stage.
  - Crack inclination (degrees): crack inclination at mid-depth of member, approximately halfway between load and support points and representing the angle between the longitudinal axis and the inclined crack.
- Miscellaneous
  - Photos: note of whether photos are available for crack patterns.
  - QA/QC columns: internal process for inputting and back-checking of data.

3.3.2. Functions

There are several features built-in to the MS-Excel formatted database that can be used to easily navigate or access specific data comprising the database. Current built-in features include: data filtering, report generation, and automatic crack information plotting. It is envisioned that the VCMED will be a “living database,” that will be updated to incorporate additional data identified over the course of the project and additional features deemed useful in the procedure development and verification stages of the project.

The first key feature and benefit to using the electronic version of the database is filtering. Each of the entry types listed in Section 3.1 can be filtered by various criteria. A dropdown menu is shown when the filter icon is selected, and the user can manually check or uncheck certain criteria based on what type of specimen users would like to access. For example, if the user was interested in comparing the cracking behaviors of members with rectangular cross sections ranging from 48 to 70 in., it simply requires applying filters to the shape and effective depth columns. In this way, the user can quickly focus attention on parameters of interest, rather than manually sifting through a lengthy database.

If the user wants to examine a specific member, or to save those results for convenient viewing later, the “Report” tab of the electronic database can be used. The report tab utilizes two dynamic drop-down menus which allow for quick filtration of data. First, simply select a source from the source list. Next, choose a member from the subsequent dropdown menu labelled “member.” The second selection will automatically populate the rest of the report sheet with data from the database. These results can be printed or exported for the user’s convenience. A sample report is given in Figure 3.13.

Another product of the report tab is plots generation. There are three default plots included in this version of the database: crack width-load level, crack inclination-load level, and crack width-crack inclination. All of these plots are updated in tandem with the rest of the report page and can be printed alongside the rest of the report for convenience.

3.3.3. VCMED Application

The previous section covered some of the built-in functions within the electronic version of the database, while this section will discuss potential uses for the database. It is envisioned that the electronic version of the database will have four primary uses: 1) as an aid in developing new crack-based shear strength assessment procedures, 2) evaluating new and existing crack-based shear strength assessment procedures, 3) providing visual benchmarks for field data, and 4) serving as a resource for future projects focused on related research areas.

As mentioned in Section 3.2, the data categories served as an internal means for the research team to effectively partition data and ensure that data that is used for model development is not also used to evaluate the effectiveness of the model. The volume of data currently available in the VCMED allowed the 0-6919 research team to develop a general approach without "double-dipping," ensuring that data used for development and calibration were not also used for validation.

Database Summary
0-1851-1
1A
1/2
12/19/2016

Source: 0-1851-1
Member: 1A

Geometric Properties:

b (in)	h (in)	d (in)	a/d ratio	cc (in)
33	36	32.875	1.642586	2

Reinforcement Details:

Tension Reinforcement:

ρs	ns	ϕs (in)	s (in)
0.579%	8	1	3.75

Compression Reinforcement:

ρ's	n's	ϕ's (in)	s' (in)
0.579%	8	1	3.75

Shear Reinforcement:

ρv	ϕv (in)	sv (in)
0.297%	0.625	6.25

Skin Reinforcement:

ρh	nh	ϕh (in)	sh (in)
0.191%	2	0.625	9.75

Material Properties:

Concrete:

f'c (psi)	da (in)
6217	1

Steel:

fy (ksi)	f'y (ksi)	fyv (ksi)	fyh (ksi)
60	60	60	60

Measured Capacity:

Vcrack (k)	Vtest (k)
-	190

Cracking Information:

Load Level	wk (in)	θ
0%	0.000	-
32%	0.005	-
42%	0.013	47.°
53%	0.016	-
63%	0.025	-
74%	0.030	-
84%	0.040	-
100%	-	39.°
-	-	-
-	-	-
-	-	-

Database Summary
0-1851-1
1A
2/2
12/19/2016

Figure 3.13 Sample report with specimen data (Left), figures created from the database (Right)

Additionally, there were some procedures identified over the course of the literature review that were not extensively vetted against experimental data, most notably the mechanics-based procedure developed by Lantsoght et al. (2016). In order to make final recommendations regarding potential crack-based shear strength assessment procedures, this database should be appropriate for evaluating existing procedures with a variety of data from unique sources to test how robust the model's assumptions are.

This database can provide functions similar to the Oregon DOT *Bridge Inspection Pocket Coding Guide* (Bridge Engineering Section Oregon Department of Transportation, 2009) for the Receiving Agency. There are several different member shapes and sizes recorded at a variety of different reinforcement ratios and concrete strengths over several load levels. Using the filtering features to isolate the relevant data for a given bridge member under inspection, this database could be used as a tool to assist the inspector's experience and judgement in evaluating the extent of damage from the observable structural cracking.

Finally, there is a wealth of information stored within this database that will ideally serve future researchers in related endeavors. As research continues to advance in the assessment of visually observed damage in RC infrastructure, it is anticipated that this database will grow and continue to assist TxDOT and future researchers beyond the completion of Project 0-6919.

3.3.4. VCMED Data Analysis

As mentioned in the previous section, there is a wealth of information stored within the VCMED which can be used to provide insight into the structural cracking response of a wide range of shear-sensitive RC bridge members. Figure 3.14 presents all of the maximum measured RC element crack widths plotted with respect to their corresponding load level (i.e., the ratio of applied load to ultimate load required to cause the crack width) from the VCMED. Ranges for effective depth (d), shear-span-to-depth ratio (a/d), shear reinforcement ratio (ρ_v), and skin reinforcement ratio (ρ_h) are summarized in the bottom right corner of Figure 3.14. In cases where large diagonal crack widths (e.g., on the order of 0.05 inches and greater) are developed and observed in an RC element, it is reasonable to assume that a broad range of damage assessment tools/techniques, including traditional inspection methods, would ultimately conclude that a structural element is likely to be exhibiting signs of severe structural distress. Thus, from Figure 3.14, it is not surprising to see that the RC structural elements populating the VCMED, have either failed (i.e., reached 100 % shear resistance) after developing a diagonal crack width of 0.05 inches, or are approaching failure (i.e., are nearing 100 % shear resistance). However, in cases in which diagonal crack widths that were less than 0.05 inches in width were measured, it becomes significantly more difficult to interpret the level of damage based on measured crack widths alone. For example, depending on the specific characteristics of the RC member and on the basis of the data presented, the applied load required to develop a diagonal crack width of approximately 0.02 inches can range anywhere from 10 to 100 % of the member's ultimate shear resistance. In essence, it is apparent that there are many factors that influence the structural cracking response of RC members. Several of these parameters are highlighted and examined in greater detail in Section 4.1.1 of the following chapter.

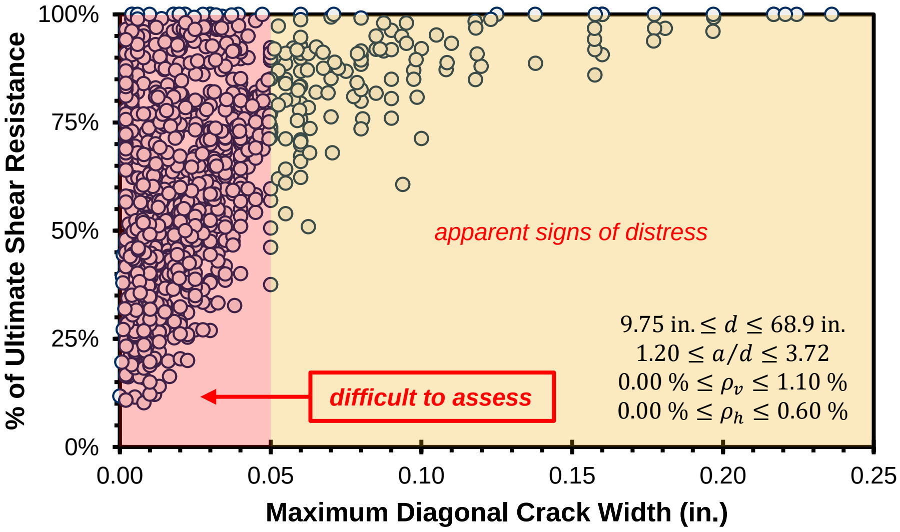

Figure 3.14 Percent of ultimate shear resistance vs maximum diagonal crack width for all load stages recorded in the VCMED

To further demonstrate the significance of the different parameters that may influence the structural cracking behavior of an RC member, consider the diagonal crack width-load level results obtained from two different inverted-tee bent cap test specimens and presented in Figure 3.15. DS1-42-1.85-03 and DS1-42-1.85-06 were constructed and tested as part of TxDOT Project 0-6416. The inverted-tee bent caps were nearly-identical in all respects, with one key exception: DS1-42-1.85-03 was constructed with a shear reinforcement ratio of 0.30 % and DS1-42-1.85-06 was constructed with a shear reinforcement ratio of 0.60 %. While the shear reinforcement level is expected to have major implications in terms of member shear strength, from the figure it can be seen that it also played a major role in terms of serviceability limit states and the interpretation of visually observed cracking. More specifically, a crack width of approximately 0.02 inches was shown to be an indicator of greater shear distress for specimen DS1-42-1.85-06 than for DS1-42-1.85-03. There was a difference of around 30 % in terms of the measured load levels (% of ultimate resistance) at the same level of cracking damage. In that light, it is important to observe that "*a crack width is not a crack width*." That is to say that similar sized crack widths on members which appear outwardly identical do not necessarily correspond to the same relative level of damage. Thus, it is necessary to consider additional information (e.g., reinforcement detailing, shear-span-to-depth ratio, size, etc.) combined with behavioral models to more accurately assess the performance of in-service structures based on visually measured cracks.

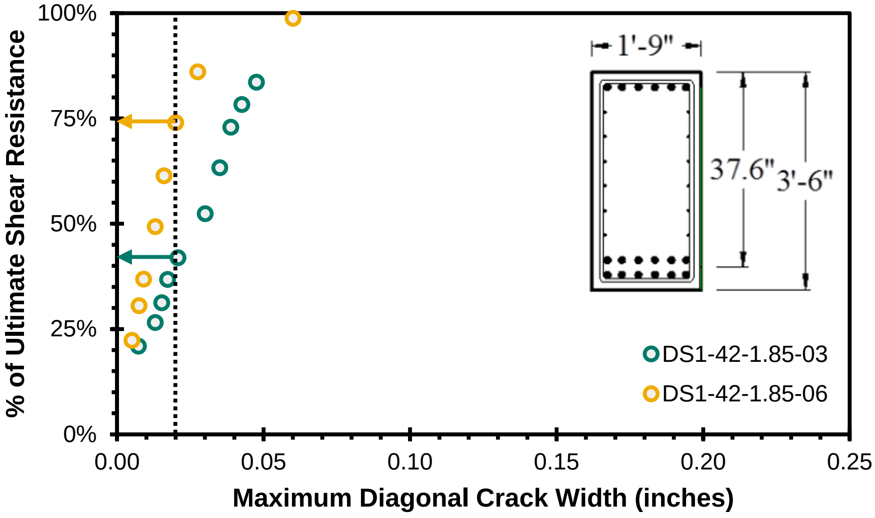

Figure 3.15 Crack behavior comparison for two different levels of shear reinforcement (0.30 & 0.60 %) from TxDOT Project 0-6416

3.3.5. Quality Control

All inputs in the VCMED were checked by members of the research team. Note that the researcher who made the initial input was not the same who checked these entries. This approach ensured that errors associated with data entry or data/report interpretation were identified and resolved prior to ultimately employing the VCMED.

3.4. Notation

a_v	shear span, equal to the distance from center of concentrated load to either (a) face of support for continuous or cantilevered members, or (b) center of support for simply supported members (in.)
a/d	shear span – depth ratio (-)
b_w	web width of rectangular, inverted T, and I girder’s cross section, or thickness of panel element (in.)
c_c	clear cover (in.) on the top/bottom and sides of the cross section
d	distance from extreme compression fiber to centroid of longitudinal tension reinforcement (in.)

d_a	maximum aggregate size (in.)
d_{bl}	flexural reinforcement bar diameter (in.)
d_{bl}’	compression reinforcement bar diameter (in.)
d_{bv}	shear reinforcement bar diameter (in.)
d_{bh}	skin reinforcement bar diameter (in.)
f'_c	specified cylindrical compressive strength of concrete (psi)
f_y	specified minimum yield strength of reinforcing bars (ksi)
f'_y	specified minimum yield strength of compression reinforcement (ksi)
f_{yv}	specified yield strength f_y of transverse reinforcement (ksi)
f_{yh}	specified yield strength f_y of horizontal reinforcement (ksi)
h	height of the section (in.); side length of square panels (in.)
ρ_s	longitudinal tensile reinforcement ratio (-)
ρ'_s	longitudinal compressive reinforcement ratio (-)
ρ_v	shear reinforcement ratio (-)
ρ_h	horizontal reinforcement ratio (-)
n_s	number of tensile bars in longitudinal direction
n'_s	number of compressive bars in longitudinal direction
n_v	number of legs, of transverse shear reinforcement
n_h	number of horizontal bars at each face of the specimen, for skin reinforcement
Shape	cross-sectional shape of the specimen
Source	reference to the name of the TxDOT report number; or the name of the researcher with the publication year (see References chapter)
Name	specimen name, as defined by the researcher who conducted the experiment
V_{crack}	shear carried in the test region at the formation of the first diagonal crack (kips)
V_{test}	maximum shear carried in the critical section of the test region, including self-weight of the specimen and test setup (kips)

Chapter 4. Cracked Continuum Shear Strength Assessment

A variety of mechanics-based procedures, where the web is approximated with a 2D-membrane element, have been successfully used to predict the shear strength of reinforced concrete (RC) beams (Acevedo et al., 2009; Collins et al., 1996; J.-Y. Lee et al., 2011; Mau & Hsu, 1987). Furthermore, research in recent years has shown the potential application of this type of procedure for the purpose of damage assessment of cracked RC members (Calvi et al., 2018). In all of the above-noted procedures, reinforcement is treated as a smeared material property of the concrete.

Figure 4.1 shows an illustration of a cracked RC bent cap and an associated idealized cracked RC element representing the web region of the bent cap and being subjected to three average and uniform planar stresses: a longitudinal stress (σ_x), a transverse stress (σ_y), and a planar shear stress (τ_{xy}). The idealization and element stress conditions shown in Figure 4.1 are referenced throughout the remainder of this chapter and represent only some of the key assumptions used in the formulation of the cracked continuum approach. Other assumptions inherent to the cracked continuum approach presented herein, include:

- *Uniform Stress Conditions*: the uniform stresses acting on the idealized RC element are assumed to be adequately representative, in an averaged sense, of the stresses acting over the web of the member.
- *Uniform Reinforcement Distribution*: the reinforcement in the member is evenly spaced within the web-equivalent element and is treated as a material property of the concrete in the idealized element.
- *Uniform Crack Conditions*: cracks in the idealized RC element are assumed to have uniform width (w_{cr}) and spacing (s_{cr}). These idealized crack conditions are assumed to represent the average mid-depth shear cracking behavior of the web of real member.
- *Perfect Bond*: reinforcement is perfectly anchored to the concrete and does not fail due to bond related failure modes (e.g., pull-out failures, bar slip).
- *No strain offsets*: net strains and total strains are equal. Material strains due to Poisson's effect, thermal effects, or shrinkage or creep, have been neglected in the current procedure.

This Chapter details the development, evaluation, and refinement of the cracked continuum shear strength assessment approach. Additionally, the application of the approach to the development of crack inspection field aids is discussed. Lastly, a summary of key findings is presented.

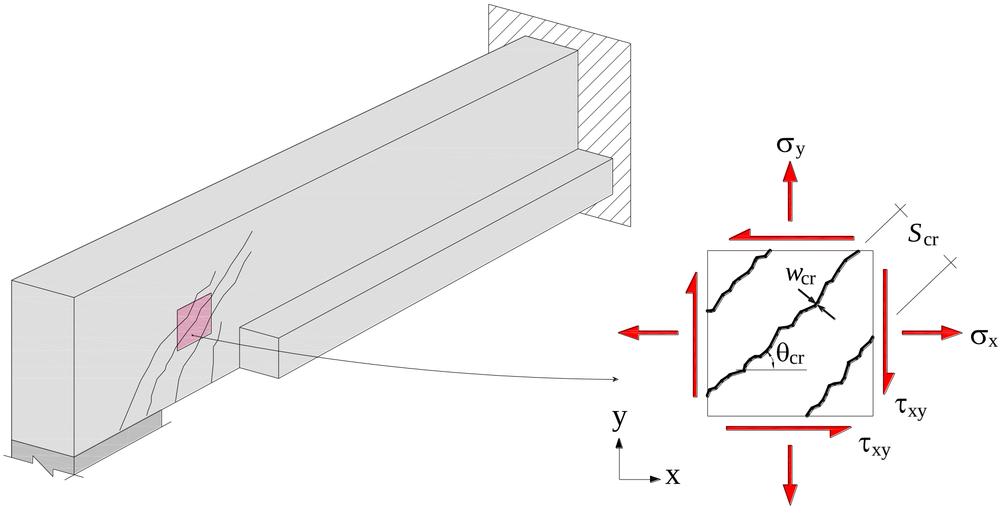

Figure 4.1 Cracked RC bent cap with idealized cracked RC element

4.1. Procedure Development

Several different models were considered, and ultimately used, for the development of the cracked continuum assessment approach. This section briefly outlines these models and other key underlying concepts: crack width/spacing models, models pertaining to disturbed region stress development, and general constitutive models for cracked RC elements.

4.1.1. Crack Spacing and Width Models

Visual crack data of RC can play an important role in diagnosing the stress conditions and strain states experienced by RC members. This section discusses the relevance of crack measurements to in-service strain states and introduces several crack spacing and width models.

Crack spacing in RC has been shown to be directly related to slip between concrete and embedded reinforcing steel (CEB-FIP, 1990). Figure 4.2 shows estimated strain distributions along the length of a member under uniaxial tension for two load cases ($N = N_r$ and $N > N_r$). Across the width of a crack, the concrete stress, and therefore the concrete strain (ε_c), is assumed to be zero and, as a result, reinforcing steel must carry all the load across the crack. However, within the uncracked regions of the concrete, the sound concrete can still develop tensile stress. It should be noted that the mean strains (i.e., strains averaged over both cracked and uncracked sections) are typically used in calculating the anticipated crack widths for RC members in many of the models summarized hereunder.

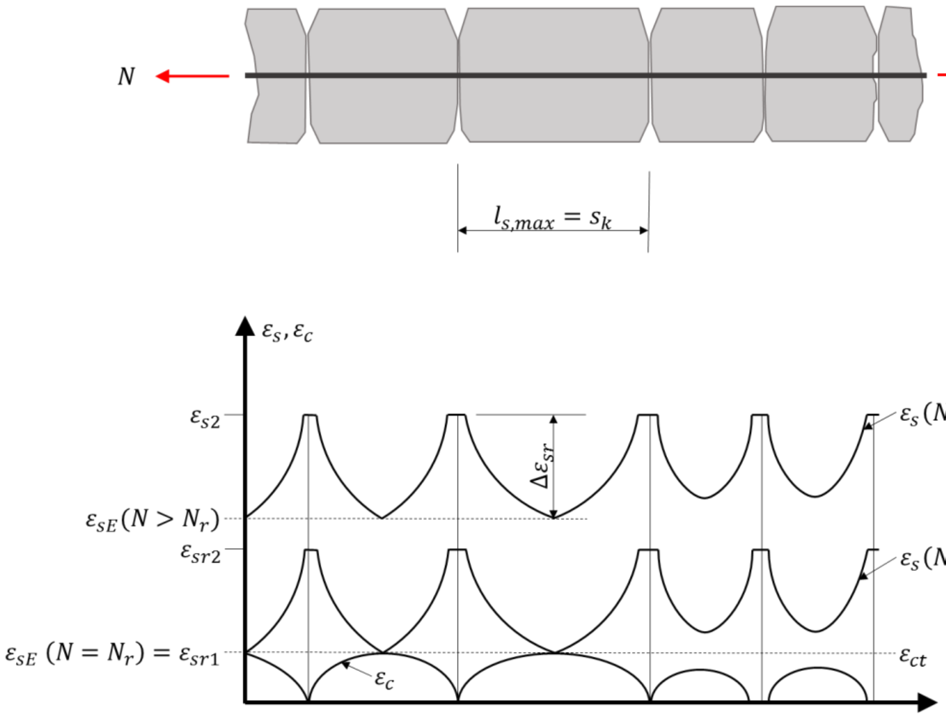

Figure 4.2 Strain distribution in RC tension member (CEB-FIP, 1990)

Several investigators have shown the importance of crack width on RC's ability to transfer shear stresses across crack surfaces. Figure 4.3 illustrates the shear stress transfer across a crack via the aggregate interlock effect. In some cases, the aggregate interlock effect has been estimated to account for up to 75 % of the shear stress carried across shear cracks in RC members (Campana et al., 2013; Cavagnis et al., 2018).

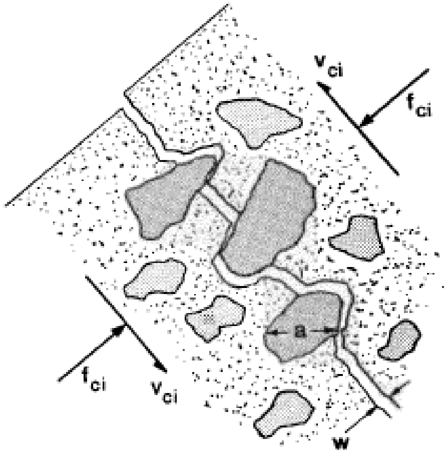

Figure 4.3 Aggregate interlock effect (Vecchio & Collins, 1986)

Several analytical models currently available for estimating the response of cracked RC under variable stress conditions, such as the modified compression field theory

(MCFT) (Vecchio & Collins, 1986), employ what are referred to as "smeared cracking procedures," treating concrete cracking in an averaged sense and in-line with the mean strain concept used by many of the existing concrete crack spacing models. Further, many existing cracked concrete behavioral models are rotating crack models meaning that the orientations of the principle stress and principle strain axes are assumed to be perfectly aligned with each other and re-orient because of concrete damage (i.e., changing material stiffness) or changing loading conditions. Of significance in the context of assessing RC member structural cracking, one could reasonably assume that the crack inclinations developed in a RC member are expected to coincide with the orientation of the principal stresses, since cracks are likely to form perpendicularly to the principal tensile stress. Therefore, measured crack inclinations can be used to estimate the orientation of the principle stress and strain axes for in-service RC members. An important note regarding the crack spacing models presented herein is that all but one of the models examined in the subsequent sections assume the concrete is loaded under uniaxial loading conditions. Crack spacing characteristics for multiaxial loading conditions that are not transverse to the primary reinforcement are usually calculated using various supplementary procedures using a combination of crack spacing estimates computed in individual reinforcement directions.

The application of crack spacing models in the context of providing a quantitative analysis of a damaged RC member lies within these relationships. Several models for the calculation of crack spacing and width have been developed and refined over the past half century. Calculated crack widths, spacings, and inclinations are all dependent on the stress-strain state of the member; however, the actual cracking process is random and therefore can be very difficult to predict. As such, there is typically a relatively wide scatter between the predicted data and the experimental data used for verification. Moreover, while there are several generally accepted methods/procedures that have been shown to be accurate and suitable for estimating concrete crack width development, there is still little agreeance on a single model that can be used to predict cracking conditions at various load levels (Chowdhury & Loo, 2001). Furthermore, studies have shown that a cracking model's accuracy can depend greatly on the type of member being investigated (Xiang et al., 2012).

Several crack spacing and width models have been investigated by the research team in an effort to determine their suitability for the purposes of assessing damage in RC bridge members. The common notation that has been used in the application of these models is presented in Figure 4.4.

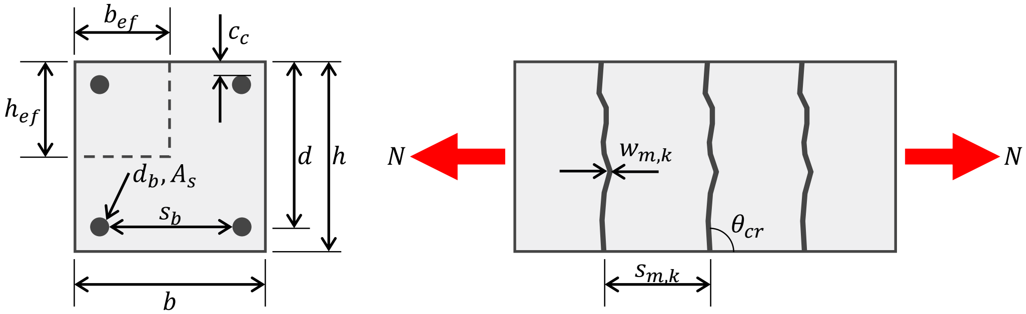

Figure 4.4 General notation

where,
A_s = reinforcement area,
$A_{c,eff}$ effective area of concrete,
= $b_{c,eff} h_{c,eff}$
b = width,
$b_{c,eff}$ effective width of concrete in tension around a reinforcing bar,
d = depth to the centroid of the reinforcing steel,
d_b = reinforcement diameter,
E_c = modulus of elasticity of concrete,
E_s = modulus of elasticity of steel,
f_c' = compressive strength of concrete,
f_r = concrete stress at first crack formation,
f_{s*} = a steel stress,
f_{sr} = steel stress at first crack formation,
f_t' = tensile strength of concrete,
h = total height,
$h_{c,eff}$ effective height of concrete in tension around a reinforcing bar,
N = axial load,
s_b = average bar spacing,
s_k = maximum crack spacing,
s_m = mean crack spacing,
c_c = concrete clear cover (top/bottom or side),
w_k = maximum crack width,
w_m = mean crack width,
α_e = modular ratio,
= E_s/E_c,
ε_{c*} = a concrete strain,
ε_{cs} = concrete shrinkage strain,
ε_{s*} = a steel strain,
θ_{cr} = crack inclination,
ρ = flexural reinforcement ratio,
= A_s/bd,
ρ_{eff} effective reinforcement ratio,
= $A_s/A_{c,eff}$.

4.1.1.1. CEB-FIP/*fib*

The European Committee for Concrete and International Federation for Prestressing (CEB-FIP), now known collectively as the International Federation for Structural Concrete (*fib*), is a European based committee that has developed model codes since the late 1970s. Thus far, three codes have been published: the 1978, 1990 and 2010 Model Codes. Each iteration has provided an updated method for the calculation of concrete crack spacing and crack widths.

4.1.1.1.1. Model Code 1978

The Model Code 1978 from the CEB-FIP (CEB-FIP, 1978), defines two general types of crack widths: maximum and mean. The maximum crack width is shown in Equation 4.1. The mean crack width is given by Equation 4.2 and is based on the mean steel elongation (Equation 4.3) over the mean spacing of the cracks (Equation 4.4).

$$w_k = 1.7 w_m \tag{4.1}$$

$$w_m = s_m \varepsilon_{sm} \tag{4.2}$$

$$\varepsilon_{sm} = \frac{f_s}{E_s}\left[1-\beta_1\beta_2\left(\frac{f_{sr}}{f_s}\right)^2\right] \tag{4.3}$$

where,

β_1 = $\frac{1}{2.5k_1}$

β_2 = 1 at first loading,

= 0.5 for loads applied in a sustained manner or for a large number of load cycles.

$$s_m = 2\left(c_c + \frac{s}{10}\right) + k_1 k_2 \frac{d_b}{\rho_{eff}} \tag{4.4}$$

where,

k_1 = 0.4 for deformed bars,

= 0.8 for plain bars and prestressing strands

k_2 = 0.125 for bending,

= 0.25 for tension,

= $\frac{0.25(\varepsilon_1+\varepsilon_2)}{2\varepsilon_1}$ for cases of eccentric tension or web regions of beams.

4.1.1.1.2. Model Code 1990

"Limit State of Cracking" from the CEB-FIP Model Code 1990 (CEB-FIP, 1990) begins with a formulation for maximum crack width, shown in Equation 4.5. It also defines two stages of cracking: unstable and stable. The maximum length over which slip occurs, i.e., the maximum crack spacing, for a stabilized cracking condition is given by Equation 4.6. The CEB-FIP 1990 also provides an expression for the calculation of the difference in mean steel and concrete strains in Equation 4.7.

$$w_k = s_k \left(\varepsilon_{sm} - \varepsilon_{cm} - \varepsilon_{cs} \right) \tag{4.5}$$

$$s_k = \frac{d_b}{3.6\rho_{eff}} \tag{4.6}$$

$$\varepsilon_{sm} - \varepsilon_{cm} = \varepsilon_s - \beta \frac{f_{sr}}{E_s} \tag{4.7}$$

where,
ε_s = steel strain at the crack,
β = empirical factor to account for the use of mean strains.

The above equations are for the anticipated maximum cracked condition, but the CEB-FIP also addresses mean crack measurements. For a stabilized crack condition, the mean spacing of the cracks can be estimated with Equation 4.8. The average crack width can be calculated by substituting the estimated mean crack spacing into Equation 4.5.

$$s_m \approx \frac{2}{3} s_k \tag{4.8}$$

4.1.1.1.3. Model Code 2010

The *fib* Model Code 2010 (International Federation for Structural Concrete, 2012) modified the crack width model from the previous edition slightly, although the general format is the same, as can be seen from Equation 4.9. Using Equation 4.10 and 4.11, the stabilized maximum crack width can be calculated. Note that there were no major updates to the stabilized crack spacing equation between the 1990 and 2010 editions; however, some portions of the model affecting the calculation of crack widths were updated.

$$w_k = s_k\left(\varepsilon_{sm} - \varepsilon_{cm} - \varepsilon_{cs}\right) \qquad 4.9$$

$$s_k = \frac{d_b}{3.6\rho_{eff}} \qquad 4.10$$

$$\varepsilon_{sm} - \varepsilon_{cm} - \varepsilon_{cs} = \left(f_s - \beta f_{sr} + \eta_r \varepsilon_r E_s\right)/E_s \qquad 4.11$$

where,
β = empirical factor to account for the use of mean strains,
η_r = shrinkage coefficient.

4.1.1.2. Deluce, Lee, and Vecchio (2014)

After a series of experimental programs examining the behavior of fiber-reinforced concrete (FRC) members containing conventional reinforcement, investigators concluded that there was a lack of accurate models available for predicting the cracking behavior of FRC (Deluce et al., 2014). The Model Code 1978 was selected as a base model which was then modified appropriately to account for fiber-reinforcement. The most salient change, within the context of using crack spacing and width models with a mechanics-based approach to damage assessment of traditional RC members, is the way biaxial stress conditions were handled. All other models discussed in this report use an x, y, z coordinate system, shown in Figure 4.5, based on traditionally used primary reinforcement directions; however, this model uses a coordinate system based on the directions of the principal axes of stress. The use of principal stress directions permits more convenient and accurate classification of cracking behavior for reinforcement which is not orthogonal to an x, y, z coordinate system and avoids the challenge of calculating cracks associated with tensile stresses that are not aligned with the x, y, z coordinate system. Equation 4.12 summarizes the portion of the model which is applicable to conventional RC members. Crack widths can be calculated with Equation 4.1 or 4.2 using principal tensile strain (ε_1).

$$s_m = 2\left(c_a + \frac{s_{b1}}{10}\right) + \frac{k_1 k_2}{s_{mi1}} \qquad 4.12$$

where,
c_a = effective concrete cover which can be taken as 1.5 times maximum aggregate size,
s_{b1} = effective longitudinal bar spacing in the principle tensile direction,
= $\frac{1}{\sqrt{\sum_i \frac{4\rho_{s,i}}{\pi\phi_{s,i}^2}\cos^4\theta_i}}$

θ_i = angle between the ith reinforcement layer and the principal tensile axis,

s_{mi1} ith reinforcement effectiveness parameter in the principal tensile direction,

= $\sum_i \frac{\rho_{s,i}}{\phi_{s,i}} \cos^2 \theta_i$

The factors k_1 and k_2 are as defined in Section 4.1.1.1.1.

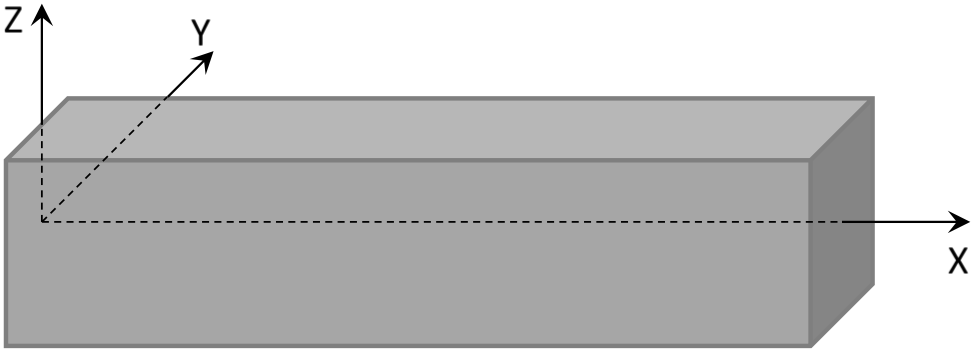

Figure 4.5 Typical x, y, z coordinate system for a beam

4.1.1.3. Eurocode 2

The Eurocode 2 is the European standard for RC design. The 1991 edition was updated in 2003. Both editions contain crack width and spacing formulations like the CEB-FIP 1978 Model Code.

4.1.1.3.1. 1991

Section 4.4.2.4 of the 1991 edition of the Eurocode 2 (European Committee for Standardization, 1991) details the calculation of maximum crack widths and average final crack spacing. The design crack width is calculated using Equation 4.13. Eurocode 2 similarly provides equations for the computation of both mean steel strain and average final crack spacing, using Equation 4.14 and 4.15, respectively. Note that the input of Equation 4.15 is restricted to units of millimeters.

$$w_k = \beta s_m \varepsilon_{sm} \tag{4.13}$$

$$\varepsilon_{sm} = \frac{f_s}{E_s}\left[1 - \beta_1 \beta_2 \left(\frac{f_{sr}}{f_s}\right)^2\right] \tag{4.14}$$

$$s_m = 50 + 0.25 k_1 k_2 \frac{d_b}{\rho_{eff}} \tag{4.15}$$

where,
β = factor which relates average crack width to design crack width,
= 1.7 for load induced cracking,
β_1 = bond property coefficient
= 1.0 for the high bond bars,
= 0.5 for plain bars,
β_2 = load duration coefficient,
= 1.0 for a single, short term loading,
= 0.5 for a sustained or cyclic load,
k_1 = bond property coefficient,
= 0.8 for high bond bars
= 1.6 for plain bars
k_2 = strain distribution coefficient,
= 0.5 for bending,
= 1.0 for pure tension,
= $\frac{(\varepsilon_1+\varepsilon_2)}{2\varepsilon_1}$ for cases of eccentric tension or web regions of beams.

4.1.1.3.2. 2003

The 2003 edition of Eurocode 2 (European Committee for Standardization, 2004), provides a formulation for crack width that is similar to the 1991 edition summarized in Equation 4.16, but employs a maximum crack spacing, rather than mean crack spacing. The maximum crack spacing is given by Equation 4.17. The formulation is similar to the average crack spacing model from the 1991 edition, but the equation is now given in a more dimensionally indistinct form, so input is no longer restricted to units of millimeters. The difference between mean steel and concrete strains may be calculated using Equation 4.18.

$$w_k = s_k(\varepsilon_{sm} - \varepsilon_{cm}) \qquad 4.16$$

$$s_k = k_3 c_c + k_1 k_2 k_4 \frac{d_b}{\rho_{eff}} \qquad 4.17$$

where,
k_1 = bond property coefficient,
= 0.8 for high bond bars,
= 1.6 for plain bars,
k_2 = strain distribution coefficient,
= 0.5 for bending,
= 1.0 for pure tension
= $\frac{(\varepsilon_1+\varepsilon_2)}{2\varepsilon_1}$ for cases of eccentric tension or web regions of beams,
k_3 = region specific coefficient,
= 3.4 for general case,

k_4 = region specific coefficient,
= 0.425 for general case.

$$\varepsilon_{sm} - \varepsilon_{cm} = \frac{f_s - k_t \dfrac{f_r}{\rho_{eff}}\left(1 + \alpha_e \rho_{eff}\right)}{E_s} \geq 0.6 \frac{f_s}{E_s} \qquad 4.18$$

where,
k_t = load duration factor,
= 0.6 for short term loading,
= 0.4 for long term loading.

4.1.1.4. Bažant, Oh, and Kang

Bažant and Oh developed a fracture mechanics approach for predicting the cracking behavior of RC. A few years later, Oh and Kang simplified the approach to make it more practical for solving typical design problems.

4.1.1.4.1. Bažant and Oh (1983)

In 1983, Bažant and Oh prepared a fracture mechanics approach using both the strength and energy criteria to predict crack spacing and widths. The strength criterion states concrete stress must reach concrete tensile strength (f'_t) to initiate cracking and provides the basis for many current methods of predicting crack spacing. Furthermore, the energy criterion states that in order for a crack to form there must be a release of energy corresponding to a reduction of stress to zero in the concrete (Bažant & Oh, 1983). Bažant and Oh noted that the crack spacing is limited by the bond strength capacity of the member. Using a combination of fracture mechanics concepts, such as stress lines and fracture energy, and bond mechanics, they proposed Equation 4.19 as an approximate solution to a lower bound of crack spacing.

$$s_m = \left(\frac{3\pi^2 k E_c \zeta_f \left(b_{eff} - d_b\right)\left(b_{eff} + d_b\right)^3}{4F_b'^2 \left(2b_{eff} + d_b\right)} \right)^{1/2} \qquad 4.19$$

where,
k = slope of the stress line,
= 0.7 from test data fitting,
ζ_f = fracture energy,
= $(2.72 + 0.0214 f_t') f_t'^2 d_a / E_c$
b_{eff} radius of an equivalent circular area of concrete around a single reinforcing bar,

d_a = maximum aggregate diameter,
F_b' = bond shear force per unit length.

Two expressions to estimate associated crack widths are shown in Equation 4.20 for sparse cracks and for closely grouped cracks.

$$w_m = \begin{cases} s_m \varepsilon_s - \left(s_m - \dfrac{b_{eff} - d_b}{k} \right) \dfrac{f_s}{E_c} & \ldots \quad s_m \geq b_{eff} - d_b / k \\ s_m \varepsilon_s & \ldots \quad s_m \leq b_{eff} - d_b / k \end{cases} \qquad 4.20$$

4.1.1.4.2. Oh and Kang (1987)

Oh and Kang (1987) simplified the previous model developed by Bažant and Oh (1983) to create a more practical crack width and spacing calculation method for flexural members. Using the aforementioned model, Oh and Kang identified key non-dimensionalized variables and used a minimization algorithm to determine the most influential variables for both maximum crack width and average crack spacing. The equations were then compared to an experimental program and fine-tuned to ensure conservatism for design. The maximum crack width is given by Equation 4.21 and the average crack spacing is given by Equation 4.22. Note that the area of steel being considered in each equation is for a single reinforcement bar in its effective area of concrete.

$$\frac{w_k}{\phi_s} = a_0 \left(\varepsilon_s + a_1 \right) R \qquad 4.21$$

where,
a_0 = $159 \left(\frac{c_c}{h_2}\right)^{4.5} + 2.83 \left(\frac{A_1}{A_s}\right)^{1/3}$,
h_2 = distance from the extreme tension fiber to the neutral axis,
A_1 = average effective area of concrete around each reinforcing bar,
= bh_1/n_{bars},
a_1 = 0,
= 0.0002 for conservative design,
R = h_2/h_3

$$\frac{s_k}{\phi_s} = c_0 + \frac{0.236 \times 10^{-6}}{\varepsilon_s^2} \qquad 4.22$$

where,
c_0 = $25.7 \left(\frac{c_c}{h_2}\right)^{4.5} + 1.66 \left(\frac{A_1}{A_s}\right)^{1/3}$

4.1.1.5. Gergely-Lutz Crack Width Expression

Gergely and Lutz (1968) proposed equations for the calculation of maximum crack widths on the side and tensile faces of RC flexural members. Using regression analysis of data obtained from several different concrete cracking investigations, the following two equations, with inputs of inches and kips per square inch, were proposed for side and bottom crack widths, respectively:

$$w_k = 91\times10^{-6}\frac{\sqrt[3]{c_c A}}{1+c_c/h_1}\left(f_s-5\right) \tag{4.23}$$

$$w_k = 91\times10^{-6}\sqrt[3]{c_c A}R\left(f_s-5\right) \tag{4.24}$$

where,
A = effective area of concrete around a reinforcing bar,
= A_c/n_{bars},
A_c = effective area of concrete,
= $2b(h-d)$,
h_1 = $(1-k)d$,
k = ratio of distance from neutral axis to compression face to the effective depth of the beam,
R = h_2/h_1,
h_2 = $h-kd$.

Note that clear cover should be measured for the side in Equation 4.23 and for the bottom in Equation 4.24.

4.1.1.6. Chowdhury and Loo (2001)

Chowdhury and Loo developed an equation for the predication of crack spacing and width using a statistical regression analysis, similar to Gergely and Lutz (Chowdhury & Loo, 2001). However, the data used in the analysis included both RC and partially prestressed concrete flexural members. The solution of the statistical regression yielded Equation 4.25 for crack spacing and Equation 4.26 for crack widths.

$$s_m = 0.6\left(c_c - s_b\right) + 0.1\frac{d_b}{\rho} \tag{4.25}$$

$$w_m = s_m\frac{f_s}{E_s} \tag{4.26}$$

4.1.1.7. Comparison of Methods

To compare and contrast crack spacing and crack width estimates obtained using the different models summarized above, consider the axial RC member presented in Figure 4.4. Calculations were performed considering two reinforcement ratios, 0.5 % and 1.0 %, from which additional reinforcement characteristics were calculated. For each model the mean crack spacing and maximum crack width was computed for the two reinforcement ratios. The values were then averaged, and each model was compared to the average. Results are summarized in Figures 4.6 and 4.7, for mean spacing and maximum crack widths, respectively. More detailed results are also included in Tables 4.1 and 4.2. For other section properties, the following was assumed:

b = 10 in.
h = 10 in.
E_c = 5000 ksi
E_s = 29000 ksi
f_c' = 5 ksi
f_r = 424 psi
c_c = 2 in.
N = 18 kip (0.6f_y for 0.5 % and 0.3f_y for 1.0 %, neglecting concrete tensile stresses)

In general, there is reasonable grouping between most of the models. Typically, the values fall within 30 % of the average predicted value, and many of the models are within 10-15 % of each other. The three editions of the Model Code perform similarly but exhibited closer grouping at the higher reinforcement ratio (1.0 %). The modified 1978 Model Code crack spacing model from Deluce, Lee, and Vecchio performed very similarly to the original edition. Both editions of the Eurocode 2 tended to compute larger values, with the 2003 edition computing the largest value of any model at both reinforcement ratios. Bažant and Oh’s model performance is very dependent on assumptions regarding some difficult to measure material properties.

All three editions of the Model Code use similar formulations with bar cover, bar spacing, bar diameter and effective reinforcement ratio serving as key variables. The 1978 edition is the only one to explicitly include bar spacing and clear cover, the later editions assume a contribution approximately equal to 0.09(φ_s/ρ_{eff}). At some critical (φ_s/ρ_{eff}) ratio, which is unique for a given bar spacing and clear cover, the models will predict exactly the same crack spacing. For (φ_s/ρ_{eff}) ratios larger than the critical value, the 1978 edition tends to predict smaller values than the 1990 and 2010 editions. For (φ_s/ρ_{eff}) ratios smaller than the critical value, the opposite is true. Additionally, the maximum crack width was changed between the 1978 Model and the 1990 and 2010 Models. In the 1978 edition, the maximum crack width is assumed to be $1.7w_m$, while the later editions revised this assumption to $1.5w_m$. Typically this coefficient will vary between 1.3 and 1.7 depending on the model and the experimental data being investigated (Chowdhury & Loo, 2001). The model proposed by Deluce, Lee, and Vecchio, which is a modified version of the 1978 Model Code, offers similar performance to the original edition. The primary difference is the optimization of the method for computers and finite element implementation. To allow for smeared reinforcement data, effective clear cover and bar spacing characteristics are used. Note that if the measured values were used the model would calculate identical predictions for crack spacing and width to the 1978 Model Code for this uniaxial example.

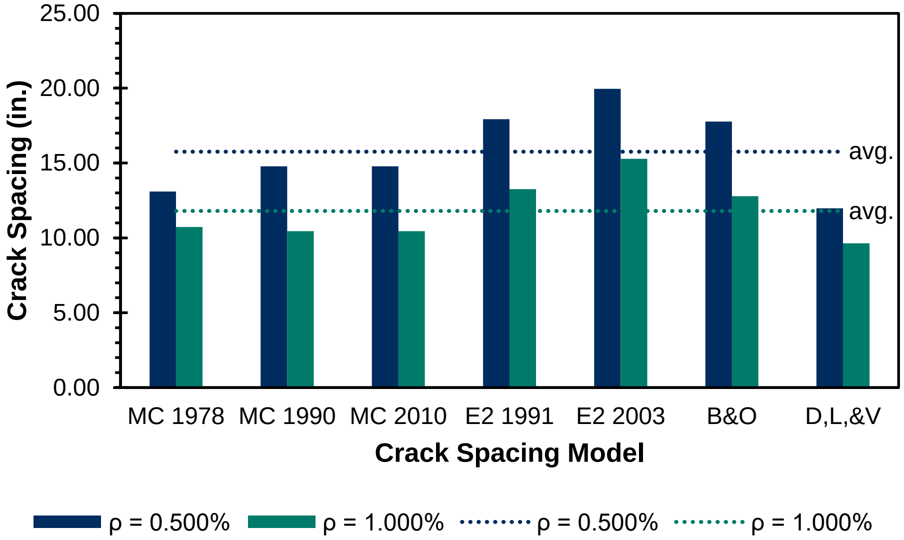

Figure 4.6 Mean crack spacing summary

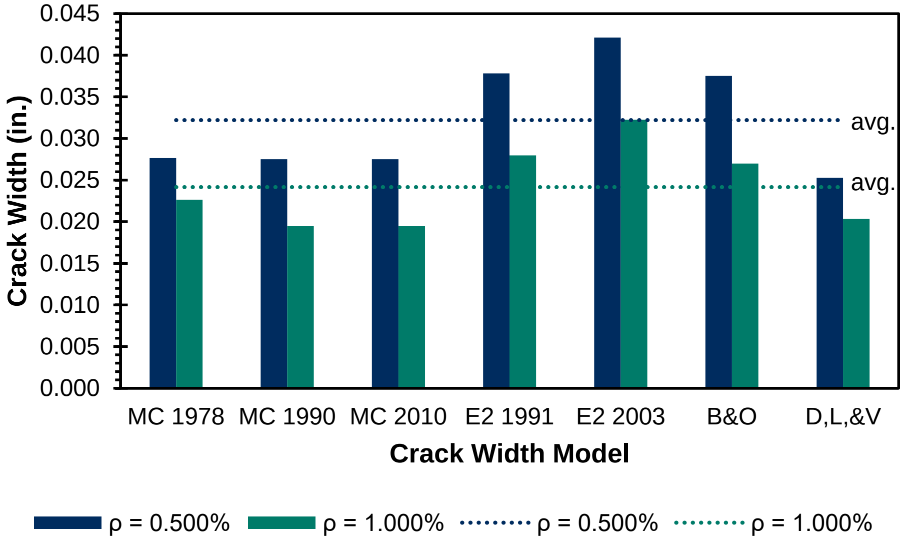

Figure 4.7 Maximum crack width summary

Eurocode 2 1991 imposes a limitation on the contribution of clear cover to crack spacing, which was removed in the 2003 edition. While the Eurocode 2 2003 and other similarly derived models allow for linear variation of crack spacing with concrete cover, the Eurocode 2 1991 assumes a maximum contribution of 50 mm (1.97 in.). However, for a minimum cover of 1.5 in., the contribution calculated by the 2003 edition of the Eurocode is 3 in, an approximately 50 % discrepancy. The relative contribution of the (φ_s/ρ_{eff}) ratio is the same for both models, at 0.20(φ_s/ρ_{eff}). Therefore, for any cover greater than 1.0 in., the 2003 edition will always predict a larger value than the 1991 edition.

Although both the Model Code and Eurocode 2 both use a linear relationship for crack spacing and the (φ_s/ρ_{eff}) ratio, the associated slopes are different (0.1 for Model Code 1978, 0.19 for Model Codes 1990 and 2010, and 0.2 for Eurocode 2). As such, the Eurocode 2 will nearly always predict larger crack spacings than the Model Code. The exception is for the 1978 Model Code at large reinforcement ratios. For identical sections, the 1978 Model Code's inclusion of the bar spacing parameter will cause it to predict slightly higher values than the Eurocode 2 1991.
The model proposed by Bažant and Oh requires the most assumptions and complicated input of any of the models considered, which makes it difficult to apply in a simple manner without making several approximations regarding the material properties. Bažant and Oh provide an estimation for slope of the stress line based on their experimental work, based on a best fit of their test data. Both fracture energy and bond shear stress are not easily measured, but Bažant and Oh provide a formula for fracture energy from a previous publication and several models are available the computation of bond shear stress, such as the Model Code 1990. However, these models require additional input such as tensile strength of concrete, slip, bond conditions, etc. This further increases the number of assumptions that need to be made, unless laboratory testing is done to measure these values. This model is very sensitive to the assumptions made regarding the tensile and bond strength characteristics of the concrete; however, if all the variables are appropriately counted for, this model can provide similar performance to the other models investigated thus far.

The models developed by Gergely and Lutz, Oh and Kang, and Chowdhury and Loo were developed specifically for flexural members and were not used in this axial member example. Although they were not created for general axial loading conditions, there are a few key insights which can be taken from a qualitative look at the models. It can be noted that several of the key parameters used in these models are the same as those noted earlier: bar diameter, bar spacing, bar cover, and effective reinforcement ratio. Also note the importance of the cubed root of the effective concrete area in tension, an empirical result first demonstrated by Gergely and Lutz and later theoretically correlated by Bažant and Oh's model (Bažant &

Xu, 1991). The primary difference between the flexural models and the “general” models is the inclusion of factors to account for the strain gradient that occurs in a flexural member. The flexural models simply do not allow for the user to opt out of a flexural loading pattern, while the general models are more flexible. Therefore, the general crack spacing and width models are expected to be better-suited to handle the treatment of RC member shear cracking.

Table 4.1 Mean crack spacing summary

Model	$\rho = 0.50$ %		$\rho = 1.00$ %	
	s_m (in.)	s_m/s_{avg}	s_m (in.)	s_m/s_{avg}
Model Code 1978	13.10	0.83	10.73	0.91
Model Code 1990	14.78	0.94	10.45	0.89
Model Code 2010	14.78	0.94	10.45	0.89
Eurocode 2 1991	17.93	1.14	13.25	1.12
Eurocode 2 2003	19.96	1.27	15.28	1.30
Bažant and Oh	17.77	1.13	12.79	1.08
Deluce, Lee, and Vecchio	11.98	0.76	9.64	0.82

Table 4.2 Maximum crack width summary

Model	$\rho = 0.50$ %		$\rho = 1.00$ %	
	w_k (in.)	w_k/w_{avg}	w_k (in.)	w_k/w_{avg}
Model Code 1978	0.028	0.86	0.023	0.94
Model Code 1990	0.028	0.85	0.019	0.81
Model Code 2010	0.028	0.85	0.019	0.81
Eurocode 2 1991	0.038	1.17	0.028	1.16
Eurocode 2 2003	0.042	1.31	0.032	1.34
Bažant and Oh	0.038	1.16	0.027	1.12
Deluce, Lee, and Vecchio	0.025	0.79	0.020	0.84

Other similar comparisons using flexural models have been done with full experimental programs. One such study (Xiang et al., 2012) on flexural members showed that section shape, which is not directly included in any of the models, can also affect the ability of various crack spacing models. An experimental program involving T-beams and box girders was completed and showed that the predicted values for the open section tended to be 10-15 % closer to the measured value than those for the closed section (Xiang et al., 2012). Therefore, the selection of the most accurate crack spacing and width model may also be dependent on the type of member being investigated.

For the procedures presented in this Chapter, the modified 1978 Model Code crack spacing and width formulation (Deluce et al., 2014) was used. Since the crack spacing is calculated relative to the principal tensile axis, it is convenient for crack-based shear strength assessment applications. For RC, the model was found to estimate larger than observed spacings for tested panel elements (Deluce et al., 2014). This is in line with previous findings regarding the performance of the original 1978 Model Code equations for beams (De Silva et al., 2008). Combining these results with the brief comparison made between the various crack spacing models in this section, it was determined that the modified 1978 Model Code equations would be most likely to provide crack spacings in line with reality.

4.1.2. Disturbed Region Analysis

In general, beams under transverse loading are assumed to be made up of two types of regions: beam regions (b-regions) and disturbed regions (d-regions). Beam regions comply with the assumptions of classical beam theory, most notably that plane sections remain plane. A consequence of classical beam theory assumptions is that transverse stresses (σ_y) are generally much smaller than longitudinal (σ_x) and shear (τ_{xy}) stresses. As such, transverse stresses are almost always assumed to be zero, or negligible, in sectional analysis and design procedures (e.g., AASHTO LRFD or CSA Design Code). Disturbed regions, on the other hand, refer to those regions that deviate from these assumptions (Schlaich et al., 1987). Often disturbed regions are located near concentrated loads or supports, as illustrated in Figure 4.8.

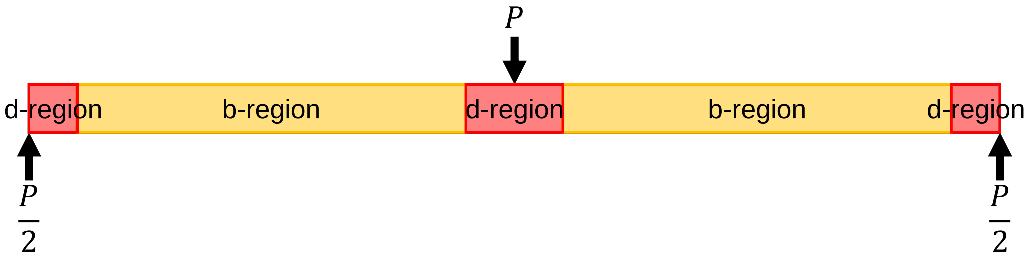

Figure 4.8 Beam and disturbed regions in point loaded beam

For beams with shear-span-to-depth (a/d) ratios less than 2.0 to 2.5, the entire member effectively behaves as a disturbed region. These types of beams are typically classified as “deep beams” and exhibit markedly different behavior than beams that are slender in shear. Typically, a beam is considered slender in shear if the shear-span-to-depth ratio is approximately 3.0 or greater. In the case of deep beams, non-linear strain distributions and direct strut action can dominate member behavior. Note that the term “deep” is relative to the shear span of the beam and does not necessarily correlate to the physical size (height) of member. For beams classified as being deep, the flow of forces developed in these members tend to be influenced by direct strut action, as is shown schematically in Figure 4.9. Essentially, compression forces flow directly to the support and the longitudinal reinforcement is forced into tension to satisfy equilibrium. In this case, transverse stresses can become quite large, particularly as the flow of compressive force becomes closer to vertical (i.e., as the shear-span-to-depth ratio decreases).

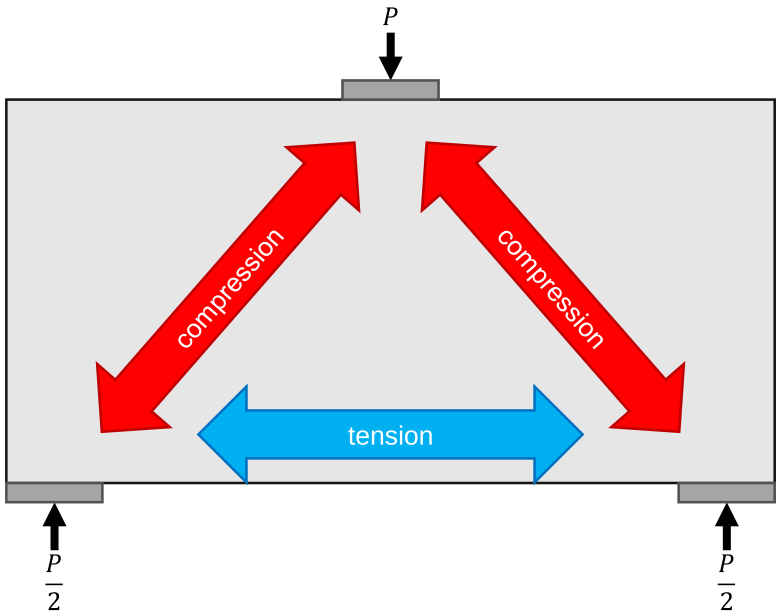

Figure 4.9 Schematic of direct-strut action in a deep beam

For beams that develop significant transverse stresses, typical sectional analyses do not accurately represent behavior and alternative methods of analysis are generally used. Research efforts carried-out over the past two decades have been aimed at developing expressions for the estimation of transverse stress distributions and magnitudes, based on beam geometry and loading conditions (Acevedo et al., 2009; Uzel, 2003). These expressions were subsequently used to modify different types of sectional analysis procedures and it was shown that their inclusion within sectional analyses led to improved (i.e., more accurate) ultimate strength predictions. To satisfy the condition of uniform stresses for the procedure presented herein, a through-depth average transverse stress based on the equations presented by Uzel (2003) was used. Equations 4.27 and 4.28 show the equations as they have been implemented in the current damage-based assessment procedure. Equation 4.27 calculates the length of the disturbed region relative to the edge of the bearing plate and Equation 4.28 calculates the transverse stress proportion based on member geometry. In the original formulation presented by Uzel (2003), multiple bearing plates in a disturbed region were handled with superposition; however, in the crack-based analysis procedure it was found that averaging multiple transverse stress ratios from the simplified expression (Equation 4.28), rather than adding, provided better results.

$$c = \left(2 - \frac{l_b}{a}\right) \cdot 0.75h \qquad 4.27$$

where,

l_b = bearing plate length along longitudinal axis of the beam

a = shear span

h = total height of beam

$$\frac{\sigma_y}{\tau_{xy}} = \begin{cases} \frac{1}{2}\frac{h}{a}\left(\frac{2.5}{0.6+4\frac{x_{cr}}{c}} - 0.5\right) & \ldots \quad x_{cr} < c \\ 0 & \ldots \quad x_{cr} \geq c \end{cases} \qquad 4.28$$

where,

x_{cr} = location of critical section along longitudinal axis of the beam

= $\frac{a}{2}$ for $\frac{a}{d} < 2.5$

= $(1.0 \sim 1.5) \cdot d$ for $\frac{a}{d} \geq 3.0$

4.1.3. Constitutive Relations

The procedure initially developed and presented in this chapter primarily uses the cracked concrete constitutive models of the MCFT (Vecchio & Collins, 1986). The MCFT is a smeared fully-rotating crack model for the analysis of RC elements under uniform stresses (σ_x, σ_y, and τ_{xy} as in Figure 4.1). As an aside, the preliminary cracked continuum procedure proposed herein is more accurately classified as a hybrid fixed-/rotating-crack model due to the use of a fixed crack angle to characterize the principal strain axis. Examples of fixed crack or hybrid procedures can be found in (Maekawa et al., 2003) or (Vecchio, 2000), respectively. A summary of the equations of the MCFT is shown in Figure 4.10.

Of primary interest are the key constitutive models presented in the MCFT: tension stiffening, compression softening, and the influence of stress conditions at crack locations. Often it is assumed, particularly for RC design purposes, that cracked RC only carries tensile stresses by way of reinforcement; however, experimental results obtained by Vecchio and Collins (1986), and others (Scanlon, 1971), have shown that even after cracking, concrete can continue to resist tensile stresses between crack locations and, as a result, stiffens the cracked concrete under tension. This phenomenon is now referred to as concrete tension stiffening. Furthermore, and from the same experimental investigation performed by Vecchio and Collins (1986), the compressive strength of cracked concrete was found to be negatively impacted, or “softened”, in the presence of transverse cracking. Thus, cracked RC under multi-axial stress conditions is assumed to be impacted by concrete "compression softening", resulting in a reduction of both the compressive strength and the coinciding concrete strain at the peak resistance of the concrete, as a result of cracking. Crack surface stress conditions include local tensile stress increases in the reinforcement across crack locations and shear stresses that develop on the crack surface (i.e., aggregate interlock stresses). Increased reinforcement stresses at the locations of cracks develop due to the fact that, at these crack locations, reinforcement alone must transfer all tensile stresses. This local increase in the reinforcement stress is equilibrated by shear stresses on the crack surfaces which are assumed to be resisted by aggregate interlock mechanisms.

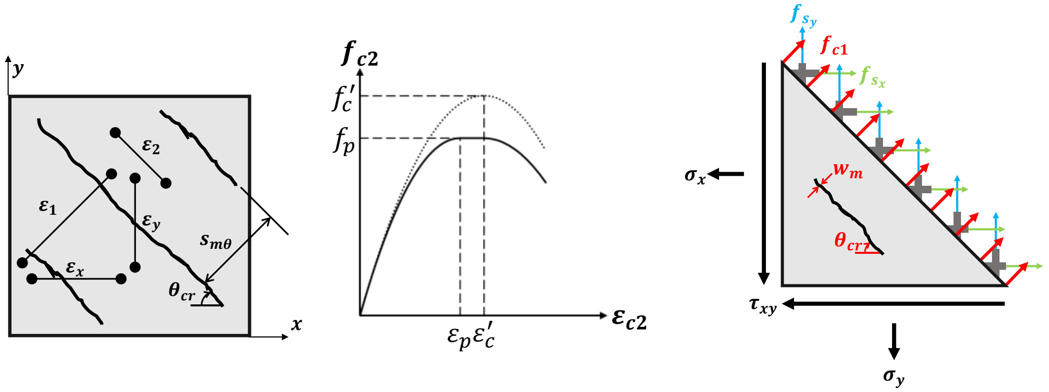

Geometric Conditions:	***Constitutive:***	***Equilibrium:***
Compatibility:	**Concrete:**	**Average Stresses:**
$\varepsilon_x = \varepsilon_{cx} = \varepsilon_{sx}$ (1)	$f_{c1} = \dfrac{f_t'}{1 + \sqrt{C_t \varepsilon_1}}$ (7)	$\sigma_x = f_{cx} + \rho_x f_{sx}$ (16)
$\varepsilon_y = \varepsilon_{cy} = \varepsilon_{sy}$ (2)	$C_t = 91.4 \cdot 0.6m$ (8)	$\sigma_y = f_{cy} + \rho_y f_{sy}$ (17)
	$m = \sum \dfrac{4\rho_i}{d_{bi}} \lvert \cos\theta_{ni} \rvert$ (9)	$\tau_{xy} = v_{cxy}$ (18)
	$f_{c2} = -\beta_d f_c' \left[2\left(\dfrac{\varepsilon_2}{\beta_d \varepsilon_c'}\right) - \left(\dfrac{\varepsilon_2}{\beta_d \varepsilon_c'}\right)^2 \right]$ (10)	
	$\beta_d = \dfrac{1}{1 + C_s C_d} \leq 1$ (11)	
	$C_s = \begin{cases} 1.00\ (no\ crack\ slip) \\ 0.55\ (crack\ slip) \end{cases}$ (12)	
	$C_d = 0.35\left(-\dfrac{\varepsilon_1}{\varepsilon_2} - 0.28\right)^{0.8}$ (13)	
Average Strains:	**Reinforcement:**	**Crack Stresses:**
$\varepsilon_x = \varepsilon_1 \sin^2\theta_{cr} + \varepsilon_2 \cos^2\theta_{cr}$ (3)	$f_{si} = E_{si}\varepsilon_i \leq f_{yi}$ (14)	$f_{c1} = \sum \rho_i (f_{scri} - f_{si}) \cos^2\theta_{ni}$ (19)
$\varepsilon_y = \varepsilon_1 \cos^2\theta_{cr} + \varepsilon_2 \sin^2\theta_{cr}$ (4)		$v_{ci} = \sum \rho_i (f_{scri} - f_{si}) \cos\theta_{ni} \sin\theta_{ni}$ (20)
$\gamma_{xy} = (\varepsilon_1 - \varepsilon_2) \sin 2\theta_{cr}$ (5)		
Crack Conditions:	**Shear Stress on Crack:**	
$w_{cr} = \varepsilon_1 s_{cr}$ (6)	$v_{ci} \leq \dfrac{2.17\sqrt{f_c'}}{0.31 + \dfrac{24 w_{cr}}{a + 0.63}}$ (psi, in.) (15)	

Figure 4.10 Summary of MCFT equations (Adapted from Bentz et al., 2006)

4.1.4. Solution Procedure

The information provided in the previous sections summarize the key element comprising the mechanics-based damage assessment procedure for cracked RC. The outline of the general procedure used to incorporate all of these elements (refer to Figures 4.11 and 4.12), roughly follows the organization of Section 4.1 and is re-iterated below:

- Estimate the principal tensile strain using Equations 4.2 and 4.12
  - Note: ε_1 should be used in place of ε_{sm}
- Calculate the target transverse stress proportion (σ_y/τ_{xy}) using Equations 4.27 and 4.28
- Make an initial guess for the principal compressive strain (ε_2)
- Use the estimated strains and related constitutive models of the MCFT to calculate concrete and reinforcement stresses (Figure 4.10)
- Establish element equilibrium (Figure 4.10)
- Check if the target disturbed region stress proportion is satisfied
  - If it is, then starting load stage of the analysis is finished
  - If not, make a new guess for the principal compressive strain (ε_2)
- Forecast member response to determine residual capacity (see below)

Forecasting member response is accomplished in this procedure by fixing the longitudinal stress proportion (σ_x/τ_{xy}), which was previously unknown, based on the results from the starting load stage. At this point in the analysis, all load proportions have been computed and are assumed to be maintained going forward using a typical forward fixed-crack analysis procedure. Starting from a known load stage, strains are calculated, and crack characteristics (e.g., crack widths, inclinations, etc.) are estimated. The load is then incrementally increased until the stiffness of the cracked concrete element is no longer capable of carrying the applied loads, which is indicative of failure. When an estimate of the failure load level (i.e., stress level) is achieved, Equation 4.29 or Equation 4.30 can be used to estimate utilization or residual capacity, respectively. Furthermore, Equation 4.2 can be used to estimate a failure crack width. It is worth noting that this iterative analysis procedure is similar to the AASHTO LRFD *General Method* that is also an iterative process when used for analysis.

$$Utilization = \frac{\tau_{xy,a}}{\tau_{xy,u}} \times 100\% \qquad 4.29$$

where,

$\tau_{xy,a}$ = shear stress estimated from starting load stage

$\tau_{xy,u} =$ shear stress estimated at failure load stage

$$Residual\ Capacity = 100\% - Utilization \qquad 4.30$$

For this procedure, the resulting relative stress values (i.e., the utilization or the residual capacity) or estimated crack widths can be used to better interpret visual inspection data. An example of a typical analysis is shown for beam DS3-42-1.85-03 is shown in Figure 4.13. The procedure provides very reasonable estimates for the residual capacity and crack behavior in this example case.

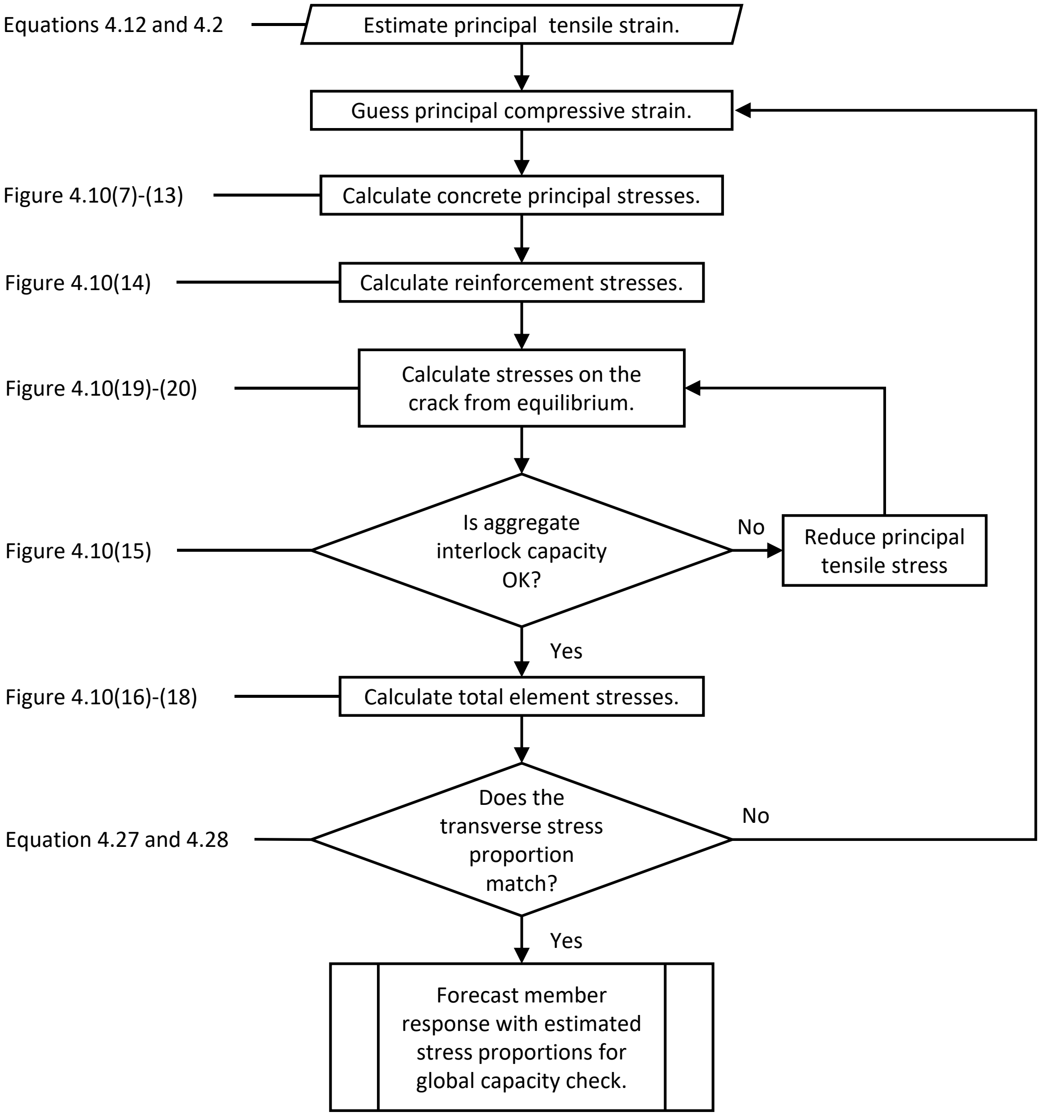

Figure 4.11 Flowchart of cracked continuum procedure

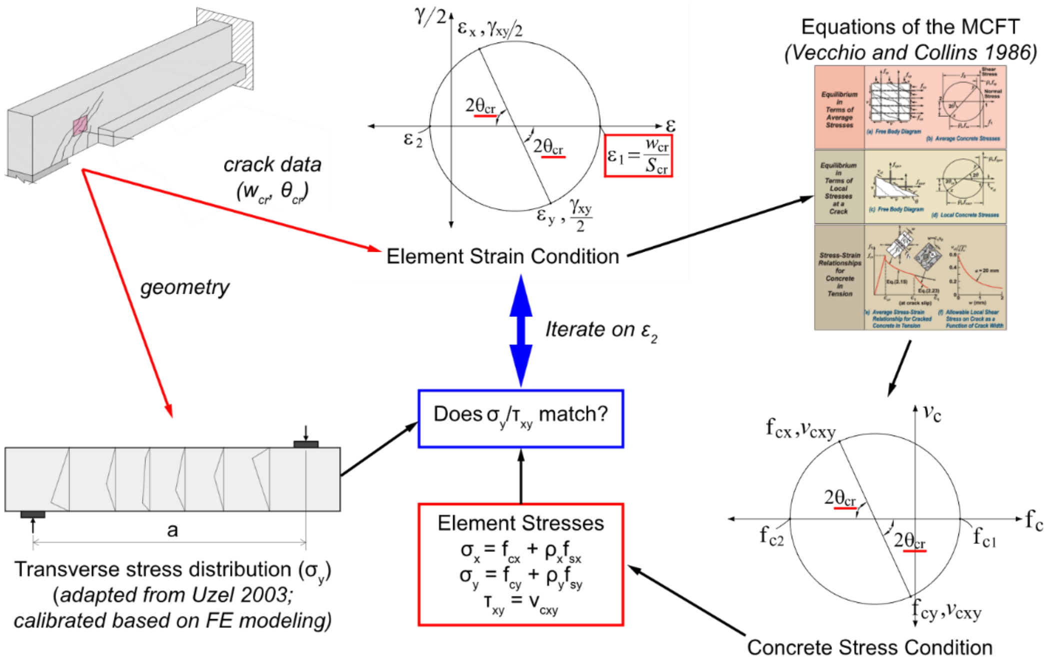

Figure 4.12 Graphical overview of cracked continuum procedure

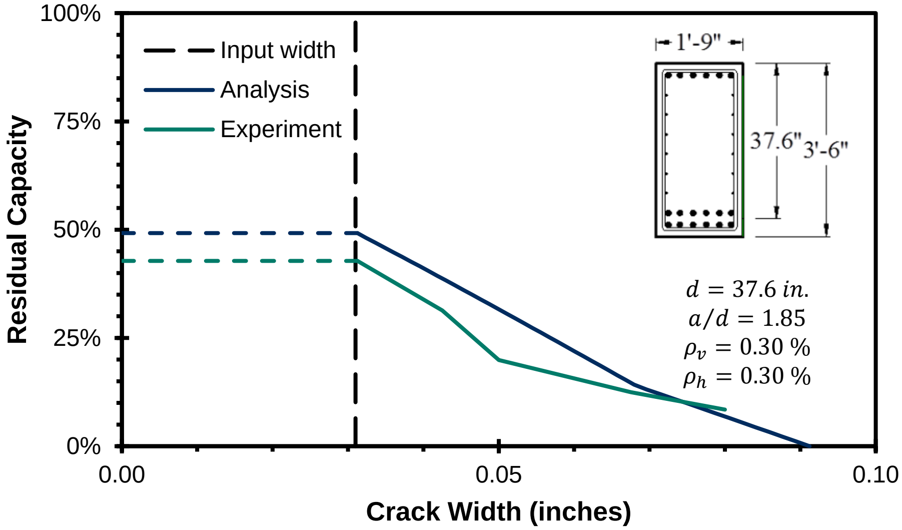

Figure 4.13 Sample analysis results for DS3-42-1.85-03 (Larson et al., 2013)

4.2. Evaluation and Refinement

This section covers the evaluation of the preliminary procedure, followed by a discussion of the investigated refinements. Lastly, the refined procedure is presented and re-evaluated.

4.2.1. Procedure Evaluation

Due to the nature of the data comprising the Visual Crack Measurement Evaluation Database (VCMED), the inherent variability of cracking in concrete, and the limited assumptions made about member loading in the procedure, there is a relatively high amount of variation in the residual capacity prediction results. For evaluation purposes, Category 1, 2, and 3 data are presented in separate figures with separate discussions. The data categories are summarized below:

- **Category 1:** Data which is directly relevant to Texas Department of Transportation (TxDOT) bridge infrastructure and with crack data reported over several load levels. Category 1 data was the most strictly regulated in terms of filtering. For the analyses presented herein, only load stages which had both crack widths and inclinations measured were considered.
- **Category 2:** Data for specimens which are similar in either scale or detailing to TxDOT bridge infrastructure and with crack data reported over several load levels. Category 2 was less regulated than Category 1 and many of the inclinations used in the analyses were interpreted based on reported final measured crack inclinations or from nearby load stages.
- **Category 3:** Data for specimens which were not extensively documented. Like the Category 2 data, assumptions were made about crack inclinations based on whatever information was available in the original reports.

4.2.1.1. Category 1

Category 1 data was comprised of 103 analyses on RC beams from three TxDOT projects: 0-6416 (Larson et al., 2013), 0-5253 (Birrcher et al., 2009), and 0-1851 (Bracci et al., 2001). All three projects focused on deep beams (shear-span-to-depth ratios less than approximately 2.5) and represent a variety of geometries, reinforcement detailing, and sizes of bent caps found in bridge infrastructure. Additional information regarding individual members can be found in the VCMED.

Figure 4.14 shows the plot of estimated versus measured load levels for Category 1 data. Each of the different colored markers correspond to a different experimental series and the diagonal line represents perfect agreement between the predictions and experiments. While there are outliers, most of the 103 analyses agree with the experiments, albeit slightly un-conservatively. The average predicted-to-experiment ratio is 0.87 with a standard deviation of 0.30, yielding a coefficient of variation of 34 %. Given the level of precision associated with crack comparators and the inherent variability in cracked concrete, this value seems reasonable for the initially-developed procedure (i.e., without any form of modification or calibration). Figure 4.15 shows analyses on Category 1 data omitting members that were constructed without shear reinforcement. As will be shown in Section 4.2.1.2, the procedure generally offers very different levels of performance for members without shear reinforcement; as such, it is of interest to check how many outlying data points correspond to members without reinforcement. In this case, the results were reasonable for the one beam without shear reinforcement in Category 1.

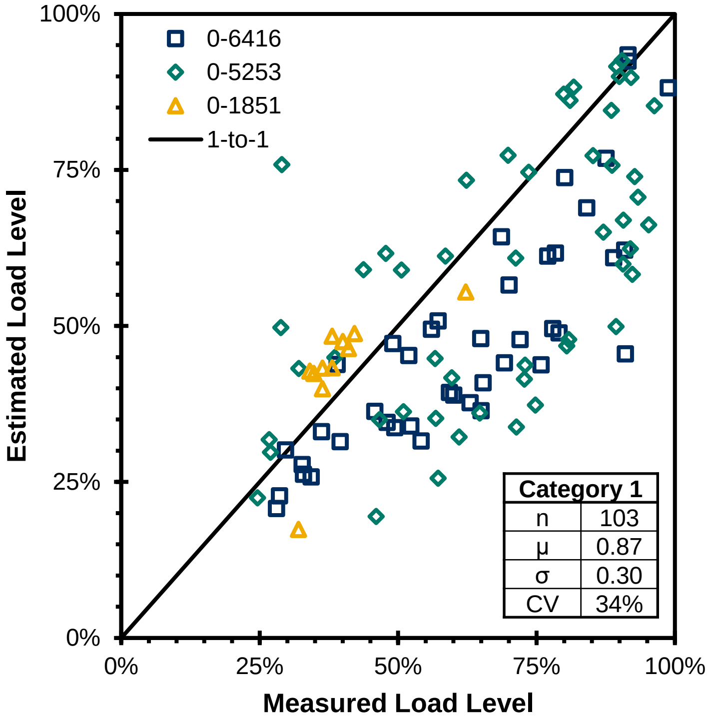

Category 1	
n	103
μ	0.87
σ	0.30
CV	34%

Figure 4.14 Estimated versus measured load levels for Category 1 data (preliminary)

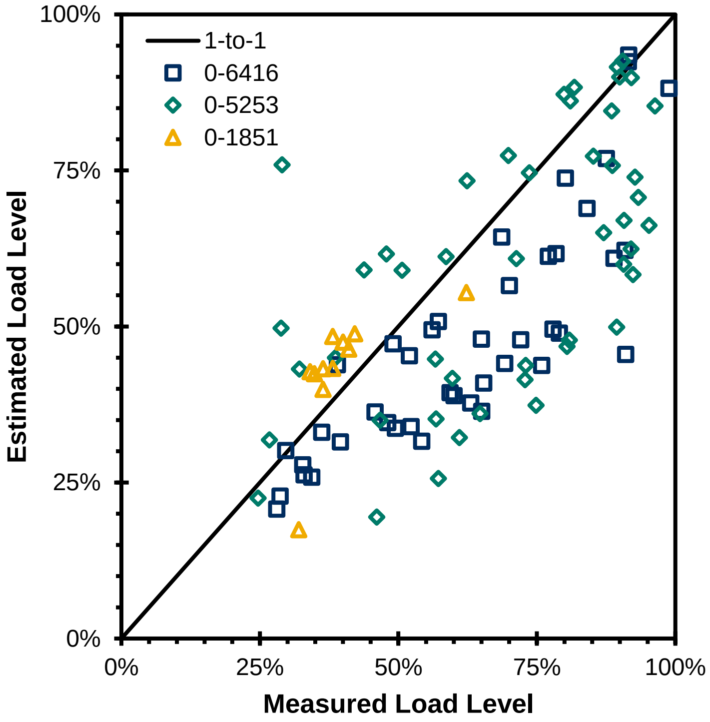

Figure 4.15 Estimated versus measured load levels for Category 1 data (preliminary, omitting members reinforced in one direction only)

Two alternative visualizations of the results are shown in Figure 4.16. Note that the most variation tends to occur at small crack widths (i.e., with typically low load levels) and very steep (> 50 degrees) or very shallow crack (< 30 degrees) angles.

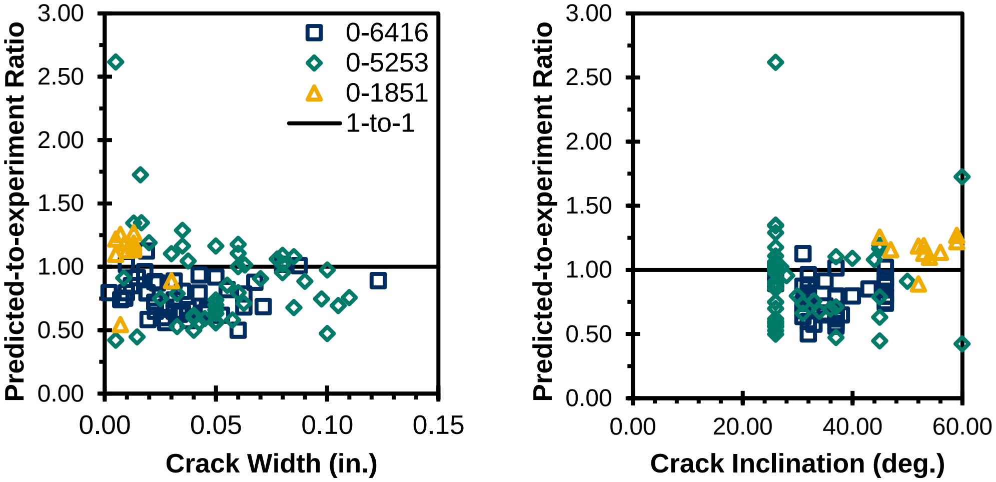

(a) *(b)*

Figure 4.16 Average predicted residual capacity to measured residual capacity ratios versus (a) crack width; (b) crack inclination

4.2.1.2. Category 2

Results for Category 2 analyses are presented in Figure 4.17, representing 142 analysis cases from three experimental studies (Aguilar, 2011; De Silva et al., 2008; Sherwood, 2008). Aguilar (2011) and De Silva et al. (2008) were comprised of typical I-girder shapes used in bridge infrastructure. Sherwood's (2008) tests were similar in scale to bent cap style members, but all except two were constructed without shear reinforcement. This analysis series showed significantly less agreement than Category 1 data; however, given the concessions made (e.g., crack inclinations could be assumed from nearby load stages), this was to be expected. Analyses on beams tested by Aguilar (2011) and De Silva et al. (2008) show a general trend, but the results deviate greatly from the anticipated values. The analyses on Sherwood's (2008) specimens show a cloud – there is very little consistent agreement between the predictions and the experiments.

The primary cause of the discrepancies in the assessment results obtained for Sherwood's (2008) beams is related to reinforcement detailing. All but two of the beams were constructed without shear reinforcement. In beams with uneven levels of reinforcement, the stress and strain axes can deviate significantly. One of the assumptions made in the first step of the procedure is that principal stress and strain axes are coincident, which likely led to errors in those analyses. Figure 4.18 shows the results for all members with shear reinforcement and it can be seen that similar trends to the results in the Category 1 analyses are found.

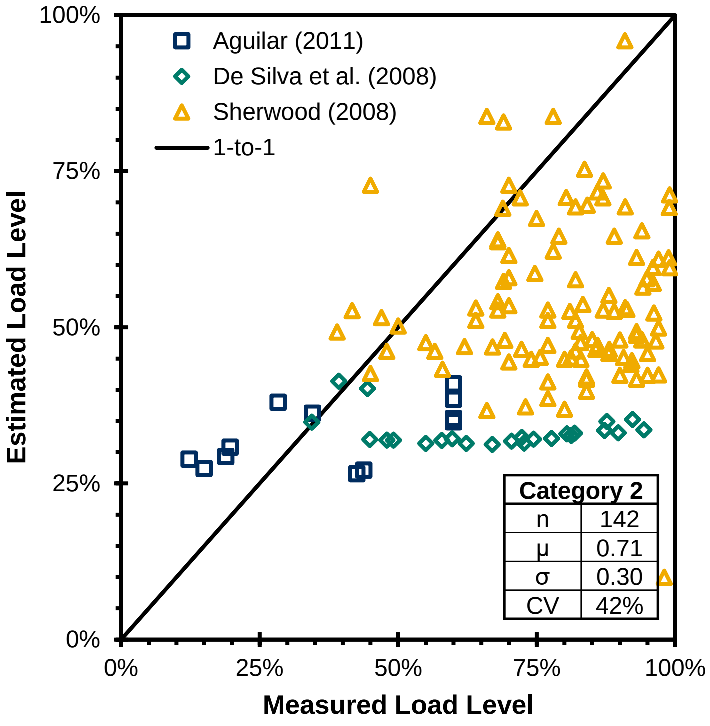

Figure 4.17 Estimated versus measured load levels for Category 2 data (preliminary)

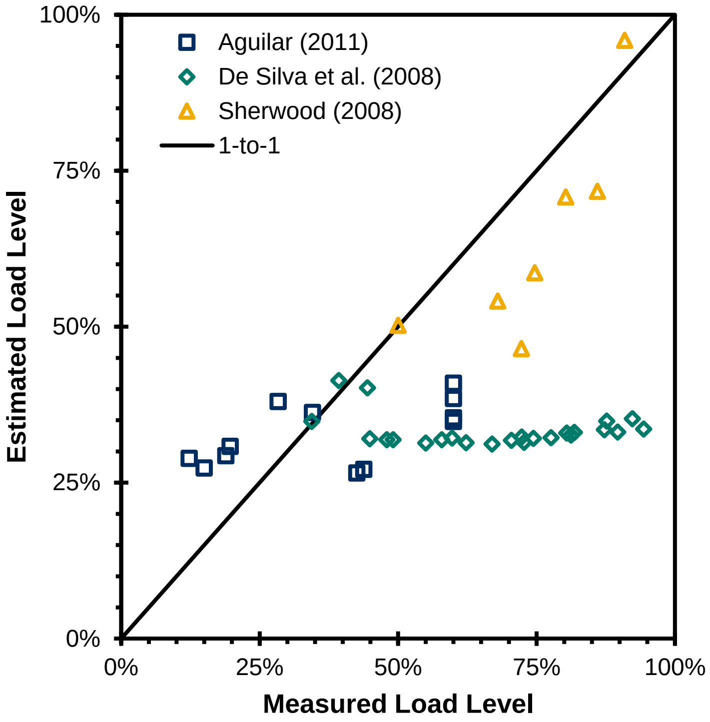

Figure 4.18 Estimated versus measured load levels for Category 2 data (preliminary, omitting members reinforced in one direction only)

4.2.1.3. Category 3

Two experimental studies (J. Y. Lee et al., 2015; Yoon et al., 1996) from Category 3 were used to evaluate the preliminary procedure. Figure 4.19 shows the results of 153 analyses. The results from Lee et al. (2015) are like those from Aguilar (2011) and De Silva et al. (2008), in that they are closely grouped but substantially underestimate the load levels in most cases. Results from Yoon et al. (1996) show some level of agreement, but underestimate load levels slightly, like Category 1 data results.

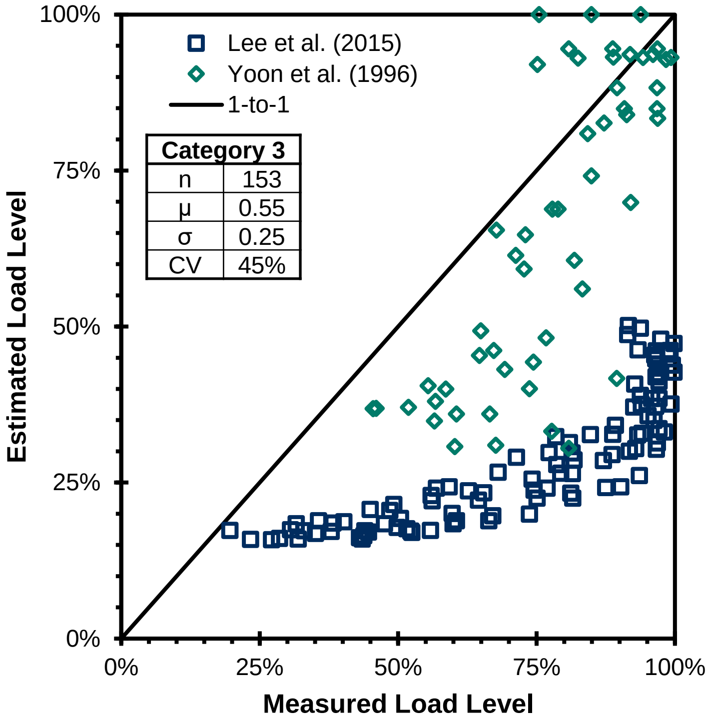

Figure 4.19 Estimated versus measured load levels for Category 3 data (preliminary)

4.2.1.4. Discussion

Using the initially-developed analysis procedure, many of the analyses provided reasonable estimates for load level; however, there are several analysis series which demonstrated there are some deficiencies in the preliminary procedure. Some of these deficiencies are inherent to the problem at hand, that is, estimating relative load level based on measured cracks. Additionally, certain ranges of crack widths and inclinations were shown to present complications in the procedure. Furthermore, lightly reinforced members were found to be ill-suited for this procedure due to deviations between the principal stress and strain axes. *Overall, where members were reinforced in two directions and experimentally exhibited diagonal cracking, reasonable predictions for load level/residual capacity were typically obtained.*

4.2.2. Procedure Refinement

After evaluating the performance of the preliminary analysis procedure, several potential refinements were investigated. Table 4.3 summarizes these refinements and provides summaries of their influence on the procedure. Further details regarding their implementation and effect are covered in Sections 4.2.2.1 through 4.2.2.3.

Table 4.3 Summary of refinements investigated for cracked continuum approach

Section	Refinement	Influence
4.2.2.1	Crack slip condition	Improved normalized predictions for shear.
4.2.2.2	Crack parameters	Reduced numerical difficulties and errors caused by cracks due to flexure (as opposed to shear).
4.2.2.3	Disturbed region stress influence	Reduced conservatism at low load levels (less than approximately 40 % of ultimate).

4.2.2.1. Crack Slip Condition

In the preliminary procedure presented in this Chapter, crack slip (i.e., displacement on the crack plane parallel to the crack plane) was assumed to be zero. This was to satisfy zero-slip conditions assumed by the MCFT, which was used as the base for the first step of the preliminary procedure. The remainder of the procedure, however, considered crack slip in a typical fixed crack modeling procedure. To unify steps one and two of the cracked continuum approach, it was desirable to include crack slip in all stages of loading. Similar procedures have accomplished this by using measured crack slips as input (Calvi et al., 2018); however, this is extremely difficult to do accurately and without prior knowledge of the crack's kinematics.

In lieu of using measured crack slips, various assumptions or estimations can be made for other parameters which allow for the estimation of crack surface slip. One potential solution is to assume that the uniform longitudinal strain (ε_x) is proportional to the strain at the level of the flexural reinforcement (i.e., tensile strain due to bending moment), which has been used successfully to analyze the response of both slender (e.g., Collins et al., 1996) and deep beams (e.g., Acevedo et al., 2009). This requires knowledge of the moment-to-shear ratio or the use of a kinematic model, which may also assume certain loading conditions, to estimate the longitudinal strain. Another solution is to assume information about the average longitudinal stress (σ_x). Other web-equivalent procedures (Kong & Rangan, 1998; J.-Y. Lee et al., 2011; Mau & Hsu, 1987) have shown success by assuming that the average longitudinal stress should correspond to the resultant axial force in the member. For a beam in a typical gravity load scenario, this corresponds to an average stress of zero. These types of procedures have also often incorporated additional requirements regarding bending moment. For example, the longitudinal reinforcement may be reduced by an equivalent area being used in flexural action.

For the refined procedure presented in this section, the zero longitudinal stress assumption was used and flexural effects were neglected. This assumption was selected for simplicity and because it was suitable for all members comprising the VCMED. However, to generalize the procedure for columns and prestressed construction, this assumption would need to be revised since the resultant axial force would no longer be zero. Also, note that if bending moment effects are not included, the predicted response tends to be stiffer and stronger than reality; however, as shown later in this Chapter, the normalized response (i.e., utilization and residual capacity) can still be predicted reasonably well.

The use of a fixed crack approach requires some type of constitutive model to calculate the shear stress on the crack surface. In this procedure the Contact Density Model (Baolu Li & Maekawa, 1987) was selected. Equation 4.31 summarizes the basic form of the model used.

$$v_{c1'2'} = 106\sqrt[3]{f_c^{'}}\,\frac{(\gamma_{1'2'}/\varepsilon_{1'})^2}{1+(\gamma_{1'2'}/\varepsilon_{1'})^2} \qquad 4.31$$

where,

$f_c^{'}$ = compressive strength of concrete, psi

$\gamma_{1'2'}$ = shear strain on crack surface

$\varepsilon_{1'}$ = tensile strain normal to the crack surface

4.2.2.2. Crack Parameters

Based on the evaluation of the preliminary procedure, it was found that cases in which involving very steep and of very shallow crack angles led to extremely poor residual capacity predictions. Steep crack angles are generally indicative of flexural damage and, thus, are not relevant input for this diagonal cracking evaluation procedure. As such, it was determined that crack angles greater than approximately 50 degrees should not be used in the procedure. Shallow crack angles, on the other hand, can present numerical difficulties. To control for these problems the condition presented in Equation 4.32 is recommended. This lower bound on crack inclination is based on geometry (shown in Figure 4.20) and was found to resolve numerical difficulties for load stages with shallow crack inclinations.

$$\theta_{cr} \geq \tan^{-1}\left(\frac{d_v}{a-\frac{l_{b1}}{2}-\frac{l_{b2}}{2}}\right) \qquad 4.32$$

where,

d_v = effective shear depth

a = shear span

l_{b_i} = i^{th} bearing plate length

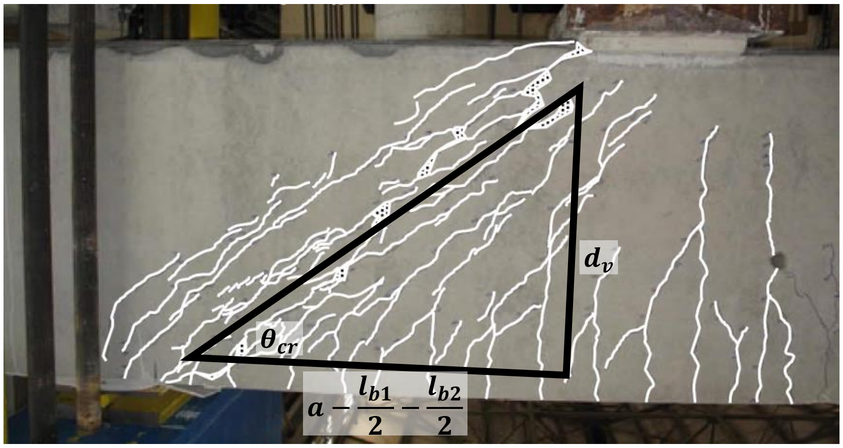

Figure 4.20 Crack inclination limit based on geometry (Adapted from Birrcher et al., 2009)

An additional limit has also been imposed on crack spacing. For the analysis of lightly-reinforced concrete beams, the calculated crack spacing can become quite large. It has been found that limiting the computed crack spacing to the effective shear depth (Equation 4.33), led to an increase in prediction accuracy.

$$s_{cr} \le d_v \tag{4.33}$$

Additionally, the 1.7 factor for crack width was removed, that is, the measured diagonal crack width is used directly in calculating the tensile strain perpendicular to the crack.

4.2.2.3. Disturbed Region Stress Influence

In the preliminary procedure, beams with shear-span-to-depth ratios less than approximately 2.5 were assumed to have constant transverse stress proportions (σ_y/τ_{xy}) over the entire duration of loading. These proportions were computed on the basis of a procedure developed at the University of Toronto (Uzel, 2003) that generally assumed that the member loaded to a level representing approximately 90 % of ultimate. However, based on the findings from a numerical parametric investigation that was performed using VecTor2 (Wong et al., 2013), a nonlinear finite element analysis program for RC structures, it was determined that the transverse stress proportions in these members were not fully developed until approximately 40 – 60 % of the failure load had been applied. Figure 4.21a shows the finite element mesh that was used for the numerical investigation, as well as the different parameters that were investigated. The red arrows on the mesh of Figure 4.21a correspond to the different concentrated loading conditions that were considered in the finite element modeling and used to investigate six different shear-span-depth ratios: 0.50, 1.00, 1.50, 2.00, 2.50, and 3.00. Additionally, three concrete strengths and several different reinforcement layouts were varied. To accommodate all of these different parameters, a total of 810 nonlinear finite element analyses were performed. Six sample results presenting transverse stress-to-shear stress ratio development obtained from the parametric study are shown in Figure 4.21b and demonstrate the aforementioned load level influence on the transverse stress proportions. On the basis of the results obtained from the numerical investigation, Equation 4.34 was developed as a reduction factor for the transverse stress proportions presented by Uzel (2003). The equation assumes that the transverse stress proportion increases linearly with longitudinal strain and that the full transverse stress proportion is developed when the flexural bars have reached approximately 25 % of yield. If the flexural bar strain is not known, it is permissible to assume it is twice the predicted longitudinal strain in the web. This is similar to assumptions made by others in previously noted procedures (Acevedo et al., 2009; Collins et al., 1996) in Section 4.2.2.1. It should also be noted that only one third of the numerical results were used to calibrate Equation 4.34 and the remaining two thirds of the data were used to validate it. On average, Equation 4.34 was found to improve the baseline predictions of transverse stress proportions provided by Uzel's expressions and this refinement was generally found to improve residual capacity predictions at small crack widths (i.e., widths at loads corresponding to less than approximately 40 % of ultimate). Figure 4.22 shows a schematic implementation of Equation 4.34 on Uzel's original model.

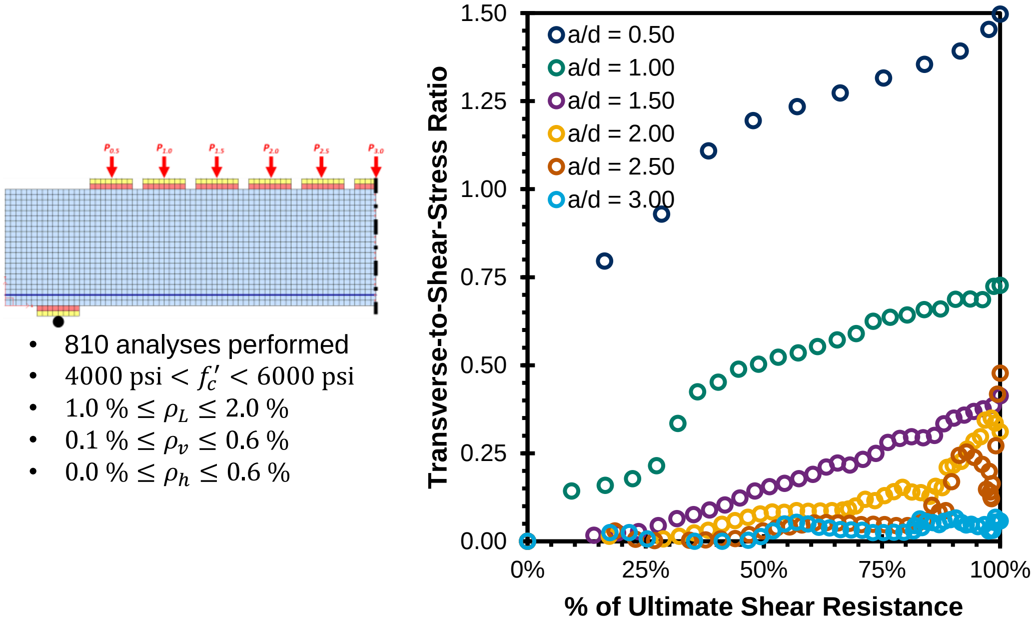

- 810 analyses performed
- 4000 psi $< f_c' <$ 6000 psi
- 1.0 % $\leq \rho_L \leq$ 2.0 %
- 0.1 % $\leq \rho_v \leq$ 0.6 %
- 0.0 % $\leq \rho_h \leq$ 0.6 %

(a) *(b)*

Figure 4.21 (a) Overview of finite element mesh and variables investigated; (b) Sample transverse-to-shear-stress ratio development plots

$$\Phi_{\varepsilon} = C_1\left(\frac{\varepsilon_l}{\varepsilon_{yl}}\right) + C_2 \qquad 4.34$$

where,

C_1 = $1.25\frac{a}{d} + 1.125$

a = shear span

d = effective depth

ε_l = strain at flexural reinforcement level, may be taken as $2\varepsilon_x$

ε_{y_l} = yield strain of flexural reinforcement

$$C_2 = \begin{cases} \frac{4}{15}\left(\frac{a}{d}-2\right)^2 & \cdots \quad 0 < \frac{a}{d} \le 2.00 \\ 0 & \cdots \quad \frac{a}{d} > 2.00 \end{cases}$$

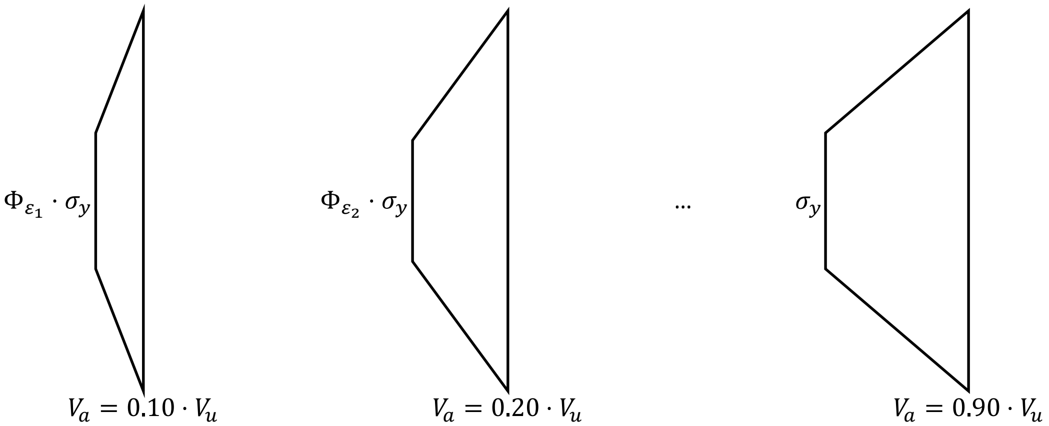

Figure 4.22 Schematic of transverse stress distribution development through web using Equation 4.34

4.2.2.4. Discussion

A flowchart showing the outline of the refined procedure is given in Figure 4.23. Note that the Mohr's circle relationships from Figure 4.10 must have the shear terms added in to account for the shear on the crack in a fixed crack procedure. These modifications are shown in the worked example in Appendix C. The refinements were made to address the deficiencies in the procedure uncovered by the evaluation of the initially-developed preliminary procedure. The VCMED was used again to evaluate the suitability of the refinements. The number of analyses, *n*, has been reduced in many of the "refined" analyses due to the crack geometry restrictions proposed in Section 4.2.2.2. A summary of the general influence of the refinements was given in Table 4.3, but more discussion will be provided in this section.

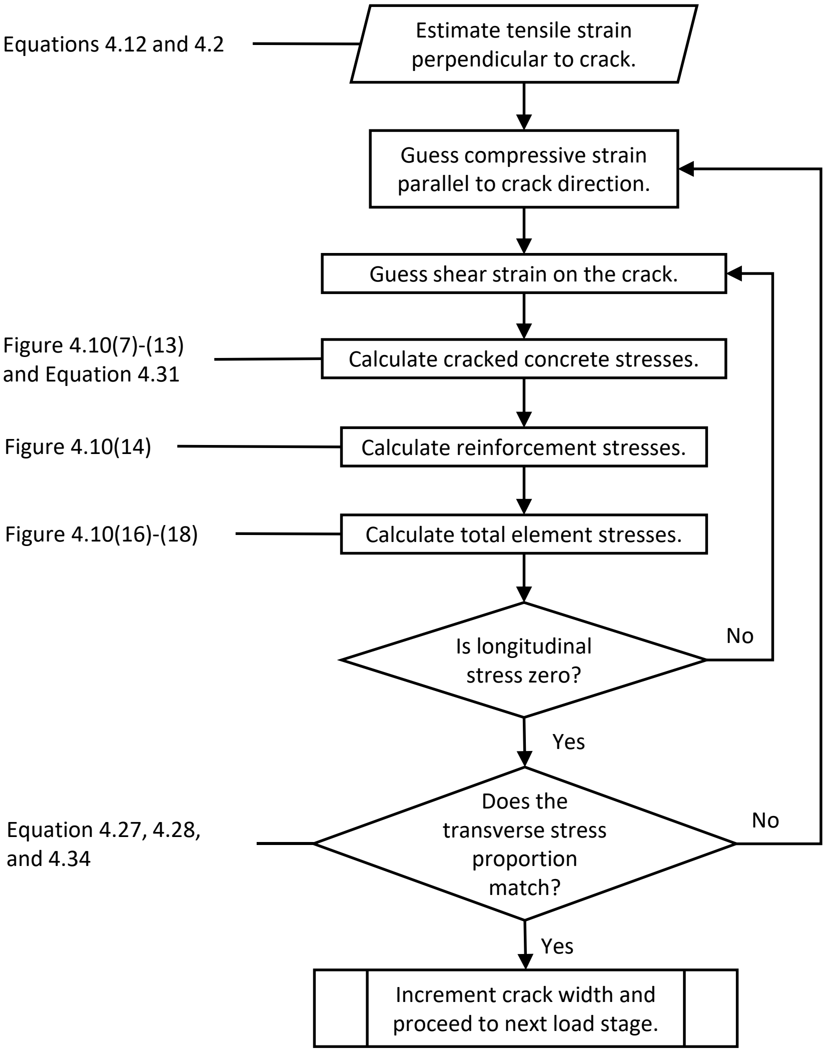

Figure 4.23 Flowchart for refined procedure

The refined results for Category 1 data are presented in Figure 4.24. The procedure now gives an average predicted-to-experiment ratio of 1.09, as opposed to 0.87, which suggests the refinements made the procedure somewhat more conservative. Of note is the reduction in the coefficient of variation (CV) which was reduced from 34 % to 19 %, demonstrating that the refined procedure is more consistent in its ability to predict slightly conservative estimates for load level. Figure 4.25 shows results for only the Category 1 data pertaining to members constructed with shear reinforcement.

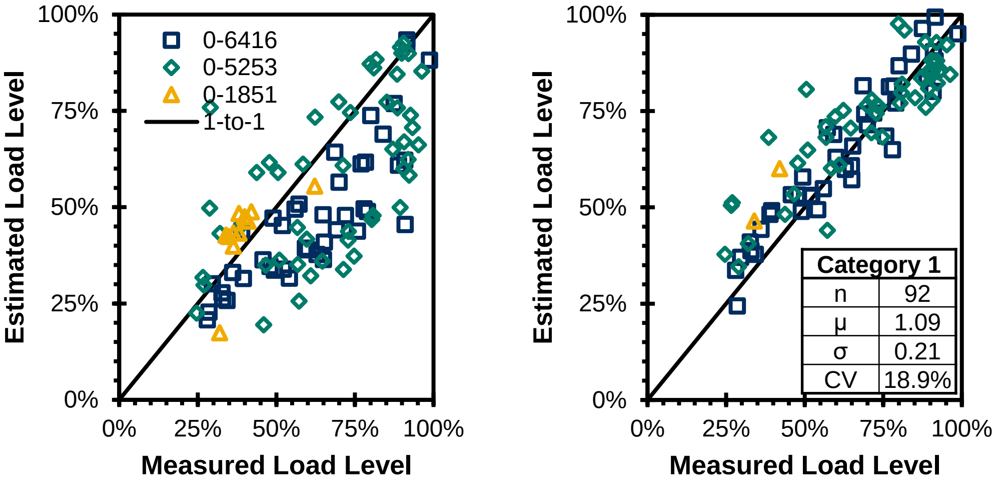

(a) *(b)*

Figure 4.24 Estimated versus measured load levels for Category 1 data (a) preliminary and (b) refined

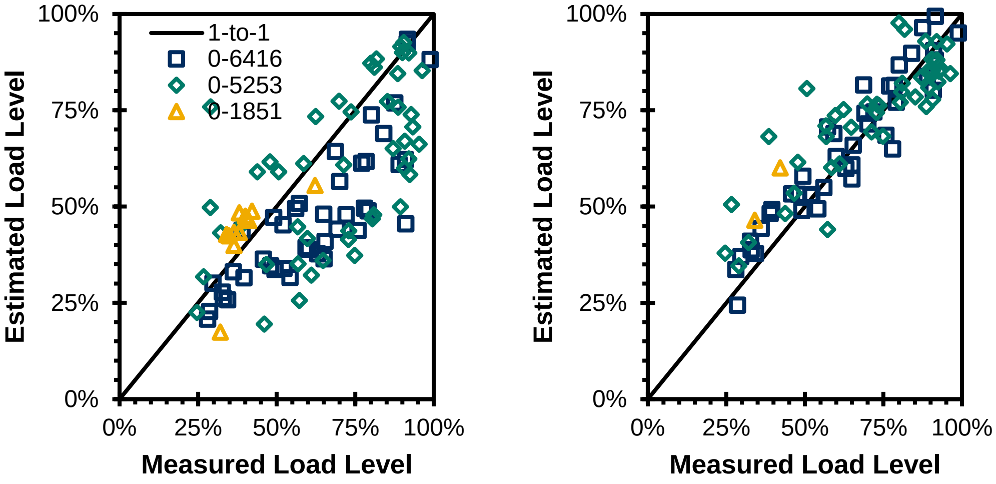

(a) *(b)*

Figure 4.25 Estimated versus measured load levels for Category 1 data (a) preliminary and (b) refined (omitting members reinforced in one direction only)

Refined results for Category 2 data are shown in Figure 4.26. There is still significant variation in the analyses for beams tested by Sherwood (2008), but the results from Aguilar (2011) and De Silva et al. (2008) show a better trend than in the preliminary procedure. Although results for beams tested by Aguilar (2011) are quite conservative and those for De Silva et al. (2008) are slightly unconservative, they are no longer significantly unconservative as was the case in the preliminary analysis procedure. Figure 4.27 shows Category 2 results with uniaxially-reinforced members (i.e., without shear reinforcement) removed. As before, predictions for beams with shear reinforcement from Sherwood (2008) show reasonable agreement with experimentally measured values.

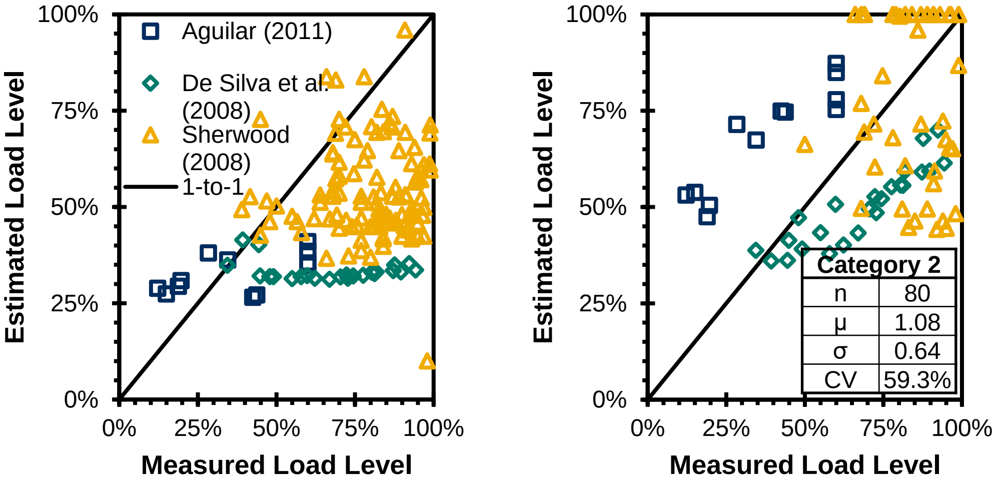

(a) *(b)*

Figure 4.26 Estimated versus measured load levels for Category 2 data (a) preliminary and (b) refined

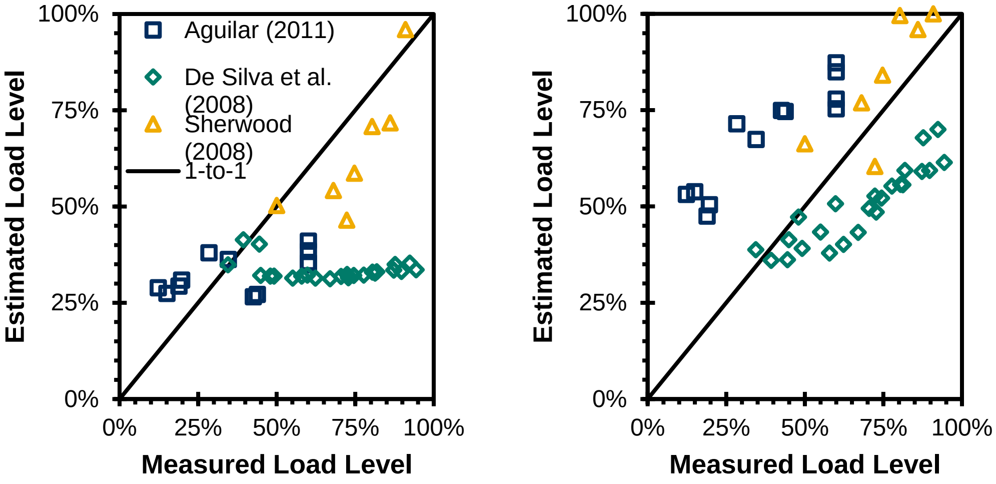

(a) *(b)*

Figure 4.27 Estimated versus measured load levels for Category 2 data (a) preliminary (b) refined (omitting members reinforced in one direction only)

Figure 4.28 shows refined results for all Category 3 data. Variation has been significantly reduced (from 46 % to 20 %) and both analysis series show a reasonable trend with experimental values. Results from this dataset were unconservative by approximately 9 % on average. This is still a vast improvement from the results obtained using the preliminary procedure where results were significantly more unconservative on average.

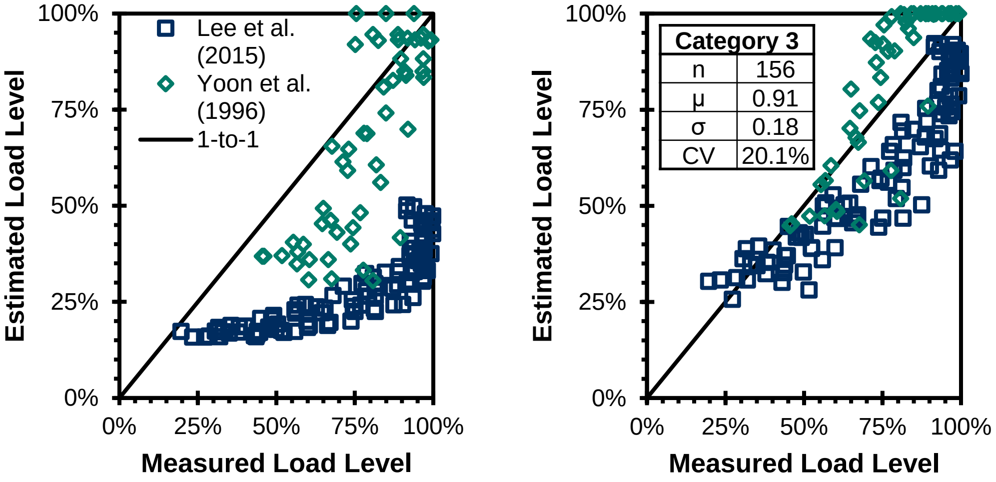

(a) (b)

Figure 4.28 Estimated versus measured load levels for Category 3 data (a) preliminary (b) refined

Overall, the procedure refinements led to improved prediction results, with one exception being uniaxially-reinforced beams from Sherwood's (2008) tests, which were still subject to more scatter than any other test series that was analyzed. The most impactful refinement of the procedure was obtained by switching to a totally fixed-crack procedure (crack slip condition) which, in addition to making the procedure somewhat more straightforward to employ, also appears to be the primary reason for the improved load level/residual capacity predictions obtained using the refined procedure. The refinements to crack parameters (i.e., limiting crack inclinations) primarily only influenced analyses which suffered convergence issues due to shallow crack angles; however, they also provided insight into which types of cracking are most suitable for this type of procedure. Lastly, the disturbed region refinement moderately improved predictions for a small range of crack input, where experimental load levels were less than about 40 %.

Based on the results from the VCMED presented in this section, it is recommended that refined procedure outlined in Figure 4.23 be used; however, additional work should be completed to address some issues/limitations that have been identified:

- **Crack slip estimates.** The refined procedure performed well for beams with no axial load; however, it is not designed to handle members with non-zero axial loads. To further generalize the procedure, the estimates for crack slip should be made with as little knowledge of loading conditions (e.g., moment-to-shear ratio, axial load) as possible.

- **Members without shear reinforcement.** Although it was anticipated that the refined procedure would provide better estimates for beams without shear reinforcement, it generally had limited impact on the results obtained for these members. Addressing this issue is of importance for procedures such as these, due to the face that many older in-service structures have been constructed with very low shear reinforcement ratios.

4.3. Field Aid Construction

A sample field aid is presented in Figure 4.29. Since these field aids are assumed to be of greatest use when completed prior to the inspection such that they may be employed in the field, the initial/starting crack widths and inclination are unknown and must be assumed. A proposed procedure for field aid construction is outlined as follows:

- Estimate relevant member properties from available design documents or typical standards (e.g., concrete strength, reinforcement ratios, shear-span-to-depth ratio, etc.)
- Select a minimum of three crack inclinations to provide an envelope estimate of residual capacity. Crack inclinations of 30, 40, and 50 degrees are recommended to bracket and address typical crack inclinations that are likely to be observed.
- Starting crack widths should be selected according to Equation 4.35; however, the starting crack width need not be less than 0.002 in.
- Follow the cracked continuum procedure outlined in Sections 4.1 and 4.2, until failure is reached.
- Repeat for each crack inclination.

$$w_{cr}^{initial} = \varepsilon_{cr} s_{cr} \qquad 4.35$$

where,

ε_{cr} = cracking strain for concrete

= f_{cr}/E_c

f_{cr} = cracking strength of concrete ($\approx 4\sqrt{f_c'}$ in units of psi)

E_c = initial tangent modulus of concrete ($\approx 1000 \cdot f_c'$ in units of psi)

s_{cr} = calculated crack spacing

In the field, measured diagonal crack widths can be reference to the x-axis of the plot shown in Figure 4.29 and a preliminary estimate of residual capacity can be obtained from the y-axis of the plot. For example, if using this member-specific aid to assess the implications of 0.050-inch wide crack with an inclination of 40 degrees, it would be estimated that the residual capacity of the member was on the order of 34 % (refer to Figure 4.30). Note that, as shown in Section 4.2, the procedure was, on average, typically found to be accurate within about 20 % of the measured experimental values for members with shear reinforcement. For the purposes of using these field aids, this error should be accounted for in making recommendations. Combining results from the field aid with inspector judgement, more quantitative assessments of visually observed cracking can be made.

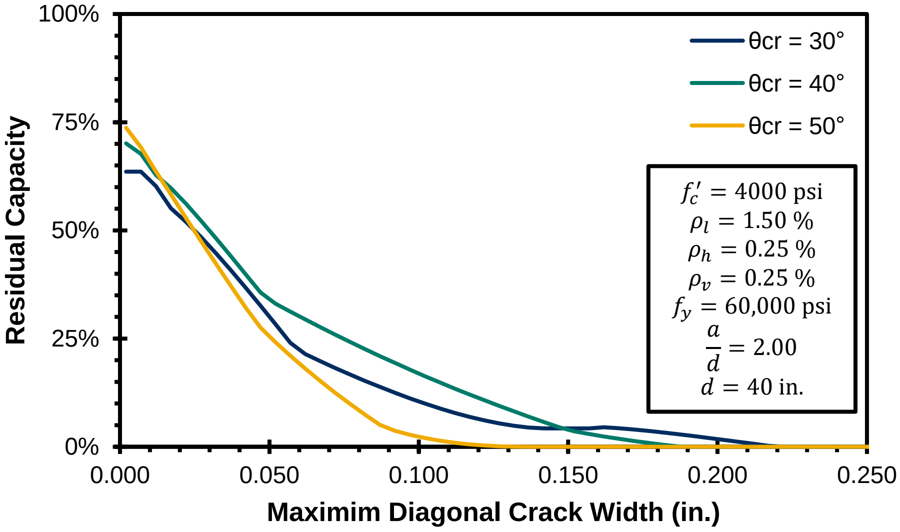

Figure 4.29 Sample field aid construction

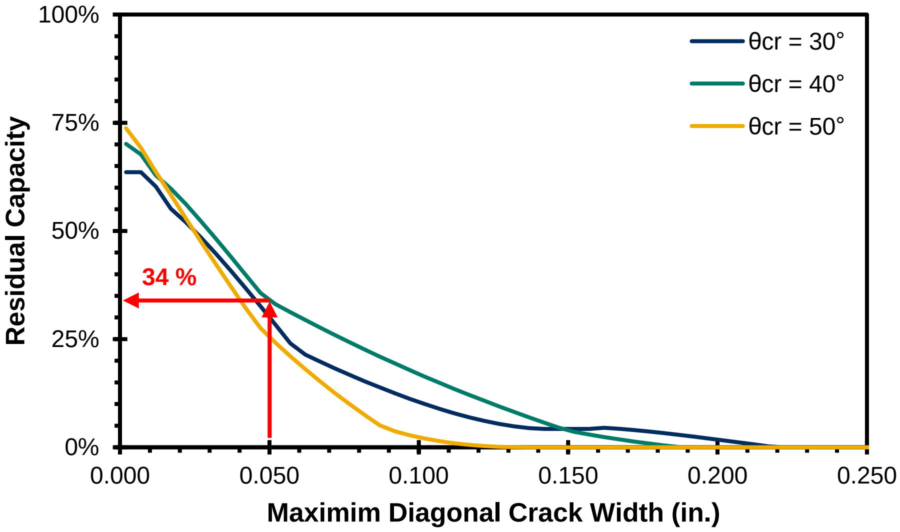

Figure 4.30 Application of sample field aid

4.4. Summary

The cracked continuum approach developed through this project was shown to be a viable approach for simple damage assessment of cracked concrete bridge structures. The viability of the procedure was illustrated in Section 4.2 of this chapter using over 300 analyses on data from the VCMED. Thus, the key success obtained regarding this procedure are:

- **Crack-based input can be used to estimate utilization and residual capacity (%).** This information can be used to assist inspector judgement when evaluating RC infrastructure based on visual measured crack data. Analyses performed on Data Categories 1 and 3 were able to estimate the residual capacity within approximately 10 % on average and a coefficient of variation of 20 %.
- **Crack-based input can be used to estimate failure or "critical" crack widths.** In this case, "critical" is user-defined. For example, an allowable maximum crack width could be set based on 25 % residual capacity. In this way, crack width growth can be monitored in a more rational manner.
- **Additional input (e.g., geometry, reinforcement details, etc.) can generally be referenced from design documents or may be estimated based on the bases of known design values.** All input can be easily defined from design drawings, estimated, or assumed without the need for supplemental material testing or complicated calibration procedures required for more complex material models.

Despite the successes shown in the results presented in Section 4.2, there are also limitations which should be taken under advisement when using the cracked continuum procedure. These limitations are as follows:

- **Evaluation and refinement of the procedure continues to be based on available crack data.** The crack input that has been used to date in the development of this procedure has been, to some degree, limited by the types of crack measurements taken and reported by other researchers. While the reported data are useful, it is difficult to determine the optimal crack characteristics for use in the continuum procedure. For example, crack widths are frequently reported as maximum per span and other potentially useful values are left out.
- **The procedure should generally not be used to predict non-normalized loads (i.e., $V_a = x$ kips).** The procedure is less effective in predicting non-normalized load information, on the basis of crack data (e.g., the residual capacity in terms of residual shear force). This is seemingly due to the large amount of uncertainty introduced by assuming simplified/unknown load proportions. The refinements presented in Section 4.2 improved these predictions for certain data series but not all of them; however, recall that the normalized predictions did correlate well with experimentally measured load levels.

- **Long-term effects and other factors potentially influencing the performance real-world structures are not yet accounted for.** Additional factors influencing real-world bridge infrastructure (i.e., those not born in a laboratory) have not been accounted for in the present formulation, which may or may not influence the performance of the cracked continuum procedure. The incorporation of time-dependent effects (e.g., creep and shrinkage) is envisioned to be a relatively simple modification to the current cracked continuum analysis procedure; however, there is little data available to assist in evaluating performance.
- **Analyses performed on beams without shear reinforcement typically exhibit large error.** In cases where damage assessment of a member without transverse reinforcement is required, this procedure is not an adequate standalone method.

The following recommendations are made for using the cracked continuum procedure:

- Use pseudo-averaged crack widths ($w_{cr} = w_{max}/1.7$) for the preliminary procedure, where maximum crack width is measured at approximately mid-depth, halfway between the support and load point.
- Use the mid-depth measured crack width directly for the refined procedure.
- Crack inclination should be measured at approximately the same location.

Recommended future work is as follows:

- Develop generalized conditions for estimating crack slip.
- Investigate uniaxially-reinforced beam behavior. Currently, beams with no shear reinforcement (e.g., the type tested by Sherwood, 2008 and others) are the biggest source of error in the procedure based on verification results obtained using the VCMED.

Chapter 5. Crack Pattern Quantification Using Fractal Analysis

Interpretation of crack patterns can serve as a major predictor of damage in reinforced concrete (RC) structures. Currently, visual inspection techniques are the most common approach to inspect transportation infrastructures, such as bridges. In the United States, for example, both the state and federal departments of transportation are using visual inspection as their predominant nondestructive inspection technique (TxDOT, 2013). However, the reliability of visual inspection for highway bridges is still questionable (Moore et al., 2001). This is primarily due to the fact that current practice relies on the inspectors' experience and, further, many current inspection techniques are costly and resource intensive.

Researchers have tried to quantify the properties of simple crack patterns using parameters like average crack spacings and average crack widths. Mechanics-based formulations presented in the literature such as MCFT and other similar methods (Vecchio, 2000; Vecchio & Collins, 1986), and also the formulation presented in the previous chapter of this report, can be used to estimate the stiffness of a concrete element based on surface crack measurements. However, the assessment of a structure still requires performing a manual field crack survey.

To bridge the gap between fast inspections and accuracy, the research team explored the application of fractal analysis in the inspection process. Inherent to that approach, it is assumed that the spatial properties of crack patterns can be used as a predictor for the estimation of damage and for the classification of different cracking types. Computational procedures (i.e., fractal and multifractal analyses) are used to pave the way toward explicit quantification and characterization of crack patterns. In this project, procedures were developed to extract data from crack patterns and to harvest those data for useful information that can relate cracking pattern properties to structural behavior properties and response.

The organization of the chapter is as follows: The first section provides background material related to digital image processing, then an algorithm for the application of fractal and multifractal analysis is presented. Artificial crack patterns are used for the numerical evaluation of the algorithm and representative results obtained are presented and discussed.

5.1.1. Two-dimensional Digital Images

Currently the vast majority of cameras on the market are digital. A digital camera can capture photographs and store them in data storage devices. Computers can only handle data, which are held by the storage devices as a sequence of on and off signals (i.e. 1s and 0s). Although computers can store large volumes of raw data, without appropriate processing, the user cannot extract any information from them. Relevant to the work performed in Project 0-6919, an image of a cracked RC bridge member may provide meaningful information to an experienced bridge inspector; however, for the computer, it is interpreted as a sequence of numbers. An example of such a data sequence is presented in Figure 5.1.

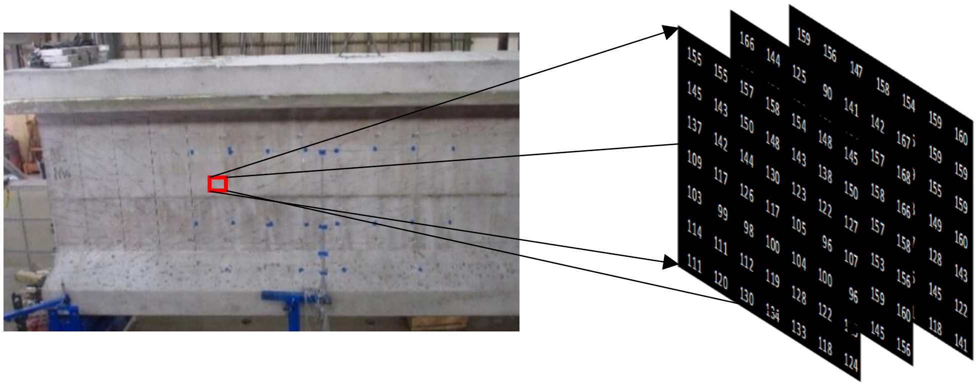

Figure 5.1 Digital image of cracked beam and data corresponding to a 7px by 7px region

Each physical point on the image is represented by a pixel. The illumination intensity of each pixel is variable and is typically represented by three components that define the intensities of Red, Green and Blue (RGB color model). A three-dimensional volume can visualize the combinations of the different color intensities. Those combinations of the three components are presented in Figure 5.2. Note that the intensity values of pixels, are not binary. Their range is defined by the color model used. An example of the pixels and the corresponding intensity values is presented on Figure 5.3 Although the RGB color model is the most widespread, there are other models like the Cyan, Magenta, Yellow, Black model (CMYK color model).

The amount of data included on a two-dimensional image can be processed using image processing algorithms, like binarization and edge detection, to permit easier identification of cracks. For example, in Figure 5.4 a schematic of the procedure followed for the processing of a crack image is presented. Another approach also investigated in this research project, was to manually trace the cracks. Although manually tracing of the cracks was a more tedious process, it provided a faster way to process image data and feed them to the fractal and multifractal framework. Further, it is also worth noting that the focus of the work comprising Project 0-6919 was not centered on crack data extraction, but rather the main contribution is the development of an image quantification algorithm (i.e., what to do with the information after it is extracted). Further research is required to develop a comprehensive image acquisition and interpretation system.

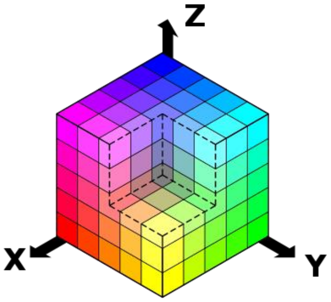

Figure 5.2 Mapping of the Red-Green-Blue color model into a cube. The X Y and Z axis, correspond to the intensities of red, green and blue color respectively, adapted from (Wikipedia contributors, 2018)

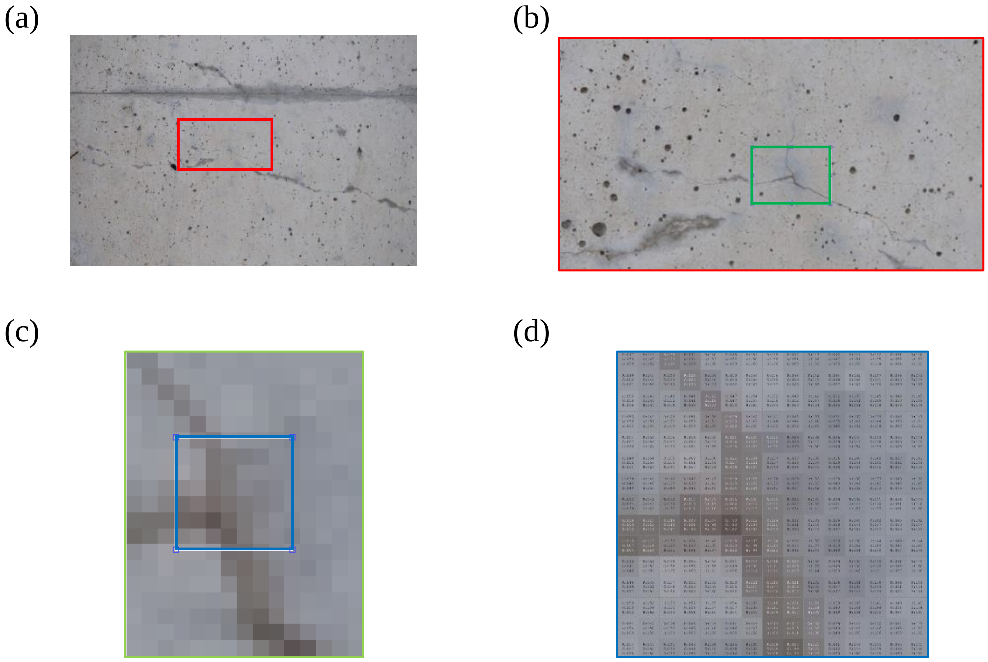

Figure 5.3 As a portion of the image enlarges, we can observe individual pixels that are rendered as small squares; (a) portion of the beam, (b) zoomed region on a crack, (c) individual pixels, (d) pixels with the corresponding intensity values.

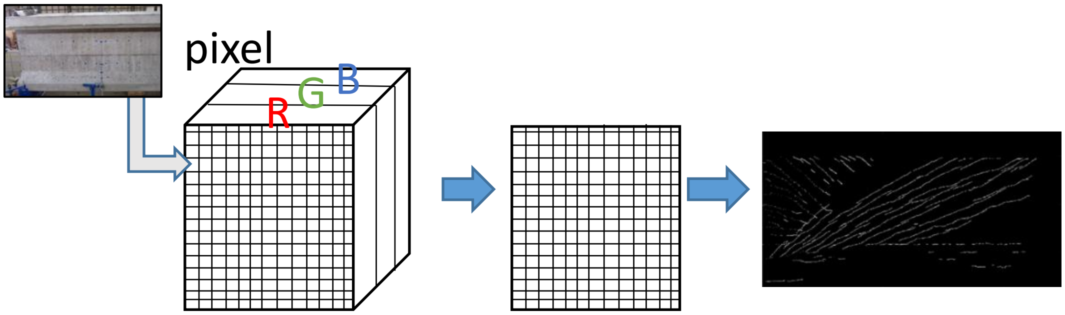

Figure 5.4 Schematic of the image processing procedure

5.1.2. Fractal & Multifractal Analyses

In this section, an overview of the fractal and multifractal analyses employed in this project is provided. The word fractal is used to describe complicated patterns that are built from components which are repeated in reduced size (Cambridge, 2018). From a linguistic standpoint, the root of the word ‘fractal’ is ‘fraction’. Thus, the components of a fractal pattern, can be considered as fractions of the total pattern.

Figure 5.5 The Barnsley fern, a mathematically generated pattern that has basic self-similar properties (Moler, 2005)

The term “fractal dimension” (FD) was first introduced in the 1960s as an index for characterizing the complexity of a fractal pattern (Falconer, 2014). Specifically, this index quantifies how a recorded detail varies as a function of measurement resolution (i.e., measurement scale). For example, in the context of measuring the length of a single crack, a high value FD corresponds to a crack which appears with strong sinuosity (i.e., having many inflection points), and a low value FD corresponds to a weak sinuosity crack (i.e., a straight line). As the pattern becomes more complex due to evolution of additional/continued cracking, the corresponding values of the FD increase. An example of the fractal properties that can be used to characterize the measured surface cracking of a pretensioned concrete girder is presented in Figure 5.6. A set of different scales is used for the measurement of the crack. As the scale size decreases, both the estimated total length of the crack and the sinuosity increase. The estimated length can be calculated by multiplying the number of pieces required to cover the crack by the size of the scale. The sinuosity is represented by the misalignment of the endpoints of the scales. Several researchers have tried to develop models to estimate the amount of damage in concrete members using FD techniques, on the basis of measured crack patterns (Cao et al., 2006; Carrillo et al., 2017; Farhidzadeh et al., 2013).

The evaluation of the FD related to a set of cracks can be performed numerically. The box-counting algorithm is the most widely used approach for the estimation of the FD. Box-counting is appropriate for the analysis of two dimensional (2-D) datasets, like surface cracking patterns. The fundamental procedure that comprises a box-counting algorithm is the division of the crack pattern into smaller box-shaped pieces. This “breaking” of the crack pattern is repeated using different box sizes, and the properties of each box are recorded in a database. The total number of boxes required to completely cover the pattern is N . Since this total number of boxes is a function of the box size, it is usually represented by way of $N(r)$. This quantity is also called the number of active boxes. The distribution of active boxes for a range of different box sizes is presented in Figure 5.7 and note that an end region cracking pattern from a full-scale pretensioned girder is presented in Figure 5.7a. Different sets of square boxes, with side length ranging from 256 to 16 pixels, divide the image into smaller pieces. The active pieces of the image are marked white while the inactive ones are marked black on Figure 5.7b to f. These figures represent the distribution of active pixels for different box sizes and can be used to extract the number of active pixels corresponding to different box sizes.

For images with fractal properties, a monomial relationship relates the number of active boxes and the inverse of the box size, as presented in Equation 5.1:

$$N(r) \propto \left(\frac{1}{r}\right)^{D} \qquad 5.1$$

where D is the FD of the crack. A common approach (Clauset et al., 2009) to linearize a monomial equation is to take the logarithm of the equation (with an arbitrary base), which yields:

$$\log(N(r)) = D\log\left(\frac{1}{r}\right) + \log a \qquad 5.2$$

In the above equation, α is an arbitrary constant. Setting $X = \log(1/r)$ and $Y = \log(N(r))$ yields the equation of a straight line with a slope D. Therefore, to calculate the FD, one could fit a line to the log-log plot of $N(r)$ versus $1/r$. The slope of that line is an estimator of the FD of the curve (*D*). The range of r used for the curve fitting depends on the resolution and the size of the curve. More detailed discussion on the selection of the range is available in (Farhidzadeh et al., 2013).

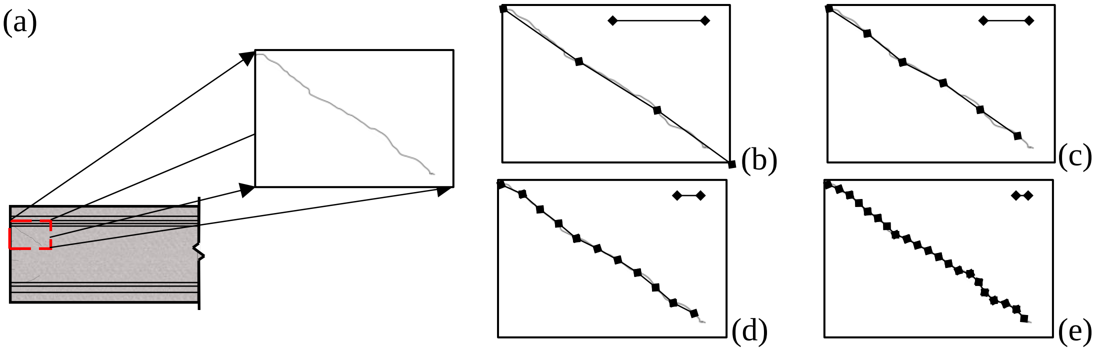

Figure 5.6 Fractal properties of an arbitrary crack (a) cracked end-region of a prestressed girder & extracted crack and corresponding measurement scale, (b)(c) (d) (e) measurement of the length of a crack using different scales

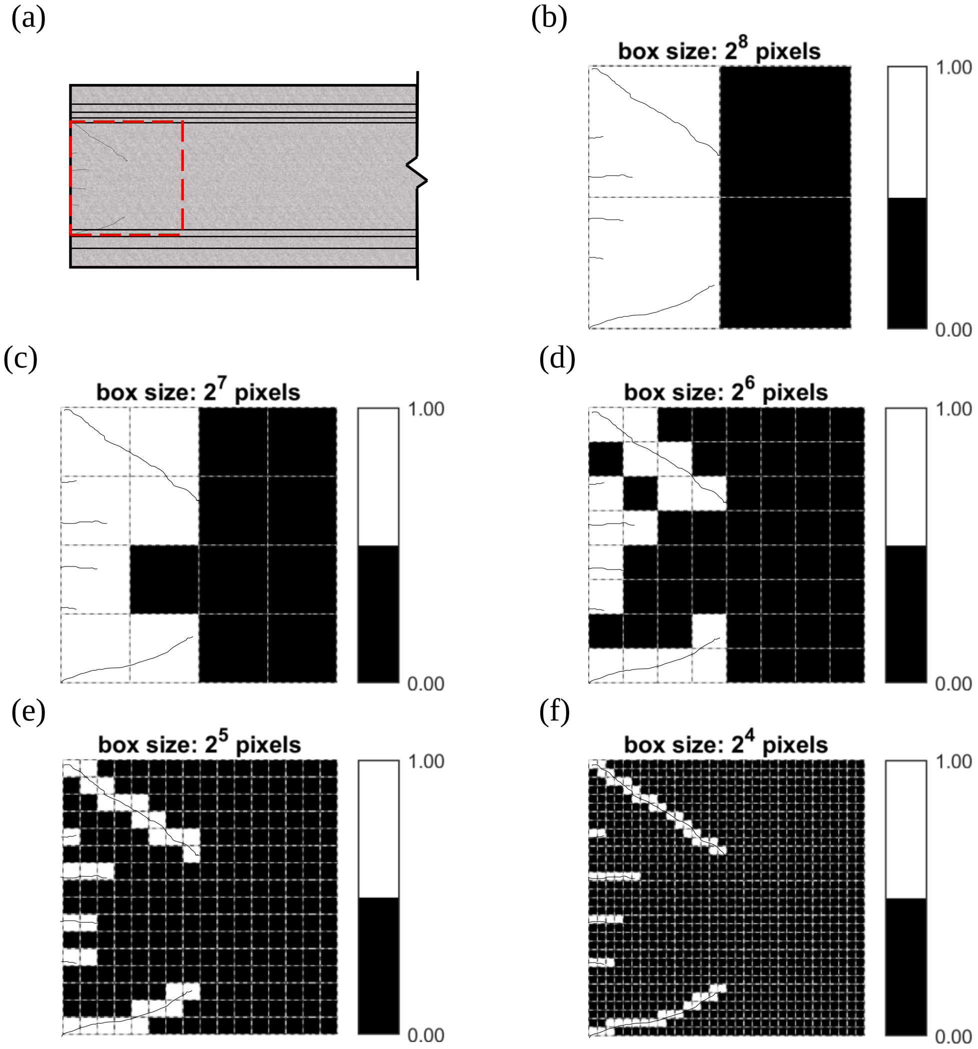

Figure 5.7 Distribution of active pixels for a crack pattern, using different box sizes (a) region analyzed, (b),(c),(d),(e),(f) active boxes for different box sizes

Multifractal analysis is an extension of the fractal analysis concept, and can be used to provide better insight into self-similar properties of a signal (Harte, 2001), like the one included on a binary image of a crack pattern. In contrast to fractal analyses, which are based on the relationship between the number of active boxes (N) and the corresponding box size (r), multifractal analysis introduces the weighting of each active box based by way of its intensity level. In other words, for an image representing the surface cracking of a concrete element, multifractal analysis can capture the significance of each box based on the number of active pixels it contains. Thus, multifractal analysis is not limited to a global single output (i.e., the Fractal Dimension), but it provides information as a function of the singularity strength α which is a local property of each box (Seuront, 2010).

The numerical estimation of a signals multifractal properties is summarized in the following paragraph. Generalized dimensions D_q can be used to represent the measure of a cracks' scale-invariant properties (Rényi, 1961), and can be defined as:

$$D_q = \frac{1}{1-q} \lim_{r \to 0} \frac{\log \sum_{i=1}^{N(r)} P_i^q(r)}{\log(r)} \qquad 5.3$$

where q is a real value moment order and $P_i(r)$ is the measure (or weight) associated with the i-th box. For a crack pattern depicted on a digital binary image, $P_i(r)$ can be considered as the probability of having active pixels in that box, that is (Cao et al., 2006):

$$P_i(r) = \frac{N_i(r)}{\sum_{i=1}^{N(r)} N_i(r)} \qquad 5.4$$

where $N_i(r)$ is the number of active pixels inside the i-th box of size r, and $N(r)$ is the total number of boxes that contain at least one active pixel.

The family of generalized dimensions has some characteristic quantities: the capacity dimension (D_0), the information dimension (D_1), and the correlation dimension (D_2). In general, D_q is a monotonically decreasing function of the real value moment order q. If D_q is a single-valued function, equal to the FD defined above, the object is referred to as monofractal (Lopes & Betrouni, 2009). Overall, the parameter q serves as a "magnifying lens" that analyzes the object at different scales (Lopes & Betrouni, 2009). Using multifractal analysis, one can also determine the number of boxes having similar local scaling, that is the same α , and define $f(\alpha)$ as the FD of the set of boxes with singularities α. The curve $f(\alpha)$, also called singularity spectrum, is a convex function whose maximum corresponds to D_0. As $q \to -\infty$, $\alpha \to \alpha_{\max}$, and as $q \to +\infty$, $\alpha \to \alpha_{\min}$. In general, when $f(\alpha)$ and D_q are smooth functions of α and q, a Legendre transformation can be used to derive $f(\alpha)$ from D_q (Chhabra & Jensen, 1989). However, $f(\alpha)$ can also be directly calculated, without knowing D_q, by using the method proposed by (Chhabra & Jensen, 1989). The first step of this approach consists of defining a family of normalized measures $\mu_i(q,r)$, defined as:

$$\mu_i(q,r) = \frac{P_i(r)^q}{\sum_{i=1}^{N(r)} P_i(r)^q} \tag{5.5}$$

For each box i, the normalized measure $\mu_i(q,r)$ depends on the order of the statistical moment, and on the box size and it takes values in the range [0,1] for any value of q. Then, the two functions $\alpha(q)$ and $f(q)$ are evaluated:

$$\alpha(q) = \lim_{r\to 0} \frac{\sum_{i=1}^{N(r)} \mu_i(q,r)\log(P_i(r))}{\log(r)} \tag{5.6}$$

$$f(q) = \lim_{r\to 0} \frac{\sum_{i=1}^{N(r)} \mu_i(q,r)\log(\mu_i(q,r))}{\log(r)} \tag{5.7}$$

For each q, values of $\alpha(q)$ and $f(q)$ are obtained from the slope of plots of $\sum_{i=1}^{N(r)} \mu_i(q,r)\log(P_i(r))$ versus $\log(r)$, and $\sum_{i=1}^{N(r)} \mu_i(q,r)\log(\mu_i(q,r))$ versus $\log(r)$ over the entire range of box sizes under consideration. Finally, the two data sets of $\alpha(q)$ and $f(q)$ are plotted with respect to each other and can be used to construct the singularity spectrum (i.e., to generate a plot of α vs. $f(\alpha)$).

Figure 5.8 presents the spatial probability for the same crack pattern examined in Figure 5.7a. It should be noted that on each box, a probability value was assigned which ranges between zero and one [0,1] and the color map on those distributions represents the pixel intensity of the corresponding box. Note that the scale is not constant along each box size, due to the fact that the sum of the probability distribution must be equal to 1. This can be expressed by the following:

$$P_{\Omega}\left(r\right)=\sum_{i=1}^{N(r)}\mu_i(q,r)=1 \tag{5.8}$$

As a result, as the number of boxes which compose the domain increases, the values of the corresponding probabilities decrease. For example, in Figure 5.8a, the value of probability which corresponds to each box is an order of magnitude greater than the probabilities observed in Figure 5.8f.

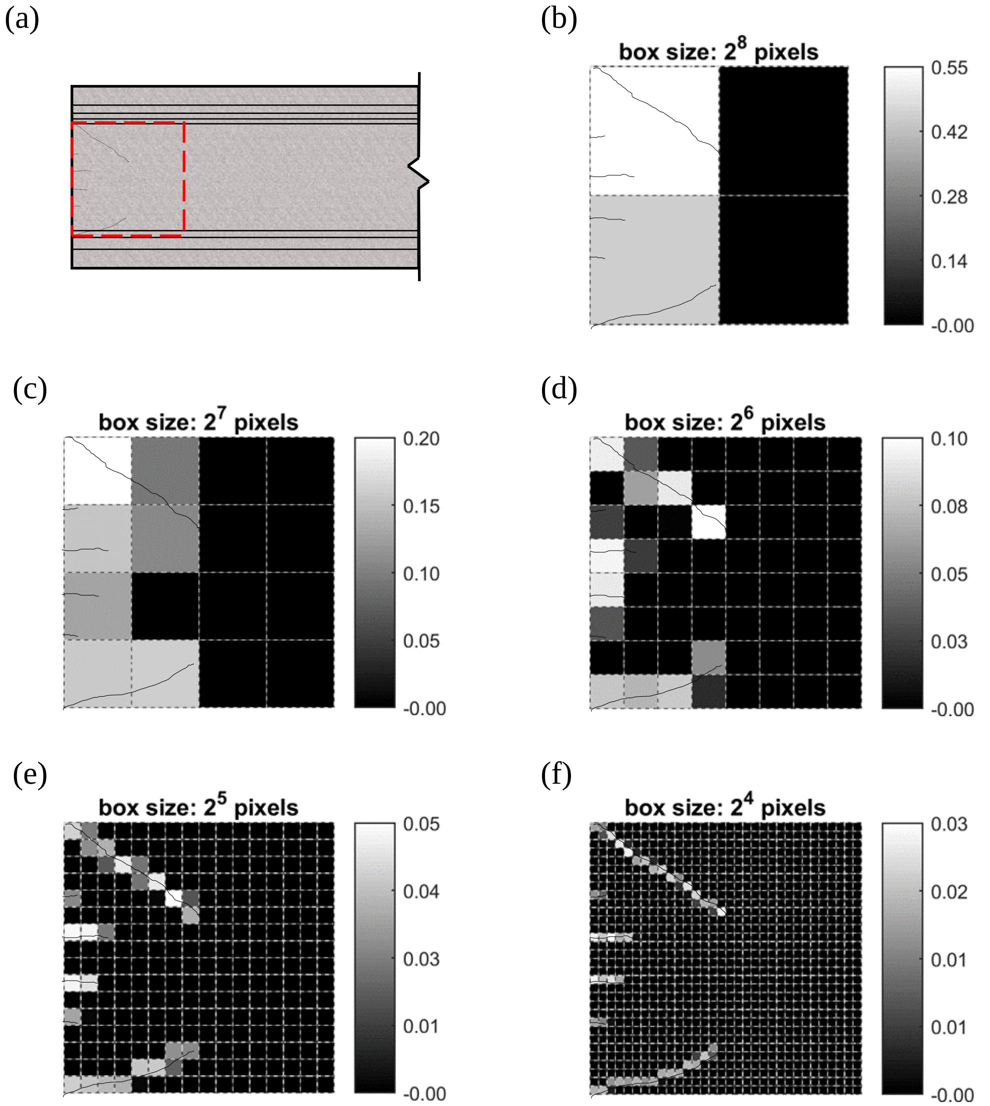

Figure 5.8 Spatial pattern of probabilities for zero distortion ($q=1$) used for the multifractal analysis

Multifractal analysis permits the identification of noise in analyzed patterns. The term noise is used to describe irregular fluctuations associated with the shape of a crack pattern due to the introduction of new crack clusters. For example, if a single inclined crack is added to the analysis domain, that additional crack will be automatically be depicted on the shape of the singularity spectrum. To support this argument, a single inclined crack is added to an example the crack cluster. Figure 5.9 presents the initial, as well as the augmented, cracking patterns. Both patterns were analyzed, and the resulting singularity spectrums are presented in Figure 5.10. It can be observed that the original pattern has a parabolic shape which verifies its multifractal nature. The shape of the singularity spectrum is typically a concave curve, which can be approximated with a parabola (Pachepsky et al., 2003). Moreover, for every multifractal crack pattern, the resulting singularity spectrum is tangent to the identity function $f(a)=a(q)$. The main parameters which control the shape of the singularity spectrum are the location of the peak (capacity dimension), and the width of the parabola. On the other hand, the augmented crack pattern once it reaches the point at which $f(a)=a(q)$, tangles and forms a knot. That is a typical response of a non-multifractal set. Notice that the branches of the singularity spectrum are parallel offsets of the original multifractal singularity spectrum. The augmented crack presents fractal properties similar to those of the original crack, but with a reduced FD. This transition from multifractal to fractal, as well as the reduction on the fractal dimension, can be considered as significant indicators of initiation of a new crack type.

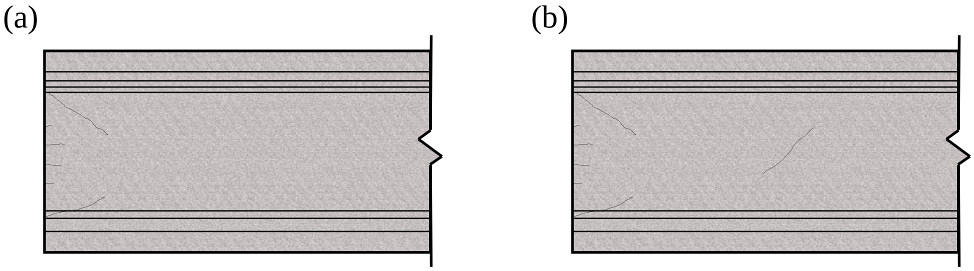

Figure 5.9 Faces of the beam (a) with only end-region cracking – 'initial' (b) with end-region cracking and a diagonal crack – 'augmented'

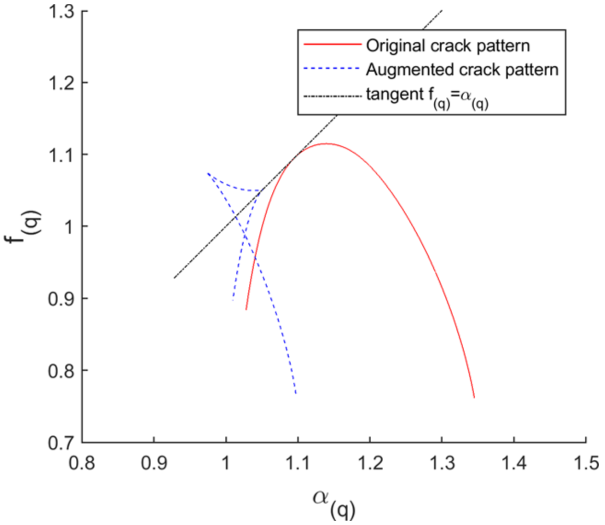

Figure 5.10 Comparison between the singularity spectrum for a multifractal and a non-multifractal pattern

5.2. Image Monitoring of Cracked Concrete Components

For the development of the image based cracking assessment approach, the research team attempted to compile a comprehensive database of crack patterns that evolve over increasing applied shear loading. Although several shear tests have been performed over the past decades, researchers have generally made limited efforts to monitor the evolution of cracking. In particular, the state of practice in structural testing is to report average values to document the spatial properties of crack patterns, such as the crack spacing and the crack width. The recent advancements in digital image acquisition has allowed the research community to document the crack pattern evolution as a function of structural response. Two examples of structural experiments that utilized those new technologies are:

- Prestressed girder shear testing (TxDOT Project 0-6831, Katz et al., 2017)
- RC panels under shear loading (Ruggiero et al., 2016)

To evaluate the shear capacity of cracked RC bent caps, the research team analyzed cracking datasets (i.e., images of crack patterns and structural response data) of the structural experiments on a girder and a series of RC panels. The utilization of computational tools such as fractal and multifractal analysis has permitted the quantification of the cracking patterns. The following subsections provide an overview of these experiments as well as images of the crack patterns that developed in the structural components.

5.2.1. Prestressed Girder under Shear Loading

This section discusses the crack formation mechanisms as well as the features and characteristics of typical cracks on prestressed girders. For discussion purposes, the cracks developed on the prestressed girder are divided into two categories: 1) end-region cracks, and 2) shear cracks (refer to Figure 5.11). This classification is based on the location and mechanism of cracking. End-region cracks are those which appear immediately after the release of the prestressing strands (i.e., following prestress transfer). Such cracks further divide into two groups: a) spalling cracks, and b) bursting cracks. Shear cracks, which will typically only form after the subsequent application of external loading and may also be divided into two groups: a) inclined shear cracks, and b) horizontal shear cracks.

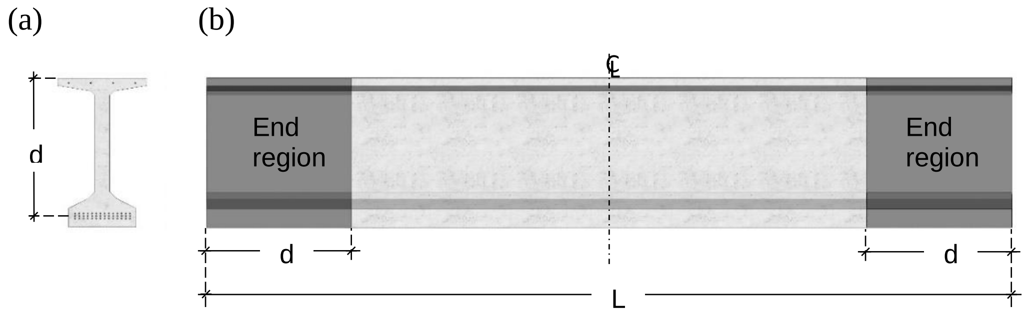

Figure 5.11 (a) Bulb tee cross section (b) side view of the girder with highlighted end regions

Figure 5.12 shows the locations and orientations of the different types of cracks that may form in pretensioned girders following prestress transfer and under subsequent application of mechanical loads.

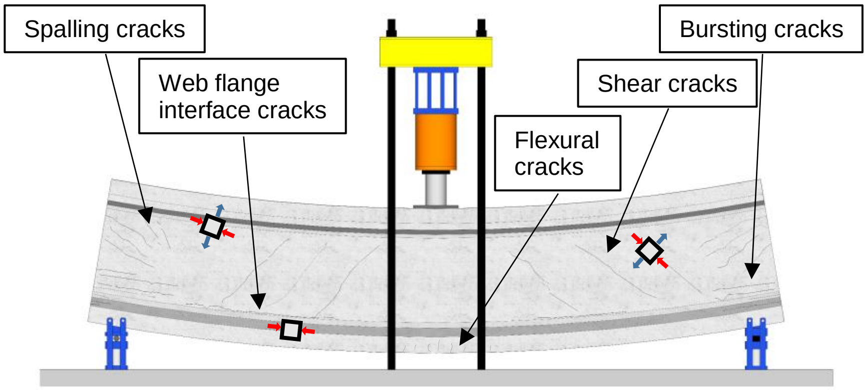

Figure 5.12 Schematic diagram of expected crack types on prestressed girders; differential elements indicate principal state of stresses.

To validate the fractal and multifractal properties of crack patterns in prestressed highway girders, data obtained from experiments conducted on a large-scale Tx-girder were used (Katz et al., 2017; Salazar et al., 2018; Yousefpour et al., 2017). The overall depth of the specimen was 70 in. (see Figure 5.13). Figure 3.3a and b show the side view of the specimen and its cross section, respectively. The girder was simply supported and spanned a distance of 28.5 ft. The fabrication of the girder was performed using a large scale prestressing bed facility at The University of Texas at Austin. This bed is good for manufacturing prestressed girders of up to 30 ft long (approximately 9.1m). Due to the size limitation of the prestressing bed facility, the length of the girder was far less than that typically employed by in-service prestressed concrete girders; however, a full-scale cross section was used resulting in a low span-to-depth ratio (L/d=4.9). To simulate the presence of the concrete deck on the girder, an additional concrete layer was cast in place on the top of the specimen (see Figure 5.13a). The general design of the girder was in accordance with the AASHTO LRFD Bridge Design Specifications (AASHTO, 2016); however, it should be noted that the girder was constructed using atypicallylarge 0.7-in. (18-mm) seven-wire diameter prestressing strands. The end region reinforcement detailing of the girder was constructed in accordance with the standard details provided by the Texas Department of Transportation (TxDOT, 2015).

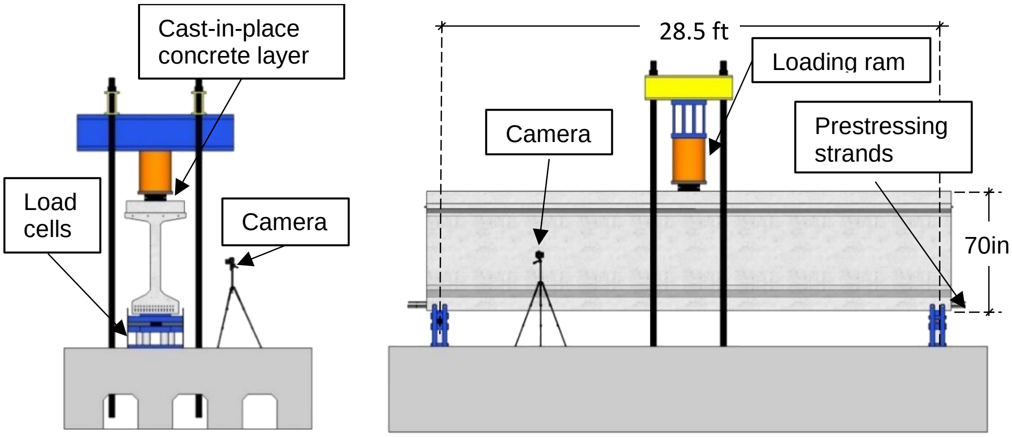

Figure 5.13 Specimen: a) cross section, b) west face view

5.2.2. Reinforced Concrete Panels under Shear

In addition to the member-level analysis presented in Chapter 5.2.1 (prestressed girder), a significant effort was made to study the cracking response of idealized RC membrane elements. Membrane elements are typically used to simulate, or represent, a small part or region of a larger structural component such as a beam, shear wall, and or bridge member. Membrane elements allow us to examine the cracking response of large structures by testing only the cracked region of the element. This study focuses on extracting the spatial features of rectangular RC panels using multifractal analysis and identifying which of these properties are correlated with the damage level. A series of ten RC panels was used to compose a database of crack patterns. Every panel was comprised of at least six load stages. Further, the loading of the panels was done using a series of well-defined load stages, which permitted the documentation of the element’s cracking response. Figure 5.14 presents a schematic of the image-based procedure used for the damage classification on RC panels.

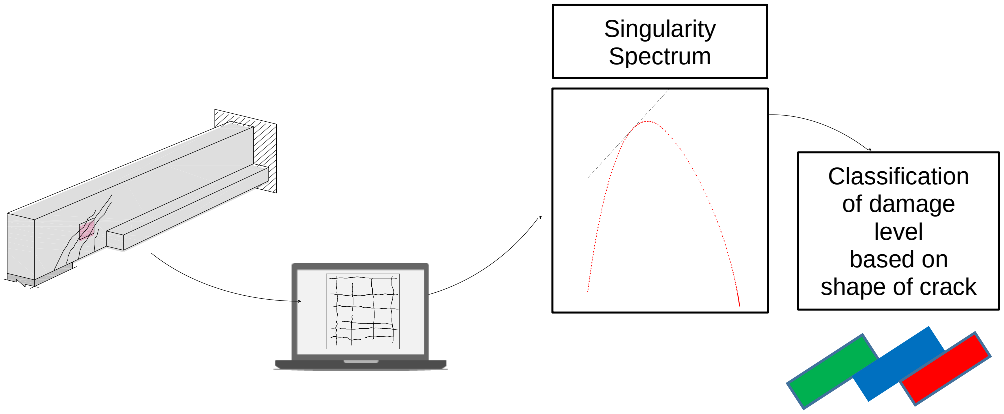

Figure 5.14 Schematic of the procedure followed for the automatic damage classification

The RC panels were tested using what is referred to as the shell element tester at the University of Toronto (Stevens et al., 1991). A schematic of the test setup is presented in Figure 5.15. The shell/panel elements were square with side dimensions of 60 in. and were 11.4-in. thick. The actuators that were used to apply loads were configured in a manner to apply pure in-plane shear forces on the panel element.

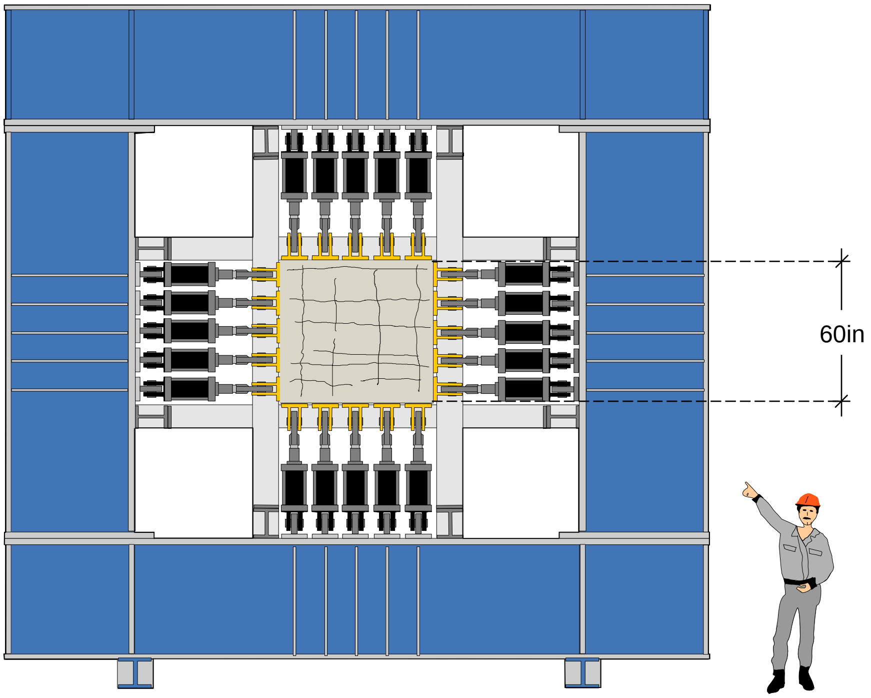

Figure 5.15 The shell element tester apparatus, used for the shear testing of the reinforced concrete panels

The data collected during this experimental program included:

(1) digital images of both panel's faces, and
(2) local strain measurements

The combination of information about the shape of the crack patterns and the mechanical properties of the cracked panel provided data required to classify every panel based on its damage level. Figure 5.16 presents a visualization of the data collected during the testing of a RC panel and the corresponding damage level assigned to the crack pattern. Both the crack patterns (Figure 5.16a & b) and the local strain distributions (Figure 5.16c & d), were collected during two load stages (second and fifth, respectively). The third column of Figure 5.16 presents the color-coded tags assigned and used to identify the levels of damage assigned to each load stage based on the level of local strain on the element.

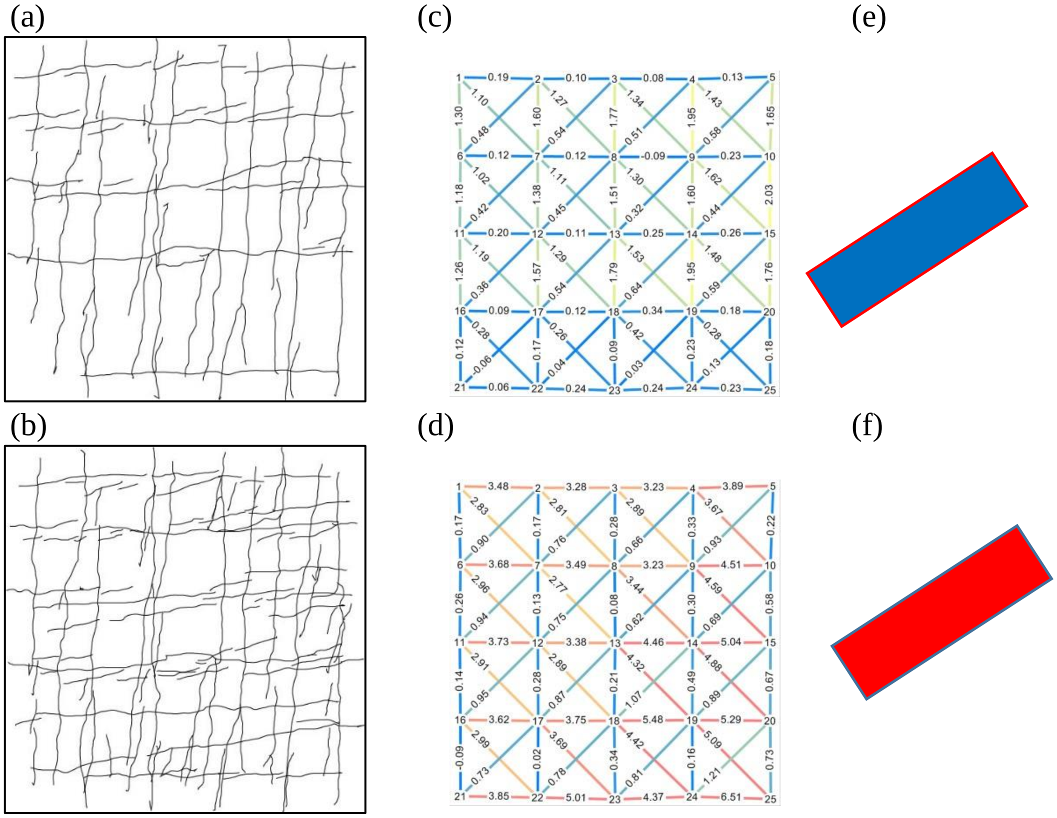

Figure 5.16 Assignment of damage levels into crack patterns (a) crack pattern of panel SR-5 at load stage 2, (b) crack pattern of panel SR-5 at load stage5, (c)-(d) local strain measurements based on Zurich gauges (Ruggiero et al., 2016)*, (e)-(f) color coded tag corresponding to damage level*

The effect of increased local strains is also depicted on the average (global) response of the reinforced concrete panel. In Figure 5.17, it can be seen that the shear strain that corresponds to load stage 5, is significantly greater than the shear strain corresponding to load stage 2. That increased level of shear strain reveals that the element is more damaged (i.e., the stiffness has decreased), and that the degree of permanent/plastic strain has increased.

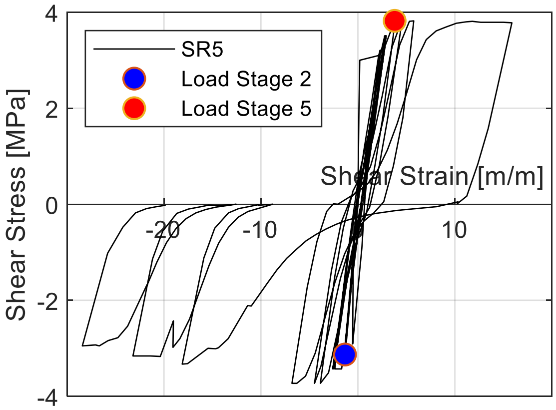

Figure 5.17 Shear stress - strain response of a reinforced concrete panel under reversed cyclic shear loading. Two load stages are annotated as well as the corresponding damage levels

5.3. Fractal and Multifractal Analysis Results

This section presents observations and remarks obtained from the analysis of the crack patterns. The research team used fractal analysis to study the features of cracks on the prestressed girder. Multifractal analysis procedures were utilized for the RC panels. The large amount of high-quality RC panel data examined in the current study permitted the training of a model for the classification of RC panels based on their damage levels. Finally, the last part of this section presents information about the accuracy of the model.

5.3.1. Prestressed Girder

Figure 5.18 presents the measured load-deflection response of the girder. Figure 5.19 presents the evolution of the fractal dimension (FD) from the time at which the formwork of the girder was removed (day 0) until the failure of the girder that occurred due to subsequent loading (at a load level of 1613 kips). The x-axis is divided into two parts, both time and loading are used as independent variables depending on which phase the specimen is examined. Results for the west and the east faces of the north half-span are presented on Figure 5.19a and b, respectively. It can be noted that the FD does not increase in a strictly monotonic fashion. That is, drops/reductions as well as plateaus can be observed in the time/load history of the FD. The end-region cracking continued to gradually evolve and the evolution was accompanied by a slight increase in the FD. Specifically, the FD shifted by 0.05 from the 7th to the 28th day. Although the FD increased monotonically during the construction stage, this trend did not continue after the application of load. For example, Figure 5.19a, shows a decrease of the FD for the northwest side of the girder immediately after the application of the load. The reason for this decrease is due to the appearance of minor cracks that formed outside the end-region of the girder. Those new cracks can be considered as noise that reduces the self-similarity of the whole pattern and this reduction is denoted with an arrow on Figure 5.19. While the load on the girder was in the serviceability levels (between 0 and 600 kips), only minor surface cracking was observed. This was primarily the result of no additional damage development as the load increased over the linear load-displacement response of the girder (refer to Figure 5.18). In addition, this load range coincides with a plateau in the evolution of FD indicating that no new cracks appeared in that load range.

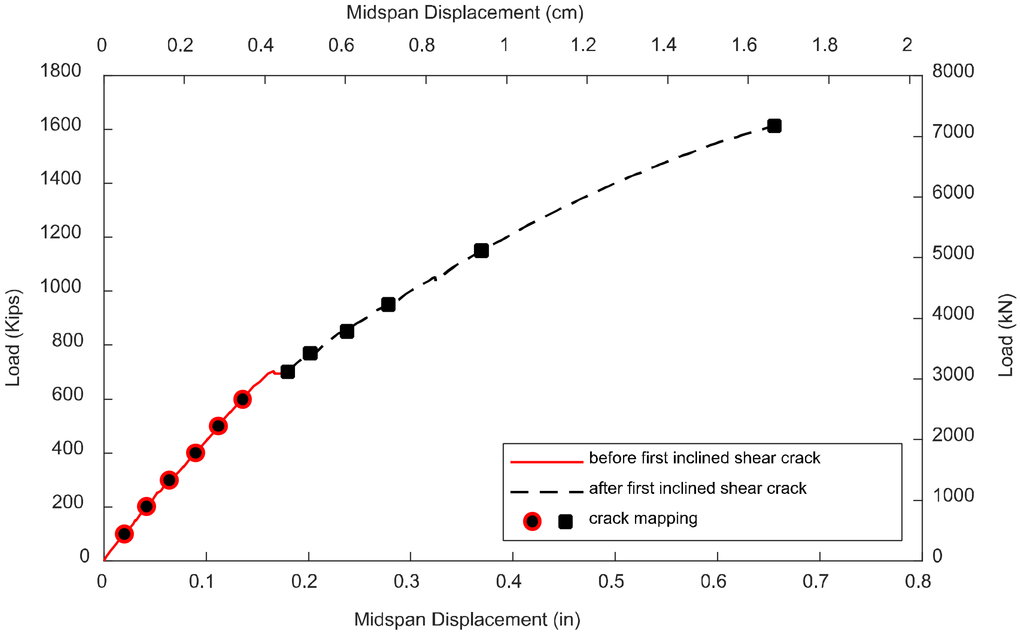

Figure 5.18 Load deformation response of the girder, and load stages at which the loading was paused to perform crack mapping.

Although inclined shear cracks are often treated as through-thickness, the shear crack in this experiment first appeared only on the west face of the girder (on the north half-span). The reason for this observation could be the immediate pause in the loading procedure (described in Section 4), which did not let the crack propagate through the full width of the web. As a result, there were no surface shear cracks recorded on the east face for that load stage (600 kips, equivalent to 2670 kN). The variation of the crack pattern between the west and the east faces caused a discrepancy in the evolution of the FD. Specifically, the fractal value on the west and east faces were 1.45 and 1.41, respectively. In other words, the inclined shear crack decreased the FD on the west face while the FD remained approximately constant on the east face. The decrease in the FD was due to the introduction of the noise (i.e., the inclined shear crack) in the fractal pattern. That decrease on the FD shows that the addition of an inclined shear crack influences the scale invariance of the pattern. Thus, the decrease of the FD obtained between sequential inspections (i.e., between sequential load stages) can be considered as a significant indicator regarding the initiation of new crack types.

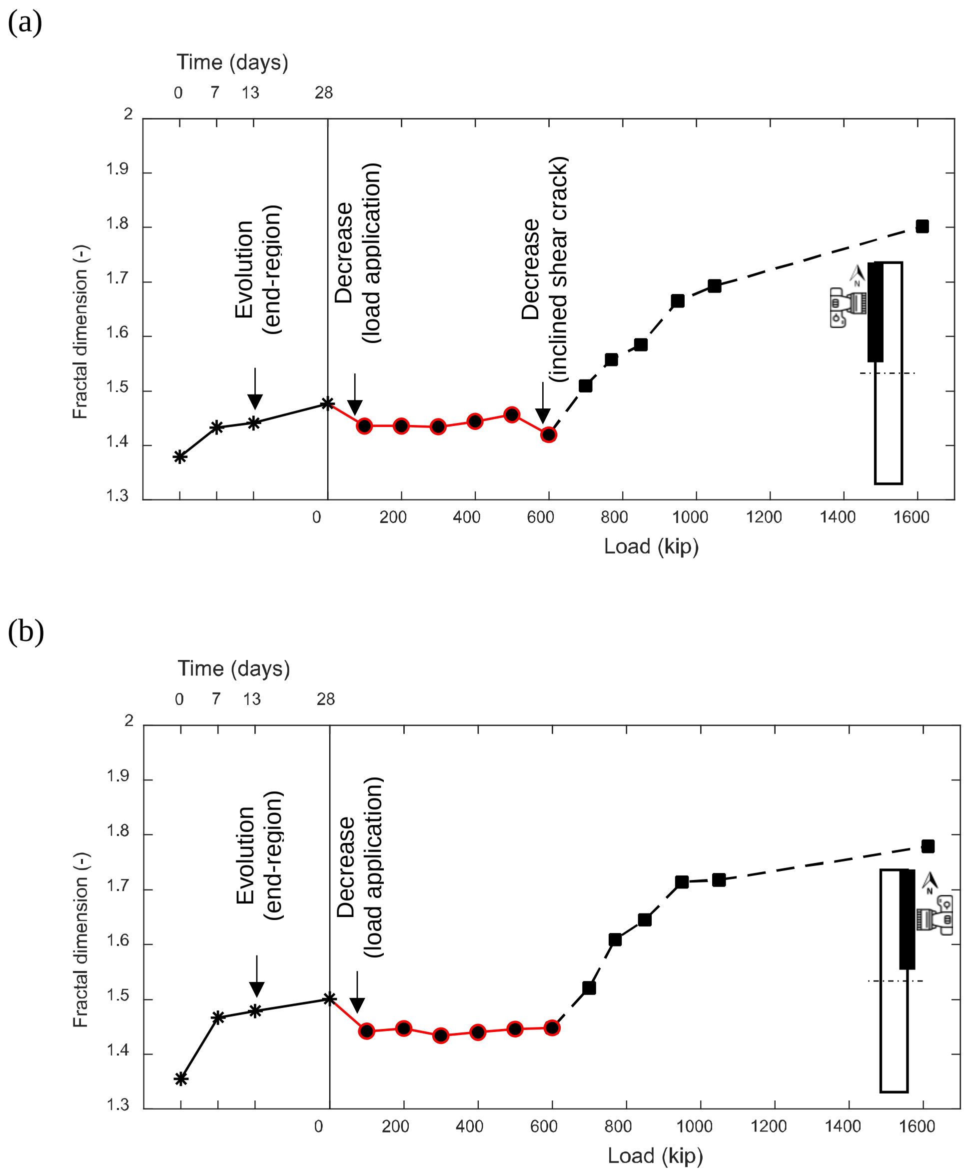

Figure 5.19 Fractal dimension (FD) evolution as a function of time and load on the north half-span: a) west face; b) east face

5.3.2. Reinforced Concrete Panels

The analysis of the RC panel elements consists of two parts: (a) the actual extraction of features, and spatial characteristics of the crack pattern, using multifractal analysis, and (b) the development of the classification model.

5.3.2.1. Multifractal Results

The algorithm developed by the research team was used to analyze an extensive set of crack patterns of reinforced concrete panels. No considerations were made about the variation of width along a crack, or the average crack width. The centerline of each crack was manually extracted and saved on binary images. A sample of the input images is presented in Figure 5.20. The spatial properties of a crack pattern are correlated with the amount of damage on a concrete component.

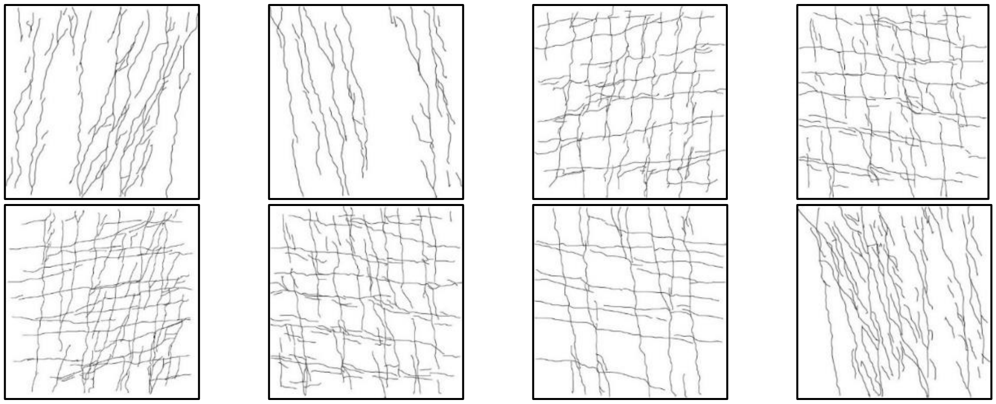

Figure 5.20 Example of crack patterns used for the training and the validation of the approach

Fractal dimension is not an adequate measure to monitor the evolution of cracking on different panels because it a single measure which can capture only specific aspects of the cracking evolution, such us the introduction of noise in the pattern, or the global changes in the pattern. The type of cracking on those RC components, required the introduction of additional measures to capture necessary details regarding the element’s spatial properties. Figure 5.21a present the singularity spectra corresponding to 119 multifractal analyses corresponding to 119 crack patterns. Each crack pattern corresponds to a single singularity spectrum (i.e., a single parabolic curve). The color-coded tags assigned to each pattern (as presented in section 5.2.2), are used to categorize each singularity spectrum. Note that each damage level is grouped together into a cluster. Those equal damage clusters (i.e. sets of singularity spectra that correspond to the same damage level) are isolated and presented separately in Figure 5.21b, c, and d. Identifying the clustering of the damage-singularity relationship, the research team employed artificial intelligence tools in an effort to predict the damage level of RC panels, on the basis of crack pattern.

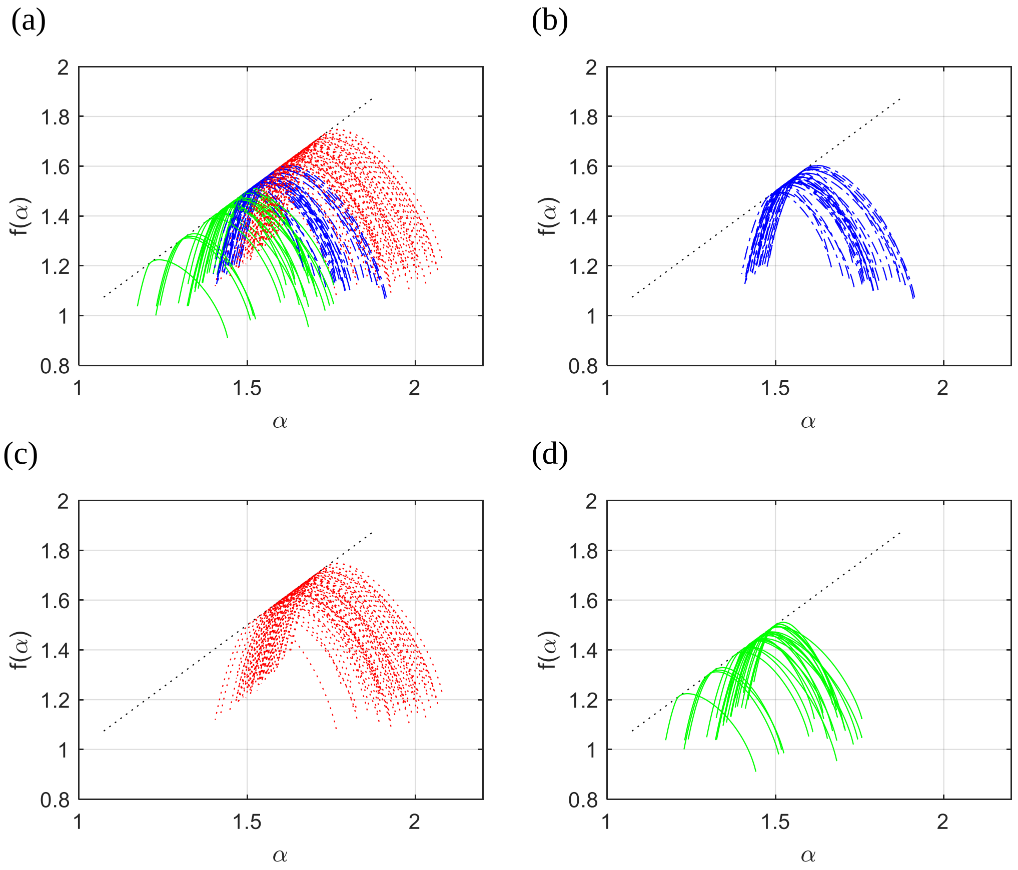

Figure 5.21 Overview of multifractal spectrums based on the corresponding damage level (a) green category – slightly damaged, (b) blue category – severely damaged, (c) red category – heavily damaged, (d) combined view – all damage categories

5.3.2.2. Classification based on Singulatiry Spectrum's Geometrical Properties

Classification problems for small datasets can be an easy problem for humans, but that is not the case for large datasets. Recent advancements in computer science allow us to analyze significant amounts of data and create prediction models. The research team defined a set of linearly independent parameters which can accurately describe the geometric properties of an approximate parabolic shape, such as a singularity spectrum. The parameters defined and considered consist of i) the peak of the parabola, ii) the total width of the parabola, iii) the area of the region under the left branch of the parabola, and iv) the area of the region under the right branch of the parabola. Each of these parameters are visualized in Figure 5.22.

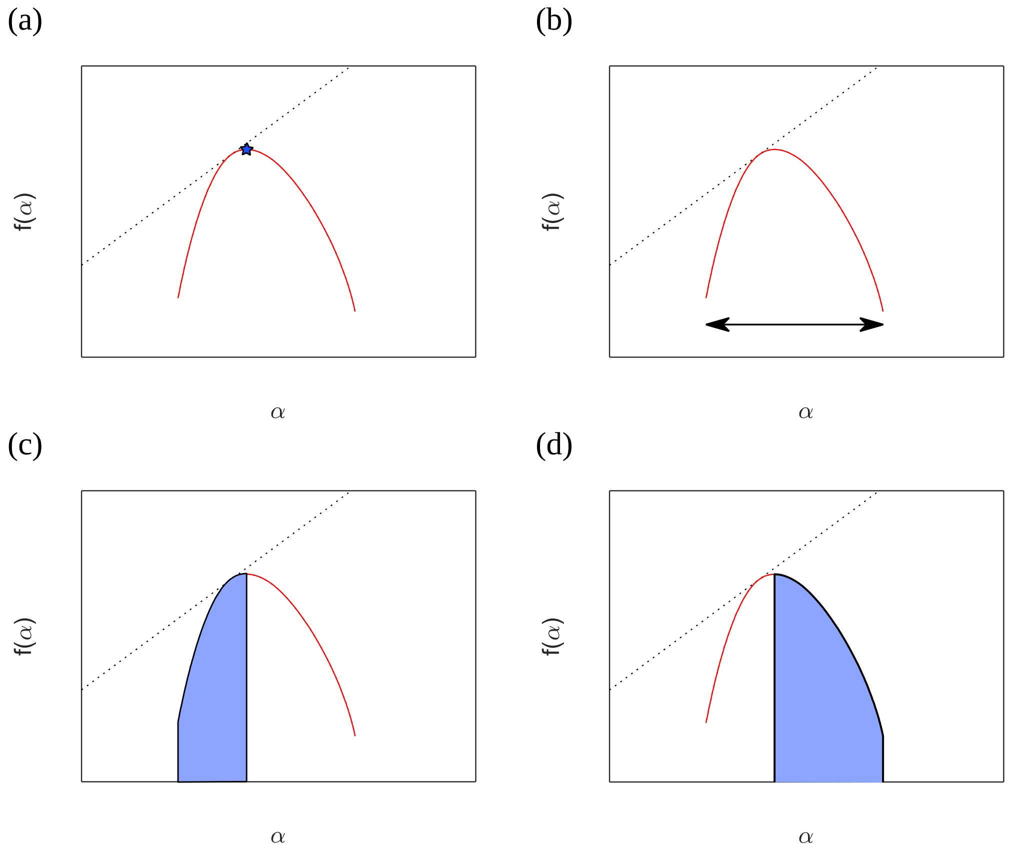

Figure 5.22 Geometric properties used as predictors in the classification model (a) Peak of the spectrum - FD, (b) width of the spectrum, (c) area of the region under the left branch of the parabola, (d) are of the region under the right branch of the parabola

Collecting the above-noted parameters from the multifractal spectra yielded a significant amount of information which was also well-clustered according to damage level. A visualization of the relationship between the geometric parameters of the multifractal spectra are presented in Figure 5.23.

The data obtained were fed into a machine learning engine with the goal of this effort being to make predictions about the damage level, using the aforementioned geometric parameters of the multifractal spectra. The best fit was obtained using an ensemble bagged tree (Goodfellow et al., 2015). That supervised learning algorithm is commonly used and, in this case, yielded a 91.4 % predicted accuracy. More insight of the model's capabilities can be provided by the confusion matrix (Figure 5.24). Confusion matrices are a means of visualizing the performance of a model. Note that predictions for the green category are always correct (100 % accuracy), and that the occurrence wrong predictions were limited. Figure 5.24 shows the absolute number of observations used for the training (the sum of the rows and the columns is 119), and Figure 5.24b presents the percentage rate of each possible outcome. For the sake of completeness, the efficiency measure of the machine learning model for the classification of damage level, is presented in Figure 5.25.

Additional information about these measures is available elsewhere (Goodfellow et al., 2015)

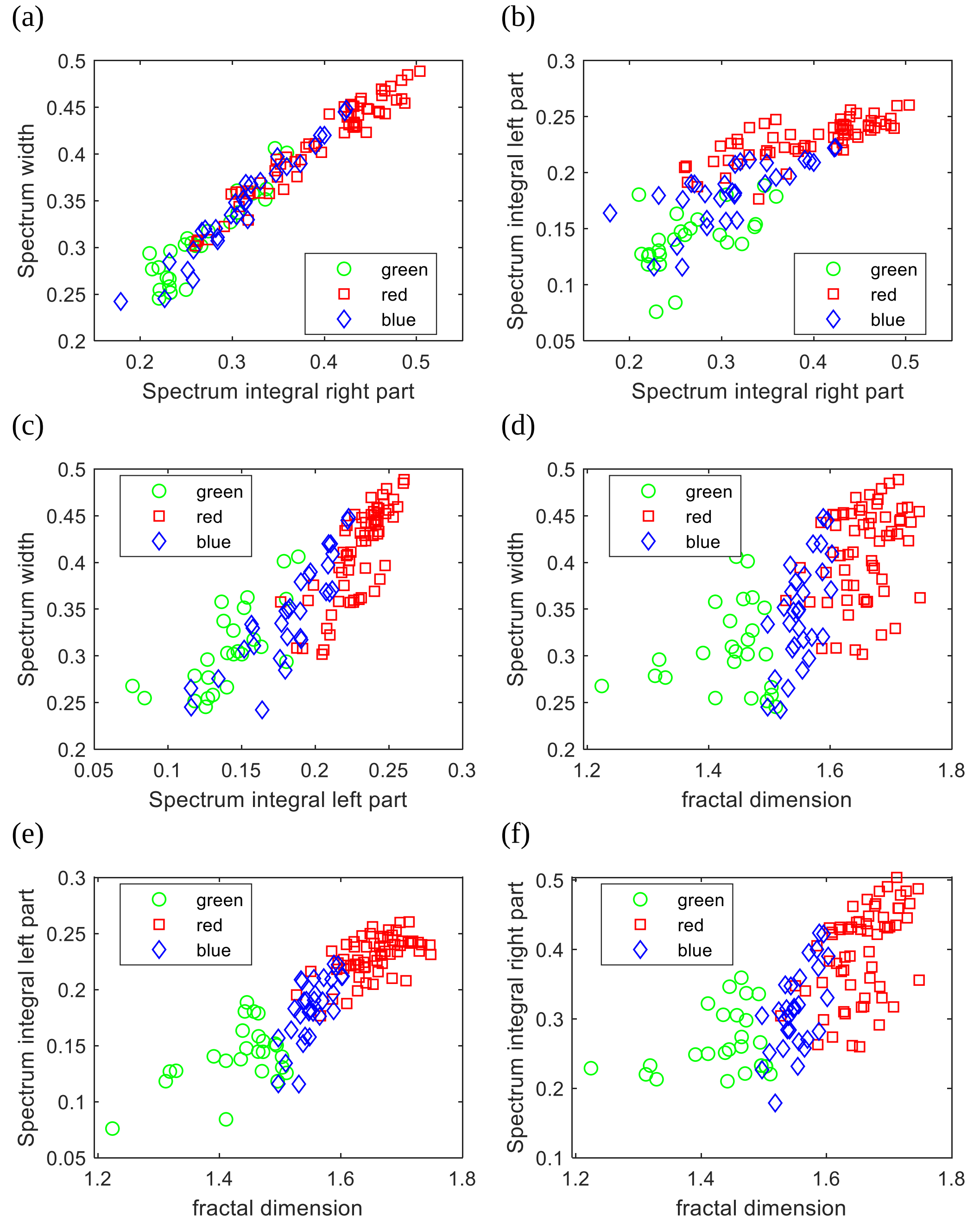

Figure 5.23 Scatter plots of geometric control parameters. (a) width – right part integral, (b)left part integral – right part integral, (c) width – left part integral, (d) width – fractal dimension, (e) left part integral – fractal dimension, (f) right part integral – fractal dimension

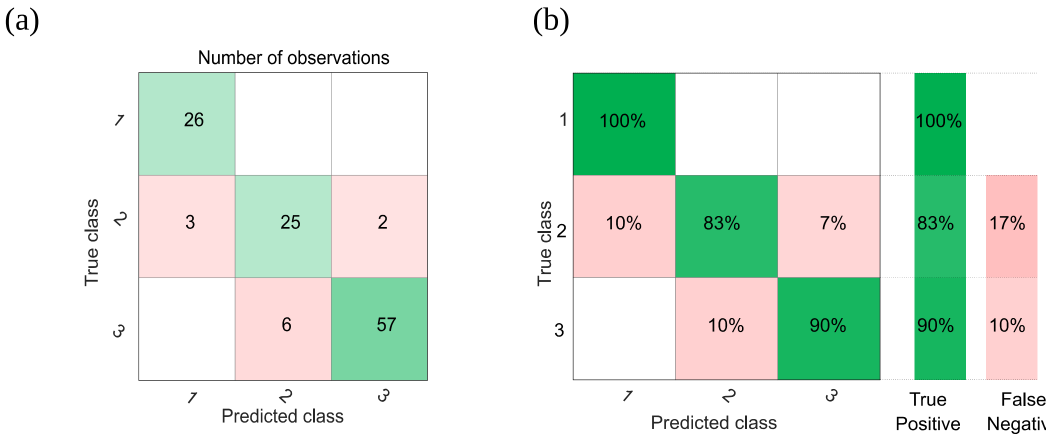

Figure 5.24 Confusion matrices: (a) number of observations, (b) True Positive – False Negative rates

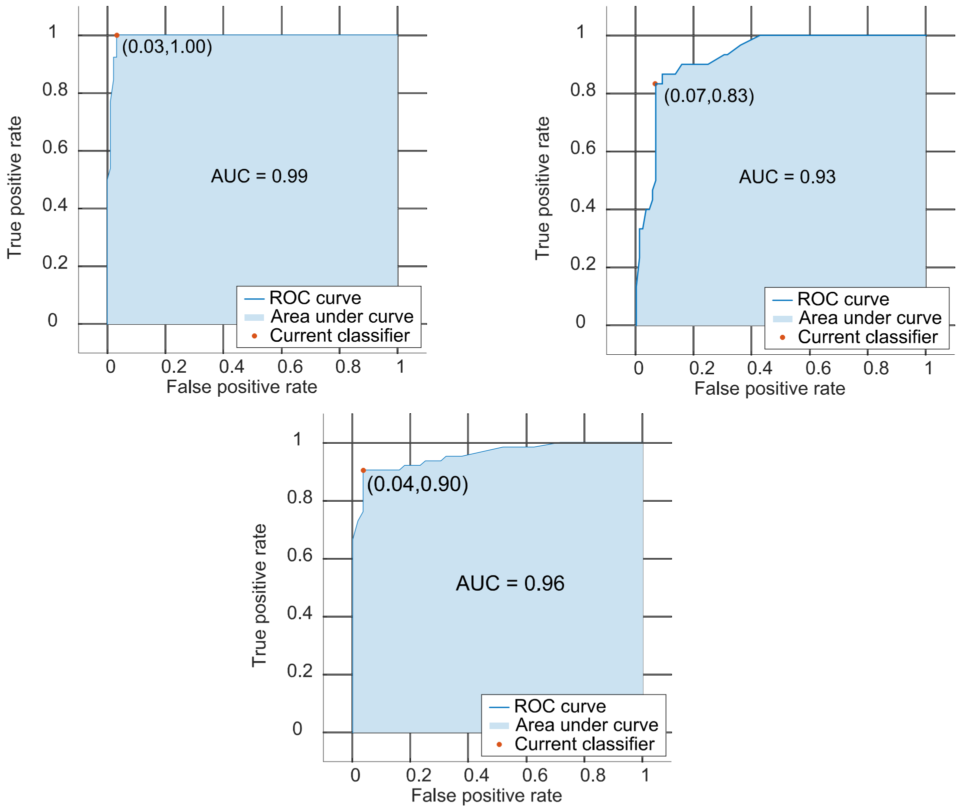

Figure 5.25 Receiver Operating Characteristic curves

5.4. Summary

The fractal-based crack pattern quantification approach developed through this project was shown to be a viable approach for damage assessment of concrete structures. Potential application of the procedure was illustrated using two different data sets, one involving a prestressed girder and the second corresponding to a series of RC panel elements. The main outcomes regarding this procedure are:

- **It can be used to identify changes in crack patterns such as the introduction of a new crack mechanisms**. This information can be used to assist the automation of the inspection procedure.
- **It provides direct correlation between the structural damage and the singularity spectrum**. It became evident that in cases at which minor changes occur in the crack pattern, those can be identified an based on the location of the singularity spectrum, an inspector can assess how much damage has occurred on the structural component.
- **Parameters such as the angle of the cracking and the spacing can be estimated using the singularity spectra**. Since the spatial distribution of cracking is directly correlated with the structural response, the classification of singularity spectra into damage levels, can reveal significant information about the structural health of a structure.

Despite the successes shown in the results presented, there are also limitations which should be taken under advisement when using the fractal-based crack pattern quantification procedures. These inherent limitations are as follows:

- **Each model developed is element specific**. The models and observations made cannot be generally applied in to different structural elements.
- **The application of the approach requires the acquisition of digital images**. Currently the visual inspections do not include high resolution digital documentation of cracking. This severely limits its implementation within the framework of current inspection procedures and post-inspection assessment methods.

Fractal-based approaches require further development to become applicable in more structural members. This can be achieved by further analysis of well-documented experimental data. Collecting images and structural response data on multiple load stages during structural tests, can accelerate the development of fractal-based crack assessment procedures.

Chapter 6. Summary and Conclusions

This portion of the report provides a summary of the work accomplished as part of Texas Department of Transportation (TxDOT) Project 0-6919 and the relevant conclusions obtained over the course of the project.

6.1. Summary

Diagonal cracking of reinforced concrete (RC) bent caps has been reported across the state of Texas; however, while traditional methods of damage assessment can aid in identifying signs of distress, they do not correlate crack data with structural capacity. Various methods have been proposed in the past several decades to address this problem and have been met with various levels of success. This project aimed to develop and verify crack-based shear strength assessment procedures which could be used as supplemental tools for decision making, to assist in prioritizing maintenance and repair efforts, and to identify critical strength-related deficiencies. Two procedures were developed, evaluated, and refined to address this need. To accomplish this goal, the following tasks were accomplished:

1. Conduct a review of literature and relevant field data to determine the following:
    i. State of the art in damage-based structural assessment (Chapter 2)
    ii. Structural cracking in existing TxDOT Bridges (Section 3.1)
    iii. Available experimental structural crack measurement data (Section 3.2)
2. Assemble a Visual Crack Measurement Evaluation Database using data collected during the literature review (Section 3.3)
3. Develop two crack-based shear strength assessment procedures:
    i. Cracked continuum shear strength assessment (Section 4.1)
    ii. Crack pattern quantification using fractal analysis (Chapter 5)
4. Evaluate and refine preliminary crack-based strength assessment procedures (Section 4.2)
5. Create “visual crack inspection field aids” based on the refined procedure (Section 4.3)

6.2. Conclusions

The conclusions of TxDOT Project 0-6919 are presented in this section.

6.2.1. State of the Art in Damage-Based Assessment

There are several methods available for damage-based (or more specifically, crack-based) assessment of RC structures, some of which are currently employed in practice and others that have only been examined through research programs. Many of these models rely on similar underlying assumptions about the behavior of RC, but vary in terms of their levels of accuracy, their ease-of-use, and level of validation that has been performed in assessing their adequacies. The following presents the key findings obtained from the literature related to current, or previously proposed, methods for carrying-out damaged-based assessment of RC infrastructure:

- Methods currently employed in practice to evaluate RC structures are generally practical in terms of their abilities to recommend action based on visually inspected damage without the use of advanced or expensive tools. Additionally, these methods are simple to implement as they usually require limited user-input and the output is straightforward with clear guidelines for remedial action. Further, these methods are also well established and have been used for several decades; as such, there is a level of familiarity and experience with their usage. However, the quality of the observations and results obtained from current inspection methods are highly dependent on the individual inspector's experience. Additionally, these methods typically provide little-to-no information regarding the structural implications of visually observed diagonal cracking in RC bridge members.
- Nonlinear finite element analyses (NLFEA) can be extremely powerful, and are potentially very capable, tools for estimating the structural capacity of cracked concrete members. However, it is important to note that proper application of NLFEA can be a costly and time-consuming process, and their successful usage requires experienced users to build high resolution finite element models that adequately reflect the structure details and damage. Further, it should also be noted that accurate modeling of RC infrastructure still represents an existing challenge as a result of complex concrete behavior modeling, and no single approach or material modeling strategy has been shown capable of providing good results over the large spectrum of structural details and loading conditions encountered in practice (Vecchio, 2001).
- In general, empirical methods, such as charts or equations, are easy to use and usually do not require computational power. However, due to the fact that they are derived from highly focused experimental data, these empirical tools are always restrictive in that they are limited/bound to the specific member types, member scales, reinforcement conditions, material properties, and loading conditions that were referenced in their development.

- Methods that utilize concrete mechanics-based procedures may have the potential to be the most general in terms of their applicability to real world scenarios while retaining the balance between required computational cost/effort and ease of use. A review of the existing literature thus far indicates that there are only few concrete mechanics-based models available for crack-based assessment of RC infrastructure, and essentially none of them have been extensively validated with members typical of TxDOT bridges.

6.2.2. Visual Crack Measurement Evaluation Database

The Visual Crack Measurement Evaluation Database (VCMED) is an evaluation database in the form of a catalogue spreadsheet. VCMED was used to verify the crack-based shear strength assessment procedures developed and to gain insights regarding the breadth of diagonal cracking characteristics (e.g., crack widths, crack inclinations, crack spacings, etc.) that are likely to be encountered in the field. One particularly noteworthy finding obtained from the analysis of the data employing the VCMED, is that diagonal crack widths, on their own, are not reliable indicators of member shear damage or residual member shear capacity. More specifically, without consideration of other crack characteristics (e.g., crack inclination, crack spacing, etc.) and without consideration of member-specific properties and design details (e.g., reinforcement details, material properties, loading and support conditions, etc.), examination of diagonal crack width may lead to misleading assessments for likely member shear capacity.

While the VCMED is comprised of a large number of structural crack measurement data that were populated from a broad range of testing research testing programs, much of the data were found to be unsuitable for analysis procedure verification purposes. More specifically, much of data obtained that were acquired were reported with inadequate crack measurement data documentation (i.e., reporting data over limited load stages, reporting data with missing information, or simply reporting in a vague manner that could not be definitively interpreted by the researchers). Thus, the limited damage monitoring/data acquisition and the limited crack damage documentation that was reported for many of structural tests unfortunately limited the development efforts of the crack-based assessment procedures. In particular, a lack of high resolution crack pattern images severely limited the degree of development and validation that could be performed for the image-based assessment procedures that were explored through this work. Nevertheless, using the data currently available in the literature, the research team was able to compile a high-quality series of crack data. Based on the details provided and the relevance of each data source, the data were classified into three data categories.

6.2.3. Cracked Continuum Shear Strength Assessment

The cracked continuum shear strength assessment procedure developed through this project was shown to be a viable approach for carrying-out low-cost and simple-to-perform damage assessments of cracked concrete bridge infrastructure. The key findings obtained regarding the proposed procedure are:

- **Crack-based input can be used to estimate shear capacity utilization and residual shear capacity (%).** In the case of Category 1 data that involved diagonally-cracked RC members constructed with shear reinforcement (92 total data points), the crack-based continuum shear strength assessment procedure was able to estimate the residual capacity of these members within 8 % on average (e.g., 60 % ± 8 %), with an absolute maximum error of 30 % (i.e., for a single case), and a coefficient of variation of 19 %. Obtaining meaningful estimates regarding likely member shear strength can be used to assist, or supplement, inspector judgement when evaluating RC infrastructure with visual-observed diagonal cracking.
- **Crack-based input can be used to estimate failure or "critical" crack widths.** The procedure developed permits the development of residual capacity-diagonal crack width relationships that can be used as member-specific field aids or for member-specific decision making. Thus, employing this tool, it is possible to pre-define "critical" diagonal crack widths that may serve as likely indicators of severe member distress. For example, the critical crack width could be defined as the crack width corresponding to 25 % residual capacity. In this way, crack width growth can be monitored in a more rational manner.
- **Additional input (e.g., geometry, reinforcement details, etc.) referenced from design documents and known design values is suitable.** All input can be easily defined from design drawings, and estimated material properties without the need for supplemental material testing or complicated calibration procedures.

Despite the successes shown in the results presented in Section 4.2, there are also limitations which should be taken under advisement when using the cracked continuum shear strength assessment procedure. These limitations are as follows:

- **Evaluation and refinement of the procedure continues to be based on available crack data.** The crack input that has been used to date in the development of this procedure has been, to some degree, limited by the types of crack measurements taken and reported within the literature. While the typical crack data reporting is useful and did permit procedure development, it is not sufficient for determining the optimal crack characteristics for use in the continuum procedure. For example, crack widths are frequently reported as a maximum width per span with little attention paid in reporting which crack, or where along the length of the crack, the measurement was taken.

- **Long-term effects have been neglected.** Additional factors influencing real-world bridge infrastructure (i.e., those not born in a laboratory) have not been accounted for in the present formulation, which may, or may not, influence the performance of the cracked continuum procedure. The incorporation of time-dependent effects (e.g., creep and shrinkage) is envisioned to be a relatively simple modification to the current cracked continuum analysis procedure; however, there is little data available to assist in evaluating suitability and performance of such modifications.
- **Analyses performed on beams without shear reinforcement were found to typically exhibit large error.** In cases where damage assessment of a member without transverse reinforcement is required, this procedure does not serve as an adequate standalone method.

6.2.4. Crack Pattern Quantification Using Fractal Analysis

Fractal and multifractal analyses are powerful numerical procedures for the quantification of two-dimensional crack patterns. Listed are some of the major successes identified from the development and application of these approaches:

- **Fractal approaches do not require significant computational resources.** As a result, the algorithm can be executed even on handheld devices like smartphones or into single-board computers (i.e., Raspberry PI, etc.).
- **The approaches are capable of capturing minor crack pattern changes.** Fractal analysis procedures show the potential for image-based structural assessment, potentially reducing the need for frequent and costly human interaction. In other words, fractal and multifractal analyses can serve as a tool to partially-automate the inspection process and to compare and contrast data from images obtained from bridge infrastructure over time.
- Combining *data interpretation methods* like fractal and multifractal analyses, with an automated crack detection system will enable automated inspection procedures, will permit the documentation of cracking evolution over time, and will facilitate improved estimations regarding the remaining strength and performance of cracked structural elements.

Although fractal and multifractal analyses are tools which enable the explicit quantification of crack patterns, building the appropriate models requires an extensive series of well-documented experimental results. In this context, well-documented experimental results are defined as those which include load-displacement histories accompanied by high resolution images of the crack patterns, for multiple load stages over the course of testing. Until only recently, researchers have generally not acquired and documented high-resolution images of the crack pattern evolution during structural testing. That made the interpretation of fractal and multifractal results challenging. Obtaining more images from large-scale tests of RC elements will permit further development of the crack quantification model.

6.3. Concluding Remarks

In this research project, a comprehensive literature review was completed on the state of the art in damage-based structural assessment and existing experimental crack measurement data, which led to the assembly of the Visual Crack Measurement Evaluation Database. This preliminary work informed the development and refinement of two procedures: cracked continuum shear strength assessment and crack pattern quantification using fractal analysis. Using the current body of experimental data, the procedures were validated and recommendations for their use were made. These tools have the potential to enhance the traditional inspection procedure by way of providing quantitative insight about structural health based on visually observed cracking.

References

AASHTO. (2005). *Guide manual for condition evaluation and LRFR of highway bridges: 2005 interim revisions*.

AASHTO. (2010). *AASHTO bridge element inspection guide manual* (1st ed.).

AASHTO. (2016). *AASHTO LRFD bridge design specifications, customary U.S. units*. *AASHTO load and resistance factor design bridge design specifications*.

Acevedo, A. B., Bentz, E. C., & Collins, M. P. (2009). Influence of clamping stresses in the shear strength of concrete slabs under uniform loads. In *Journal of Earthquake Engineering* (Vol. 13, pp. 1–17). https://doi.org/10.1080/13632460902813190

Aguilar, G. (2011). *Effect of High-Strength Concrete on Web Reinforcement Requirements for Reinforced Concrete Bridge Girders For*. https://doi.org/UMI 3402307

Alembagheri, M., & Ghaemian, M. (2013). Damage assessment of a concrete arch dam through nonlinear incremental dynamic analysis. *Soil Dynamics and Earthquake Engineering*, *44*, 127–137. https://doi.org/10.1016/j.soildyn.2012.09.010

Bažant, Z. P., & Oh, B. H. (1983). Spacing of cracks in reinforced concrete. *Journal of Structural Engineering*, *109*(9), 2066–2085. https://doi.org/10.1061/(ASCE)0733-9445(1983)109:9(2066)

Bažant, Z. P., & Xu, K. (1991). Size Effect in Fatigue Fracture of Concrete. *ACI Materials Journal*, *88*(4), 390–399.

Bentz, E. C., Vecchio, F. J., & Collins, M. P. (2006). Simplified Compression Field Theory for Calculating Shear Strength of Reinforced Concrete Elements. *ACI Structural Journal*, *103*(S65), 614–624. https://doi.org/10.14359/16438

Birrcher, D., Tuchscherer, R., Huizinga, M., Bayrak, O., Wood, S. L., & Jirsa, J. O. Strength and Serviceability Design of Reinforced Concrete Deep Beams (2009). https://doi.org/10.1017/CBO9781107415324.004

Bracci, J. M., Keating, P. B., & Hueste, M. B. D. Cracking in RC Bent Caps (2001). Texas Transportation Institute, College Station, Tex: FHWA/TX-01/1851-1. Retrieved from https://library.ctr.utexas.edu/

Bridge Engineering Section Oregon Department of Transportation. (2009). *Bridge inspection pocket coding guide*. Retrieved from ftp://ftp.odot.state.or.us/Bridge/Coding_Guide_Chittrat/2009_Coding_Guide/ODOT_CodingGuide2009_BridgeWeb.pdf

Calvi, P. M., Bentz, E. C., & Collins, M. P. (2018). Model for assessment of cracked reinforced concrete membrane elements subjected to shear and axial loads. *ACI Structural Journal*, *115*(2), 501–509. https://doi.org/10.14359/51701093

Cambridge. (2018). Cambridge Online Dictionary. Retrieved from https://dictionary.cambridge.org/

Campana, S., Fernández Ruiz, M., Anastasi, A., & Muttoni, A. (2013). Analysis of shear-transfer actions on one-way RC members based on measured cracking pattern and failure kinematics. *Magazine of Concrete Research*, *65*(6), 386–404. https://doi.org/10.1680/macr.12.00142

Cao, M., Ren, Q., & Qiao, P. (2006). Nondestructive Assessment of Reinforced Concrete Structures Based on Fractal Damage Characteristic Factors. *Journal of Engineering Mechanics*, *132*(9), 924–931. https://doi.org/10.1061/(ASCE)0733-9399(2006)132:9(924)

Carpinteri, A. (1984). Stability of Fracturing Process in RC Beams. *Journal of Structural Engineering, ASCE*, *110*(3), 544–558.

Carrillo, J., Dominguez, D., & Prado, N. (2017). Seismic damage index based on fractal dimension of cracking on thin reinforced concrete walls. *ACI Structural Journal*, *114*(6), 1649–1658. https://doi.org/10.14359/51700919

Cavagnis, F., Fernández Ruiz, M., & Muttoni, A. (2018). An analysis of the shear-transfer actions in reinforced concrete members without transverse reinforcement based on refined experimental measurements. *Structural Concrete*, *19*(1), 49–64. https://doi.org/10.1002/suco.201700145

CEB-FIP. (1978). *Model Code for Concrete Structures* (3rd ed.). Comite Euro-International du Beton.

CEB-FIP. (1990). *Model Code for Concrete Structures*. Comite Euro-International du Beton.

Červenka, V., & Červenka, J. (2015). *ATENA Program Documentation Part 2-2: User's Manual for ATENA 3D*. Prague, Czech Republic: Červenka Consulting.

Chhabra, A., & Jensen, R. (1989). Direct determination of the f(α) singularity spectrum. *Physical Review Letters*, *62*(12), 1327–1330. https://doi.org/10.1103/PhysRevLett.62.1327

Chowdhury, S. H., & Loo, Y. C. (2001). A New Formula for Prediction of Crack Widths in Reinforced and Partially Prestressed Concrete Beams. *Advances in Structural Engineering*, *4*(2), 101–110. https://doi.org/10.1260/1369433011502390

Clauset, A., Shalizi, C. R., & Newman, M. E. J. (2009). Power-Law Distributions in Empirical Data. *SIAM Review*, *51*(4), 661–703. https://doi.org/10.1137/070710111

Collins, M. P., Mitchell, D., Adebar, P., & Vecchio, F. J. (1996). A general shear design method. *ACI Structural Journal*. https://doi.org/10.14359/9838 de Borst, R., Crisfield, M. A., Remmers, J. J. C., & Verhoosel, C. V. (2012). *Nonlinear Finite Element Analysis of Solids and Structures* (2nd ed.). Chichester: John Wiley & Sons.

de Borst, R., Remmers, J. J. C., Needleman, A., & Abellan, M.-A. (2004). Discrete vs smeared crack models for concrete fracture: bridging the gap. *International Journal for Numerical and Analytical Methods in Geomechanics*, *28*(7–8), 583–607. https://doi.org/10.1002/nag.374

De Silva, S., Mutsuyoshi, H., & Witchukreangkrai, E. (2008). Evaluation of Shear Crack Width in I-Shaped Prestressed Reinforced Concrete Beams. *Journal of Advanced Concrete Technology*, *6*(3), 443–458. https://doi.org/10.3151/jact.6.443

Deluce, J. R., Seong-Cheol, L., & Vecchio, F. J. (2014). Crack model for steel fiber-reinforced concrete members containing conventional reinforcement. *ACI Structural Journal*, *111*(1), 93–102. https://doi.org/10.14359/51686433

Ebrahimkhanlou, A., Farhidzadeh, A., & Salamone, S. (2016). Multifractal analysis of crack patterns in reinforced concrete shear walls. *Structural Health Monitoring*, *15*(1), 81–92.

European Committee for Standardization. (1991). *Eurocode 2: Design of concrete structures - Part 1: General rules and rules for buildings*.

European Committee for Standardization. (2004). *Eurocode 2: Design of concrete structures - Part 1-1: General rules and rules for buildings*.

Falconer, K. J. (2014). *Fractal geometry : mathematical foundations and applications* (3rd ed.). Chichester: John Wiley & Sons.

Farhidzadeh, A., Dehghan-Niri, E., Moustafa, A., Salamone, S., & Whittaker, A. (2013). Damage Assessment of Reinforced Concrete Structures Using Fractal Analysis of Residual Crack Patterns. *Experimental Mechanics*, *53*(9), 1607–1619. https://doi.org/10.1007/s11340-013-9769-7

FHWA. (1995). *Recording and Coding Guide for the Structure Inventory and Appraisal of the Nation's Bridges*. Report No. FHWA-PD-96-001.

Gergely, P., & Lutz, L. A. (1968). Maximum crack width in reinforced concrete flexural members. *Causes, Mechanism, and Control of Cracking in Concrete, SP.20,* (6), 87–117. https://doi.org/10.14359/17348

Goodfellow, I., Bengio, Y., & Courville, A. (2015). *Deep Learning*. *Scholarpedia* (Vol. 10). https://doi.org/10.4249/scholarpedia.32832

Gulkan, P., & Yakut, A. (1996). An Expert System for Reinforced Concrete Structural Damage Quantification. *Special Publication*, *162,* 53–72.

Harte, D. (2001). *Multifractals : theory and applications*. Chapman & Hall/CRC.

Hillerborg, A., Modéer, M., & Petersson, P. E. (1976). Analysis of crack formation and crack growth in concrete by means of fracture mechanics and finite elements. *Cement and Concrete Research*, *6*, 773–782.

IAEA. (2002). *Guidebook on non-destructive testing of concrete structures*. Vienna, Austria.

International Federation for Structural Concrete. (2012). *Bulletin No. 65: fib Model Code*. Lausanne, Switzerland.

Kabir, S., Rivard, P., He, D.-C., & Thivierge, P. (2009). Damage assessment for concrete structure using image processing techniques on acoustic borehole imagery. *Construction and Building Materials*, *23*(10), 3166–3174.

Katz, A., Yousefpour, H., Kim, H. su, Abyaneh, R. A., Salazar, J., Hrynyk, T., & Bayrak, O. (2017). Shear Performance of Pretensioned Concrete I-Girders Employing 0.7 in. (17.8 mm) Strands. *ACI Structural Journal*, *114*(5), 1273–1284. https://doi.org/10.14359/51689789

Kong, P. Y. L., & Rangan, B. V. (1998). Shear Strength of High-Performance Concrete Beams. *ACI Structural Journal*, *95*(6), 677–688. https://doi.org/10.14359/581

Kono, S., Bechtoula, H., Sakashita, M., Tanaka, H., Watanabe, F., & Eberhard, M. O. (2006). Damage Assessment of Reinforced Concrete Columns Under High Axial Loading. *ACI Special Publication*, *237*(11), 165–176. https://doi.org/10.14359/18252

Lantsoght, E. O. L., van der Veen, C., Walraven, J. C., & Boer, A. de. (2016). Case Study on Aggregate Interlock Capacity for the Shear Assessment of Cracked Reinforced-Concrete Bridge Cross Sections. *Journal of Bridge Engineering*, *21*(5), 10. https://doi.org/10.1061/(ASCE)BE.1943-5592.0000847

Larson, N., Gomez, E. F., Garber, D., Bayrak, O., & Ghannoum, W. M. (2013). *Strength and Serviceability Design of Reinforced Concrete Inverted-T Beams* (Vol. 7). https://doi.org/10.1017/CBO9781107415324.004

Lee, J.-Y., Kim, S.-W., & Mansour, M. Y. (2011). Nonlinear Analysis of Shear-Critical Reinforced Concrete Beams Using Fixed Angle Theory. *Journal of Structural Engineering*, *137*(10), 1017–1029. https://doi.org/10.1061/(ASCE)ST.1943-541X.0000345

Lee, J. Y., Lee, D. H., Lee, J. E., & Choi, S. H. (2015). Shear behavior and diagonal crack width for reinforced concrete beams with high-strength shear reinforcement. *ACI Structural Journal*, *112*(3), 323–333. https://doi.org/10.14359/51687422

Li, B., & Maekawa, K. (1987). Contact density model for cracks in concrete. *IABSE Reports = Rapports AIPC = IVBH Berichte*, *54*, 51–62.

Li, B., Nair, A., & Kai, Q. (2012). Residual Axial Capacity of Reinforced Concrete Columns with Simulated Blast Damage. *Journal of Performance of Constructed Facilities*, *26*(3), 287–299. https://doi.org/10.1061/(ASCE)CF.1943-5509.0000210

Lopes, R., & Betrouni, N. (2009). Fractal and multifractal analysis: A review.

Medical Image Analysis, *13*(4), 634–649. https://doi.org/10.1016/j.media.2009.05.003

Maekawa, K., Pimanmas, A., & Okamura, H. (2003). *Nonlinear Mechanics of Reinforced Concrete*. Spon Press.

Mau, S. T., & Hsu, T. T. C. (1987). Shear Strength Prediction for Deep Beams With Web Reinforcement. *ACI Structural Journal*, *84*(6), 513–523. https://doi.org/10.14359/2739

Melchor-Lucero, O., & Ferregut, C. (1996). Earthquake damage assessment of reinforced concrete members using an expert system. In *Eleventh World Conference on Earthquake Engineering*. Acapulco, Mexico.

Michigan Department of Transportation. (2011). *MDOT BSIR rating guides*.

Moler, C. B. (2005). Numerical computing with MATLAB. *Choice Reviews Online*, *42*(06), 42-3475-42–3475. https://doi.org/10.5860/CHOICE.42-3475

Montana Department of Transportation. (2015). *Bridge inspection and rating manual*.

Moore, M., Phares, B., Graybeal, B., Rolander, D., & Washer, G. (2001). *Reliability of Visual Inspection for Highway Bridges*. *FHWA* (Vol. II). Retrieved from http://www.tfhrc.gov/hnr20/nde/01020.htm

NEN Committee 351001. (1995). *Technishe Grondslagen voor Bouwvoorschriften, Voorschriften Beton TGB 1990-Constructieve Eisen en Rekenmethoden (VBC 1995)*. NEN 6720:1995, Dutch Normalization Institute, Delft, the Netherlands.

Oh, B. H., & Kang, Y. J. (1987). New Formulas for Maximum Crack Width and Crack Spacing in Reinforced Concrete Flexural Members. *ACI Structural Journal*, *84*(2), 103–112. https://doi.org/10.14359/11681

Ohio Department of Transportation. (2014). *Manual of bridge inspection*.

Oregon Department of Transportation. (2009). *2009 bridge inspection pocket coding guide*.

Paal, S. G., Jeon, J.-S., Brilakis, I., & DesRoches, R. (2015). Automated Damage Index Estimation of Reinforced Concrete Columns for Post-Earthquake Evaluations. *Journal of Structural Engineering*, *141*(9), 04014228. https://doi.org/10.1061/(ASCE)ST.1943-541X.0001200

Pachepsky, Y. (Yakov), Radcliffe, D. E., & Selim, H. M. (Hussein M. (2003). *Scaling methods in soil physics*. *books.google.com*. CRC Press.

Pang, X. (1991). *Constitutive laws of reinforced concrete in shear*. University of Houston, Dept. of Civil & Environmental Engineering.

Park, S., Stubbs, N., Bolton, R., Choi, S., & Sikorsky, C. (2001). Field verification of the damage index method in a concrete box-girder bridge via visual inspection. *Computer-Aided Civil and Infrastructure Engineering*, *16*, 58–70. https://doi.org/10.1111/0885-9507.00213

Pennsylvania Department of Transportation. (2009). *PENNDOT publication #100A*.

Rényi, A. (1961). On measures of information and entropy. In *Proc. of Berkeley Symposium on Mathematics, Statistics and Probability* (Vol. 547, pp. 547–561). Berkeley: University of California Press.

Ruggiero, D. M., Bentz, E. C., Calvi, G. M., & Collins, M. P. (2016). Shear Response under Reversed Cyclic Loading. *ACI Structural Journal*, *113*(6), 1313–1324. https://doi.org/10.14359/51689033

Sain, T., & Kishen, J. M. C. (2007). Prediction of Fatigue Strength in Plain and Reinforced Concrete Beams. *ACI Structural Journal*, *104*(5), 621–628.

Salazar, J. L., Yousefpour, H., Abyaneh, R. A., Kim, H. su, Katz, A. T., Hrynyk, T. D., & Bayrak, O. (2018). End-Region Behavior of Pretensioned I-Girders Employing 0.7 in. (17.8 mm) Strands. *ACI Structural Journal*, *115*(1), 91–102. https://doi.org/10.14359/51700783

Scanlon, A. (1971, December). *Time dependent deflections of reinforced concrete slabs*. University of Alberta.

Schlaich, J., Schafer, K., & Jennewein, M. (1987). Toward a Consistent Design of Structural Concrete. *PCI Journal*, *32*(3), 74–150. https://doi.org/10.15554/pcij.05011987.74.150

Seuront, L. (2010). *Fractals and multifractals in ecology and aquatic science*. CRC Press/Taylor & Francis.

Shdid, C., Ansley, M., & Hamilton III, H. (2006). Visual Rating and Strength Testing of 40-Year-Old Precast Prestressed Concrete Bridge Piling. *Transportation Research Record: Journal of the Transportation Research Board*, *1975*, 3–9.

Sherwood, E. G. (2008). *One-Way Shear Behaviour of Large , Lightly-Reinforced Concrete Beams and Slabs By : A thesis submitted in conformity with the requirements for the degree of Doctor of Philosophy Department of Civil Engineering University of Toronto*. University of Toronto.

Slowik, V., Plizzari, G. A., & Saouma, V. E. (1996). Fracture of Concrete under Variable Amplitude Fatigue Loading. *ACI Materials Journal*, *93*(3), 272–283.

Stevens, N., Uzumeri, S., & Collins, M. (1991). Reinforced concrete subjected to reversed cyclic shear--Experiments and constitutive model. *ACI Structural Journal*, *88*(February), 135–146. https://doi.org/10.14359/2880

Susetyo, J. Fibre Reinforcement for Shrinkage Crack Control in Prestressed, Precast Segmental Bridges (2009). Retrieved from https://tspace.library.utoronto.ca/handle/1807/19096

Talley, K. G., Asce, M., Arrellaga, J., Breen, J. E., & Asce, D. M. (2014). Computational Modeling of Existing Damage in Concrete Bridge Columns, *140*(12), 1–6. https://doi.org/10.1061/(ASCE)ST.1943-541X.0001115.

Texas Department of Transportation. (2013). *Bridge inspection manual*.

TxDOT. (2013). Bridge Inspection Manual. *Texas Department of Transportation*, *1*(5), 147. https://doi.org/10.1093/jmp/jht061

TxDOT. (2015). Bridge Design Manual - LRFD, (October).

Uzel, A. (2003). *Shear design of large footings*. University of Toronto.

Vamvatsikos, D., & Cornell, C. A. (2002). Incremental dynamic analysis. *Earthquake Engineering & Structural Dynamics*, *31*(3), 491–514. https://doi.org/10.1002/eqe.141

Vecchio, F. J. (2000). Disturbed stress field model for reinforced concrete: formulation. *Journal of Structural Engineering*, *126*(9), 1070–1077. https://doi.org/10.1061/(ASCE)0733-9445(2000)126:9(1070)

Vecchio, F. J. (2001). Non-linear finite element analysis of reinforced concrete: at the crossroads? *Structural Concrete*, *2*(4), 201–212.

Vecchio, F. J., & Collins, M. P. (1986). The modified compression-field theory for reinforced concrete elements subjected to shear. *ACI Journal Proceedings*, *83*(2), 219–231. https://doi.org/10.14359/10416

Veletzos, M., Panagiutou, M., Restrepo, J., & Sahs, S. (2008). *Visual inspection & capacity assessment of earthquake damaged reinforced concrete bridge elements*. Sacramento CA: California Dept. of Transportation Division of Research and Innovation.

Walraven, J. C. (1980). *Aggregate Interlock: a Theoretical and Experimental Analysis*. Delft University.

Walraven, J. C. (1981a). Aggregate interlock. *Cement*, *33*(6), 406–412.

Walraven, J. C. (1981b). Fundamental analysis of aggregate interlock. *Journal of the Structural Division*, *107*(11), 2245–2270.

Wang, J., Shi, Z., & Nakano, M. (2013). Strength degradation analysis of an aging RC girder bridge using FE crack analysis and simple capacity-evaluation equations. *Engineering Fracture Mechanics*, *108*, 209–221. https://doi.org/10.1016/j.engfracmech.2013.04.011

Wikipedia contributors. (2018). RGB color model. Retrieved March 30, 2018, from https://en.wikipedia.org/w/index.php?title=RGB_color_model&oldid=829576033

Wong, P. S., Vecchio, F. J., & Trommels, H. (2013). VecTor2 & FormWorks User’s Manual. *New York*. Toronto, Ontario, Canada: University of Toronto.

Xiang, Y., Xu, J., & Wu, Q. (2012). Crack width calculation methods of reinforced concrete bridges and application of box girder bridge. *Journal of High and Transportation Research and Development*, *6*(3), 39–43.

Yoon, Y. S., Cook, W. D., & Mitchell, D. (1996). Minimum Shear Reinforcement in Normal and High Strength Concrete Beams. *ACI Structural Journal*, *93*(93), 576–584.

Yousefpour, H., Kim, H. su, Bonetti, R., Abyaneh, R. A., Katz, A., Longshaw, A., … Bayrak, O. (2017). End-Region Behavior and Shear Strength of Pretensioned Concrete Girders Employing 0.7-in. Diameter Strands. Austin, TX: FHWA/TX-17/0-6831-1. Retrieved from https://library.ctr.utexas.edu/

Zhu, R. R. H., Wanichakorn, W., Hsu, T. T. C., & Vogel, J. (2003). Crack width prediction using compatibility-aided strut-and-tie model. *ACI Structural Journal*, *100*(4), 413–421.

Appendix A. The Visual Crack Measurement Database

Category 1

	Member		Geometric Properties							Reinforcement Details												Material Properties						Force Data	
	Source	Name	Shape	b_w (in)	h (in)	d (in)	a/d ratio	c_c (in) [side]	c_c (in) [top/bot]	ρ_s	ρ'_s	ρ_v	ρ_h	n_s	n'_s	n_v	n_h (E.F.)	d_{bl} (in)	d_{bl}' (in))	d_{bv} (in)	d_{bh} (in)	f'_c (psi)	d_a (in)	f_y (ksi)	f'_y (ksi)	f_{yv} (ksi)	f_{yh} (ksi)	V_{crack} (k)	V_{test} (k)
1	0-1851-1	1A	Rectangular	33.0	36.0	32.9	1.64	2	2	0.579%	0.579%	0.297%	0.095%	8	8	2	2	1	1	0.625	0.625	6217	1	60.0	60.0	60.0	60.0	-	190
2	0-1851-1	1B	Rectangular	33.0	36.0	32.9	1.64	2	2	0.579%	0.579%	0.297%	0.095%	8	8	2	2	1	1	0.625	0.625	5820	1	60.0	60.0	60.0	60.0	-	213
3	0-1851-1	2A	Rectangular	33.0	36.0	32.9	1.64	2	2	0.579%	0.579%	0.297%	0.108%	8	8	2	3	1	1	0.625	0.5	6217	1	60.0	60.0	60.0	60.0	-	200
4	0-1851-1	2B	Rectangular	33.0	36.0	32.9	1.64	2	2	0.579%	0.579%	0.297%	0.108%	8	8	2	3	1	1	0.625	0.5	5820	1	60.0	60.0	60.0	60.0	-	195
5	0-1851-1	3C	Rectangular	33.0	36.0	32.9	1.64	2	2	0.609%	0.578%	0.297%	0.108%	11	8	2	3	0.88	1	0.625	0.5	6035	1	60.0	60.0	60.0	60.0	-	210
6	0-1851-1	3D	Rectangular	33.0	36.0	32.9	1.64	2	2	0.609%	0.578%	0.297%	0.108%	11	8	2	3	0.88	1	0.625	0.5	5508	1	60.0	60.0	60.0	60.0	-	225
7	0-1851-1	4C	Rectangular	33.0	36.0	32.7	1.65	2	2	0.821%	0.582%	0.297%	0.108%	7	8	2	3	1.27	1	0.625	0.5	6035	1	60.0	60.0	60.0	60.0	-	220
8	0-1851-1	4E	Rectangular	33.0	36.0	32.7	1.65	2	2	0.821%	0.582%	0.297%	0.108%	7	8	2	3	1.27	1.00	0.63	0.50	7722	1	60.0	60.0	60.0	60.0	-	230
9	0-1851-1	5D	Rectangular	33.0	36.0	32.9	1.64	2	2	0.796%	0.579%	0.297%	0.108%	11	8	2	3	1.00	1.00	0.63	0.50	5508	1	60.0	60.0	60.0	60.0	-	235
10	0-1851-1	5E	Rectangular	33.0	36.0	32.9	1.64	2	2	0.796%	0.579%	0.297%	0.108%	11	8	2	3	1.00	1.00	0.63	0.50	7722	1	60.0	60.0	60.0	60.0	-	240
11	0-1851-1	6F	Rectangular	33.0	36.0	32.7	1.65	2	2	0.586%	0.582%	0.595%	0.108%	5	8	4	3	1.27	1.00	0.63	0.50	5460	1	60.0	60.0	60.0	60.0	-	213
12	0-1851-1	6G	Rectangular	33.0	36.0	32.7	1.65	2	2	0.586%	0.582%	0.595%	0.108%	5	8	4	3	1.27	1.00	0.63	0.50	5320	1	60.0	60.0	60.0	60.0	-	190
13	0-1851-1	7F	Rectangular	33.0	36.0	32.9	1.64	2	2	0.796%	0.579%	0.595%	0.108%	11	8	4	3	1.00	1.00	0.63	0.50	5460	1	60.0	60.0	60.0	60.0	-	250
14	0-1851-1	7H	Rectangular	33.0	36.0	32.9	1.64	2	2	0.796%	0.579%	0.595%	0.108%	11	8	4	3	1.00	1.00	0.63	0.50	5727	1	60.0	60.0	60.0	60.0	-	240
15	0-1851-1	8G	Rectangular	33.0	36.0	32.9	1.64	2	2	0.579%	0.579%	0.595%	0.108%	8	8	4	3	1.00	1.00	0.63	0.50	5320	1	60.0	60.0	60.0	60.0	-	220
16	0-1851-1	8H	Rectangular	33.0	36.0	32.9	1.64	2	2	0.579%	0.579%	0.595%	0.108%	8	8	4	3	1.00	1.00	0.63	0.50	5727	1	60.0	60.0	60.0	60.0	-	238
17	0-5253-1	I-03-2	Rectangular	21.0	44.0	38.5	1.84	0.75	1	2.290%	1.160%	0.290%	0.163%	42	6	2	5	0.75	1.41	0.50	0.50	5240	0.75	73.0	73.0	67.0	67.0	144	569
18	0-5253-1	I-03-4	Rectangular	21.0	44.0	38.5	1.84	0.75	1	2.290%	1.160%	0.300%	0.163%	42	6	4	5	0.75	1.41	0.38	0.50	5330	0.75	73.0	73.0	73.0	67.0	-	657
19	0-5253-1	I-02-2	Rectangular	21.0	44.0	38.5	1.84	0.75	1	2.290%	1.160%	0.200%	0.098%	42	6	2	5	0.75	1.41	0.50	0.50	3950	0.75	73.0	73.0	67.0	67.0	121	454
20	0-5253-1	I-02-4	Rectangular	21.0	44.0	38.5	1.84	0.75	1	2.290%	1.160%	0.210%	0.098%	42	6	4	5	0.75	1.41	0.38	0.50	4160	0.75	73.0	73.0	73.0	67.0	-	528
21	0-5253-1	II-03-CCC2021	Rectangular	21.0	42.0	38.6	1.84	0.75	1	2.310%	1.150%	0.310%	0.450%	12	6	2	4	1.41	1.41	0.63	0.63	3290	0.75	64.0	64.0	65.0	65.0	139	500
22	0-5253-1	II-03-CCC1007	Rectangular	21.0	42.0	38.6	1.84	0.75	1	2.310%	1.150%	0.310%	0.450%	12	6	2	4	1.41	1.41	0.63	0.63	3480	0.75	64.0	64.0	65.0	65.0	-	478
23	0-5253-1	II-02-CCC1007	Rectangular	21.0	42.0	38.6	1.84	0.75	1	2.310%	1.150%	0.200%	0.190%	12	6	2	4	1.41	1.41	0.63	0.50	3140	0.75	69.0	69.0	64.0	63.0	-	335
24	0-5253-1	II-02-CCC1021	Rectangular	21.0	42.0	38.6	1.84	0.75	1	2.310%	1.150%	0.200%	0.190%	12	6	2	4	1.41	1.41	0.63	0.50	4620	0.75	69.0	69.0	67.0	62.0	132	329
25	0-5253-1	II-03-CCT1021	Rectangular	21.0	42.0	38.6	1.84	0.75	1	2.310%	1.150%	0.310%	0.450%	12	6	2	4	1.41	1.41	0.63	0.63	4410	0.75	66.0	66.0	71.0	71.0	-	636
26	0-5253-1	II-03-CCT0507	Rectangular	21.0	42.0	38.6	1.84	0.75	1	2.310%	1.150%	0.310%	0.450%	12	6	2	4	1.41	1.41	0.63	0.63	4210	0.75	66.0	66.0	71.0	71.0	146	598
27	0-5253-1	II-02-CCT0507	Rectangular	21.0	42.0	38.6	1.84	0.75	1	2.310%	1.150%	0.200%	0.190%	12	6	2	4	1.41	1.41	0.63	0.50	3120	0.75	69.0	69.0	64.0	63.0	94	401
28	0-5253-1	II-02-CCT0521	Rectangular	21.0	42.0	38.6	1.84	0.75	1	2.310%	1.150%	0.200%	0.190%	12	6	2	4	1.41	1.41	0.63	0.50	4740	0.75	69.0	69.0	67.0	62.0	-	568

	Member		Geometric Properties							Reinforcement Details												Material Properties						Force Data	
	Source	Name	Shape	b_w (in)	h (in)	d (in)	a/d ratio	c_c (in) [side]	c_c (in) [top/bot]	ρ_s	ρ'_s	ρ_v	ρ_h	n_s	n'_s	n_v	n_h (E.F.)	d_{bl} (in)	d_{bl}' (in))	d_{bv} (in)	d_{bh} (in)	f'_c (psi)	d_a (in)	f_y (ksi)	f'_y (ksi)	f_{yv} (ksi)	f_{yh} (ksi)	V_{crack} (k)	V_{test} (k)
29	0-5253-1	III-1.85-00	Rectangular	21.0	42.0	38.6	1.84	0.75	1	2.310%	1.150%	-	-	12	6	-	4	1.41	1.41	-	-	3170	0.75	66.0	66.0	-	-	98	365
30	0-5253-1	III-2.5-00	Rectangular	21.0	42.0	38.6	2.47	0.75	1	2.310%	1.150%	-	-	12	6	-	4	1.41	1.41	-	-	3200	0.75	66.0	66.0	-	-	-	82
31	0-5253-1	III-1.85-02	Rectangular	21.0	42.0	38.6	1.84	0.75	1	2.310%	1.150%	0.200%	0.190%	12	6	2	4	1.41	1.41	0.63	0.50	4100	0.75	69.0	69.0	64.0	62.0	112	488
32	0-5253-1	III-1.85-025	Rectangular	21.0	42.0	38.6	1.84	0.75	1	2.310%	1.150%	0.240%	0.140%	12	6	2	4	1.41	1.41	0.63	0.38	4100	0.75	69.0	69.0	64.0	73.0	-	516
33	0-5253-1	III-1.85-03	Rectangular	21.0	42.0	38.6	1.84	0.75	1	2.310%	1.150%	0.290%	0.290%	12	6	2	4	1.41	1.41	0.63	0.63	4990	0.75	69.0	69.0	64.0	63.0	137	412
34	0-5253-1	III-1.85-01	Rectangular	21.0	42.0	38.6	1.84	0.75	1	2.310%	1.150%	0.100%	0.140%	12	6	2	4	1.41	1.41	0.50	0.38	5010	0.75	69.0	69.0	63.0	73.0	-	273
35	0-5253-1	III-1.85-03b	Rectangular	21.0	42.0	38.6	1.84	0.75	1	2.310%	1.150%	0.310%	0.290%	12	6	2	4	1.41	1.41	0.50	0.63	3300	0.75	69.0	69.0	62.0	67.0	114	471
36	0-5253-1	III-1.85-02b	Rectangular	21.0	42.0	38.6	1.84	0.75	1	2.310%	1.150%	0.200%	0.190%	12	6	2	4	1.41	1.41	0.50	0.50	3300	0.75	69.0	69.0	62.0	62.0	-	468
37	0-5253-1	III-1.2-02	Rectangular	21.0	42.0	38.6	1.20	0.75	1	2.310%	1.150%	0.200%	0.190%	12	6	2	4	1.41	1.41	0.50	0.50	4100	0.75	66.0	66.0	60.0	60.0	165	846
38	0-5253-1	III-1.2-03	Rectangular	21.0	42.0	38.6	1.20	0.75	1	2.310%	1.150%	0.310%	0.290%	12	6	2	4	1.41	1.41	0.63	0.63	4220	0.75	66.0	66.0	68.0	68.0	-	829
39	0-5253-1	III-2.5-02	Rectangular	21.0	42.0	38.6	2.49	0.75	1	2.310%	1.150%	0.200%	0.190%	12	6	2	4	1.41	1.41	0.50	0.50	4630	0.75	66.0	66.0	62.0	62.0	105	298
40	0-5253-1	III-2.5-03	Rectangular	21.0	42.0	38.6	2.49	0.75	1	2.310%	1.150%	0.310%	0.290%	12	6	2	4	1.41	1.41	0.63	0.63	5030	0.75	66.0	66.0	65.0	65.0	-	516
41	0-5253-1	IV-2175-1.85-02	Rectangular	21.0	75.0	68.9	1.85	0.75	1	2.370%	1.290%	0.210%	0.190%	22	12	2	6	1.41	1.41	0.50	0.50	4930	0.75	68.0	68.0	66.0	66.0	216	763
42	0-5253-1	IV-2175-1.85-03	Rectangular	21.0	75.0	68.9	1.85	0.75	1	2.370%	1.290%	0.310%	0.290%	22	12	2	6	1.41	1.41	0.63	0.63	4930	0.75	68.0	68.0	66.0	66.0	218	842
43	0-5253-1	IV-2175-2.5-02	Rectangular	21.0	75.0	68.9	2.5	0.75	1	2.370%	1.290%	0.210%	0.210%	22	12	2	6	1.41	1.41	0.63	0.63	5010	0.75	68.0	68.0	64.0	64.0	144	510
44	0-5253-1	IV-2175-1.2-02	Rectangular	21.0	75.0	68.9	1.2	0.75	1	2.370%	1.290%	0.210%	0.210%	22	12	2	6	1.41	1.41	0.63	0.63	5010	0.75	68.0	68.0	64.0	64.0	262	1223
45	0-5253-1	IV-2123-1.85-03	Rectangular	21.0	23.0	19.5	1.85	0.75	1	2.320%	1.160%	0.300%	0.300%	12	6	2	2	1.00	1.00	0.50	0.50	4160	0.75	66.0	66.0	66.0	66.0	60	329
46	0-5253-1	IV-2123-1.85-02	Rectangular	21.0	23.0	19.5	1.85	0.75	1	2.320%	1.160%	0.200%	0.170%	12	6	2	2	1.00	1.00	0.38	0.38	4220	0.75	66.0	66.0	81.0	81.0	65	347
47	0-5253-1	IV-2123-2.5-02	Rectangular	21.0	23.0	19.5	2.5	0.75	1	2.320%	1.160%	0.200%	0.170%	12	6	2	2	1.00	1.00	0.38	0.38	4570	0.75	65.0	65.0	58.0	64.0	51	161
48	0-5253-1	IV-2123-1.2-02	Rectangular	21.0	23.0	19.5	1.2	0.75	1	2.320%	1.160%	0.200%	0.170%	12	6	2	2	1.00	1.00	0.38	0.38	4630	0.75	65.0	65.0	58.0	64.0	124	592
49	0-5253-1	M-03-4-CCC2436	Rectangular	36.0	48.0	40.0	1.85	2.00	2	2.930%	0.430%	0.310%	0.270%	27	4	4	3	1.41	1.41	0.63	0.63	4100	0.75	67.0	67.0	61.0	61.0	354	1128
50	0-5253-1	M-03-4-CCC0812	Rectangular	36.0	48.0	40.0	1.85	2.00	2	2.930%	0.430%	0.310%	0.270%	27	4	4	3	1.41	1.41	0.63	0.63	3000	0.75	65.0	65.0	63.0	63.0	-	930
51	0-5253-1	M-02-4-CCC2436	Rectangular	36.0	48.0	40.0	1.85	2.00	2	2.930%	0.430%	0.218%	0.220%	27	4	4	3	1.41	1.41	0.50	0.63	2800	0.75	65.0	65.0	63.0	63.0	256	1102
52	0-6416-1	DC3-42-1.85-03	Inverted T	21.0	42.0	37.6	1.85	1.50	1.5	2.37%	1.187%	0.300%	0.300%	12	6	2	4	1.41	1.41	0.50	0.50	4568	0.75	63.6	63.6	63.2	63.2	152	395
53	0-6416-1	DS3-42-1.85-03	Inverted T	21.0	42.0	37.6	1.85	1.50	1.5	2.37%	1.187%	0.300%	0.300%	12	6	2	4	1.41	1.41	0.50	0.50	4568	0.75	63.6	63.6	63.2	63.2	164	454
54	0-6416-1	SC3-42-1.85-03	Inverted T	21.0	42.0	37.6	1.85	1.50	1.5	2.37%	1.187%	0.300%	0.300%	12	6	2	4	1.41	1.41	0.50	0.50	5873	0.75	66.2	66.2	64.3	64.3	90	483
55	0-6416-1	SS3-42-1.85-03	Inverted T	21.0	42.0	37.6	1.85	1.50	1.5	2.37%	1.187%	0.300%	0.300%	12	6	2	4	1.41	1.41	0.50	0.50	5891	0.75	68.6	68.6	67.3	67.3	126	523
56	0-6416-1	SL3-42-1.85-03	Inverted T	21.0	42.0	37.6	1.85	1.50	1.5	2.37%	1.187%	0.300%	0.300%	12	6	2	4	1.41	1.41	0.50	0.50	5037	0.75	75.2	75.2	65.6	65.6	172	571
57	0-6416-1	SS1-75-1.85-03	Inverted T	21.0	75.0	68.2	1.87	1.50	1.5	2.40%	1.308%	0.300%	0.300%	22	12	2	9	1.41	1.41	0.50	0.50	3127	0.75	66.1	66.1	65.1	65.1	346	745
58	0-6416-1	DS1-42-1.85-03	Inverted T	21.0	42.0	37.6	1.85	1.50	1.5	2.37%	1.187%	0.300%	0.300%	12	6	2	4	1.41	1.41	0.50	0.50	5258	0.75	69.2	69.2	63.1	63.1	172	712
59	0-6416-1	DS1-42-2.50-03	Inverted T	21.0	42.0	37.6	2.50	1.50	1.5	2.37%	1.187%	0.300%	0.300%	12	6	2	4	1.41	1.41	0.50	0.50	5389	0.75	69.2	69.2	63.1	63.1	-	406
60	0-6416-1	DS1-42-1.85-06	Inverted T	21.0	42.0	37.6	1.85	1.50	1.5	2.37%	1.187%	0.600%	0.600%	12	6	2	6	1.41	1.41	0.63	0.63	5024	0.75	64.1	64.1	60.7	60.7	188	621
61	0-6416-1	DS1-42-2.50-06	Inverted T	21.0	42.0	37.6	2.50	1.50	1.5	2.37%	1.187%	0.600%	0.600%	12	6	2	6	1.41	1.41	0.63	0.63	5088	0.75	64.1	64.1	60.7	60.7	-	503

	Member		Geometric Properties							Reinforcement Details												Material Properties						Force Data	
	Source	Name	Shape	b_w (in)	h (in)	d (in)	a/d ratio	c_c (in) [side]	c_c (in) [top/bot]	ρ_s	ρ'_s	ρ_v	ρ_h	n_s	n'_s	n_v	n_h (E.F.)	d_{bl} (in)	d_{bl}' (in))	d_{bv} (in)	d_{bh} (in)	f'_c (psi)	d_a (in)	f_y (ksi)	f'_y (ksi)	f_{yv} (ksi)	f_{yh} (ksi)	V_{crack} (k)	V_{test} (k)
62	0-6416-1	DL1-42-1.85-06	Inverted T	21.0	42.0	37.6	1.85	1.50	1.5	2.37%	1.187%	0.600%	0.600%	12	6	2	6	1.41	1.41	0.63	0.63	4830	0.75	67.9	67.9	64.7	64.7	168	741
63	0-6416-1	DL1-42-2.50-06	Inverted T	21.0	42.0	37.6	2.50	1.50	1.5	2.37%	1.187%	0.600%	0.600%	12	6	2	6	1.41	1.41	0.63	0.63	4986	0.75	67.9	67.9	64.7	64.7	-	622
64	0-6416-1	SS3-42-2.50-03	Inverted T	21.0	42.0	37.6	2.50	1.50	1.5	2.37%	1.187%	0.300%	0.300%	12	6	2	4	1.41	1.41	0.50	0.50	5891	0.75	69.0	69.0	67.0	67.0	140	447
65	0-6416-1	SC3-42-2.50-03	Inverted T	21.0	42.0	37.6	2.50	1.50	1.5	2.37%	1.187%	0.300%	0.300%	12	6	2	4	1.41	1.41	0.50	0.50	5873	0.75	66.2	66.2	64.3	64.3	113	329
66	0-6416-1	DS3-42-2.50-03	Inverted T	21.0	42.0	37.6	2.50	1.50	1.5	2.37%	1.187%	0.300%	0.300%	12	6	2	4	1.41	1.41	0.50	0.50	5687	0.75	63.6	63.6	64.6	64.6	143	430
67	0-6416-1	DL1-42-1.85-03	Inverted T	21.0	42.0	37.6	1.85	1.50	1.5	2.37%	1.187%	0.300%	0.300%	12	6	2	4	1.41	1.41	0.50	0.50	4929	0.75	71.0	71.0	64.4	64.4	242	626
68	0-6416-1	DL1-42-2.50-03	Inverted T	21.0	42.0	37.6	2.50	1.50	1.5	2.37%	1.187%	0.300%	0.300%	12	6	2	4	1.41	1.41	0.50	0.50	4929	0.75	71.0	71.0	64.4	64.4	-	510
69	0-6416-1	SL3-42-1.85-06	Inverted T	21.0	42.0	37.6	1.85	1.50	1.5	2.37%	1.187%	0.600%	0.600%	12	6	2	6	1.41	1.41	0.63	0.63	5250	0.75	70.4	70.4	65.0	65.0	154	744
70	0-6416-1	DC1-42-1.85-06	Inverted T	21.0	42.0	37.6	1.85	1.50	1.5	2.37%	1.187%	0.600%	0.600%	12	6	2	6	1.41	1.41	0.63	0.63	3727	0.75	64.0	64.0	63.0	63.0	107	519
71	0-6416-1	SS1-42-2.50-03	Inverted T	21.0	42.0	37.6	2.50	1.50	1.5	2.37%	1.187%	0.300%	0.300%	12	6	2	4	1.41	1.41	0.50	0.50	5703	0.75	65.4	65.4	66.6	66.6	157	398
72	0-6416-1	SS1-42-1.85-03	Inverted T	21.0	42.0	37.6	1.85	1.50	1.5	2.37%	1.187%	0.300%	0.300%	12	6	2	4	1.41	1.41	0.50	0.50	5721	0.75	65.4	65.4	66.6	66.6	-	583
73	0-6416-1	DC1-42-2.50-03	Inverted T	21.0	42.0	37.6	1.85	1.50	1.5	2.37%	1.187%	0.300%	0.300%	12	6	2	4	1.41	1.41	0.50	0.50	4035	0.75	70.1	70.1	62.4	62.4	70	365
74	0-6416-1	SL1-42-2.50-03	Inverted T	21.0	42.0	37.6	2.5	1.50	1.5	2.37%	1.187%	0.300%	0.300%	12	6	2	4	1.41	1.41	0.50	0.50	4281	0.75	69.0	69.0	64.0	64.0	167	498
75	0-6416-1	DS1-42-1.85-06/03	Inverted T	21.0	42.0	37.6	1.85	1.50	1.5	2.37%	1.187%	0.600%	0.300%	12	6	2	4	1.41	1.41	0.63	0.50	4173	0.75	66.0	66.0	65.0	65.0	-	739
76	0-6416-1	DS1-42-2.50-06/03	Inverted T	21.0	42.0	37.6	2.50	1.50	1.5	2.37%	1.187%	0.600%	0.300%	12	6	2	4	1.41	1.41	0.63	0.50	4173	0.75	66.0	66.0	65.0	65.0	115	539
77	0-6416-1	DC1-42-1.85-03	Inverted T	21.0	42.0	37.6	1.85	1.50	1.5	2.37%	1.187%	0.300%	0.300%	12	6	2	4	1.41	1.41	0.50	0.50	4303	0.75	66.0	66.0	67.0	67.0	127	517

Category 2

	Member		Geometric Properties							Reinforcement Details												Material Properties						Force Data	
	Source	Name	Shape	b_w (in)	h (in)	d (in)	a/d ratio	c_c (in) [side]	c_c (in) [top/bot]	ρ_s	ρ'_s	ρ_v	ρ_h	n_s	n'_s	n_v	n_h (E.F.)	d_{bl} (in)	d_{bl}' (in))	d_{bv} (in)	d_{bh} (in)	f'_c (psi)	d_a (in)	f_y (ksi)	f'_y (ksi)	f_{yv} (ksi)	f_{yh} (ksi)	V_{crack} (k)	V_{test} (k)
78	Aguilar (2011)	13.3-2.6-98	I-Girder	6.0	22.0	20.0	3.60	0.75	1.5	2.630%	5.270%	0.164%	-	4	8	2	-	1	1	0.25	-	13290	0.5	78.2	78.2	59.0	-	20	57.9
79	Aguilar (2011)	14.5-2.6-98	I-Girder	6.0	22.0	20.0	3.60	0.75	1.5	2.630%	5.270%	0.164%	-	4	8	2	-	1	1	0.25	-	14540	0.5	78.2	78.2	59.0	-	18	63.5
80	Aguilar (2011)	13.3-5.4-98	I-Girder	6.0	22.0	19.5	3.69	0.75	1.5	5.400%	2.700%	0.164%	-	8	4	2	-	1	1	0.25	-	13290	0.5	78.2	78.2	59.0	-	25	58.8
81	Aguilar (2011)	14.5-5.4-98	I-Girder	6.0	22.0	19.5	3.69	0.75	1.5	5.400%	2.700%	0.164%	-	8	4	2	-	1	1	0.25	-	14540	0.5	78.2	78.2	59.0	-	25	57.1
82	Aguilar (2011)	13.2-4.3-451	I-Girder	6.0	22.0	19.9	3.62	0.75	1.5	4.260%	7.710%	0.545%	-	4	2\6	2	-	1.27	1\1.27	0.5	-	13160	0.5	67.6	78.2\67.6	81.2	-	20	105.9
83	Aguilar (2011)	15.3-4.3-687	I-Girder	6.0	22.0	19.9	3.62	0.75	1.5	4.260%	7.710%	0.467%	-	4	2\6	2	-	1.27	1\1.27	0.5	-	15520	0.5	67.6	78.2\67.6	81.2	-	20	101.7
84	Aguilar (2011)	13.2-7.9-902	I-Girder	6.0	22.0	19.4	3.72	0.75	1.5	7.920%	4.370%	1.091%	-	2\6	4	2	-	1\1.27	1.27	0.5	-	13160	0.5	78.2\67.6	67.6	81.2	-	20	163.1
85	Aguilar (2011)	15.3-7.9-902	I-Girder	6.0	22.0	19.4	3.72	0.75	1.5	7.920%	4.370%	1.091%	-	2\6	4	2	-	1\1.27	1.27	0.5	-	15250	0.5	78.2\67.6	67.6	81.2	-	25	166.6
86	De Silva et al. (2008)	IRC-1	I-Girder	5.9	19.7	17.7	3.00	0.98	0.98	1.130%	0.860%	0.338%	-	4	4	2	-	1	0.87	0.236	-	5845	0.79	104.0	57.6	63.5	-	14.2	45
87	De Silva et al. (2008)	IRC-2	I-Girder	5.9	19.7	17.7	3.00	2.71	0.98	1.130%	0.860%	0.338%	-	4	4	2	-	1	0.87	0.236	-	6584	0.79	104.0	57.6	63.5	-	24.4	45.1
88	De Silva et al. (2008)	IRC-3	I-Girder	5.9	19.7	17.7	3.00	0.98	0.98	1.130%	0.860%	0.338%	-	4	4	2	-	1	0.87	0.236	-	6381	0.79	104.0	57.6	63.5	-	15	44.8
89	Pang (1991)	A1	Panel	7.0	55.0	-	-	-	-	-	-	0.596%	0.596%	-	-	-	-	-	-	0.445	0.445	6124	0.75	-	-	64.5	64.5	-	127
90	Pang (1991)	A2	Panel	7.0	55.0	-	-	-	-	-	-	1.193%	1.193%	-	-	-	-	-	-	0.63	0.63	5983	0.75	-	-	67.1	67.1	-	300
91	Pang (1991)	A3	Panel	7.0	55.0	-	-	-	-	-	-	1.789%	1.789%	-	-	-	-	-	-	0.768	0.768	6040	0.75	-	-	64.8	64.8	-	428
92	Pang (1991)	A4	Panel	7.0	55.0	-	-	-	-	-	-	2.982%	2.982%	-	-	-	-	-	-	0.992	0.992	6159	0.75	-	-	68.1	68.1	-	632
93	Pang (1991)	B1	Panel	7.0	55.0	-	-	-	-	-	-	0.596%	1.193%	-	-	-	-	-	-	0.445	0.63	6562	0.75	-	-	64.5	67.1	-	221
94	Pang (1991)	B2	Panel	7.0	55.0	-	-	-	-	-	-	1.193%	1.789%	-	-	-	-	-	-	0.63	0.768	6392	0.75	-	-	67.1	64.8	-	342
95	Pang (1991)	B3	Panel	7.0	55.0	-	-	-	-	-	-	0.596%	1.789%	-	-	-	-	-	-	0.445	0.768	6508	0.75	-	-	64.5	64.8	-	243
96	Pang (1991)	B4	Panel	7.0	55.0	-	-	-	-	-	-	0.596%	2.982%	-	-	-	-	-	-	0.445	0.992	6491	0.75	-	-	64.5	68.1	-	283
97	Pang (1991)	B5	Panel	7.0	55.0	-	-	-	-	-	-	1.193%	2.983%	-	-	-	-	-	-	0.63	0.992	6213	0.75	-	-	67.1	68.1	-	400
98	Pang (1991)	B6	Panel	7.0	55.0	-	-	-	-	-	-	1.789%	2.982%	-	-	-	-	-	-	0.768	0.992	6230	0.75	-	-	64.8	68.1	-	511
99	Sherwood (2008)	AT-1-East	Rectangular	79.4	39.6	36.1	2.95	-	3	0.763%	-	-	-	20	-	-	-	1.18	-	-	-	9862	0.38	67.4	-	-	-	-	273
100	Sherwood (2008)	AT-1-West	Rectangular	79.4	39.6	36.1	2.95	-	3	0.763%	-	-	-	20	-	-	-	1.18	-	-	-	9862	0.38	67.4	-	-	-	-	293
101	Sherwood (2008)	AT-2/250N	Rectangular	9.8	18.5	17.2	2.95	-	2	0.930%	-	-	-	2	-	-	-	1	-	-	-	5468	0.38	67.4	-	-	-	-	26.3
102	Sherwood (2008)	AT-2/250W	Rectangular	9.8	18.5	17.2	2.95	-	2	0.930%	-	-	-	2	-	-	-	1	-	-	-	5584	0.38	67.4	-	-	-	-	25.9
103	Sherwood (2008)	AT-2/1000N	Rectangular	39.4	18.5	17.2	2.95	-	2	0.930%	-	-	-	8	-	-	-	1	-	-	-	5497	0.38	67.4	-	-	-	-	101.4
104	Sherwood (2008)	AT-2/1000W	Rectangular	39.4	18.5	17.2	2.95	-	2	0.930%	-	-	-	8	-	-	-	1	-	-	-	5656	0.38	67.4	-	-	-	-	108.3
105	Sherwood (2008)	AT-2/3000	Rectangular	118.1	18.5	17.2	2.95	-	2	0.930%	-	-	-	24	-	-	-	1	-	-	-	5889	0.38	67.4	-	-	-	-	295.2
106	Sherwood (2008)	AT-3/N1	Rectangular	27.4	13.3	12.1	3.39	-	1.25	0.947%	-	-	-	4	-	-	-	1	-	-	-	5439	0.75	67.4	-	-	-	-	54.3
107	Sherwood (2008)	AT-3/T1	Rectangular	27.8	13.3	12.0	3.39	-	1.25	0.938%	-	-	-	4	-	-	-	1	-	-	-	5381	0.75	67.4	-	-	-	-	59
108	Sherwood (2008)	AT-3/N2	Rectangular	27.6	13.3	12.0	3.39	-	1.25	0.946%	-	-	-	4	-	-	-	1	-	-	-	5482	0.75	67.4	-	-	-	-	57.8

	Member		Geometric Properties							Reinforcement Details												Material Properties						Force Data	
	Source	Name	Shape	b_w (in)	h (in)	d (in)	a/d ratio	c_c (in) [side]	c_c (in) [top/bot]	ρ_s	ρ'_s	ρ_v	ρ_h	n_s	n'_s	n_v	n_h (E.F.)	d_{bl} (in)	d_{bl}' (in))	d_{bv} (in)	d_{bh} (in)	f'_c (psi)	d_a (in)	f_y (ksi)	f'_y (ksi)	f_{yv} (ksi)	f_{yh} (ksi)	V_{crack} (k)	V_{test} (k)
109	Sherwood (2008)	AT-3/T2	Rectangular	27.8	13.3	12.1	3.39	-	1.25	0.935%	-	-	-	4	-	-	-	1	-	-	-	5381	0.75	67.4	-	-	-	-	56.8
110	Sherwood (2008)	L-10N1	Rectangular	11.8	58.1	55.1	2.89	-	2	0.840%	0.140%	-	-	5	2	-	-	1.18	0.77	-	-	5568	0.37	65.5	65.6	-	-	-	59.6
111	Sherwood (2008)	L-10N2	Rectangular	11.8	58.1	55.1	2.89	-	2	0.840%	0.140%	-	-	5	2	-	-	1.18	0.77	-	-	5843	0.37	65.5	65.6	-	-	-	54.4
112	Sherwood (2008)	L-10H	Rectangular	11.8	58.1	55.1	2.89	-	2	0.840%	0.140%	-	-	5	2	-	-	1.18	0.77	-	-	10672	0.37	65.5	65.6	-	-	-	54
113	Sherwood (2008)	L-10HS	Rectangular	11.8	58.1	55.1	2.89	-	1.2	1.344%	0.140%	0.101%	-	8	2	1	4	1.18	0.77	0.375	-	10324	0.37	65.5	65.6	110.2	-	-	159.6
114	Sherwood (2008)	L-20N1	Rectangular	11.8	58.1	55.1	2.89	-	2	0.840%	0.140%	-	-	5	2	-	-	1.18	0.77	-	-	4553	0.75	65.5	65.6	-	-	-	59.6
115	Sherwood (2008)	L-20N2	Rectangular	11.8	58.1	55.1	2.89	-	2	0.840%	0.140%	-	-	5	2	-	-	1.18	0.77	-	-	4814	0.75	65.5	65.6	-	-	-	59.8
116	Sherwood (2008)	L-40N1	Rectangular	11.8	58.1	55.1	2.89	-	2	0.840%	0.140%	-	-	5	2	-	-	1.18	0.77	-	-	4075	1.5	66.5	65.6	-	-	-	54.4
117	Sherwood (2008)	L-40N2	Rectangular	11.8	58.1	55.1	2.89	-	2	0.840%	0.140%	-	-	5	2	-	-	1.18	0.77	-	-	4133	1.5	67.5	65.6	-	-	-	64.7
118	Sherwood (2008)	L-50N1	Rectangular	11.8	58.1	55.1	2.89	-	2	0.840%	0.140%	-	-	5	2	-	-	1.18	0.77	-	-	5945	2.01	65.5	65.6	-	-	-	61.1
119	Sherwood (2008)	L-50N2	Rectangular	11.8	58.1	55.1	2.89	-	2	0.840%	0.140%	-	-	5	2	-	-	1.18	0.77	-	-	5814	2.01	65.5	65.6	-	-	-	67
120	Sherwood (2008)	L-20L	Rectangular	11.6	58.1	57.1	2.79	-	2	0.246%	0.140%	-	-	2	2	-	-	1.02	0.77	-	-	5133	0.75	65.5	65.6	-	-	-	42.5
121	Sherwood (2008)	L-20D	Rectangular	11.6	58.1	53.4	2.96	-	2	0.705%	0.140%	-	7.660%	4	2	-	6	1.18	0.77	-	0.445	5191	0.75	65.5	65.6	-	-	-	78.68
122	Sherwood (2008)	S-10N1	Rectangular	4.8	13.0	11.0	2.89	-	-	0.836%	-	-	-	4	-	-	-	0.38	-	-	-	6076	0.37	65.6	-	-	-	-	8.228
123	Sherwood (2008)	S-10N2	Rectangular	4.8	13.0	11.0	2.89	-	-	0.836%	-	-	-	4	-	-	-	0.38	-	-	-	6076	0.37	65.6	-	-	-	-	8.61
124	Sherwood (2008)	S-20N1	Rectangular	4.8	13.0	11.0	2.89	-	-	0.576%	-	-	-	2	-	-	-	0.44	-	-	-	5684	0.75	65.6	-	-	-	-	8.79
125	Sherwood (2008)	S-20N2	Rectangular	4.8	13.0	11.0	2.89	-	-	0.576%	-	-	-	2	-	-	-	0.44	-	-	-	5525	0.75	65.6	-	-	-	-	8.588
126	Sherwood (2008)	S-40N1	Rectangular	4.8	13.0	11.0	2.89	-	-	0.836%	-	-	-	4	-	-	-	0.38	-	-	-	4220	1.50	65.6	-	-	-	-	9.397
127	Sherwood (2008)	S-40N2	Rectangular	4.8	13.0	11.0	2.89	-	-	0.836%	-	-	-	4	-	-	-	0.38	-	-	-	4220	1.50	65.6	-	-	-	-	7.846
128	Sherwood (2008)	S-50N1	Rectangular	4.8	13.0	11.0	2.89	-	-	0.836%	-	-	-	4	-	-	-	0.38	-	-	-	6308	2.01	65.6	-	-	-	-	8.655
129	Sherwood (2008)	S-50N2	Rectangular	4.8	13.0	11.0	2.89	-	-	0.836%	-	-	-	4	-	-	-	0.38	-	-	-	6308	2.01	65.6	-	-	-	-	9.127
130	Sherwood (2008)	S-20D1	Rectangular	3.8	9.8	9.8	2.94	-	-	0.810%	-	-	-	4	-	-	-	0.38	-	-	-	5887	0.75	65.6	-	-	-	-	5.575
131	Sherwood (2008)	S-20D2	Rectangular	3.8	9.8	9.8	2.96	-	-	0.830%	-	-	-	4	-	-	-	0.38	-	-	-	5916	0.75	65.6	-	-	-	-	5.8
132	Sherwood (2008)	S-10H	Rectangular	4.8	13.0	11.0	2.89	-	-	0.830%	-	-	-	4	-	-	-	0.38	-	-	-	11209	0.37	65.6	-	-	-	-	8.475
133	Sherwood (2008)	S-10HS	Rectangular	4.8	13.0	11.0	2.89	-	-	1.340%	0.076%	0.104%	-	5	2	1	-	0.40	0.23	0.2	-	11209	0.37	65.6	65.6	65.6	-	-	14.9
134	Susetyo (2009)	C1C-R	Panel	2.8	35.0	-	-	-	0.79	-	-	0.420%	3.310%	-	-	-	-	-	-	0.226	0.319	9529	0.39	-	-	64.8	80.1	27.54	76.5
135	Susetyo (2009)	C2C	Panel	2.8	35.0	-	-	-	0.79	-	-	0.420%	3.310%	-	-	-	-	-	-	0.226	0.319	13126	0.39	-	-	64.8	80.1	36.12	84

Category 3

	Member		Geometric Properties							Reinforcement Details												Material Properties						Force Data	
	Source	Name	Shape	b_w (in)	h (in)	d (in)	a/d ratio	c_c (in) [side]	c_c (in) [top/bot]	ρ_s	ρ'_s	ρ_v	ρ_h	n_s	n'_s	n_v	n_h (E.F.)	d_{bl} (in)	d_{bl}' (in))	d_{bv} (in)	d_{bh} (in)	f'_c (psi)	d_a (in)	f_y (ksi)	f'_y (ksi)	f_{yv} (ksi)	f_{yh} (ksi)	V_{crack} (k)	V_{test} (k)
136	Lee et al. (2015)	B34-3	Rectangular	14.0	19.2	15.3	2.56	1.57	1.57	3.720%	1.860%	0.724%	-	10	5	2	-	1	1	0.5	-	4873	0.98	94.0	94.0	69.6	-	45.8	152.8
137	Lee et al. (2015)	B34-5	Rectangular	14.0	19.2	15.3	2.56	1.57	1.57	3.720%	1.860%	0.603%	-	10	5	2	-	1	1	0.5	-	4873	0.98	94.0	94.0	69.6	-	45.5	151.7
138	Lee et al. (2015)	B42-2	Rectangular	14.0	19.2	15.3	2.56	1.57	1.57	3.720%	1.860%	0.724%	-	10	5	2	-	1	1	0.5	-	6106	0.98	94.0	94.0	48.4	-	43.4	149.5
139	Lee et al. (2015)	B42-3	Rectangular	14.0	19.2	15.3	2.56	1.57	1.57	3.720%	1.860%	0.724%	-	10	5	2	-	1	1	0.5	-	6106	0.98	94.0	94.0	69.6	-	1.8	180.1
140	Lee et al. (2015)	B42-4	Rectangular	14.0	19.2	15.3	2.56	1.57	1.57	3.720%	1.860%	0.724%	-	10	5	2	-	1	1	0.5	-	6106	0.98	94.0	94.0	96.7	-	32.4	180
141	Lee et al. (2015)	B42-5	Rectangular	14.0	19.2	15.3	2.56	1.57	1.57	3.720%	1.860%	0.603%	-	10	5	2	-	1	1	0.5	-	6106	0.98	94.0	94.0	69.6	-	43.5	155.4
142	Lee et al. (2015)	B42-6	Rectangular	14.0	19.2	15.3	2.56	1.57	1.57	3.720%	1.860%	0.453%	-	10	5	2	-	1	1	0.5	-	6106	0.98	94.0	94.0	96.7	-	42.4	151.4
143	Lee et al. (2015)	B68-2	Rectangular	14.0	19.2	15.3	2.56	1.57	1.57	3.720%	1.860%	0.724%	-	10	5	2	-	1	1	0.5	-	9921	0.98	94.0	94.0	48.4	-	54.0	180.1
144	Lee et al. (2015)	B68-3	Rectangular	14.0	19.2	15.3	2.56	1.57	1.57	3.720%	1.860%	0.724%	-	10	5	2	-	1	1	0.5	-	9921	0.98	94.0	94.0	69.6	-	31.4	196.4
145	Lee et al. (2015)	B68-4	Rectangular	14.0	19.2	15.3	2.56	1.57	1.57	3.720%	1.860%	0.724%	-	10	5	2	-	1	1	0.5	-	9921	0.98	94.0	94.0	96.7	-	43.2	205.6
146	Lee et al. (2015)	B68-5	Rectangular	14.0	19.2	15.3	2.56	1.57	1.57	3.720%	1.860%	0.603%	-	10	5	2	-	1	1	0.5	-	9921	0.98	94.0	94.0	69.6	-	26.9	179.5
147	Lee et al. (2015)	B68-6	Rectangular	14.0	19.2	15.3	2.56	1.57	1.57	3.720%	1.860%	0.453%	-	10	5	2	-	1	1	0.5	-	9921	0.98	94.0	94.0	96.7	-	33.1	157.8
148	Yoon et al. (1996)	N1-N	Rectangular	14.8	29.5	25.8	3.28	1.57	1.57	2.859%	0.082%	0.082%	-	10	2	2	-	1.18	0.44	0.31	-	5221	0.79	58.0	62.4	62.4	-	58.5	102.7
149	Yoon et al. (1996)	N2-S	Rectangular	14.8	29.5	25.8	3.28	1.57	1.57	2.859%	0.082%	0.081%	-	10	2	2	-	1.18	0.44	0.37	-	5221	0.79	58.0	62.4	62.4	-	45.0	81.61
150	Yoon et al. (1996)	N2-N	Rectangular	14.8	29.5	25.8	3.28	1.57	1.57	2.859%	0.082%	0.116%	-	10	2	2	-	1.18	0.44	0.37	-	5221	0.79	58.0	62.4	62.4	-	57.1	108.6
151	Yoon et al. (1996)	M1-N	Rectangular	14.8	29.5	25.8	3.28	1.57	1.57	2.859%	0.082%	0.082%	-	10	2	2	-	1.18	0.44	0.31	-	9718	0.39	58.0	62.4	62.4	-	65.0	91.05
152	Yoon et al. (1996)	M2-S	Rectangular	14.8	29.5	25.8	3.28	1.57	1.57	2.859%	0.082%	0.116%	-	10	2	2	-	1.18	0.44	0.37	-	9718	0.39	58.0	62.4	62.4	-	65.0	124.1
153	Yoon et al. (1996)	M2-N	Rectangular	14.8	29.5	25.8	3.28	1.57	1.57	2.859%	0.082%	0.164%	-	10	2	2	-	1.18	0.44	0.37	-	9718	0.39	58.0	62.4	62.4	-	65.0	154.9
154	Yoon et al. (1996)	H1-N	Rectangular	14.8	29.5	25.8	3.28	1.57	1.57	2.859%	0.082%	0.082%	-	10	2	2	-	1.18	0.44	0.31	-	12618	0.39	58.0	62.4	62.4	-	69.916	108.6
155	Yoon et al. (1996)	H2-S	Rectangular	14.8	29.5	25.8	3.28	1.57	1.57	2.859%	0.082%	0.140%	-	10	2	2	-	1.18	0.44	0.37	-	12618	0.39	58.0	62.4	62.4	-	69.916	134.4
156	Yoon et al. (1996)	H2-N	Rectangular	14.8	29.5	25.8	3.28	1.57	1.57	2.859%	0.082%	0.236%	-	10	2	2	-	1.18	0.44	0.37	-	12618	0.39	58.0	62.4	62.4	-	75.086	162.1

Appendix B. Crack Data

Category 1

Name	V_a/ V_u	w_{cr} (in)	θ_{cr}
1A	0%	0.000	-
	32%	0.005	-
	42%	0.013	47.°
	53%	0.016	-
	63%	0.025	-
	74%	0.030	-
	84%	0.040	-
	100%	-	39.°
1B	0%	0.000	-
	30%	0.010	-
	40%	0.013	-
	43%	-	60.°
	50%	0.016	-
	60%	0.035	-
	70%	0.040	-
	80%	0.040	-
	100%	-	52.°
2A	0%	0.000	-
	30%	0.009	-
	40%	0.009	52.°
	50%	0.016	-
	60%	0.020	-
	70%	0.030	-
	80%	0.040	-
	100%	-	48.°
2B	0%	0.000	-
	31%	0.005	-
	41%	0.010	53.°
	51%	0.016	-
	62%	0.025	-
	72%	0.030	-
	82%	0.040	-
	100%	-	46.°
3C	0%	0.000	-
	29%	0.007	-
	38%	0.013	59.°
	48%	0.020	-
	57%	0.030	-
	67%	0.030	-
	76%	0.040	-
	100%	-	52.°
3D	0%	0.000	-
	27%	0.003	-
	36%	0.013	-
	44%	0.016	-
	53%	0.020	-
	62%	0.030	52.°
	71%	0.030	-
	100%	-	51.°
4C	0%	0.000	-
	27%	0.005	-
	36%	0.005	54.°
	45%	0.016	-
	55%	0.030	-
	64%	0.030	-
	73%	0.050	-
	100%	-	54.°
4E	0%	0.000	-
	26%	0.003	-
	35%	0.005	59.°
	43%	0.016	-
	52%	0.016	-
	61%	0.025	-
	70%	0.030	-
	100%	-	57.°
5D	0%	0.000	-
	26%	0.002	-
	34%	0.007	45.°
	43%	0.013	-
	51%	0.020	-
	60%	0.020	-
	68%	0.030	-
	100%	-	45.°
5E	0%	0.000	-
	25%	0.003	-
	33%	0.007	-

Name	**V_a/V_u**	**w_{cr} (in)**	**θ_{cr}**
	42%	0.013	-
	50%	0.016	-
	58%	0.020	-
	67%	0.030	-
	100%	-	47.°
6F	0%	0.000	-
	29%	0.003	-
	38%	0.013	56.°
	48%	0.016	-
	57%	0.020	-
	67%	0.020	-
	76%	0.025	-
	100%	-	54.°
6G	0%	0.000	-
	33%	0.005	-
	44%	0.010	-
	56%	0.013	-
	67%	0.016	-
	78%	0.016	-
	89%	0.030	-
	100%	-	45.°
7F	0%	0.000	-
	24%	0.005	-
	32%	0.007	63.°
	40%	0.013	-
	48%	0.020	-
	56%	0.020	-
	64%	0.025	-
	100%	-	49.°
7H	0%	0.000	-
	25%	0.005	-
	33%	0.007	-
	42%	0.007	-
	50%	0.013	-
	58%	0.016	-
	67%	0.020	-
	100%	-	45.°
8G	0%	0.000	-
	27%	0.005	-
	36%	0.013	53.°
	45%	0.016	-

Name	**V_a/V_u**	**w_{cr} (in)**	**θ_{cr}**
	55%	0.020	-
	64%	0.020	-
	73%	0.040	-
	100%	-	49.°
8H	0%	0.000	-
	26%	0.005	-
	34%	0.007	-
	43%	0.013	-
	51%	0.016	-
	60%	0.020	-
	68%	0.025	-
	100%	-	43.°
I-03-2	0%	0.000	-
	15%	0.000	-
	23%	0.006	-
	33%	0.013	-
	43%	0.020	-
	53%	0.025	-
	63%	0.030	-
	73%	0.035	-
	83%	0.048	-
	93%	0.060	30.°
	100%	-	-
I-03-4	12%	0.005	-
	20%	0.012	-
	29%	0.016	-
	37%	0.023	-
	46%	0.030	-
	54%	0.035	-
	63%	0.040	-
	72%	0.050	-
	79%	0.060	-
	88%	0.080	28.°
	100%	0.125	-
I-02-2	0%	0.000	-
	29%	0.016	60.°
	42%	0.035	-
	54%	0.045	-
	67%	0.060	-
	80%	0.080	40.°
	92%	0.085	34.°

Name	**V_a/ V_u**	**w_{cr} (in)**	**θ_{cr}**
I-02-4	0%	0.000	-
	25%	0.018	-
	36%	0.023	-
	46%	0.028	-
	57%	0.030	-
	68%	0.035	-
	79%	0.500	-
	90%	0.600	-
II-03-CCC2021	0%	0.000	-
	26%	0.009	-
	31%	0.012	-
	41%	0.015	-
	52%	0.018	-
	64%	0.023	-
	77%	0.028	-
	91%	0.050	31.°
II-03-CCC1007	0%	0.000	-
	16%	0.008	-
	27%	0.010	-
	34%	0.013	-
	44%	0.016	-
	53%	0.018	-
	63%	0.025	-
	72%	0.035	-
	80%	0.038	-
	90%	0.040	-
	95%	-	31.°
II-02-CCC1007	0%	0.000	-
	46%	0.005	60.°
	57%	0.015	45.°
	70%	0.028	-
	81%	0.040	-
	92%	0.050	45.°
	100%	-	-
II-02-CCC1021	0%	0.000	-
	36%	0.016	-
	47%	0.030	-
	58%	0.045	-
	71%	0.060	-
	82%	0.085	44.°
II-03-CCT1021	12%	0.012	-
	20%	0.016	-
	31%	0.023	-
	38%	0.030	-
	47%	0.035	-
	55%	0.040	-
	66%	0.040	-
	73%	0.040	-
	82%	0.045	-
	91%	0.050	31.°
	99%	0.070	-
II-03-CCT0507	0%	0.000	-
	22%	0.013	-
	31%	0.019	-
	37%	0.023	-
	45%	0.028	-
	54%	0.033	-
	61%	0.040	-
	69%	0.048	-
	76%	0.060	-
	90%	0.080	27.°
	100%	-	-
II-02-CCT0507	0%	0.000	-
	19%	0.005	-
	29%	0.020	-
	38%	0.030	-
	48%	0.038	-
	57%	0.050	-
	66%	0.060	-
	76%	0.081	-
	85%	0.090	-
	95%	0.105	36.°
	100%	-	-

Name	**V_a/ V_u**	**w_{cr} (in)**	**θ_{cr}**
II-02-CCT0521	0%	0.000	-
	14%	0.013	-
	20%	0.020	-
	27%	0.025	-
	33%	0.030	-
	40%	0.040	-
	46%	0.050	-
	54%	0.055	-
	74%	0.080	-
	81%	0.090	-
	93%	0.110	33.°
III-1.85-00	0%	0.000	-
	17%	0.005	-
	21%	0.009	-
	27%	0.030	37.°
	33%	0.038	-
	38%	0.050	-
	51%	0.063	37.°
	61%	0.094	-
	71%	0.100	37.°
	91%	0.160	-
	100%	-	24.°
III-1.85-02	0%	0.000	-
	27%	0.020	45.°
	39%	0.035	45.°
	51%	0.050	45.°
	62%	0.060	26.°
	74%	0.063	26.°
	85%	0.070	26.°
	96%	0.090	26.°
	100%	-	-
III-1.85-025	0%	0.000	-
	37%	0.000	-
	48%	0.035	26.°
	60%	0.050	26.°
	70%	0.060	26.°
	81%	0.078	26.°
	92%	0.100	26.°
	100%	-	-
III-1.85-03	0%	0.000	-
	20%	0.000	-
	32%	0.013	26.°
	47%	0.025	26.°
	61%	0.033	26.°
	75%	0.040	26.°
	89%	0.055	26.°
	100%	-	-
III-1.85-01	0%	0.000	-
	29%	0.005	26.°
	44%	0.017	26.°
	59%	0.038	26.°
	71%	0.055	26.°
	87%	0.098	26.°
	100%	-	-
III-1.85-03b	0%	-	-
	25%	0.009	50.°
	33%	0.016	-
	40%	0.025	-
	49%	0.030	-
	57%	0.033	45.°
	65%	0.040	-
	73%	0.040	26.°
	81%	0.045	26.°
	89%	0.050	26.°
	100%	-	-
III-1.85-02b	16%	0.017	-
	25%	0.023	-
	33%	0.028	-
	41%	0.033	-
	49%	0.038	-
	57%	0.040	26.°
	65%	0.043	26.°
	73%	0.050	26.°
	80%	0.058	26.°
	89%	0.080	26.°
	100%	-	-

Name	V_a/ V_u	w_{cr} (in)	θ_{cr}
III-1.2-02	12%	0.000	-
	20%	0.012	-
	28%	0.020	-
	36%	0.028	-
	45%	0.033	-
	52%	0.035	-
	60%	0.040	-
	70%	0.045	-
	80%	0.045	-
	90%	0.050	-
	100%	-	-
III-1.2-03	0%	0.000	-
	11%	0.000	-
	21%	0.005	-
	31%	0.010	-
	41%	0.016	-
	51%	0.020	-
	61%	0.030	-
	71%	0.040	-
	81%	0.046	-
	92%	0.058	-
	100%	-	-
III-2.5-02	0%	0.000	-
	13%	0.000	-
	25%	0.000	-
	38%	0.010	-
	50%	0.025	-
	63%	0.035	-
	74%	0.050	-
	87%	0.075	-
	100%	-	-
III-2.5-03	20%	0.023	-
	27%	0.028	-
	33%	0.033	-
	40%	0.035	-
	47%	0.038	-
	53%	0.040	-
	60%	0.043	-
	67%	0.045	-
	73%	0.050	-
	80%	0.055	-
	100%	0.060	-
IV-2175-1.85-02	27%	0.015	-
	37%	0.025	-
	51%	0.033	-
	62%	0.053	-
	71%	0.060	-
	82%	0.065	-
	95%	0.085	-
IV-2175-1.85-03	24%	0.008	-
	33%	0.015	-
	45%	0.023	-
	55%	0.033	-
	64%	0.035	-
	73%	0.043	-
	85%	0.055	-
IV-2175-2.5-02	30%	0.005	-
	39%	0.015	-
	49%	0.020	-
	59%	0.030	-
	69%	0.035	-
	78%	0.040	-
	87%	0.053	-
	98%	0.088	-
IV-2175-1.2-02	26%	0.023	-
	34%	0.025	-
	43%	0.033	-
	51%	0.040	-
	61%	0.055	-
	68%	0.071	-
	76%	0.090	-
	85%	0.098	-
IV-2123-1.85-03	29%	0.012	-
	41%	0.016	-

Name	V_a/ V_u	w_{cr} (in)	θ_{cr}
	51%	0.020	-
	63%	0.025	-
	73%	0.030	-
	85%	0.038	-
	95%	0.043	-
IV-2123-1.85-02	29%	0.018	-
	38%	0.023	-
	48%	0.024	-
	58%	0.028	-
	69%	0.033	-
	79%	0.040	-
	90%	0.043	-
IV-2123-2.5-02	47%	0.020	-
	64%	0.033	-
	82%	0.048	-
	98%	0.095	-
IV-2123-1.2-02	18%	0.005	-
	24%	0.005	-
	31%	0.009	-
	39%	0.013	-
	48%	0.018	-
	55%	0.023	-
	63%	0.025	-
	70%	0.030	-
	78%	0.035	-
M-03-4-CCC2436	34%	0.013	-
	38%	0.016	-
	41%	0.020	-
	48%	0.025	-
	51%	0.030	-
	58%	0.030	-
	64%	0.040	-
	71%	0.040	-
	77%	0.050	-
	83%	0.060	-
	92%	0.060	-

Name	V_a/ V_u	w_{cr} (in)	θ_{cr}
M-03-4-CCC0812	0%	0.000	-
	26%	0.020	-
	35%	0.025	-
	43%	0.025	-
	48%	0.030	-
	60%	0.035	-
	67%	0.040	-
	71%	0.040	-
	79%	0.050	-
	87%	0.060	-
	95%	0.060	-
M-02-4-CCC2436	19%	0.005	-
	27%	0.013	-
	32%	0.020	-
	39%	0.025	-
	45%	0.030	-
	51%	0.035	-
	57%	0.045	-
	64%	0.055	-
	71%	0.060	-
	76%	0.070	-
	83%	0.080	-
DC3-42-1.85-03	0%	0.000	-
	26%	0.008	-
	33%	0.012	43.°
	39%	0.016	-
	52%	0.023	38.°
	65%	0.034	37.°
	78%	0.063	37.°
	92%	0.088	26.°
DS3-42-1.85-03	0%	0.000	-
	23%	-	-
	29%	0.002	46.°
	34%	0.009	46.°
	46%	0.019	46.°
	57%	0.031	46.°

Name	V_a/ V_u	w_{cr} (in)	θ_{cr}
	69%	0.043	46.°
	80%	0.050	46.°
	88%	0.068	46.°
	92%	0.080	46.°
DL3-42-1.85-03	0%	0.000	-
	27%	0.001	28.°
	35%	0.009	28.°
	44%	0.013	28.°
	53%	0.019	28.°
	62%	0.022	28.°
	71%	0.026	28.°
	80%	0.035	28.°
	93%	0.075	28.°
	98%	0.100	21.°
	99%	0.160	21.°
SC3-42-1.85-03	0%	0.000	-
	18%	0.004	-
	24%	0.009	-
	36%	0.015	35.°
	48%	0.023	35.°
	60%	0.031	35.°
	72%	0.046	35.°
SS3-42-1.85-03	0%	0.000	-
	11%	0.002	-
	16%	0.003	-
	22%	0.004	-
	33%	0.010	40.°
	43%	0.015	-
	54%	0.020	37.°
	65%	0.028	37.°
	76%	0.038	33.°
SL3-42-1.85-03	0%	0.000	-
	20%	-	-
	25%	0.002	-
	30%	0.010	37.°
	40%	0.019	37.°
	49%	0.028	37.°
	59%	0.038	37.°

Name	V_a/ V_u	w_{cr} (in)	θ_{cr}
	69%	0.045	37.°
	79%	0.053	37.°
	89%	0.071	37.°
	99%	0.123	26.°
SS1-75-1.85-03	25%	0.005	-
	28%	0.007	46.°
	35%	0.015	-
	42%	0.017	-
	49%	0.018	32.°
	56%	0.023	32.°
	63%	0.026	32.°
	70%	0.035	32.°
	77%	0.043	32.°
	84%	0.055	32.°
	91%	0.060	32.°
DS1-42-1.85-03	0%	0.000	-
	21%	0.007	-
	27%	0.013	-
	31%	0.015	-
	37%	0.017	-
	42%	0.021	-
	52%	0.030	-
	63%	0.035	-
	73%	0.039	-
	78%	0.043	-
	84%	0.048	-
DS1-42-2.50-03	0%	0.000	-
	32%	0.014	-
	40%	0.016	-
	56%	0.024	-
	71%	0.035	-
	87%	0.062	-
	95%	0.094	-
DS1-42-1.85-06	0%	0.000	-
	22%	0.005	-
	31%	0.008	-
	37%	0.009	-

Name	V_a/ V_u	w_{cr} (in)	θ_{cr}
	49%	0.013	-
	61%	0.016	-
	74%	0.020	-
	86%	0.028	-
	99%	0.060	-
DS1-42-2.50-06	0%	0.000	-
	20%	0.004	-
	26%	0.007	-
	39%	0.010	-
	53%	0.013	-
	66%	0.015	-
	72%	0.019	-
	80%	0.025	-
	92%	0.033	-
	99%	0.045	-
DL1-42-1.85-06	0%	0.000	-
	16%	0.002	-
	20%	0.005	-
	26%	0.005	-
	31%	0.007	-
	36%	0.008	-
	46%	0.012	-
	57%	0.014	-
	67%	0.017	-
	77%	0.022	-
	87%	0.034	-
DL1-42-2.50-06	0%	0.000	-
	27%	0.007	-
	32%	0.010	-
	42%	0.012	-
	53%	0.015	-
	64%	0.018	-
	75%	0.023	-
	80%	0.026	-
SS3-42-2.50-03	0%	0.000	-
	11%	0.002	-
	16%	0.007	-
	22%	0.006	-
	33%	0.010	-
	43%	0.017	-
	54%	0.020	-
	65%	0.026	-
	76%	0.041	-
SC3-42-2.50-03	0%	0.000	-
	21%	0.004	-
	28%	0.005	-
	43%	0.013	-
	57%	0.023	-
	71%	0.029	-
	85%	0.050	-
DS3-42-2.50-03	0%	0.000	-
	16%	-	-
	22%	0.005	-
	33%	0.014	-
	44%	0.021	-
	55%	0.026	-
	66%	0.035	-
	77%	0.048	-
	88%	0.073	-
DL1-42-1.85-03	0%	0.000	-
	30%	0.004	-
	43%	0.010	-
	55%	0.014	-
	67%	0.019	-
	79%	0.030	-
	91%	0.050	-
DL1-42-2.50-03	0%	0.000	-
	26%	0.005	-
	39%	0.010	-
	52%	0.015	-
	65%	0.019	-
	78%	0.029	-
	91%	0.055	-

Name	V_a/ V_u	w_{cr} (in)	θ_{cr}
SL3-42-1.85-06	19%	0.005	-
	22%	0.005	-
	30%	0.008	-
	37%	0.010	-
	45%	0.010	-
	52%	0.015	-
	60%	0.018	-
	67%	0.025	-
	75%	0.025	-
	82%	0.030	-
	90%	0.038	-
DC1-42-1.85-06	0%	0.000	-
	29%	0.008	-
	44%	0.012	-
	59%	0.018	-
	73%	0.025	-
	82%	0.031	-
	88%	0.035	-
SS1-42-2.50-03	0%	0.000	-
	17%	0.002	-
	33%	0.011	-
	42%	0.018	-
	58%	0.031	-
	75%	0.045	-
	92%	0.090	-
SS1-42-1.85-03	0%	0.000	-
	39%	0.019	31.°
	52%	0.024	31.°
	65%	0.031	31.°
	78%	0.035	31.°
	91%	0.063	31.°
DC1-42-2.50-03	0%	0.000	-
	18%	0.005	-
	37%	0.015	-
	55%	0.021	-
	73%	0.031	-
	92%	0.059	-

Name	V_a/ V_u	w_{cr} (in)	θ_{cr}
SL1-42-2.50-03	0%	0.000	-
	27%	0.005	-
	33%	0.012	-
	40%	0.018	-
	53%	0.025	-
	67%	0.031	-
	80%	0.048	-
	93%	0.095	-
SC1-42-2.50-03	0%	0.000	-
	47%	0.023	-
	57%	0.028	-
	75%	0.040	-
	94%	0.069	-
DS1-42-1.85-06/03	0%	0.000	-
	10%	0.008	-
	20%	0.012	-
	31%	0.014	-
	41%	0.019	-
	51%	0.025	-
	61%	0.029	-
	72%	0.035	-
	82%	0.038	-
	92%	0.051	-
DS1-42-2.50-06/03	0%	0.000	-
	18%	0.008	-
	24%	0.013	-
	36%	0.018	-
	49%	0.024	-
	61%	0.026	-
	73%	0.034	-
	85%	0.040	-
	97%	0.053	-
	99%	0.080	-
DC1-42-1.85-03	0%	0.000	-
	22%	0.008	-
	30%	0.013	-

Name	V_a/ V_u	w_{cr} (in)	θ_{cr}
	44%	0.019	-
	59%	0.024	-
	74%	0.039	-
	89%	0.071	-

Category 2

Name	V_a/ V_u	w_{cr} (in)	θ_{cr}
13.3-2.6-98	0%	0.000	-
	35%	0.010	-
	60%	0.020	-
	100%	0.160	30.°
14.5-2.6-98	0%	0.000	-
	28%	0.010	-
	60%	0.020	-
	100%	0.160	28.°
13.3-5.4-98	0%	0.000	-
	43%	0.010	-
	60%	0.020	-
	100%	0.160	28.°
14.5-5.4-98	0%	0.000	-
	44%	0.010	-
	60%	0.020	-
	100%	0.160	29.°
13.2-4.3-451	0%	0.000	-
	19%	0.010	-
	100%	0.030	30.°
15.3-4.3-687	0%	0.000	-
	20%	0.010	-
	100%	0.030	30.°
13.2-7.9-902	0%	0.000	-
	12%	0.010	-
	100%	0.030	30.°
15.3-7.9-902	0%	0.000	-
	15%	0.010	-
	100%	0.030	30.°
IRC-1	32%	0.000	-
	34%	0.003	-
	45%	0.005	-
	48%	0.008	-
	60%	0.010	-
	72%	0.011	-
	80%	0.013	-
	87%	0.015	-
	100%	0.018	39.3°
IRC-2	54%	0.000	-
	58%	0.003	-
	62%	0.004	-
	67%	0.006	-
	73%	0.009	-
	78%	0.012	-
	82%	0.014	-
	88%	0.019	-
	92%	0.020	-
	100%	0.021	42.6°
IRC-3	34%	0.000	-
	39%	0.001	-
	44%	0.001	-
	49%	0.004	-
	55%	0.006	-
	70%	0.009	-
	74%	0.011	-
	81%	0.013	-
	90%	0.015	-
	94%	0.016	-
	100%	0.018	41.5°
A1	88%	0.120	-
A2	30%	0.010	-
	52%	0.020	-
	75%	0.020	-
A3	19%	0.004	-
	36%	0.007	-
	40%	0.010	-
	56%	0.010	-
	91%	0.040	-
A4	41%	0.005	-
	57%	0.010	-
	76%	0.018	-
	92%	0.020	-
B1	45%	0.006	-
	56%	0.008	-
	68%	0.012	-
	80%	0.025	-
	92%	0.065	-

Name	**V_a/ V_u**	**w_{cr} (in)**	**θ_{cr}**
	98%	0.250	-
B2	27%	0.008	-
	62%	0.006	-
	70%	0.005	-
	80%	0.040	-
B3	42%	0.023	-
	71%	0.030	-
B4	31%	0.015	-
	58%	0.030	-
B5	35%	0.010	-
	51%	0.013	-
	60%	0.015	-
	76%	0.015	-
	86%	0.025	-
	92%	0.040	-
B6	24%	0.008	-
	32%	0.010	-
	67%	0.016	-
AT-1-East	0%	0.000	-
	75%	0.002	63.°
	88%	0.010	53.°
	97%	0.012	48.°
	100%	0.071	48.°
AT-1-West	0%	0.000	-
	69%	0.002	74.°
	82%	0.006	70.°
	90%	0.008	64.°
	94%	0.008	64.°
	100%	-	37.°
AT-2/250N	0%	0.000	-
	66%	0.002	-
	78%	0.002	-
	87%	0.004	-
	96%	0.008	36.°
	100%	-	36.°
AT-2/250W	0%	0.000	-
	45%	0.002	68.°
	67%	0.002	62.°
	81%	0.004	46.°

Name	**V_a/ V_u**	**w_{cr} (in)**	**θ_{cr}**
	89%	0.004	46.°
	98%	0.012	46.°
	100%	-	46.°
AT-2/1000 N	0%	0.000	-
	68%	0.002	48.°
	82%	0.002	45.°
	91%	0.002	45.°
	100%	-	40.°
AT-2/1000 W	0%	0.000	-
	64%	0.002	58.°
	77%	0.002	58.°
	85%	0.004	49.°
	94%	0.004	49.°
	100%	-	23.°
AT-2/3000	0%	0.000	-
	47%	0.002	58.°
	70%	0.002	56.°
	84%	0.004	56.°
	93%	0.004	56.°
	100%	-	33.°
AT-3/N1	0%	0.000	-
	58%	0.002	64.°
	73%	0.004	61.°
	84%	0.004	54.°
	95%	0.006	49.°
	100%	-	25.°
AT-3/T1	0%	0.000	-
	69%	0.002	38.°
	79%	0.004	38.°
	89%	0.004	38.°
	99%	0.004	32.°
	100%	-	32.°
AT-3/N2	0%	0.000	-
	39%	0.020	60.°
	68%	0.002	53.°
	77%	0.002	53.°

Name	**V_a/ V_u**	**w_{cr} (in)**	**θ_{cr}**
	87%	0.002	53.°
	97%	0.004	53.°
	100%	-	42.°
AT-3/T2	0%	0.000	-
	70%	0.002	63.°
	80%	0.004	63.°
	91%	0.006	39.°
	100%	-	35.°
L-10N1	0%	0.000	-
	45%	0.002	-
	70%	0.002	-
	77%	0.006	51.°
	86%	0.006	51.°
	95%	0.008	51.°
	100%	0.020	51.°
L-10N2	0%	0.000	-
	77%	0.010	58.°
	93%	0.012	40.°
	99%	0.014	40.°
	100%	-	40.°
L-10H	0%	0.000	-
	78%	0.016	45.°
	94%	0.020	42.°
	100%	-	36.°
L-10HS	0%	0.000	-
	50%	0.022	30.°
	68%	0.063	30.°
	86%	0.157	30.°
	100%	-	30.°
L-20N1	0%	0.000	-
	70%	0.002	55.°
	84%	0.008	55.°
	100%	0.047	50.°
L-20N2	0%	0.000	-
	70%	0.002	58.°
	90%	0.008	53.°
	100%	0.010	45.°
L-40N1	0%	0.000	-
	93%	0.004	55.°
	100%	-	47.°

Name	**V_a/ V_u**	**w_{cr} (in)**	**θ_{cr}**
L-40N2	0%	0.000	-
	64%	0.002	60.°
	77%	0.008	54.°
	83%	0.012	45.°
	92%	0.016	45.°
	100%	-	45.°
L-50N1	0%	0.000	-
	68%	0.006	42.°
	82%	0.020	40.°
	100%	-	32.°
L-50N2	0%	0.000	-
	62%	0.008	52.°
	74%	0.014	52.°
	80%	0.014	52.°
	88%	0.014	51.°
	100%	-	29.°
L-20L	0%	0.000	-
	66%	0.031	48.°
	100%	-	34.°
L-20D	0%	0.000	-
	82%	0.012	77.°
	97%	0.012	54.°
	100%	-	54.°
S-10N1	0%	0.000	-
	42%	0.002	-
	55%	0.004	-
	83%	0.004	57.°
	100%	-	43.°
S-10N2	0%	0.000	-
	27%	-	-
	40%	-	-
	48%	0.002	67.°
	57%	0.002	67.°
	69%	0.002	63.°
	83%	0.002	62.°
	91%	0.004	62.°
	96%	0.004	46.°
	100%	-	43.°
S-20N1	0%	0.000	-
	32%	-	-
	42%	-	-

Name	**V_a/ V_u**	**w_{cr} (in)**	**θ_{cr}**
	71%	-	-
	84%	0.002	52.°
	97%	0.002	35.°
	100%	-	-
S-20N2	0%	0.000	-
	32%	-	-
	45%	-	-
	60%	-	-
	72%	-	-
	86%	-	-
	86%	-	-
	98%	-	-
	100%	0.004	53.°
	99%	0.004	53.°
	100%	0.004	39.°
S-40N1	0%	0.000	-
	23%	-	-
	33%	-	-
	44%	-	-
	52%	-	-
	64%	-	-
	76%	0.002	61.°
	86%	0.002	59.°
	88%	0.002	59.°
	92%	0.006	53.°
	100%	-	41.°
S-40N2	0%	0.000	-
	29%	-	-
	43%	-	-
	54%	-	-
	62%	-	-
	77%	-	-
	91%	0.006	43.°
	100%	0.006	39.°
	fail	-	34.°
S-50N1	0%	0.000	-
	37%	-	-
	40%	-	-
	69%	0.002	46.°
	72%	0.002	45.°
	87%	0.002	45.°
	95%	0.006	45.°
	100%	-	42.°
S-50N2	0%	0.000	-
	31%	-	-
	44%	-	-
	56%	-	-
	69%	-	-
	81%	0.002	69.°
	93%	0.006	55.°
	100%	-	40.°
S-20D1	0%	0.000	-
	31%	-	-
	46%	-	-
	61%	-	-
	75%	-	-
	87%	-	-
	96%	0.004	51.°
	100%	-	46.°
S-20D2	0%	0.000	-
	29%	-	-
	45%	-	-
	60%	-	-
	72%	-	-
	83%	0.002	56.°
	94%	0.002	54.°
	100%	-	47.°
S-10H	0%	0.000	-
	27%	-	-
	40%	-	-
	46%	-	-
	50%	-	-
	57%	-	-
	71%	-	-
	84%	0.002	45.°
	99%	0.006	45.°
	100%	-	41.°
S-10HS	0%	0.000	-
	17%	-	-
	26%	-	-
	41%	-	-
	56%	-	-

Name	V_a/ V_u	w_{cr} (in)	θ_{cr}
	72%	0.002	50.°
	75%	0.016	38.°
	80%	0.035	38.°
	91%	0.079	37.°
	100%	-	37.°
C1C-R	21%	0.000	-
	36%	0.004	-
	46%	0.004	-
	56%	0.010	-
	63%	0.010	-
	70%	0.012	-
	77%	0.016	-
	84%	0.016	-
	90%	0.018	-
	96%	0.018	-
	100%	0.022	30.5°
C2C	25%	0.000	-
	43%	0.006	-
	51%	0.010	-
	62%	0.012	-
	81%	0.012	-
	92%	0.018	-
	100%	0.020	28.°

Category 3

Name	V_a/ V_u	w_{cr} (in)	θ_{cr}
B34-3	30%	0.000	-
	52%	0.003	-
	74%	0.010	-
	81%	0.014	-
	89%	0.020	-
	96%	0.028	-
	100%	0.034	-
B34-5	30%	0.000	-
	50%	0.004	-
	60%	0.007	-
	67%	0.011	-
	75%	0.015	-
	81%	0.021	-
	89%	0.023	-
	94%	0.028	-
	97%	0.032	-
	99%	0.035	-
	100%	0.039	-
B42-2	29%	0.000	-
	45%	0.004	-
	52%	0.005	-
	61%	0.008	-
	66%	0.008	-
	90%	0.013	-
	94%	0.015	-
	97%	0.020	-
	97%	0.028	-
B42-3	1%	0.000	-
	48%	0.008	-
	65%	0.012	-
	81%	0.016	-
	92%	0.019	-
	97%	0.023	-
	100%	0.028	-
	97%	0.034	-
	94%	0.038	-
	92%	0.038	-
B42-4	18%	0.000	-
	43%	0.005	-
	56%	0.008	-
	75%	0.013	-
	82%	0.013	-
	87%	0.015	-
	97%	0.021	-
	100%	0.031	-
	97%	0.033	-
	100%	0.034	-
	99%	0.036	-
B42-5	28%	0.000	-
	44%	0.005	-
	60%	0.010	-
	77%	0.014	-
	87%	0.018	-
	94%	0.023	-
	97%	0.028	-
	100%	0.032	-
	96%	0.034	-
	93%	0.035	-
	91%	0.037	-
B42-6	28%	0.000	-
	44%	0.004	-
	52%	0.008	-
	74%	0.017	-
	82%	0.020	-
	89%	0.026	-
	93%	0.029	-
	96%	0.036	-
	97%	0.039	-
B68-2	30%	0.000	-
	38%	0.001	-
	44%	0.003	-
	50%	0.006	-
	56%	0.009	-
	81%	0.018	-
	94%	0.025	-
	100%	0.031	-
B68-3	16%	0.000	-
	23%	0.002	-
	29%	0.002	-
	33%	0.004	-

Name	V_a/ V_u	w_{cr} (in)	θ_{cr}
	40%	0.006	-
	48%	0.008	-
	63%	0.011	-
	79%	0.015	-
	93%	0.020	-
	96%	0.022	-
	99%	0.025	-
B68-4	21%	0.000	-
	27%	0.001	-
	38%	0.007	-
	49%	0.010	-
	56%	0.011	-
	65%	0.012	-
	79%	0.015	-
	93%	0.019	-
	98%	0.022	-
B68-5	15%	0.000	-
	20%	0.001	-
	31%	0.004	-
	32%	0.005	-
	45%	0.008	-
	59%	0.012	-
	77%	0.018	-
	85%	0.021	-
	95%	0.023	-
	97%	0.025	-
	100%	0.025	-
B68-6	21%	0.000	-
	32%	0.002	-
	35%	0.004	-
	36%	0.007	-
	57%	0.013	-
	68%	0.016	-
	71%	0.018	-
	78%	0.022	-
	93%	0.031	-
	97%	0.034	-
	100%	0.037	-
N1-N	55%	0.000	-
	68%	0.008	-
	77%	0.050	-
	82%	0.069	-
	87%	0.108	-
	92%	0.158	-
	96%	0.197	-
	100%	0.217	-
N2-S	56%	0.000	-
	81%	0.013	-
	90%	0.032	-
	98%	0.118	-
	100%	0.158	-
N2-N	53%	0.000	-
	60%	0.011	-
	67%	0.024	-
	74%	0.032	-
	74%	0.040	-
	83%	0.060	-
	92%	0.086	-
	100%	0.177	-
M1-N	72%	0.000	-
	78%	0.015	-
	89%	0.109	-
	94%	0.157	-
	99%	0.197	-
	100%	0.224	-
M2-S	53%	0.000	-
	57%	0.014	-
	65%	0.024	-
	73%	0.049	-
	81%	0.099	-
	89%	0.138	-
	97%	0.181	-
	100%	0.217	-
M2-N	42%	0.000	-
	46%	0.006	-
	52%	0.008	-
	59%	0.016	-
	65%	0.032	-
	71%	0.049	-
	78%	0.060	-
	84%	0.079	-
	91%	0.118	-

Name	**V_a/ V_u**	**w_{cr} (in)**	**θ_{cr}**
	97%	0.177	-
	100%	0.221	-
H1-N	65%	0.000	-
	69%	0.013	-
	75%	0.059	-
	85%	0.118	-
	94%	0.177	-
	100%	0.236	-
H2-S	53%	0.000	-
	57%	0.007	-
	61%	0.008	-
	68%	0.027	-
	75%	0.049	-
	83%	0.059	-
	90%	0.098	-
	97%	0.157	-
	100%	0.197	-
H2-N	46%	0.000	-
	46%	0.006	-
	55%	0.013	-
	67%	0.020	-
	73%	0.040	-
	79%	0.044	-
	85%	0.049	-
	91%	0.067	-
	97%	0.118	-
	100%	0.138	-

The highlighted cells denote the data which were not directly reported, but where extracted by the scientific team, from figures, or from extrapolation of given data.

Appendix C. Example Application of Cracked Continuum Shear Strength Assessment Procedure

Input.

Geometric properties:

b_w = 20 in.
h = 44 in.
d = 40 in.
a = 80 in.
l_{b1} = 12 in.
l_{b2} = 12 in.

Concrete properties:

f'_c = -4000 psi
ε'_c = -2 me
E_c = 4000 ksi
f_{cr} = 253 psi
a_g = 1.00 in.

Reinforcement properties:

ρ_l = 1.500 %
f_{yl} = 60,000 psi
d_{bl} = 1.41 in.
ρ_h = 0.25 %
f_{yh} = 60,000 psi
d_{bh} = 0.50 in.
ρ_v = 0.25 %
f_{yl} = 60,000 psi
d_{bv} = 0.50 in.
E_s = 29,000 ksi

Crack properties:

w_{cr} = 0.05 in.
θ_{cr} = 40 degrees
x_{cr} = 34 in.

Solution. This load stage is shown as an example. To predict failure and determine the load level/residual capacity, crack width should be incremented until load starts decreasing for several load stages.

Calculate average crack spacing based on reinforcement details (Equation 4.12).

$$
\begin{aligned}
c_a &= 1.5a_g \\
&= 1.5 \text{ in.} \\
s_b &= \left(\sum_{i=1}^{3} \frac{2\cos^2\theta_{ni}}{d_{bi}}\sqrt{\frac{\rho_i}{\pi}}\right)^{-1} \\
&= 6.52 \text{ in.} \\
s_m &= \sum_{i=1}^{3} \frac{\rho_i}{d_{bi}} \cos^2\theta_{ni} \\
&= 0.00940 \text{ in.}^{-1} \\
s_{cr} &= 2\left(c_a + \frac{s_b}{10}\right) + \frac{0.1}{s_m} \\
&= 14.95 \text{ in.}
\end{aligned}
$$

Calculate tensile strain normal to crack plane (Equation 4.2).

$$
\begin{aligned}
\varepsilon_{1'} &= w_{cr}/s_{cr} \\
&= 3.345 \text{ me}
\end{aligned}
$$

Estimate compressive strain parallel to crack plane.

$$\varepsilon_2^{ic} = -0.244 \text{ me}$$

Estimate shear strain on crack plane.

$$\gamma_{12}^{ic} = 0.554 \text{ me}$$

Calculate concrete stresses on crack plane (Figure 4.10(7)-(13) and Equation 4.31).

$$
\begin{aligned}
m &= \left(\sum_{i=1}^{3} \frac{4\rho_i}{d_{bi}} |\cos\theta_{ni}|\right)^{-1} \\
&= 18.0 \\
c_t &= 91.4 \cdot 0.6 \cdot m \\
&= 988 \\
f_{c1'} &= \frac{f_{cr}}{1+\sqrt{c_t\varepsilon_{1'}}} \\
&= 90 \text{ psi} \\
C_s &= 0.55 \\
r &= -\varepsilon_{1'}/\varepsilon_{2'} \\
&= 13.71
\end{aligned}
$$

$$
\begin{aligned}
C_d &= 0.35(r-0.28)^{0.8}\\
&= 2.80\\
\beta_d &= \frac{1}{1+C_s C_d} \leq 1\\
&= 0.394\\
f_{c2'} &= \beta_d f_c' \left(2\frac{\varepsilon_{c2'}}{\beta_d \varepsilon_c'} - \left(\frac{\varepsilon_{c2'}}{\beta_d \varepsilon_c'}\right)^2\right)\\
&= \text{-823 psi}\\
v_{c1'2'} &= 106\sqrt[3]{f_c'}\,\frac{\left(\gamma_{1'2'}/\varepsilon_{1'}\right)^2}{1+\left(\gamma_{1'2'}/\varepsilon_{1'}\right)^2}\\
&= \text{45 psi}
\end{aligned}
$$

Calculate reinforcement stresses (Figure 4.10(14)).

$$
\begin{aligned}
\varepsilon_x &= \varepsilon_{1'}\sin^2\theta_{cr} + \varepsilon_{2'}\cos^2\theta_{cr} - \gamma_{1'2'}\cos\theta_{cr}\sin\theta_{cr}\\
&= \text{0.966 me}\\
\varepsilon_y &= \varepsilon_{1'}\cos^2\theta_{cr} + \varepsilon_{2'}\sin^2\theta_{cr} + \gamma_{1'2'}\cos\theta_{cr}\sin\theta_{cr}\\
&= \text{2.135 me}\\
f_{si} &= E_s\varepsilon_i \leq f_{yi}\\
f_{sl} &= \text{28,019 psi}\\
f_{sh} &= \text{28,019 psi}\\
f_{sv} &= \text{60,000 psi}
\end{aligned}
$$

Establish equilibrium in global coordinate system (Figure 4.10(16)-18)).

$$
\begin{aligned}
f_{cx} &= f_{c1'}\sin^2\theta_{cr} + f_{c2'}\cos^2\theta_{cr} - v_{c1'2'}\,2\cos\theta_{cr}\sin\theta_{cr}\\
&= \text{-490 psi}\\
f_{cy} &= f_{c1'}\cos^2\theta_{cr} + f_{c2'}\sin^2\theta_{cr} + v_{c1'2'}2\cos\theta_{cr}\sin\theta_{cr}\\
&= \text{-243 psi}\\
v_{cxy} &= (f_{c2'} - f_{c1'})\cos\theta_{cr}\sin\theta_{cr} + v_{c1'2'}(\cos^2\theta_{cr} - \sin^2\theta_{cr})\\
&= \text{-442 psi}\\
\sigma_x &= f_{cx} + \rho_l f_{sl} + \rho_h f_{sh}\\
&= \text{0 psi}\therefore OK\\
\sigma_y &= f_{cy} + \rho_v f_{sv}\\
&= \text{-93 psi}\\
\tau_{xy} &= v_{cxy}\\
&= \text{-442 psi}
\end{aligned}
$$

Check for assumed transverse stress proportion (Equations 4.27 and 4.28).

$$
\begin{aligned}
\frac{\sigma_y}{|\tau_{xy}|} &= \text{-0.211}\\
&= \sum_{i=1}^{2} -\frac{1}{2}\frac{h}{a}\left(\frac{2.5}{0.6+4\frac{x_{cr}}{c}} - 0.5\right)\\
&= \text{-0.211}\therefore OK
\end{aligned}
$$

Example of iterative solution procedure. The above example was done for a converged load stage. Typically, the compressive strain parallel to the crack and the shear strain on the crack are determined in an iterative manner. An initial guess of the compressive strain parallel to the crack is made and a corresponding shear strain on the crack is determined to satisfy the requirement that the average x-direction stress is equal to zero; then, a check is made on the y-direction stress proportion. If the anticipated stress proportion is not satisfied, the guess for compressive strain must be revised. Table C1 shows the iterations required to converge the load stage presented in this appendix.

Table C1 Example iterations for worked example

$\varepsilon_{2'}$ $(10)^{-3}$	$\gamma_{1'2'}$ $(10)^{-3}$	$f_{c2'}$ psi	$v_{c1'2'}$ psi	ε_x $(10)^{-3}$	ε_y $(10)^{-3}$	f_l psi	f_h psi	f_v psi	σ_x psi	σ_y psi	τ_{xy} psi	σ_y/τ_{xy}
-0.100	1.219	-358	197	0.723	2.522	20969	20969	60000	0	248	-186	1.332
-0.200	0.770	-688	84	0.886	2.259	25687	25687	60000	0	2	-368	0.004
-0.300	0.233	-993	8	1.091	1.954	31641	31641	56664	0	-208	-532	-0.391
-0.290	0.296	-964	13	1.066	1.989	30925	30925	57670	0	-188	-516	-0.365
-0.280	0.355	-934	19	1.043	2.022	30247	30247	58638	0	-168	-501	-0.336
-0.270	0.412	-904	25	1.021	2.054	29602	29602	59573	0	-147	-485	-0.303
-0.260	0.467	-874	32	0.999	2.086	28985	28985	60000	0	-127	-469	-0.270
-0.250	0.521	-843	40	0.979	2.116	28391	28391	60000	0	-107	-453	-0.236
-0.240	0.573	-813	48	0.959	2.146	27819	27819	60000	0	-86	-436	-0.197
-0.241	0.567	-816	47	0.961	2.143	27875	27875	60000	0	-88	-438	-0.201
-0.242	0.562	-819	46	0.963	2.140	27932	27932	60000	0	-90	-439	-0.205
-0.243	0.557	-822	45	0.965	2.137	27989	27989	60000	0	-92	-441	-0.209
-0.244	0.552	-825	44	0.967	2.134	28046	28046	60000	0	-94	-443	-0.213
-0.245	0.547	-828	44	0.969	2.131	28103	28103	60000	0	-96	-444	-0.217
-0.2449	0.547	-828	44	0.969	2.131	28097	28097	60000	0	-96	-444	-0.217
-0.2448	0.548	-827	44	0.969	2.132	28091	28091	60000	0	-96	-444	-0.216
-0.2447	0.548	-827	44	0.968	2.132	28086	28086	60000	0	-96	-444	-0.216
-0.2446	0.549	-827	44	0.968	2.132	28080	28080	60000	0	-96	-444	-0.215
-0.2445	0.549	-826	44	0.968	2.132	28074	28074	60000	0	-95	-444	-0.215
-0.2444	0.550	-826	44	0.968	2.133	28068	28068	60000	0	-95	-443	-0.215
-0.2443	0.550	-826	44	0.968	2.133	28063	28063	60000	0	-95	-443	-0.214
-0.2442	0.551	-826	44	0.967	2.133	28057	28057	60000	0	-95	-443	-0.214
-0.2441	0.551	-825	44	0.967	2.134	28051	28051	60000	0	-95	-443	-0.213
-0.2440	0.552	-825	44	0.967	2.134	28046	28046	60000	0	-94	-443	-0.213
-0.2439	0.552	-825	45	0.967	2.134	28040	28040	60000	0	-94	-443	-0.213
-0.2438	0.553	-824	45	0.967	2.134	28034	28034	60000	0	-94	-442	-0.212
-0.2437	0.554	-824	45	0.966	2.135	28028	28028	60000	0	-94	-442	-0.212
-0.2436	0.554	-824	45	0.966	2.135	28023	28023	60000	0	-94	-442	-0.212
-0.2435	0.555	-823	45	0.966	2.135	28017	28017	60000	0	-93	-442	-0.211